ISBN 978-82-326-2854-4 (printed version)
ISBN 978-82-326-2855-1 (electronic version)
ISSN 1503-8181

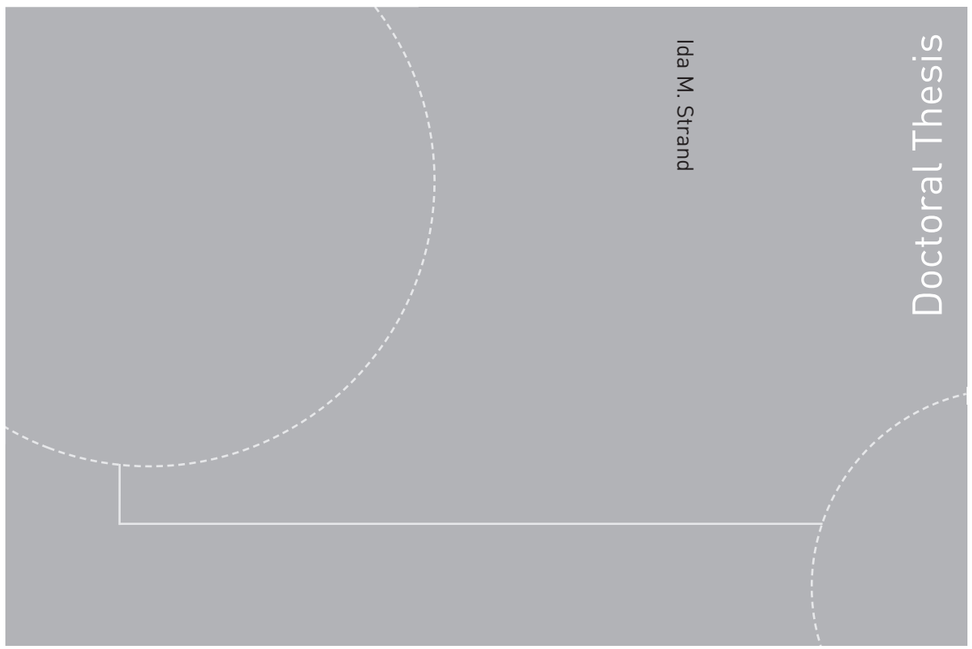

Doctoral theses at NTNU, 2018:28

Ida M. Strand

Sea Loads on Closed Flexible Fish Cages

NTNU
Norwegian University of
Science and Technology

Doctoral theses at NTNU, 2018:28

NTNU

NTNU
Norwegian University of
Science and Technology
Faculty of Engineering
Department of Marine Technology

NTNU
Norwegian University of
Science and Technology

Ida M. Strand

Sea Loads on Closed Flexible Fish Cages

Thesis for the degree of Philosophiae Doctor

Trondheim, February 2018

Norwegian University of Science and Technology
Faculty of Engineering
Department of MarineTechnology

NTNU
Norwegian University of
Science and Technology

NTNU
Norwegian University of Science and Technology

Thesis for the degree of Philosophiae Doctor

Faculty of Engineering
Department of MarineTechnology

ISBN 978-82-326-2854-4 (printed version)
ISBN 978-82-326-2855-1 (electronic version)
ISSN 1503-8181

Doctoral theses at NTNU, 2018:28

Printed by Skipnes Kommunikasjon as

Abstract

Norway has become the world's largest producer of Atlantic salmon through the use of open net structures in the sea. The aquaculture facilities have grown in both size and number. Currently, the industry faces increased attention on environmental challenges related to fish escapes, sea lice, diseases, and pollution. A possible solution is to use a closed flexible fish cage (CFFC) with impermeable membrane material instead of nets used in conventional aquaculture cages. Compared to a net-based structure the response to sea loads of the new membrane-based system changes completely. Few ocean structures exist with large, compliant submerged components, and even fewer with a free surface. It is therefore presently limited existing knowledge about how CFFCs will respond to sea loads. It is therefore a need for the development of fundamental knowledge and understandings of the physics of the CFFC. From this understanding we will develop mathematical models of the sealoads and the response of the CFFC.

Model experiments of scaled models of the CFFC in current for different filling levels have been conducted in multiple rounds to build knowledge of the system. In current, the response of the CFFC has been found to be highly dependent on the filling-level. For underfilled CFFC, a large deformation shaped like a hemispherical cup, comparable to a parachute, appear at the front facing the current. This deformation lead to a change in the geometry resulting in an increase in the drag force related to a full CFFC.

From the experiments it was observed that the problem of a CFFC in current can be characterised by a complex interaction between the membrane, the fluid masses within the CFFC and the outside fluid flow. In order to reduce the complexity of the problem, it was decided to model the system in 2D. In addition, it was chosen to shift the focus from current to waves allowing for the use of potential flow theory in the load modelling.

To develop theory and understanding of the membrane structure, and the coupling between structural response and internal water motions, the response of a 2D rectangular sloshing tank with a fabric membrane side wall subject to forced sway motion was analysed. It was found that the response and the eigenfrequencies of the coupled system relied heavily on both the membrane structure through the tension, the membrane length, and the hydrodynamic pressure.

A mathematical model of a 2D CFFC in waves was then developed. In order to analyse the CFFC in waves, equations for the geometry and initial tension of the membrane of the CFFC were found. Based on the found geometry and static tension, the wave response of a 2D CFFC in sway, heave and roll was studied. It

was found that the rigid body wave induced motion responses of a CFFC with membrane in sway, heave and roll are significantly different from the responses of a rigid CFFC. Very large ratios between free-surface elevation amplitudes and incident wave amplitude are predicted inside the tank at the first and third natural sloshing frequencies. It implies that nonlinear free surface effects must be accounted for inside the tank in realistic sea conditions, as well known from other marine sloshing applications (Faltinsen and Timokha, 2009). Within linear structural theory we require that the dynamic tension in the membrane of the CFFC is smaller than the static tension. For the analysed case with given dimensions, for significant wave heights larger than 0.5 meter, the most probable largest dynamic tension is larger than the static tension. For negative total tensions the structural model is not valid. Therefore, a higher order structural model should be used. The effect of scaling of elasticity on the rigid body motion have also been investigated. To scale the elasticity of the fabric is unfortunately not straight forward. The response of the CFFC using an elasticity available in model scale have been compared to the response of the CFFC using the elasticity for full scale. These responses where found to deviate to a large extent. This raises severe questions of the direct use of results from model scale experiments for the CFFC.

Preface

This thesis is submitted in partial fulfilment of the requirements for the degree of Philosophiae doctor (PhD) at the Norwegian University of Science and Technology (NTNU). I have done this work at the Department at Marine Technology, NTNU. My main supervisors have been Professor Asgeir J. Sørensen, NTNU and Professor Odd M. Faltinsen, NTNU. Professor Pål Lader, NTNU/ Sintef Ocean has been my co-supervisor.

This work has been financed by the Research Council of Norway through the project "External Sea Loads and Internal Hydraulics of Closed Flexible Cages" (grant no. 216127). The work has been carried out at the Centre for Autonomous Marine Operations and Systems (AMOS), supported by the Research Council of Norway through the Centres of Excellence funding scheme, project number 223254 - AMOS. The Norwegian Research Council is acknowledged as the main sponsor of AMOS.

Acknowledgments

I want to thank my supervisors Professor Asgeir J. Sørensen and Professor Odd M. Faltinsen. Professor Asgeir J. Sørensen, you find the time to give inspiring advise both on the scientific work and on life in general, and I feel that you genuinely care. Professor Odd M. Faltinsen, your immense knowledge and considerable patience in answering seemingly stupid questions have been vital for me to complete this journey. Thanks to my co-supervisor Dr. Pål Lader at SINTEF Ocean (now professor Pål Lader at NTNU) for the welcoming reception at SINTEF Ocean during my two stays there. I am also grateful for the friendly welcome in the industry group of the project "External Sea Loads and Internal Hydraulics of Closed Flexible Cages".

Thanks to Torgeir Wahl (NTNU) and Dr. Zsolt Volent (SINTEF Ocean) for giving valuable help during the two periods of experiments conducted in the spring of 2013 in the Marine Cybernetics Laboratory (Mc-Lab).

I want to thank my fellow doctoral students and post docs at AMOS and at the department, for fun and inspiring discussion over coffee and lunch. Through the arrangement of Technical Thursday, I have gotten to know many of you. Special thanks to Astrid and my office mates Signe, Thomas, Stefan and Einar.

Thanks also to Ann-Johanne at the Marine Technology library, for library guidance, small-talk and tea.

I am grateful for my family and friends, for believing in me, and forgiving me not always being physically and/or mentally present. Special thanks to my parents

and my husband Håkon, and last but not least to my daughter Ingeborg, you gave me (needed) time and perspective.

Trondheim, January 2018 *Ida M. Strand*

Contents

List of Figures

List of Tables

Nomenclature

- Only the most used symbols are listed in the following
- Superscript (i) indicates internal, and superscript (e) indicates external
- Vectors and matrices are represented with bold symbols

Abbreviations

2D	Two-dimensional
3D	Three-dimensional
CFFC	Closed flexible fish cage
HPC	Harmonic polynomial cell method
IBM	Immersed boundary method
Re	Reynolds number

Greek and mathematical symbols

α_{0m}	Fourier coefficient
α_{km}	Fourier coefficient
β_n	Generalized free surface coordinate
γ_{2n}	Hydrodynamic coefficient associated with sway motion
γ_{dnm}	Hydrodynamic coefficient associated with the wall deformations
Δh	Water height difference between inner and outer free-surface levels
Δp	Pressure difference
Δp_0	Static pressure difference
$\Delta \hat{p}$	Dynamic pressure difference
$\Delta \rho$	Density difference
ζ	Free surface elevation
ζ^i	Internal wave elevation

ζ_a	Incident regular wave amplitude
η_2	Sway motion
η_3	Heave motion
η_4	Roll motion
τ	Dynamic tension
κ_n	Wave number
λ	Filling level of the bag in experiments
λ_m	Dry structural natural frequency
λ_m^*	Wet 2D membrane eigenfrequency
μ_k	Generalized complex structural mode amplitudes in tangential direction
ν	Kinematic viscosity of the fluid
ν_m	Generalized normal complex structure mode amplitudes
ρ_c	Density of membrane material
ρ_w	Fluid density
ρ_{wi}	Density of the water inside the membrane
Σ_0	Mean free surface
Φ	Total velocity potential, composed of multiple velocity potentials
ϕ	Velocity potential
ϕ_0	Velocity potential for incident waves
ϕ_d	Diffraction velocity potential
ϕ_j	Radiation velocity potentials associated with the body motions j
ϕ_R^+	Far-field velocity potentials
$\hat{\psi}$	Dynamic angle
ψ	The angle between the membrane tangent and the $y-$ axis
ψ_0	The angle between the membrane tangent and the $y-$ axis at rest
ψ_e	The angle at the attachment point between membrane and floater
ω	Forcing frequency
ω_n	Natural sloshing frequencies
ω_n^*	Coupled sloshing frequency
Ω_{dm}	Deformation velocity potential
∇	Displaced volume of water of the CFFC per unit length

Roman symbols

A	Projected frontal area
A^+	Far-field complex wave amplitude
A_L	Area of inside wetted floater surface
A_R	Area of outside wetted floater surface
$A_w(z_e)$	Waterplane area
$a_{kj}^{(e)}$	Added mass coefficient in k direction, due to a motion in j direction in 2D
$a_{mj}^{(\Omega)}$	Coupled added mass coefficient associated with Ω
$a_{nj}^{(\phi)}$	Coupled added mass coefficient associated with ϕ
b_t	Internal distance between the floater at the free surface of the CFFC
$b_{kj}^{(e)}$	Damping coefficient in k direction, due to a motion in j direction in 2D
$\overline{C}_D(\lambda)$	Mean drag coefficient for each filling level
C_D	Drag coefficient
c_{mj}	Structure fluid restoring coefficients associated with quasi- static hydrostatic pressure change
D	Diameter of filled bag in experiments
d	Thickness of the membrane
d_F	Thickness of fabric in full scale
d_M	Thickness of fabric in model scale
E	Young's Modulus
F	Force component
F_D	Drag force
F_x	Force measurements in x direction
$f_{exc,k}$	Generalised excitation load in k direction in 2D
g	Gravitational acceleration
h	Mean liquid depth of tank
h_B	Max draft of filled bag in experiments
h_d	Deformed draft of filled bag in experiments
H_s	Significant wave height
k	Wave number

k_s	Spring stiffness for rigid wall test case
L	Length of membrane
l	Tank breadth
l_g	Geometric scale ratio
$\overline{m}_c$	Generalized modal mass
$\overline{m}_n$	Hydrodynamic coefficient associated with water mass
m_M	Membrane mass per unit area in air
$\boldsymbol{n_D}$	Dynamic normal direction of a membrane element
$\vec{n}$	Normal vector
p	Pressure
R	Radius of 2D CFFC
R_F	Radius of the floaters of the CFFC
R_n	Generalized coordinates for the velocity potential
s	Curvilinear coordinate along the membrane
S_B	Mean wetted body surface
S_M	Mean wetted membrane surface
S_∞	Vertical control surfaces between $z = 0$ and $z = -h$ at $y = \pm\infty$
S_{Fl}	Mean wetted floater surface
$\boldsymbol{t_D}$	Dynamic tangential direction of a membrane element
L/r	Non-dimensional travelled distance
T	Tension in membrane
t	Time
T_0	Reference tension
T_p	Peek period of the waves
U	Towing velocity of the bag in experiments
U_m	Structural mode
v	deformation in the $y-$ direction
V_0	Full volume of the bag in experiments
z_B	Coordinate of the center of the buoyancy
z_e	z coordinate of the attachment point between membrane and floater
z_G	Coordinate of the center of gravity

Chapter 1

Introduction

Closed flexible fish cages (CFFCs) are membrane structures made of fabric. They are proposed used in the sea for salmon fish farming trying to overcome the environmental challenges the aquaculture industry is meeting today with the conventional gravity cage net systems. Compared to a net-based structure the response of the new membrane-based system to sea loads changes completely. In this thesis, sea loads on CFFCs are studied.

This chapter starts with the motivation for the development of the CFFC. Thereafter, the CFFC system and the sea loads that work on the system is described. The history of the development of the CFFC is given in the following section. Research challenges and methods are then described, before a list of publications is given. The thesis contributions are then presented before the outline of the thesis is given at the end.

1.1 Motivation

Fish represent a vital contribution to the world's food supply. However, at the same time as the population of the world is growing, many marine capture fisheries have become depleted, and the fish are harder to catch. The question arises: "Is it possible to meet the increasing demand for seafood?" One alternative is to produce the fish in aquaculture (Tidwell and Allan, 2012).

Norway is presently the worlds biggest producer of Atlantic salmon. The traditionally used open-net-structures are probably the most important reason for the Norwegian success. The open net-structures is a simple, inexpensive technology that utilises the Norwegian advantage of abundant access to fresh and clean seawater (Rosten et al., 2013).

The very nature of aquaculture, where fish is grown at a much higher density than appearing naturally, makes it likely to affect the existing surrounding environment (Crawford and MacLeod, 2009). While the aquaculture facilities have grown in size and number, the attention related to the industry's ecological sustainability have increased. Views on shortcomings related to the traditional technology have been stated. These weaknesses concern sustainability challenges related to escapes, sea-lice, diseases and pollution (Gullestad et al., 2011).

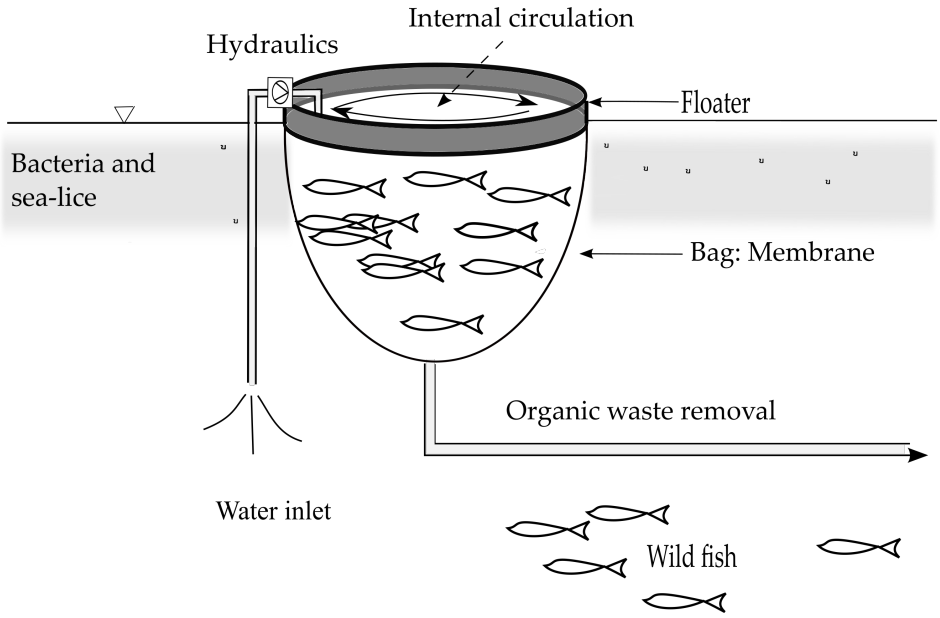

Figure 1.1: Illustration of the components of the closed flexible fish cage, including external environmental challenges.

The attention the industry faces related to environmental challenges is despite improvements in technology and operational procedures. The aquaculture industry is under pressure to develop technology and procedures that reduce the influence from the aquaculture on the environment Michael et al. (2010).The aquaculture industry in Norway is being held back from growing by the Norwegian government until they can solve the problems related to sea lice and fish escapes. To stimulate to technology development the Norwegian Directorate of Fisheries has opened for that the industry can apply for technology development licenses (Norwegian Directorate of Fisheries, 2017). The industry has responded by intensifying the work with developing technology to meet the challenges. One response to the environmental challenges lies in developing open water closed containment aquaculture technology, where CFFC is one of the proposed concepts.

1.2 The closed flexible fish cage

Closed containment technology is a term used to describe technologies that attempt to restrict and control the interaction between the farmed fish and the surrounding environment, with the goal of minimising the impact and getting better control over the aquaculture production (Michael et al., 2010). In a closed fish production system, the farmer has increased control of how the fish are exposed to and influence the environment, by controlling the flow and quality of the water entering and leaving the production system (Hægermark, 2013). The water circulation can cause a more

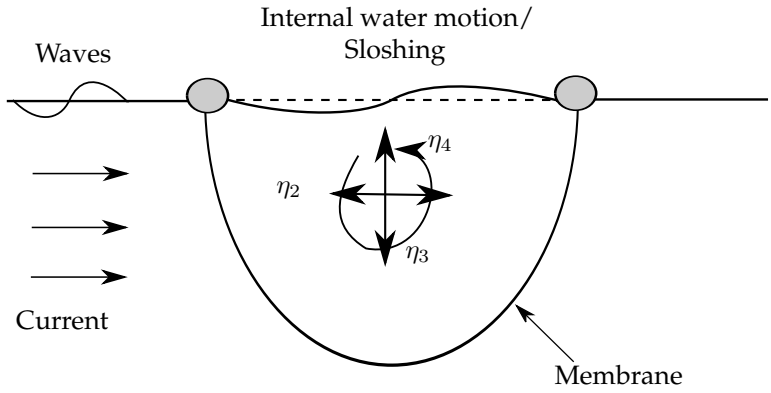

Figure 1.2: Illustration of sea loads from current, waves and internal water motions on the closed flexible fish cage. The closed flexible fish cage will in 2D move in 3 DOF, η_2, η_3 and η_4 are the motions in sway, heave and roll respectively.

stable environment inside the production system, which can be an advantage related to fish welfare and growth (Rosten et al., 2011). By controlling the flow in and out of the production system, it is also expected that the waste-pollution will be limited. As an answer to the development licenses incentive, several closed fish farming concepts have been proposed and are being tested: both rigid systems made of steel, concrete or composites and flexible systems made of fabric (Aadland, 2015).

One way of making a closed fish production system is as a closed flexible fish cage (CFFC) placed in the sea. Later we will denote the CFFC also as a bag. The industry standard of conventional aquaculture cages today are the floating gravity cages. The main components are: net cage, floating collar, weight system, and grid mooring. The main idea of the CFFC is to replace the net structure with an impermeable membrane, and potentially reuse the floater and mooring system of conventional aquaculture gravity net cage systems. By reusing available components, the CFFC may be easier to put directly into operation at existing sites. The membrane is a tight barrier, and it is, therefore, crucial to secure adequate water quality inside the cage for the fish to thrive. By hydraulics, the water is pumped in and out to ensure a sufficient flow-through and circulation inside the cage and removal of the waste. The hydraulics will require a continuous power supply. See illustration of the system elements in Figure 1.1.

The CFFC is subject to waves and current loads. Additionally, due to the open internal free surface, the cage will also experience internal water motions known as sloshing, see Figure 1.2. The CFFC is flexible and behaves hydro-elastically. This means that the deformation of, and hydrodynamic forces on the bag are closely coupled, see Figure 1.3 for illustration. The deformations and forces on the CFFC depend on both the external and internal hydrodynamic pressure as well as the structure dynamics. In a rigid system such as ships and offshore oil platforms, the structural response and the hydrodynamic forces are decoupled.

The flexibility of a fabric structure is governed by the elasticity of the material

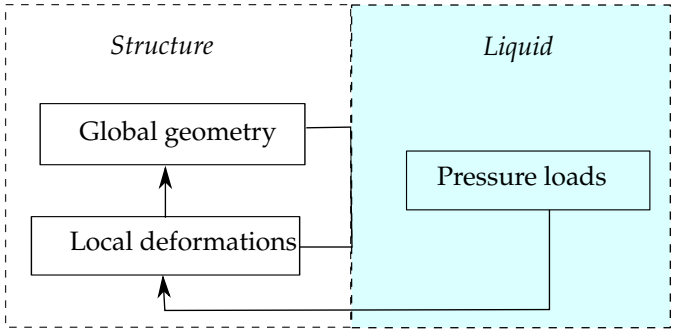

Figure 1.3: Hydro-elastic relations

and the tension in the fabric. When a flexible structure is exposed to external loads, the reaction is a change in shape. Due to this response, it is no longer possible to decouple the hydrodynamic and the structural analysis, and the problem must be treated hydro-elastically (Løland and Aarsnes, 1994). Few other ocean structures exist with large, compliant submerged components, and even fewer with a free surface. It is therefore presently limited existing knowledge about how CFFCs will respond to sea loads (Rosten et al., 2011).

To be able to design a robust CFFC system, knowledge of the behaviour of the closed flexible fish cage when subjected to sea loads is vital. An industry research project managed by SINTEF Ocean (former SINTEF Fisheries and Aquaculture) with NTNU as one of the partners called "External Sea Loads and Internal Hydraulics of Closed Flexible Cages" have been run to secure this knowledge. This PhD project is a part of that industry research project.

1.3 The historical development of the closed flexible fish cage

Different versions of the CFFC concept have been tested out on earlier occasions. One of the first Norwegian attempts was at a research-station at Matre, Norway around 1988. The system was then referred to as promising (Rosten et al., 2011).

A similar system was tried out at the start of the nineties, at Støytland Fisk in Flekkefjord also in Norway, as part of a research project run by Agder Research Foundation. A full scale test facility was made as illustrated in Figure 1.4 (Skaar and Bodvin, 1993). The aim of the project was to reduce/control the influence of the environmental effects, mainly algae blooms, fish-lice and extreme temperature variations on the fish production. A design project was also attached to this project that considered environmental loads on the cage (Solaas et al., 1993). An upscaled version of the Flekkefjord facility was later tried out close to Arendal in 1995. This facility experienced a total breakdown after a short time, due to material fatigue, and the concept was abandoned for a time (Rosten et al., 2011).

From September 2009 to September 2011 an EU research project coordinated by Plast Sveis AS called Closed Fish Cage were run (Johannessen, 2013). They aimed to develop a closed, escape proof, constant volume, sea-based cage for fish farming

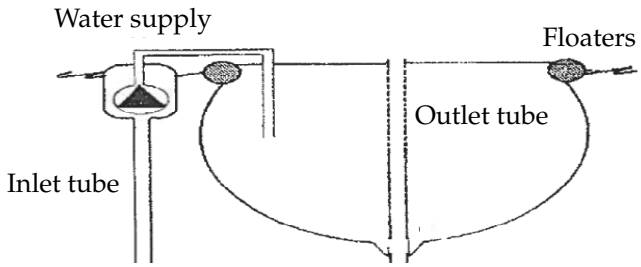

Figure 1.4: Technical illustration of the historical bag system used in Flekkefjord in 1990 in calm water. The bag is axisymmetric, with membrane, water supply, inlet tube, outlet tube and floaters. Adapted from Skaar and Bodvin (1993).

based on a flexible polymer plastic net pen. A pilot facility was tested out in Toft, Brønnøysund from September 2010 until June 2011. During this time they claimed that the system was working without problems and showed promising results related to sea-lice infestations.

The company Botngaard Systems AS has presently produced three full-scale systems for commercial use, presently in the sea (personal communication with Harald Tronstad at Botngaard Systems). One is presently used as a waiting cage before slaughtering of contagious fish to meet food authorities regulations. The cages can also be used for post-smolt (fish up to 400-1000 g) or full-size fish production aimed at the consumer marked (Botngaard Systems, 2017).

The company AkvaDesign AS develops closed fish cage systems. They have been able to run a full production cycle of farmed salmon without sea lice infestation (Akvafuture, 2017).

1.4 Research challenges

The previous experience with the CFFCs is limited. Before designing and deploying CFFC systems in the sea, the loads on and response of such a system in waves and current with internal water motion should be properly understood. To gain the needed knowledge the importance of conducting fundamental research on marine hydrodynamics to understand the behaviour and operation of the CFFC in the sea, cannot be emphasised enough. When the cage is less than full, the static tension in the membrane is zero and the geometry of the cage is given by the bending stiffness of the membrane. The bending stiffness of a fabric is in general negligible. Hence, the shape of the cage is therefore easily deformed. Since it is possible that the response of the cage changes with reduced filling levels, it is important to investigate how the cage behaves for filling levels less than 100%, to secure an adequate mooring and safety system. Here, the 100% filling level of the CFFC is defined according to the theoretical full volume of the CFFC.

Many physical phenomena can be encountered related to sea loads on the CFFC. The main focus in this thesis will be limited to loads on the hydroelastic membrane system from waves, current, and the internal water motions, coupled

with the structural deformation of the membrane. Research methodology will be to combine experimental observations with theoretical studies and numerical analyses to create knowledge about the behaviour of CFFCs subject to current and wave loads. With limited a priori knowledge of the physics of the CFFC, we will, :

- Conduct and use model experiments to acquire the basic understanding of the physics of the system through observations and response measurements.
- Study the effect of varying filling level on the drag forces acting on the CFFC in ambient current from model experiments.
- Develop mathematical models to describe the physics of a closed membrane structure with a free surface and internal water motions.

In the future it will be advantageous to optimise the response of the system by active control of the water inflow. To design proper control systems, sufficient physical understanding is required to formulate control objectives and propose control strategies to meet these objectives.

The following loads and effects will not be covered: Waves and current in combination, the coupling between the closed flexible fish cage and other potential objects (such as nets and boats), the biological aspect (the presence of the fish) and local flow effects due to the water exchange.

The gained knowledge from this project will contribute to raising the industry's understanding of the physics of such closed flexible fish cages. We will develop knowledge on modelling of response to sea loads on the CFFC. This will give the industry a better understanding of the behaviour, operation, and reliability of closed flexible fish cages, and second, it will give the scientific community a starting point for further work on these systems.

1.5 List of publications

The following papers published are considered part of this thesis.

Journal papers

- I. M. Strand and O. M. Faltinsen. Linear wave response of a 2d closed flexible fish cage. *Submitted to: Journal of Fluids and Structures*, 2018
- I. M. Strand and O. M. Faltinsen. Linear sloshing in a 2d rectangular tank with a flexible sidewall. *Journal of Fluids and Structures*, 73:70 – 81, 2017
- I. M. Strand, A. J. Sørensen, Z. Volent, and P. Lader. Experimental study of current forces and deformations on a half ellipsoidal closed flexible fish cage. *Journal of Fluids and Structures*, vol. 65, 2016

Additional authored and co-authored papers are considered background for the thesis.

Journal papers

- P. Lader, D. W. Fredriksson, Z. Volent, J. DeCew, T. Rosten, and I. M. Strand. Wave response of closed flexible bags. *Journal of Offshore Mechanics and Arctic Engineering*, 139(5), 2017

- P. Lader, D. W. Fredriksson, Z. Volent, J. DeCew, T. Rosten, and I. M. Strand. Drag forces on, and deformation of, closed flexible bags. *Journal of Offshore Mechanics and Arctic Engineering*, 137(August):041202, 2015

Conference papers

- P. Lader, D. W. Fredriksson, Z. Volent, J. DeCew, T. Rosten, and I. M. Strand. Wave Response of Closed Flexible Bags. In *ASME 2016 35th International Conference on Ocean, Offshore and Arctic Engineering*, volume 6: Ocean Space Utilization; Ocean Renewable Energy, 2016
- I. M. Strand, A. J. Sørensen, and Z. Volent. Closed flexible fish cages: Modelling and control of deformations. In *Proceedings of 33rd International Conference on Ocean, Offshore and Arctic Engineering. June 8-13, 2014, San Francisco, USA*, 2014
- P. Lader, D. W. Fredriksson, Z. Volent, J. DeCew, T. Rosten, and I. M. Strand. Drag forces on, and deformation of, closed flexible bags. In *Proceedings of 33rd International Conference on Ocean, Offshore and Arctic Engineering. June 8-13, 2014, San Francisco, USA*, 2014
- I. M. Strand, A. J. Sørensen, P. Lader, and Z. Volent. Modelling of drag forces on a closed flexible fish cage. In *9th IFAC Conference on Control Applications in Marine Systems. Osaka, Japan*, 2013

1.6 Thesis contributions

The main scientific contribution of the work is the following:
Chapter 3:
We have used model experiments to develop an understanding of the physics of the closed flexible fish cage in ambient current through observations and response measurements. The main findings are:

- For underfilled cages, a large deformation shaped like a hemispherical cup, comparable to a parachute, appear at the front facing the current. This deformation leads to a change in the geometry, resulting in an increase in the drag force related to a full cage.
- The problem of an under filled CFFC in current can be characterised by a complex interaction between the membrane, the water masses within the CFFC and the outside water flow.

Chapter 4:

- A 2D rectangular sloshing tank with a fabric membrane side wall in sway motion is studied in order to develop theory and understanding of the membrane structure, and the coupling between structural response and internal water motions.
- It was found that the eigenfrequencies of the system was found to be lower than the rigid tank sloshing eigenfrequencies, the eigenfrequencies was dependent on both the membrane tension and 2D membrane length. For low

tensions, more than one eigenfrequency of the coupled system may exist between the sloshing frequencies of a rigid tank.

Chapter 5:

- A mathematical model for the static equilibrium geometry and tension for a 2D membrane in calm water with a hydrostatic pressure difference have been developed. Direct solutions to these equations under certain assumptions have been found.

Chapter 6:

- A mathematical model of a 2D closed flexible fish cage in waves has been developed.
- It is found that the response of the rigid body motions in sway, heave and roll of a CFFC are significantly different from the response of a rigid CFFC.
- Very large ratios between free-surface elevation amplitudes and incident wave amplitude are predicted inside the tank at the first and third natural sloshing frequencies. It implies that nonlinear free surface effects must be accounted for inside the tank in realistic sea conditions, as well known from other marine sloshing applications (Faltinsen and Timokha, 2009).
- Within linear structural theory we required that the dynamic tension τ is smaller that the static tension T_0. For significant wave heights larger than 0.5 meter, the most probable largest dynamic tension is larger than the static tension. This indicated that a higher order structural model should be used.
- The effect of scaling of elasticity on the rigid body motion have been investigated. The results for a case using the full scale elasticity deviates to a large extent from the results using an elasticity used in model scale. This raises severe questions of the use of the results from model scale experiments.

1.7 Thesis outline

The thesis is organised as:

Chapter 2: presents the theoretical background for sea loads on CFFCs.

Chapter 3: gives experimental results for the effect of filling level on the drag forces on a half ellipsoidal closed flexible fish cage is presented and discussed. The study extends the results published in Strand et al. (2013) and Lader et al. (2015).

Chapter 4: uses potential flow theory to investigate linear sloshing in a 2D rectangular tank with a flexible side wall. The case is analysed both analytically and numerically. The deformation of the flexible wall is modelled by a modal approach. The effect of the wall deformation on the eigenfrequencies of the considered system is investigated.

Chapter 5: presents the analysis of a 2D static membrane under overpressure due to a hydrostatic pressure difference. The aim is to find the static geometry and the static tension in the membrane. Equations for the system is found and analysed in a case study.

Chapter 6: presents the development of the linear theory of a 2D closed flexible fish cage in waves. The theory is used to analyse the response of the CFFC in waves. The results from a 2D case study with relevant full scale dimensions, considering a half circularly shaped CFFC with floaters is given.

Chapter 7: presents general conclusions and recommendations for further work.

Appendix A: gives expressions for coefficients in equations for linear sloshing in a 2D rectangular tank with a flexible side wall.

Appendix B: presents the background formulations of the numerical potential theory harmonic polynomial cell (HPC) method.

Appendix C: presents full scale parameters of a commercial cage from Botngaard systems.

Appendix D: gives the membrane equation system for the membrane deformations for a semi- circular membrane.

Appendix E: gives the derivation of the relation between radiated wave amplitude and damping for finite water depth.

Appendix F: gives the plot of structural normal mode shapes for modes from one to ten.

Appendix G: presents error estimation of hydrodynamic coefficients.

Appendix H: presents a convergence study of number of structural modes.

Chapter 2

Theoretical background: Sea loads on closed flexible fish cages

Aquaculture in the sea located along the Norwegian coast is subjected to sea loads. The same sea loads will also work on the closed flexible fish cages, but in addition, the CFFC will also be subjected to forces from internal water motion, known as sloshing, as illustrated in Figure 1.2. Limited scientifically published material is available related to the effect of sea loads on closed flexible fish cages. Results from the design project done by the SINTEF group in the 90thies, that considered environmental forces on the bag were reported in Solaas et al. (1993). Results published as part of the project "External Sea Loads and Internal Hydraulics of Closed Flexible Cages" are given in Strand et al. (2013), Strand et al. (2014) , Lader et al. (2015) and Lader et al. (2017). Due to the limited background theory of sea loads on CFFCs, theory for comparable structures will be used as background knowledge and for comparison.

In this chapter the theoretical background for sea loads on CFFCs will be presented. The chapter starts with presenting background theory for comparable structures. The chapter ends with presenting the knowledge we have on sea loads on closed flexible fish cages.

2.1 Sea loads on comparable structures

Background knowledge and theory of aquaculture net cages and liquid filled membrane structures, also known as closed containment bags will be presented in the following.

2.1.1 Sea loads on aquaculture net cages

It may be convenient to compare the CFFC with conventional net cages used by the industry today. In NS9415 a classification of the wave and current loads according to the degree of exposure of the aquaculture site is given, see Table 2.1. Aquaculture net structures are also shown to behave hydroelastically with large dependencies

Table 2.1: Norwegian aquaculture site clasification scheme for waves and current, from NS9415. H_s is significant wave height, T_p is peak period of the wave spectrum and U_c is the current velocity.

Wave	H_s (m)	T_p (s)	**Degree of exposure**	**Current**	U_c (m/s)	**Degree of exposure**
A	0.0-0.5	0.0-2.0	Small	a	0.0-0.3	Small
B	0.5-1.0	1.6-3.2	Moderate	b	0.3-0.5	Moderate
C	1.0-2.0	2.5-5.1	Medium	c	0.5-1.0	Medium
D	2.0-3.0	4.0-6.7	High	d	1.0-1.5	High
E	>3.0	5.3-18.0	Extreme	e	>1.5	Extreme

between forces and deformations. The aquaculture net cages are not closed volume structures, and will therefore not have sloshing challenges.

Both structural and hydrodynamic models have been developed to analyse the loads on the structure in waves and current. Numerical simulation with experimental validation, in both waves, current and combined waves and current with satisfactory agreement have been conducted (Kristiansen and Faltinsen, 2015; Lader and Fredheim, 2006; Zhao et al., 2007; Kristiansen et al., 2015). Aquaculture net cage systems are composed of multiple interacting moving components. The total system consists of a net cage, floater, mooring lines and bottom weights. The importance of modelling the effect of all components in interaction have been emphasised in Kristiansen and Faltinsen (2015). For aquaculture net structures, it has been found that the drag decrease for increasing current compared to a rigid structure at the same current velocity due to large deformations decreasing the exposed area, see Lader and Enerhaug (2005). Due to the large variation between dimensions of components from large scale floaters to net twines, numerical analysis using Navier Stokes is considered too difficult and too computationally expensive. Simplified screen models in combination with a dynamic structural truss model (Kristiansen and Faltinsen, 2012) or simplified Morrison truss models are therefore used (Lader and Fredheim, 2006; Moe et al., 2010).

2.1.2 Sea loads on floating liquid filled membrane structures

A similar structure resembling the CFFC is the flexible containment bag used for transportation of fresh water or oil, first described by Hawthorne (1961). The closed containment bags have been subjected to both numerical and experimental studies. The research was first concerned with static shapes and tensions of the bags, directional stability of a flexible container under tow and later, stresses, motions and shapes of flexible containers in waves. Additionally, even though the container does not have an internal free surface as the CFFC, it has internal liquid motions, effecting the global response. The internal liquid motions have a resonance behaviour due to the elasticity of the bag.

For the flexible containment bags, the elasticity of the material and the tension in the fabric govern the shape and flexibility of a fabric structure (Løland and Aarsnes, 1994). It has been found that the shape and tension are strongly dependent on

the filling level, as presented in Hawthorne (1961), Zhao and Triantafyllou (1994) and Zhao (1995). The static tension decreases with decreasing filling level until it reaches zero. Theoretically, it is possible with negative static tension in membranes. However, membranes have negligible compression stiffness, and will buckle when subjected to negative tension (Shaw and Roy, 2007).

The effect of towing resistance of the bag was also examined by Hawthorne (1961). It was found that the main components of the drag were due to skin friction on the long body. It should be noted that the nose of the bag in the towing direction was designed rigid, not allowing any deformation of this part. Challenges with towing stability, related to decreased towing speeds, oscillatory behaviour of the rigid body and flexural instabilities resulting in flutter of fabric or buckling of the shape were experienced. Paidoussis and Yu (1976) found that the stability of the bag in tow is mainly controlled by appropriate design of the shape of the tail and nose sections of the body.

The response of the floating liquid filled fabric structure in waves have been examined and analysed both numerically and experimentally by Zhao and Triantafyllou (1994), Løland and Aarsnes (1994), Zhao (1995) and Phadke and Cheung (2001). Bottom mounted liquid filled membranes have also been examined, but will not be covered her. Mathematical models of the containment bags have mostly been formulated in 2D. The total pressure on the bag is an interaction between the internal and external pressure forces. Hawthorne (1961) modelled the internal water motion as a one-dimensional problem in the longitudinal direction, with one equation of motion of the liquid inside that membrane and one equation of continuity. The solution of these equations gave several resonances dependent on the wave length of the incoming wave and the length of the storage container. However, in experiments it was observed that the surrounding water introduced significant wave radiation damping, and these resonances were highly damped (Hawthorne, 1961). Zhao and Triantafyllou (1994) observed peaks in the numerical results of the dynamic pressure and dynamic tension due to resonant internal water motion. While Phadke and Cheung (2001) found that the peak in the dynamic tension and the peak in motion response did not necessarily coincide in frequency. All cited references have used linear theory both for the liquid and the structure in their numerical evaluations. However, Zhao and Aarsnes (1998) stated that linear structural theories for flexible containers are only valid for small incident wave amplitudes. This differs from theories for ship motions and is due to the requirement of a positive total tension in the membrane. Due to the still water body shape at the free surface, there are also strong hydrodynamic non-linearities. This implies that linear theory cannot be used for design wave or sea state condition calculations (Løland and Aarsnes, 1994).

2.1.3 Sloshing in tanks

Wave-induced sloshing (interior wave motion) becomes an issue as well-known from many engineering applications (Faltinsen and Timokha, 2009). Liquid sloshing in tanks represents a challenge both in the naval, air and space, civil and in the nuclear industry, and have therefore been thoroughly studied (Faltinsen and Timokha, 2009; Ibrahim, 2005). Since marine applications involve relatively large

excitation amplitudes, resonant sloshing can involve important non-linear free-surface effects. The viscous boundary layer damping is very small. However, if breaking waves occur, the associated hydrodynamic damping is not negligible. Lateral tank excitations with periods near the highest natural sloshing period are of primary concern. The highest natural sloshing period in rigid half-filled spherical tank of radius R_0 is $T_{11} = 2\pi\sqrt{R_0/1.56016g}$ with g as acceleration of gravity Faltinsen and Timokha (2009). Structural elastic membrane effects for flexible cages will influence the natural sloshing frequencies.

Experimental and theoretical studies of sloshing in a vertical circular cylinder with horizontal harmonic forcing show that different overlapping wave regime involving planar waves, swirling waves and irregular chaotic waves occur (Faltinsen and Timokha, 2009). Irregular chaotic waves mean that no steady-state condition occur while the planar and swirling waves are steady state. The waves are a consequence of non-linear transfer of energy between sloshing modes. Which wave regime occurs depends on initial and transient conditions. Swirling waves have been of particular concern in designing spherical LNG tanks. A reason is the large horizontal forces occurring with components in-line and perpendicular to the forcing direction. It matters for the tank support and in the buckling analysis of the sphere.

There is important coupling between sloshing and the external flow through the body motions (Rognebakke and Faltinsen, 2003). When considering a CFFC, we must account for normal and tangential deformations of the membrane structure.

2.2 Sea loads on closed flexible fish cages

In this section, results from Solaas et al. (1993), Strand et al. (2013), Strand et al. (2014), Lader et al. (2015) and Lader et al. (2017).

2.2.1 Static pressure forces and deformations

For an overfilled closed flexible fish cage, Solaas et al. (1993) stated that to maintain the shape of the bag, a positive pressure difference inside the bag given as $\Delta p = p_i - p_o$, where p_i is the internal pressure and p_o is the external pressure, is essential. A positive pressure difference is also essential for the water exchange.

Strand et al. (2014) looked at the load history effects on an under-filled bag under static conditions, where under-filled implied that the bag had less filling level related to the theoretic geometric volume than 100%. Filling levels from 100% to 70% were examined. The bag was subjected to different load histories from waves and current, with and without applied horizontal braces. The horizontal braces were thin plastic tubes introducing stiffness in the circumferential direction. Experimental data were analysed related to deformations on the bag for different filling levels. They found that the bag had a clear tendency to deform when the bag was less than 100% full. These deformations increase in magnitude with decreasing filling level. Multiple deformation patterns were found dependent on filling level and load history. The deformations were different for current and wave load

histories. For the braced bag only one deformation pattern was found independent of load history.

2.2.2 Wave loads

Wave loads and motions will introduce dynamic tensions in the fabric. Solaas et al. (1993) reported from the results from model experiments that the dynamic tension in the fabric was described as relatively small. However, concern was expressed related to observed wave motions in the fabric propagating downwards. The concern was related to that these wave motions could introduce critical local peak loads in the fabric if the fabric motions were suppressed for instance by a penetrating tube.

Lader et al. (2015) investigated the behaviour of the CFFC in regular waves through model experiments in a small wave tank. The model was subjected to regular waves with wave periods from 0.5s to 1.5s. The wave length of these waves corresponded to 0.5-4.6 times the bag diameter. Three different wave steepnesses were used; 1/60, 1/30 and 1/15. The bag was tested in $100\%^{+}$ filling level, which is close to a condition intended used in production and a 70% filling level, which is a damage condition. The filling level is related to the theoretic volume of the geometric shape. When the bag was under-filled, it was allowed to globally deform. From the experimental results, it was concluded that the deflated bags (70% filling level) had a better behaviour related to motions and water integrity inside the bag than the inflated bags ($100\%^{+}$ filling level). The integrity of the bags, i.e. whether water entered or left the bag over the floater was challenged for smaller waves for the inflated bags. In total, the interaction and coupling between the bag, the internal water and the floater were described as complex, with significant non-linear characteristics. The fabric tension and motion were not measured, but violent fluttering was observed from underwater video recording. This fluttering was described as most violent for the inflated case, and concern for snap-loads in the fabric was expressed.

2.2.3 Current loads

Solaas et al. (1993) modelled the effect of current forces and deformation on a full bag pen, which is an early version of the CFFC. They found both global and local deformation patterns. The global deformation of the bag pen was approximated based on moment equilibrium. A symmetric deformation of both the front and the back wall of the bag were found, comparable to deformations of a rigid beam under pressure as in Figure 2.1. Local deformations of the bag wall were approximated based on the varying pressure distribution around a rigid circular cylinder in a steady flow. Due to these pressure variations, the front of the bag was pressed inwards in an area of $\pm 30\,\mathrm{deg}$ upstream of the bag, see Figure 2.1.

Strand et al. (2013) and Lader et al. (2015) studied the effect of varying filling level on the drag force for different geometries experimentally. The experiments were conducted in the small towing tank at the US Naval Academy in August 2012. Strand et al. (2013) analysed the results for a cylindrical bag, and Lader et al. (2015) compared four different geometries: a cylindrical bag with a cone at the bottom,

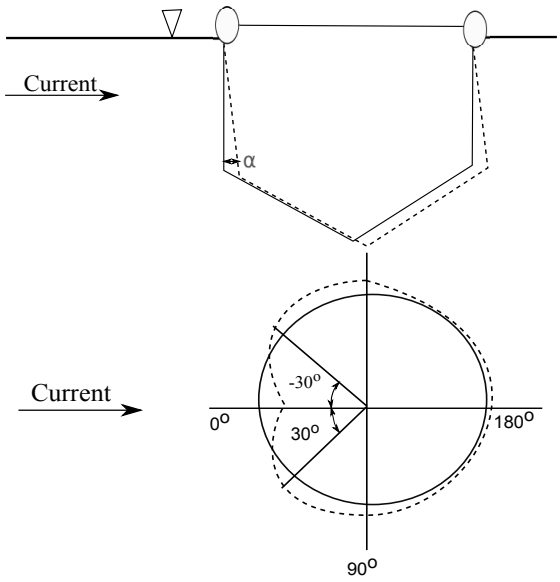

Figure 2.1: Deformations of a bag pen in current, adapted from Solaas et al. (1993). Top: Global horizontal deformation of bag pen, side view. Bottom: Local deformation of bag in current, top view. The deflection is magnified for illustration purposes.

a cubical bag with a pyramid at the bottom, a conical bag and a pyramidal bag. Velocities in the range 0.021-0.127 m/s were studied, giving Reynolds numbers on the range $Re = 1 - 8 \cdot 10^4$. The Reynolds number is based on the diameter and given as $Re = UD/\nu$. The Reynolds number is a non-dimensional measure of the characteristics of the flow regime, D is the diameter, U is the velocity, and ν is the kinematic viscosity of the fluid, here fresh water. They found that the drag forces on all the different geometries increased with decreasing filling levels. However, for the cylindrical and cubical bags, the drag forces had a larger increase than for the conical and pyramidal bags. This increase in drag was found to be due to a local deformation in the front, apparent for filling levels less than 100%, affecting the drag coefficient unfavourably. This deformation was most pronounced for the cylindrical and cubical structures. The deformation resembled the local deformation pattern given by Solaas et al. (1993), on a larger scale.

For Reynolds numbers ($Re > 4 \cdot 10^4$) at filling levels below 90 % the local deformations in the front described by Strand et al. (2013), Lader et al. (2015) and Solaas et al. (1993) could resemble the shape of a regular parachute. Even though the parachute is an open volume, and the CFFC is a closed volume and thereby also dependent on the internal flows and motions of the bag, parallels can be drawn. The drag coefficients found for the cylindrical and cubical bag in Strand et al. (2013) and Lader et al. (2015) were close to the drag coefficient range found for parachutes and hemispherical cups (Hoerner, 1958).

For Reynolds numbers below $Re \leq 4 \cdot 10^4$ (low velocities), the bag did not

appear to deform but remained the shape as it appeared for only static pressure (Strand et al., 2013). The form of the bag in still water for pure static pressure was found to be dependent on the load history of the bag (Strand et al., 2014). This indicates that the initial shape of the bag can affect the experimental results.

The Reynolds number in model and full scale are not equal, and the drag coefficient is known to be dependent on both the geometry and the Reynolds number, care should therefore be taken before these results are applied in full scale.

2.2.4 Sloshing

Sloshing inside the bag pen was observed experimentally by both Solaas et al. (1993) and Lader et al. (2017). For resonant conditions, the bag experienced large deformations and water was thrown out of the bag. Solaas et al. (1993) suggested that the resonant internal water motions, would introduce peak loads in the fabric. They also estimated the first sloshing frequency based on a given cylindrical rigid geometry.

2.3 Following work

To develop knowledge and hypothesis of how the closed flexible fish cage behaves under current for varying filling levels model experiments have been conducted. The result of some of these will be presented in the following chapter.

Chapter 3

Experimental study of current forces and deformations on a half ellipsoidal closed flexible fish cage

The modelling and investigations of sea loads on CFFCs will start with locations in less exposed waters, where current gives a larger contribution to the loads on the structure than waves. We assume that the main operational condition of the CFFC will be full or overfilled/inflated. However, there might arise situations where the bag is in a condition where it is less than full. The basic understanding of the physics of the sea loads of an under-filled CFFC is limited. Basic understanding and hypothesis of the physics of a system can be gained through observations and response measurements in model experiments. Model experiments of a CFFC for varying filling levels in current have therefore been conducted, and the results analysed.

In this chapter experimental work considering a half ellipsoidal CFFC for four filling levels between 70 and 100% and different towing velocities are presented and discussed. The 100% filling level of the bag is defined according to the theoretical full volume of the bag. The model test data and observations are used to formulate mathematical models of the CFFC in current, in particular, drag coefficients are found. This chapter is a continuation of the works presented in Strand et al. (2013), and Lader et al. (2015), but considering a different geometry, a larger range of Reynolds numbers, and running longer experimental runs in the towing tank, that is longer travelled distance. The results in this Chapter have earlier been published in Strand et al. (2016).

3.1 Experimental set-up and instrumentation

To study the effect of current loads on a half ellipsoidal CFFC, a number of experimental runs of a model scale bag at different filling levels and current velocities were done in the Marine Cybernetics Laboratory (MC-Lab) at NTNU in Trondheim, Norway. All the experiments turned out to be of great importance in the

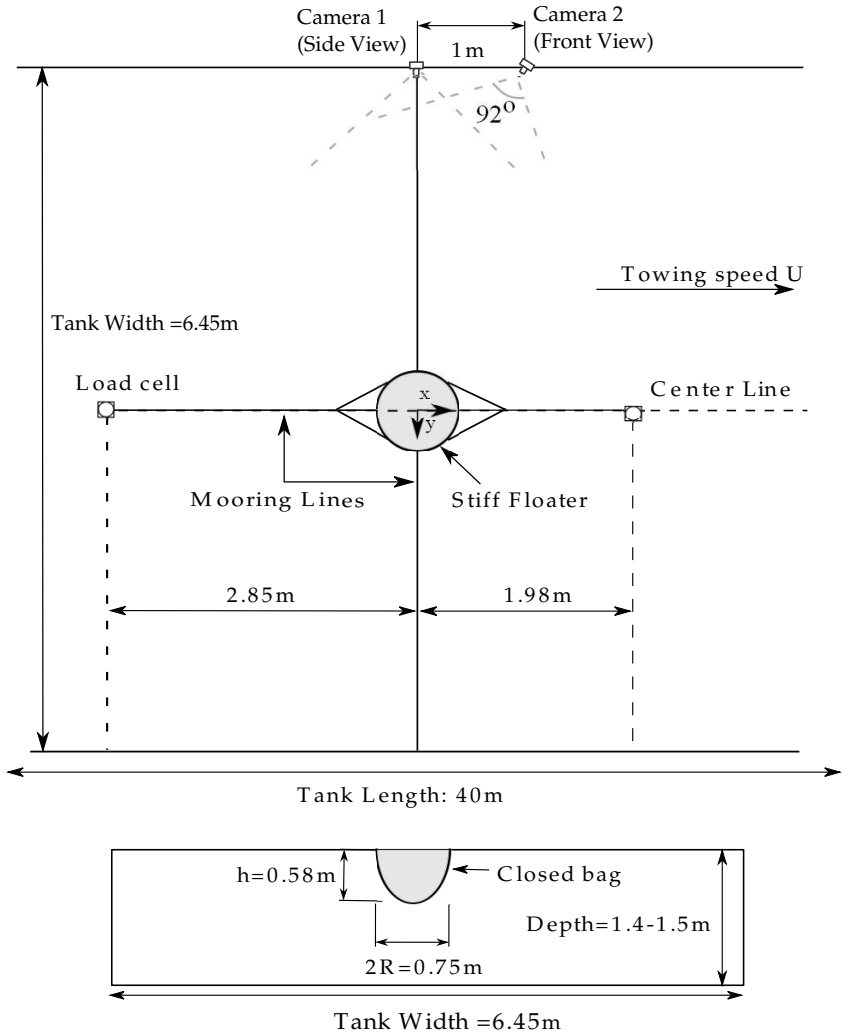

Figure 3.1: Experimental set-up. Upper: Top view. Lower: Front view. Tank dimensions of the MC-Lab are 40 m $\times$ 6.45 m $\times$ 1.5 m. The Cartesian coordinate system is located in the centre of the floater in the free surface. The floater is stiffened in the free surface to avoid ovalisation and is moored by four moorings; front, aft and two side moorings.

understanding of relevant physics and future development and verification of the mathematical models of the CFFC in a current.

The MC-Lab is a small towing tank, 40 m long, 6.45 m wide and with a depth varying from 1.4 m to 1.5 m. Experiments were run in March and May 2013. In March, the 70 % and 100 % filling levels were tested. In May, the aim was to repeat the experiments from March and also run tests at 80 and 90 % filling levels. In the following, the different experimental runs will be designated as March 2013

and May 2013. The dimensions of the bag was: diameter $D = 0.75$ m, and the max draft $h_B = 0.58$ m, giving a volume $V_0 = 180$ l. See Figure 3.1 for model and measurement set-up for the experiment, and Table 3.1 for the test matrix describing the various test runs.

The CFFC consists of three parts: The bag itself, the bag content, and an attachment system. The bag was tailored in a half ellipsoidal shape of ripstop nylon, of thickness 0.05 mm and weight 40 g/m^2. Cotton thread was used in the sowing to reduce the permeability at the seams. A floater placed inside the fabric at the water surface was used as attachment system, inspired by Kristiansen and Faltinsen (2015). The floater was made by a corrugated plastic tube in PVC with diameter 25 mm, a mass of 0.104 kg/m, and stiffened by ropes in the horizontal water plane to avoid ovalization. The floater was connected by four nearly horizontal mooring lines to the carriage in the centre line of the tank. The mooring lines were made of 2 mm nylon halyard.

A flow meter with an accuracy of 3 % was used to measure the amount of water in the bag. The Nylon fabric used for the bag model is to some extent permeable giving a net flow through the fabric when subjected to pressure differences. The intention in the present experiments was that the volume inside the bag should remain constant during the experiments. The amount of water in the bag was measured after each filling level experiment. The leakage out of the bag during the different run series for each filling level was found to be within 3-4 % of the intended filling level.

The current was simulated by towing the model under the carriage, with towing velocities U in the range $U = 0.04 - 0.22$ m/s. The towing carriage was experienced to be steady and accurate for the given velocity range. Kristiansen and Faltinsen (2015) have tested the accuracy of MC-Lab carriage velocity and found it to be highly stable, and within 0.2% of the desired value, reducing the possibility that an experimental bias introduced by the carriage.

Drag forces were measured in the towing direction by load cells in the front and aft mooring line. The load cells were sampled at 200 Hz. The uncertainty of the load cell was found to be 0.05 N, which is ≥ 10 % of the mean drag force for the two lowest velocities, and ≤ 6 % and decreasing for the higher velocities. Mean drag forces were found by taking the average over 40 seconds of the measurement time interval with the smallest standard deviation, after the initial startup, for each run. This time interval will be referred to as the middling time interval. Each time series was between 90-120 seconds long.

Two underwater cameras of the type Go Pro 3 were used to measure/observe the deformations of the bag. The cameras had a fixed 92-degree wide angle lens (Figure 3.1). One capturing the side of the bag, and the other capturing the front/side. The cameras followed the model during the test attached to the towing carriage. Both cameras were placed to avoid disturbing the incoming current.

Quantitative measures of the geometry of the bag were obtained from the image material. Deformed drafts were calculated for all the current experiments conducted in the MC-Lab. Coordinates from the pictures from camera 1 (see Figure 3.1), were translated to real world coordinates by an image analysis. In the image analysis, coordinates of the waterline and the bottom of the bag were used to estimating a deformed draft of the bag. The 100% filling level images together

Table 3.1: Test matrix showing filling levels, and towing velocities for the model experiments of a half ellipsoidal closed flexible fish cage. λ is the filling level of the bag, and U the towing velocity

	λ (%)	U (m/s)
March 2013	70,100	0.04, 0.05, 0.07, 0.10, 0.12, 0.15, 0.17, 0.19, 0.22
May 2013	70-100	

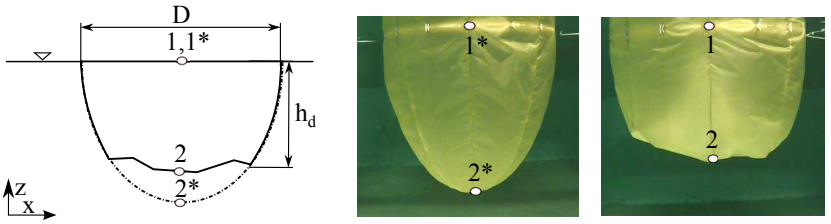

Figure 3.2: Illustration of marker placement under estimation of deformed draft from images. Left: Sketch of marker placement for the deformed draft (1,2) and reference used for calibration in 100% full images ($1^*, 2^*$). Middle: Image of 100% full bag used to calculate reference draft ($1^*, 2^*$), taken by camera 1. Right: Example of marker placement on deformed bag, 70% full bag (1,2).

with the known full draft were used to define a calibration coefficient, to transform the pixel information into length measures. The deformed draft h_d was found according to:

$$h_d = \frac{h_B}{z_{2^*} - z_{1^*}}(z_2 - z_1), \tag{3.1}$$

where z_{2^*}, z_{1^*} are the z-coordinates of the reference picture, and z_2, z_1 are the z-coordinates of the deformed draft picture. The points were placed as illustrated in Figure 3.2. The estimated error of the placement of the coordinates is in the order of ± 0.5 cm (± 1 %) . This estimated error was found based on the variance of the draft of the 100 % filling level in the stationary condition, which is known.

3.2 Results

The results of the experiments will be analysed in the following subsections.

The drag force on a structure is known to be dependent on the shape of the structure, and the projected area. The drag force on a structure in a uniform flow is given by the drag equation:

$$F_D = \frac{1}{2}\rho_w A C_D U^2 \ , \tag{3.2}$$

where ρ_w is the fluid density, and A is the projected frontal area. The drag coefficient C_D is dependent upon the shape of the body, the flow regime around the body and the Reynolds number (Faltinsen, 1990).

3.2.1 Force measurements

Force measurements for four different velocities are plotted and compared in Figure 3.3. For all but the lowest velocity at $U = 0.05$ m/s the force measurements for the lower filling levels are substantially higher than the 100 % filling level. All the drag force measurements indicate that the drag force is dependent on the filling level.

Some oscillations are observed in the force measurement time series. They are small for the three smallest presented velocities. However, for the 0.22 m/s velocity, the oscillations are large, especially for the 70 % filling level.

3.2.2 Bag deformations

A hemispherical cup was seen forming at the front when the bag was exposed to current, for $U \geq 0.07$ m/s, as illustrated in Figure 3.4 right part. The deformation is shown for the 80% filling level in Figure 3.4 left part, and the hemispherical cup is indicated with the black dotted line. This deformation increase as the filling level decreases and the current velocity increases, see Figure 3.5. In Figure 3.5, images from the two cameras are shown for the same velocities as the force measurements. The images are taken within the middling time interval around $t = 60$ s. The image material shows that the bag deforms for all filling levels. The deformations appear to be dependent on both filling level and velocity. For filling levels below 100 %, a large deformation of the front can be observed for all $U \geq 0.07$ m/s. This deformation is consistent with the local deformation pattern described by Solaas et al. (1993) shown in Figure 2.1 left part, and what have been found for other geometrical shapes in Strand et al. (2013) and Lader et al. (2015). For the 100 % filling level we observe small deformations, but these deformations do not appear to effect the drag forces.

For $U \leq 0.05$ m/s ($Re \leq 4 \cdot 10^4$), the bag did not appear to reach a fully deformed shape, but stayed closer to the initial zero velocity shape. This was also an effect which was found for the same velocity range in Strand et al. (2013) for a cylindrically shaped bag.

The back wall relative to the current was observed deforming only for the very highest velocities. This can be seen on the images of all the filling level at the 0.22 m/s current velocity in Figure 3.5, where the back wall of the bag deforms out of the borders of the reference. Deformation of the back wall is in accordance with the global current deformations described by Solaas et al. (1993), and contrary to Strand et al. (2013) which studied a circular bag. The reason why these deformations were not found in Strand et al. (2013) can be that lower current velocities were considered.

Measurements of the draft of the deformed bag indicate a decrease in draft for lower filling levels. This can also be seen when the contour of the zero current 100 % filling level is compared to the deformed shape of the bag in Figure 3.5. The deformed draft in the images was estimated using (3.1), and plotted in Figure 3.6. The plot indicates a general significant decrease in the draft, and subsequently a reduction in the exposed area for decreasing filling levels. The magnitude of the draft appears close to constant within each filling level, for $U \geq 0.07$m/s. The

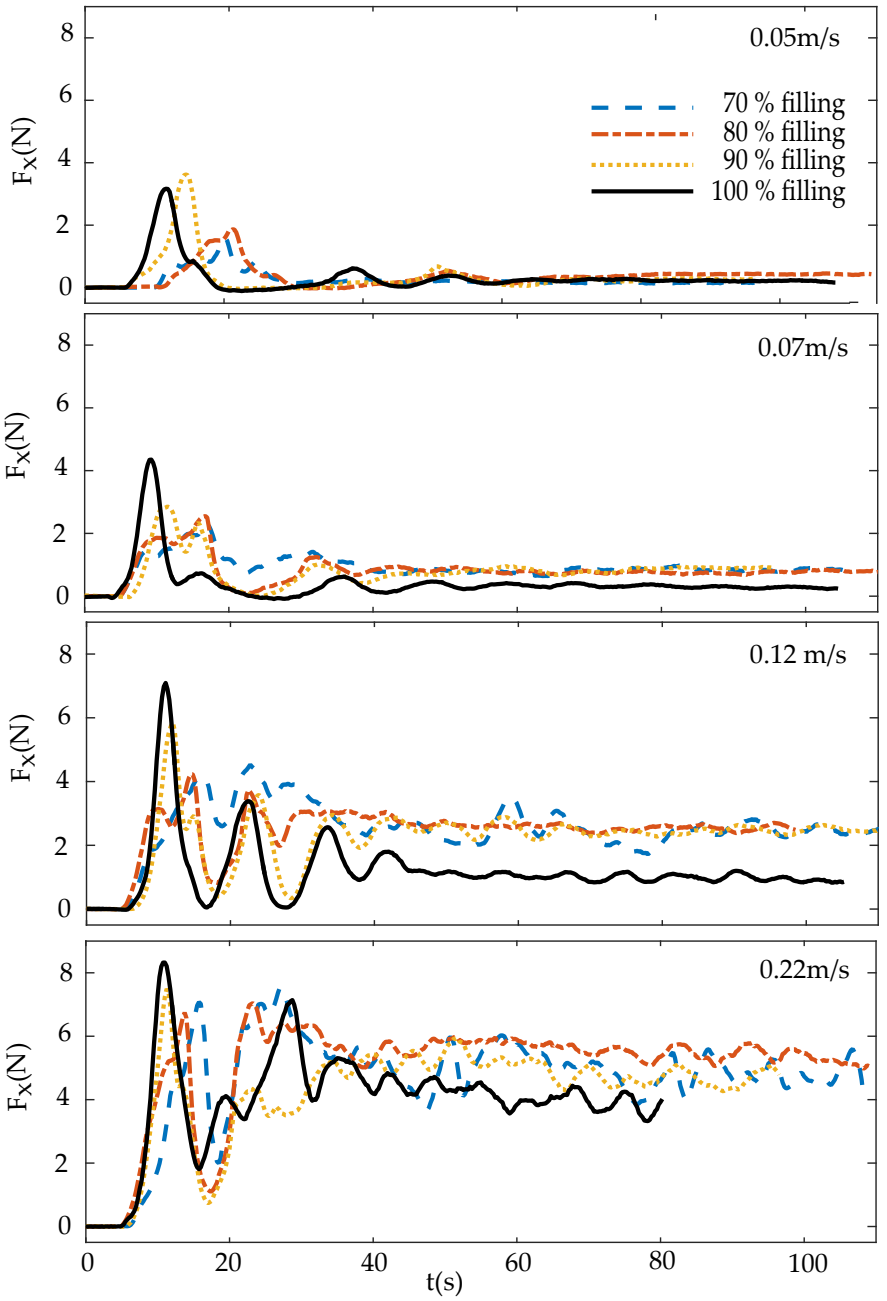

Figure 3.3: Comparison plot of force measurements for four different current, $U = 0.05$ m/s, 0.07 m/s, 0.12 m/s and 0.22 m/s, for all the four filling levels, from the May 2013 experiments.

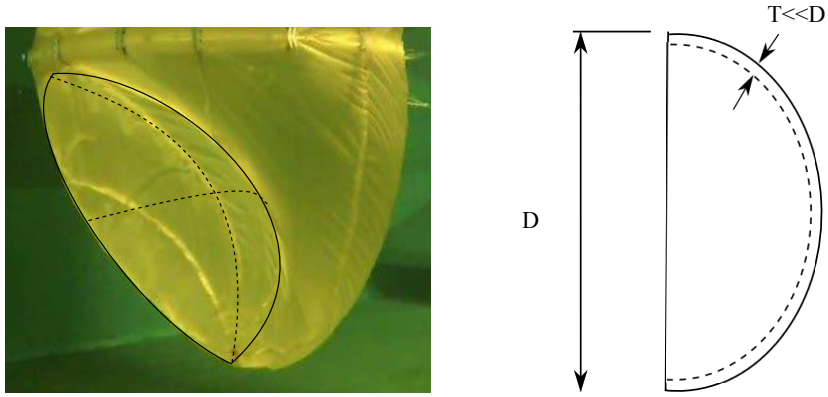

Figure 3.4: Illustration and image of front deformation for underfilled closed flexible fish cage in current. Left: Deformation pattern of the CFC at U =0.12 m/s at filling level 80%. Primary deformation indicated with lines. Right: Illustration of thin hemispherical cup. Illustration adapted from Blevins (1984)

decrease in the draft for decreasing filling levels were also found for a cylindrical bag in Strand et al. (2013).

For the May 2013 experiments, the videos show an oscillatory behaviour with fluttering in the front facing the current. The drag measurements from these velocities also showed the same tendencies by exhibiting a larger standard deviation and more peaks in the force measurement, within the middling time, see Figure 3.7. If the force measurement plot is compared to the images taken at the marked time instances, only small variations in shape can be observed. No general clear, direct connection between the images and the time series can be seen, as it appears to be only small differences in the shape for image 1-3. Although, within this time period a force variation of 3 N can be observed for the force measurements. Image 2 and 6, which are the images taken at the force peaks could appear to have a slightly larger deformed draft and a deformation with fewer wrinkles in the centre, but the differences compared to remaining images are as earlier mentioned small. The presented measurement was taken at 0.15 m/s, at higher velocities both the time series and the videos of the bag appeared more chaotic. This can be seen in the times series at 0.22 m/s in Figure 3.3.

The increase in drag force on the bag appear to happen simultaneously as the large deformations for lower filling levels appear. The density of the water is kept constant, and the velocity is known. Both the drag coefficient and the projected area in (3.2) are dependent on the deformed shape of the bag. The projected frontal area of the bag is decreasing for decreasing filling levels. It is therefore plausible that the increase in drag is caused by the change in shape, affecting the drag coefficient.

3.2.3 Drag Forces

Reduced data for all the filling levels at all the velocities are plotted in Figure 3.8. Error bars are included to indicate the variation in the force measurement

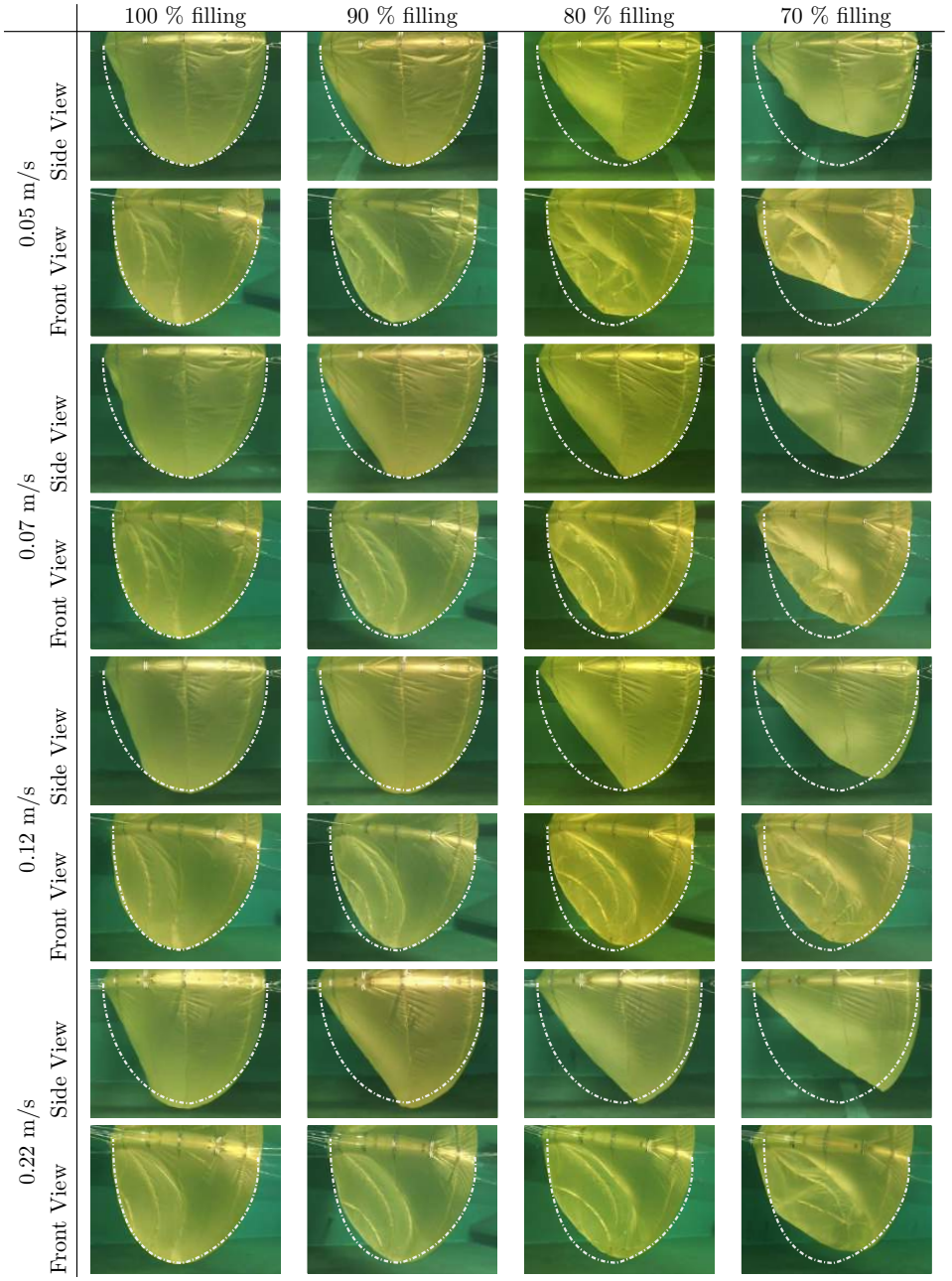

Figure 3.5: Comparison images of deformed closed flexible fish cages for given filling levels and velocities. Image material, camera 1 (Side View) and 2 (Front View), taken during the May 2013 experiments. Deformation patterns for 100 %, 90 %, 80 and % 70 % filling levels, for selected current velocities from 0.05 m/s to 0.22 m/s. 100 % filling level 0 m/s used as reference, see white dotted line.

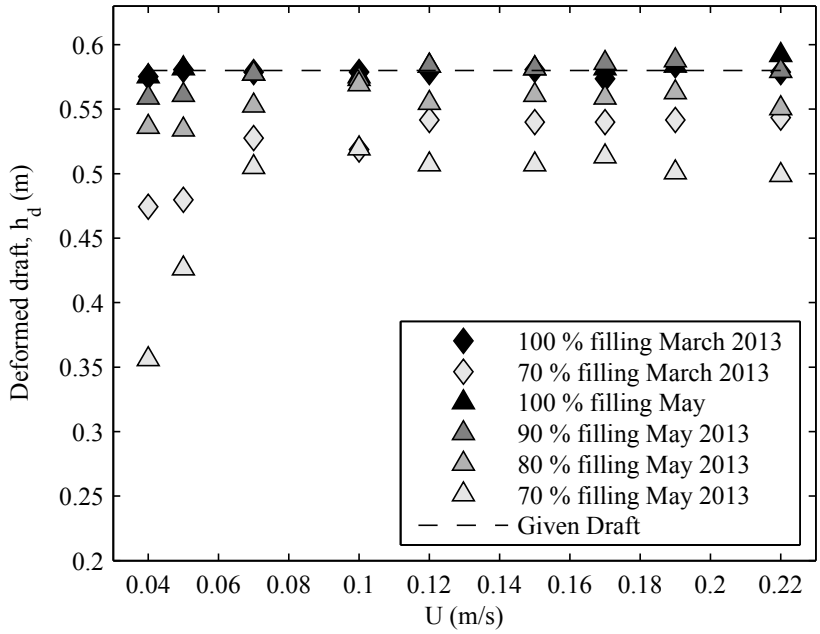

Figure 3.6: Measured deformed draft for bag exposed to current at different filling levels.

within the middling time interval. The error bars on the measurement points are calculated based on the standard deviation of the measurement time series within the middling time.

The solid lines in Figure 3.8 are the empirical drag given by (3.2) with constant area A and the drag coefficient C_D. The drag coefficient used here is the empirical mean drag for a sphere which is $C_D = 0.47$ at $Re = 10^5$ (Hoerner, 1958). A half ellipsoid and a sphere are different, and the free surface is known to affect the drag coefficient. However, since no other comparison drag coefficient was found more appropriate, a sphere will be used. The dashed line interval is the drag coefficient range for a hemispherical cup at $C_D = [1 - 1.42]$ given by Hoerner (1958). This range is based on decreasing the depth over diameter ratio of a hemispherical cup from a deep hemispherical cup where $C_D = 1.42$, until the drag coefficient of a flat plate/disk where $C_D = 1$.

An increase in drag is observed for decreasing filling levels for all velocities, see Figure 3.8. When the drag force measurements are compared with (3.2), the drag force seems to be proportional to U^2, independent on the filling level. The solid line, based on the sphere drag coefficient captures the trend for the drag at the 100 % filling level. When the filling level decreases, the trend changes, such that the measurement points appear to be within the hemispherical cup interval given by Hoerner (1958). These results are comparable related to other geometries presented

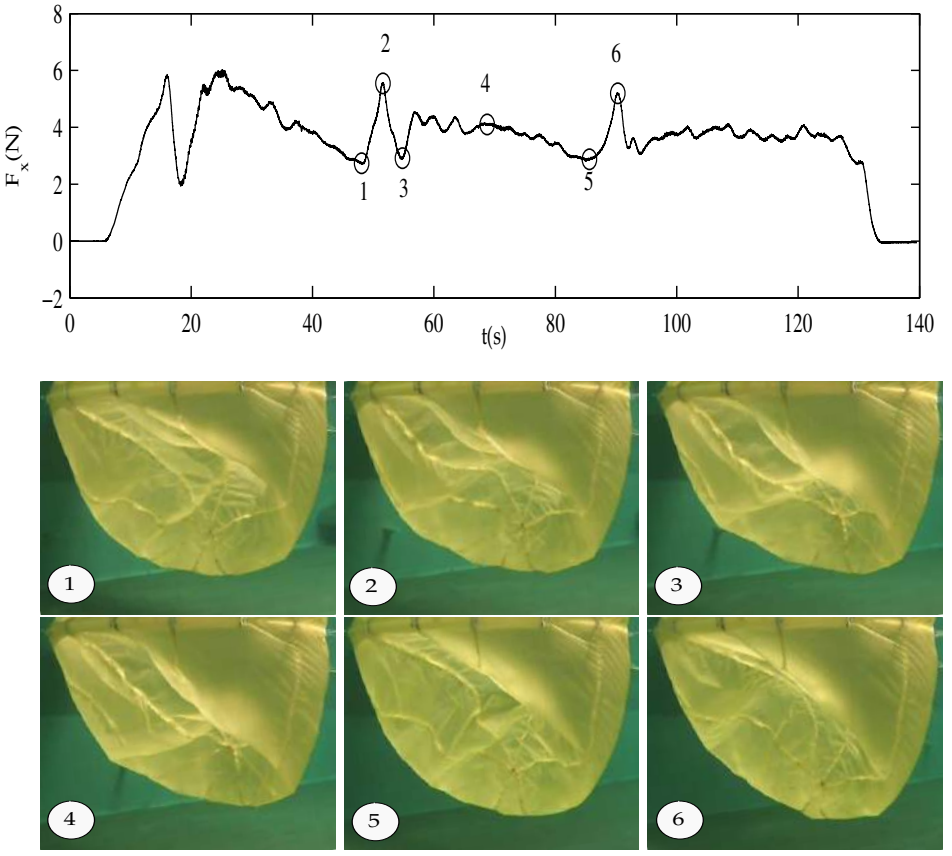

Figure 3.7: Force measurement and images for oscillating behaviour of membrane. Top: Force measurement time series for 70 % filling level at U=0.15 m/s. Bottom: Images from camera 2 (Front view) taken at the time instances 1-6, marked in the time series. Only small changes in the geometry can be observed. From the May 2013 experiments.

in Strand et al. (2013) and Lader et al. (2015). For the lower filling levels, the bag displayed significant deformations of the shape, simultaneously as the drag forces on the bag increased, though to a smaller level than earlier published.

The error bars in Figure 3.8 reflect the standard deviation of the measurements within the middling interval. The May 2013, 70% filling level deviates from the general trend, with a larger standard deviation.

3.2.4 Drag coefficient

The undeformed projected area $A = \pi hD/4$ was used in the calculation of the drag coefficient C_D. C_D was plotted against the Reynolds number in Figure 3.9 for all the filling levels.

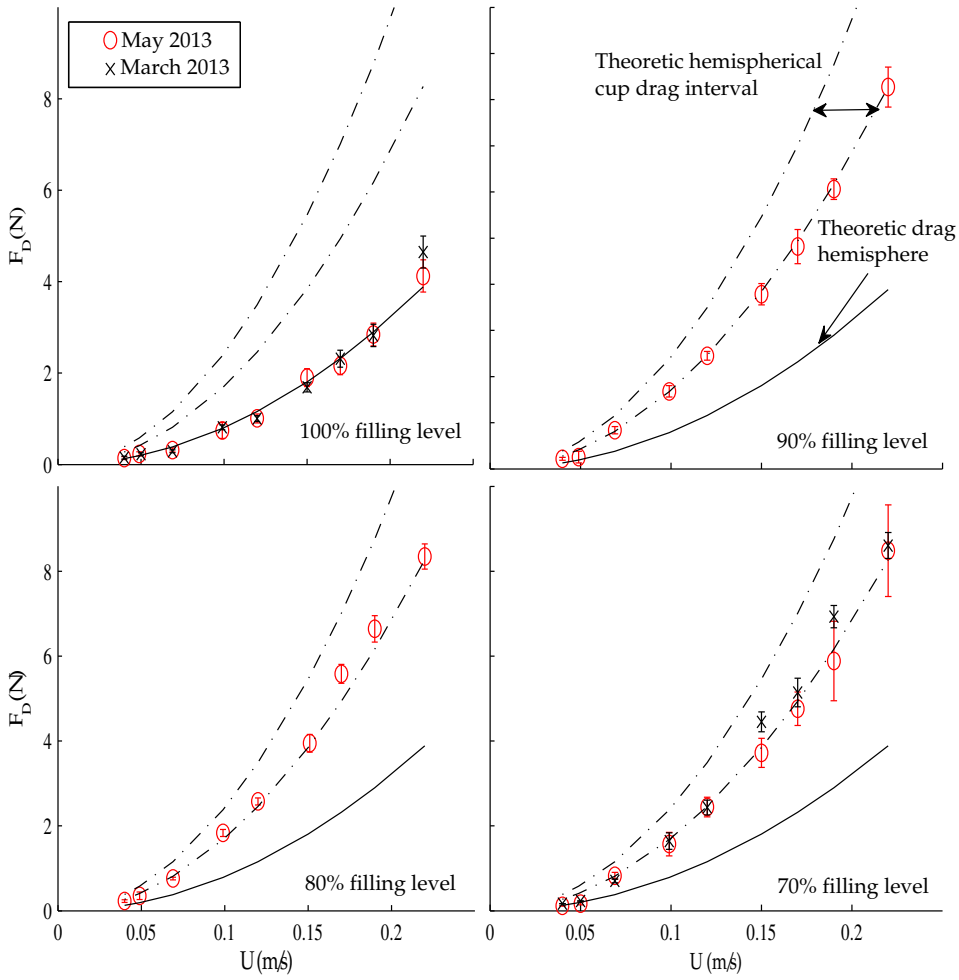

Figure 3.8: Plot of drag forces found from all the experiments, for 100%, 90%, 80 % and 70 % filling level. Solid line gives theoretic drag for a sphere, and dotted line interval gives the theoretic hemispherical cup drag interval, given by (Hoerner, 1958).

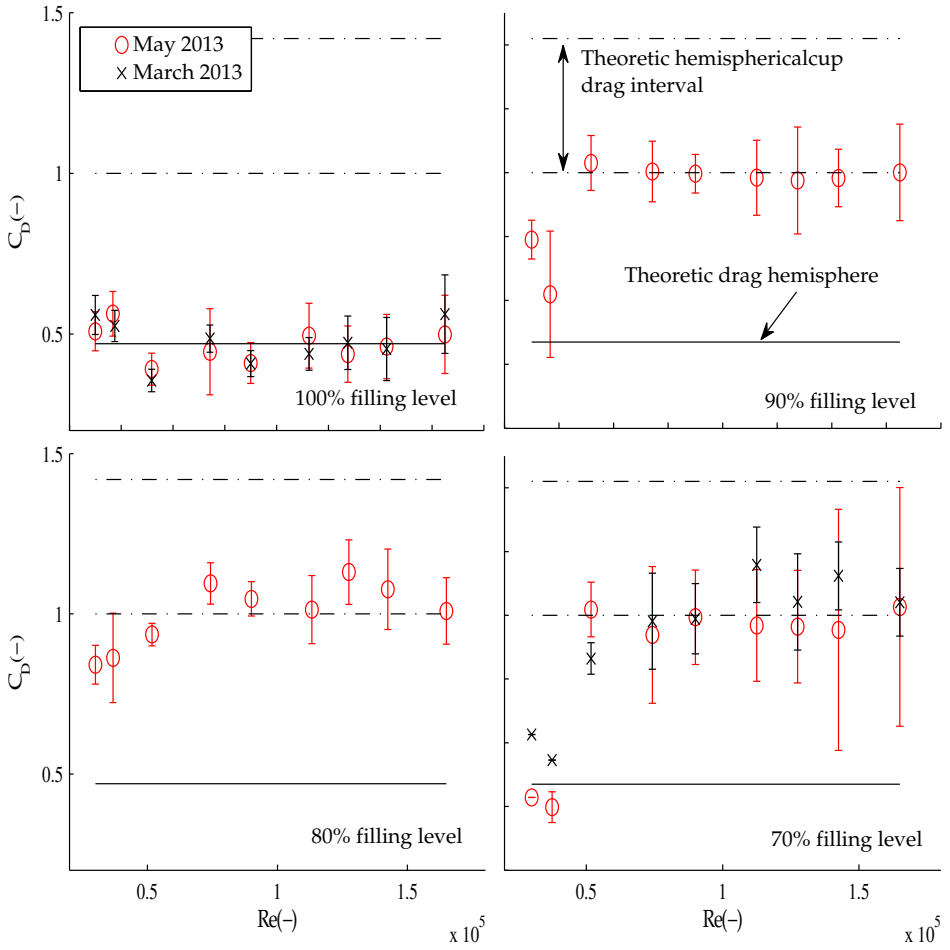

Figure 3.9: Plot of drag coefficients C_D for all the experiments, for 100%, 90%, 80 % and 70 % filling level. The solid line gives theoretic drag coefficient for a sphere, and dotted line interval gives the drag coefficient interval for a thin hemispherical cup, given by (Hoerner, 1958).

The drag coefficient reflects the observed deformation patterns, supporting the theory of a significant increase in drag coefficient for decreasing filling levels. Figure 3.9 indicates a drag coefficient close to the empirical drag coefficient of a sphere of 0.47 for the 100% filling level (Hoerner, 1958). The drag coefficient C_D increases up to the interval for the hemispherical cup given by Hoerner (1958) for the filling levels under 100%.

For $Re \leq 4 \cdot 10^4$, at filling levels below 100 % the drag coefficients are lower than the drag coefficients at higher Reynolds numbers. Hence, that the bag does not deform will affect the drag coefficients, which can also be observed in Figure 3.9. The drag coefficient at the 70 % filling level is considerably smaller than the rest of the Reynolds numbers for the lowest filling levels at the lowest Reynolds numbers, $Re < 5 \cdot 10^4$. Since the large cup deformation has not appeared, and the draft is small, it is plausible that the drag coefficient is lower.

For the 70- 90% filling level for $Re > 4 \cdot 10^4$, the drag coefficient increases to the drag coefficient interval for the hemispherical cup, see Figure 3.9 and Table 3.2. This is consistent with the deformation patterns observed in Section 3.2.2, for velocities over $Re \geq 4 \cdot 10^4$, which is when the characteristic hemispherical cup have appeared. The trend of the measurement points appears to approach a constant value. C_D appears close to constant also for the 70% filling level, for $Re > 11 \cdot 10^4$, despite the observed oscillations in shape and forces. This indicates that these oscillations do not have a significant effect on the mean force. However, the standard deviation indicated by the error bars have grown substantially larger, see Figure 3.8.

The presented experimental results also indicate a quick transition in drag coefficient between 90 and 100 % filling level. This is a much more rapid change than what was found in Lader et al. (2015) and Strand et al. (2014), where the change in drag coefficient appeared to happen more gradually related to the filling level. Only one run for each filling level was reported for these experiments for each geometry. However, since only one run was reported for the presented experiments for the 80 and 90 % filling level, no firm conclusions of the transition filling level can be made.

Mean drag coefficients ($\overline{C}_D$) were calculated for each filling level λ for each experimental series, and are given in Table 3.2. Three different mean drag coefficients have been calculated, one general mean using all the data points and two mean drag coefficients divided by Reynolds number. One for $Re \leq 4 \cdot 10^4$ ($\overline{C_{D_{\leq}}}$) and one for $Re > 4 \cdot 10^4$ ($\overline{C_{D_{>}}}$). This division is based on the observed deformation patterns and also the trend of the drag coefficients in Figure 3.9.

The mean drag coefficient ($\overline{C_D}$) for all the filling levels below 100 % are either within or close to the hemispherical cup interval. All the means are affected by the first two measurement points, reducing the value. If we consider the mean drag for $Re > 4 \cdot 10^4$, the average drag is increased relative to the total mean ($\overline{C_D}$). The average drag coefficient for the 100 % filling level for the March and May 2013 experiments are equal. For the 70 % filling level, $\overline{C_D}$ is lower for the May 2013 experiments than for the March 2013 experiments. From Section 3.2.2 we observed that the draft was smaller for the May 2013 experiments, which would influence the drag, and thereby the drag coefficient. It should be taken into consideration

Table 3.2: Mean drag coefficients for the experiments conducted in March and May 2013. $\overline{C_D}$ is the mean drag coefficient for all the data points within a filling level. $\overline{C_{D\leq}}$ is the mean drag coefficient for $Re \leq 4 \cdot 10^4$ and $\overline{C_{D>}}$ is the drag coefficient for $Re > 4 \cdot 10^4$.

	March			May		
	$\overline{C_{D\leq}}$	$\overline{C_{D>}}$	$\overline{\mathbf{C_D}}$	$\overline{C_{D\leq}}$	$\overline{C_{D>}}$	$\overline{\mathbf{C_D}}$
70 %	0.59	1.03	**0.93**	0.41	0.98	**0.85**
80 %	-	-	-	0.85	1.04	**1.00**
90 %	-	-	-	0.70	1.00	**0.93**
100 %	0.54	0.45	**0.47**	0.54	0.45	**0.47**

that Figure 3.6 shows that the deformed draft is less than the undeformed draft. This would affect the actual drag coefficient, resulting in a further increase of the drag coefficients for the lower filling levels.

3.3 Discussions

The repeatability of the results is viewed as acceptable. The difference in mean drag force between the March and May 2013 experiments for the 100% filling level is within 1% and within 6% for the 70% filling level.

The CFFC is a complex system, and for the presented experiments we have limited to no information of the fluid flow inside and around the CFFC during the experiments. We have observed a complex interaction between the membrane, the fluid masses within the CFFC and the outside fluid flow. To have better control of all variables, it would have been useful to also have information about the tension in the fabric and the fluid flow around and inside the CFFC.

3.3.1 Experimental results

It can then be questioned if the bag deformations have not had time to develop, due to slow dynamics for $U = 0.04$ m/s and $U = 0.05$ m/s. However, when the force measurement was examined directly with the emphasis of slow changes, no changes were found within the averaging time interval. Both the 0.04 m/s and the 0.05 m/s velocity have low variance in the force measurements after the transient period. The 0.07 m/s velocity exhibits a quick change in geometry during the transient phase, before stabilising at a higher drag force level with the deformation pattern seen in the higher velocities.

It appears to be a significant difference between the 70 % filling level drafts of the May and March 2013 experiments. Both the first two velocities, but also the mean is lower for the May 2013 experiments. These results can indicate that filling level is smaller than intended. The differences in shape and deformed drafts (see Figure 3.6) between the March and May 2013 for the lowest velocities in the range $U \leq 0.05$ m/s ($Re \leq 4 \cdot 10^4$), can be explained by different initial shape. Strand et al. (2014) reported significant variations in shape and connected draft for the 70%

filling level at zero current, still water, and for these velocities the shape does not appear to change much from the static shape, as also seen in Strand et al. (2013).

For velocities above 0.12 m/s for the 70 % filling level, in the May 2013 experiments, the deformation in front became unsteady. This does not happen for the March 2013 experiments. If the lower draft for the May 2013 experiments indicates a lower than intended filling level, the oscillations can indicate that a new phenomenon appears when the filling level reaches some level below 70 %. What can be the reason for that the front of the CFFC becomes unsteady? Moreover, how can these small oscillations be the cause of the significant variations in drag seen in Figure 3.7? One possible explanation can be found if we look at parachutes. The shape of parachutes is known to oscillate under some unfavourable conditions (Hoerner, 1958). The oscillation of the form/diameter is called "breathing", and is caused by the interaction between the near-wake fluid forces and the fabric (Johari and Desabrais, 2005). This behaviour leads to a fluctuation in the drag force and is associated with a clear vortex shedding frequency in the response. The fluctuations in the drag have been reported to be up to 27 % of the mean, see Johari and Desabrais (2005). The standard deviations compared to the mean drag force for the presented results were 10-16% above the mean. For parachutes, most of this drag fluctuations are associated with added mass fluctuations. The time series of the performed experiments were too short to capture any dominant vortex shedding frequency, to prove that this could be the case for the CFFC. To further study this phenomenon more information about the flow inside and around the CFFC, and a longer towing tank than the MC-Lab is be needed.

The increase in drag coefficient for the presented experiments is lower than the increase found for decreasing filling levels for other geometries in Strand et al. (2013) and Lader et al. (2015). However, in Strand et al. (2013) and Lader et al. (2015) shorter time series were used, and the experiments were run in series with three velocities in each run, 120 s in total. In the experiments presented here, the time series are between 90 and 120 s long. Sarpkaya (2010) studied the effect of travelled distance on a circular cylinder in an impulsively started flow. He defined non-dimensional travelled distance as L/r, where $L = Ut$ and r is the radius of the cylinder. He found that the drag coefficient in the initial stages $(Ut/r \leq 4)$ of an impulsively started flow can exceed its steady value by as much as 30%. Sarpkaya (2010) defined a transient interval between $L/r \approx [0, 17]$ for Reynolds numbers from $10^4 - 10^5$. The same phenomenon has been found for spheres, with the same tendency to overshoot the stationary drag coefficient in the transient phase, but with a longer transient phase (Roos and Willmarth, 1971). For the March and May 2013 experiments we get $L/r \in [9, 64]$, where all the velocities except U=0.04 m/s and U=0.05 m/s are outside the transient range. The results reported by Strand et al. (2013) and Lader et al. (2015) are in the range $L/r \in [4, 19]$. This could indicate that the larger drag coefficients found in Lader et al. (2015) and Strand et al. (2013) are due to effects of transients on the drag coefficients.

3.3.2 Error Sources

Blockage effects have been shown to have an effect on the drag coefficient for large blocking ratios, see, e.g. Maskell (1965). The blockage ratio is calculated as the

projected area of the bag (0.34 m^2) divided by the tunnel cross-section area in the towing direction (9.03-9.68 m^2). The variance in the blockage ratio is due to the varying depth. The largest blockage ratio was 3.8% for the presented experiments. West and Apelt (1982) have carried out a study of the effect of blockage on the drag coefficient for a circular cylinder in the Reynolds number range $[10^4 - 10^6]$. They concluded that for blockage ratios less than 6% the effect on the drag coefficient was small.

The results presented in this work showed that the drag force is highly dependent on the filling level of the bag. The bag was to some extent permeable. For parachutes, drag has been shown to be dependent on the permeability of the fabric (Hoerner, 1958). The permeability of the nylon used in the experiments was not measured, but since parachute nylon was used, it will be assumed that the permeability is not far from 1-2% (Johari and Desabrais, 2005). Permeability at this level can lead to a small reduction in the drag compared to non-permeable structures. The filling level of the bag was measured after each experiment. However, the flow meter has an error of 3 %, and the measured filling level was also for the May 2013, 70 % filling level, 4 % lower than the intended filling level. If this error has accumulated in the same direction, the filling level could have been 7% less than intended, something which would influence the results.

3.3.3 Application to full scale

Typical full scale current velocities at aquaculture sites in Norway are in the range $U_c = 0.1 - 1.0\text{m/s}$. Ideally for this results to apply to full-scale dimensions, we should have equality in Reynolds numbers. However, due to known physical and economic limitations of the towing tank, this is not feasible (Hoerner, 1958). To transfer the results to full scale, Froude scaling was used. The Froude number is given as $Fn = V/\sqrt{gl}$ and is typically used in relation to free surface flows. When geometric scale $l_g = D_M/D_F$, were D_M is the model scale diameter, and D_F is the full-scale diameter, we have experimental data covering the scaling range from $l_g =$ 1:17 to 1:50. These scales correspond to full-scale diameters used by the aquaculture industry in Norway today from 13-38 m.

Model current velocities will not give equality in Reynolds number between model and full scale. The Reynolds number interval for full-scale current velocities gives $Re = [10^6 - 10^7]$, while the Reynolds numbers in model scale are in the interval $Re = [10^4 - 10^5]$. The drag coefficient is known to be dependent on both the transition to turbulent flow, which again is dependent on the Reynolds Number, the geometry and the material of the structure (Blevins, 1984). For the lower filling levels, the bag was observed to deform, introducing changes in the bag geometry. Blevins (1984) stated that when sharp corners are introduced, the drag coefficient was independent of Re for $Re > 10^4$. This makes the drag coefficient scalable for these conditions since the drag coefficient is pressure drag dominated and mainly dependent on the placement of the separation point for clearly defined separation points. However, this requires that the large front deformation has appeared. From the results, we have seen that for $Re \leq 4 \cdot 10^4$ the characteristic deformation in front does not appear. When the hemispherical cup appears in full scale in terms of Reynolds number cannot be decided. However, the most critical condition in terms

of drag loads must be when the large front deformation appears. The biggest drag force should be ruling for the dimensioning of the mooring system of the CFFC; this would then be when the large hemispherical cup has appeared.

In general, it is required for an elastic model that elastic similarity for the material is satisfied (Løland and Aarsnes, 1994). Requiring that $E_M d_M = E_F d_F/\tau^2$, where subscript M denotes model, and subscript F denote full scale. The CFFC is made of fabric with a low E-modulus (low in-plane stiffness). It has not been possible to find a usable material in model scale that satisfies the elastic similarity condition. With $E_M \approx E_F$, $d_M = 0.05$ mm and $d_F \approx 1$ mm, the bag fabric is 100-1000 times to stiff in model scale. No literature was found regarding the scaling-effects of the stiffness of the fabric on drag for CFFCs. The effect of scaling of in plane stiffness on parachutes in water has, however, been investigated. It has been found that the overall geometry of a parachute is not much affected by the stiffness of the fabric (Johari and Desabrais, 2005). The drag force on the bag is highly dependent on the global shape of the bag. Since the shape is not affected by the fabric stiffness, this will most probably not influence the application of the results to full scale.

3.4 Conclusions and following work

To utilise membrane technology at an industrial level more knowledge is needed about the effect of sea loads. Drag forces on a CFFC for different filling levels and current velocities have been experimentally studied. A significant increase in the drag force was experienced as the filling level decreased. A large deformation shaped like a large hemispherical cup comparable to a parachute, appeaed at the front facing the current for lower filling levels than 100%. This deformation lead to a change in the geometry, resulting in an increase in the drag force related to a full bag. The drag coefficient experienced a smaller increase than observed in Strand et al. (2013) and Lader et al. (2015). This can be due to transients affecting the results, caused by too short experimental runs in Strand et al. (2013) and Lader et al. (2015). The largest drag force should be ruling for the dimensioning of mooring of the CFFC. Then the drag response of underfilled cages should be considered. The problem of an under filled CFFC in current can be characterised by a complex interaction between the membrane, the fluid masses within the CFFC and the outside fluid flow.

To better predict the forces and deformations on the bag, mathematical models taking into account the dependency between force and deformation should be developed. The deformations, motions, and forces of the bag appear from the experiments to be highly tree dimensional. However, due to the complexity of the coupling between the internal flow inside the bag, the external flow, and the forces and deformations, we attempt to capture some of the main deformation patterns and forces by a reduced 2D model. In order to develop theory and understanding of the membrane structure, and the coupling between structural response and internal water motions, a 2D rectangular sloshing tank with a fabric membrane side wall is studied. Results from the analysis of this system will be given in the next chapter.

Chapter 4

Linear sloshing in a 2D rectangular tank with a flexible side wall

The hydroelastic analysis of a rectangular tank with a fabric membrane side wall of different lengths can introduce new knowledge of the effect of internal motions and flow in a membrane structure with a free surface. Most considered hydroelastic problems are too complex to analyse analytically, numerical and/ or experimental methods are therefore used. For this particular system, there exists an analytical solution. The analytical solution can give an understanding of the coupled system and can be utilized for verification of a numerical code, intended used for the end problem.

In this chapter an analytical solution for the coupled fluid- membrane interaction problem in the time, and frequency domain in 2D have been found. Coupled eigenfrequencies and the transfer functions of wave elevation for two different membrane lengths from sway excitation have been found both analytically and numerically. The results in this chapter have earlier been published in Strand and Faltinsen (2017).

4.1 Linear sloshing in a 2D rectangular tank with an elastic wall

A two-dimensional rectangular tank with breadth l and mean liquid depth h with a flexible left wall, where the tank is forced with prescribed horizontal tank motion is considered. The effect of hydrostatic pressure is not considered since the end application of the theory and knowledge is with water on both sides of the membrane.

In the considered system one of the walls is modeled as a fabric membrane, meaning that the tension stiffness dominates, with bending stiffness as a minor effect. When tension dominates, the structural natural frequencies may very well be in the range of the sloshing frequencies. Bauer (1981) and Bauer and Eidel (2004) has analytically considered a comparable system with a sloshing tank with an elastic bottom. They found that the coupled eigenfrequencies were slightly lower than for a rigid tank. The hydroelastic behavior of a rectangular tank with a fabric membrane sidewall of different lengths has earlier partly been studied by Schulkes

(1990). Schulkes (1990) investigated the case where the lower part of one of the side walls was modeled as a membrane. He showed by analytical means that when part of the rigid wall was replaced with a membrane, the eigenfrequencies of the total system decreased. The extent of this decrease in eigenfrequency depend on the proportion of the membrane length relative to the length of the tank wall, and the tension applied to the membrane.

A special case of what we consider is a container with a rigid moving wall, attached to an outside spring. Lu et al. (1997) and Chai et al. (1996) have analytically solved this coupled fluid-structure system and found the pressure contribution on the rigid movable wall. Lu et al. (1997) used a similar method as our analytical method, while Chai et al. (1996) solved the problem by incorporating a wave maker solution.

We define a Cartesian coordinate system Oyz with the origin in the center and at the mean free surface with positive z upwards (see Figure 4.1).

A stretched 2D membrane is assumed, and bending stiffness and structural nonlinearities are neglected. The membrane deformations are represented in terms of structural eigenmodes with unknown time-dependent generalized structure mode amplitudes $\nu_m(t)$ associated with each dry structural eigenmode $U_m(z)$. A vertical 2D membrane of length L at $y = -l/2$ is fixed at the tank bottom, free surface piercing and fixed at the upper end, models the flexible wall. In 2D, a flexible membrane is a cable, and the cable theory by Irvine (1981) can be used. The differential equation for the considered membrane is

$$\rho_c d\frac{\partial^2 v(z,t)}{\partial t^2} - T\frac{\partial^2 v(z,t)}{\partial z^2} = F(z,t). \tag{4.1}$$

Here ρ_c and d are the density and thickness of the membrane, respectively. t is the time variable, v is the deformation in the $y-$ direction, T the tension and F is the force component per unit length in the $y-$ direction. The force per unit length on the right hand side of (4.1) is

$$F(z,t) = \begin{cases} -p, & -h \le z \le 0 \\ 0, & 0 \le z \le L-h \end{cases} \tag{4.2}$$

where p is the dynamic water pressure.

We will represent the deformation in terms of dry eigenmodes. That means we consider non-trivial solutions of (4.1) without the effect of the water pressure:

$$\rho_c d\frac{\partial^2 v(z,t)}{\partial t^2} - T\frac{\partial^2 v(z,t)}{\partial z^2} = 0, \tag{4.3}$$

with harmonic oscillations together with fixed end conditions. The dry eigenmodes of the 2D membrane, are

$$U_m(z) = \sin(\frac{m\pi}{L}(z+h)), \tag{4.4}$$

which are connected to the dry natural frequency $\lambda_m = \frac{m\pi}{L}\sqrt{\frac{T}{\rho_c d}}$, with L as the length of the 2D membrane. Then the deformation can be expressed as

$$v(z,t) = \sum_m \nu_m(t) U_m(z). \tag{4.5}$$

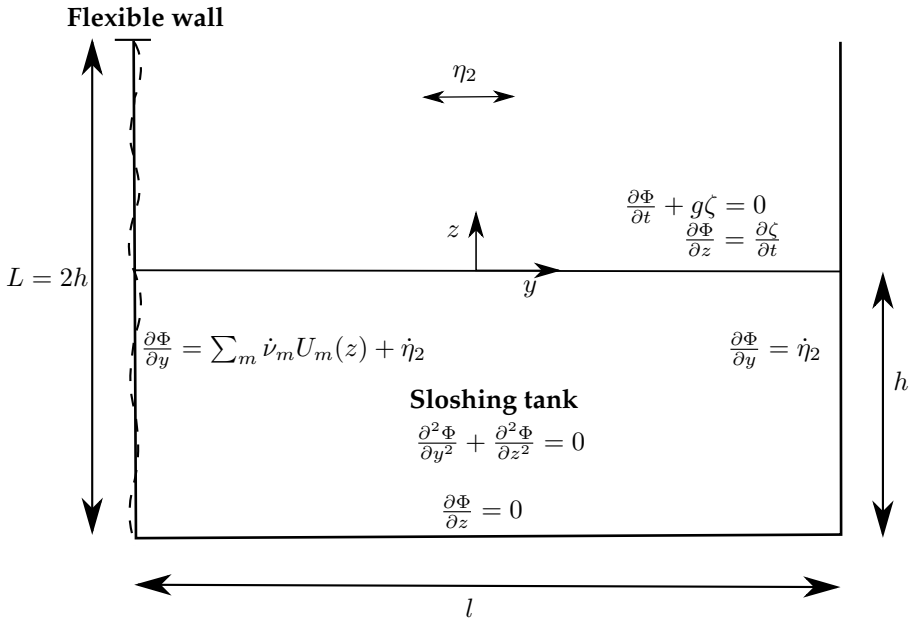

Figure 4.1: Boundary conditions for a two-dimensional rectangular tank with breadth l and mean liquid depth h with a flexible left wall of length L that is forced with prescribed horizontal tank motions η_2 in the time domain.

We assume linear potential flow of an incompressible liquid. The velocity potential and the free surface elevation are denoted as Φ and ζ, respectively. The boundary value problem of the linear sloshing problem in a rectangular tank with a flexible wall can be expressed as:

$$\frac{\partial \Phi^2}{\partial y^2} + \frac{\partial \Phi^2}{\partial z^2} = 0 \text{ for } -\frac{1}{2}l < y < \frac{1}{2}l, -h < z < 0, \tag{4.6}$$

$$\left.\frac{\partial \Phi}{\partial z}\right|_{z=-h} = 0,$$

$$\left.\frac{\partial \Phi}{\partial y}\right|_{y=-\frac{1}{2}l} = \dot{\eta}_2 + \sum_m \dot{\nu}_{dm} U_m(z),$$

$$\left.\frac{\partial \Phi}{\partial y}\right|_{y=\frac{1}{2}l} = \dot{\eta}_2,$$

$$\left.\frac{\partial \Phi}{\partial z}\right|_{z=0} = \frac{\partial \zeta}{\partial t}, \tag{4.7}$$

$$\left.\frac{\partial \Phi}{\partial t} + g\zeta\right|_{z=0} = 0. \tag{4.8}$$

A dot above the variable means time derivative, $\dot{\eta}_2$ is the prescribed horizontal rigid body tank velocity (sway velocity), and g is the gravitational acceleration.

The deformation velocity of the wall is expressed as $\sum_m \dot{\nu}_{dm} U_m(z)$. The boundary value problem for the liquid flow in the tank is illustrated in Figure 4.1.

4.1.1 Analytical time-domain solution

Our analytical hydrodynamic method can be classified as a multimodal method (Faltinsen and Timokha, 2009, page 193), which has been successful in solving linear and nonlinear sloshing problems within potential flow theory of an incompressible liquid. The method transfers the solution of the Laplace equation for the velocity potential with initial and boundary conditions to a system of ordinary differential equations that, for instance, facilitates analytical hydrodynamic stability analysis, and detection of , multiple solutions and wave regimes. Furthermore, the method facilitates coupling with structural dynamics because acceleration dependent internal load effects can be explicitly identified, both for linear and non-linear sloshing problems.

The liquid flow can be described analytically by the multimodal method (Faltinsen and Timokha, 2009, page 198). It implies that the free surface elevation ζ is expressed as the Fourier series:

$$\zeta(y,t) = \frac{1}{l}\sum_{m=1}^{\infty} \nu_m(t) \int_{-h}^{0} U_m(z)dz + \sum_{n=1}^{\infty} \beta_n(t) f_n(y), \tag{4.9}$$

where $f_n(y) = \cos(\pi n(y + \frac{1}{2}l)/l)$, and $\beta_n(t)$ are the generalized free surface coordinates. The spatially constant term in the Fourier series is a consequence of liquid mass conservation and elastic wall deformations.

The velocity potential Φ is expressed as:

$$\Phi(y,z,t) = \dot{\eta}_2(t)y + \phi(y,z,t) + \sum_{m=1}^{\infty} \Omega_{dm}(y,z)\dot{\nu}_m(t) + C(t), \tag{4.10}$$

similarly as in Faltinsen and Timokha (2009, page 224), except for their missing spatially constant $C(t)$, which gives an important contribution to the dynamic pressure. The first term in the velocity potential takes care of the body boundary condition associated with the rigid body motions. The terms associated with the deformation velocity potential Ω_{dm} take care of the body boundary conditions due to the membrane deformations. The ϕ term is a sum of sloshing eigenmodes satisfying homogeneous Neumann body boundary conditions, i.e:

$$\phi(y,z,t) = \sum_{n=1}^{\infty} R_n(t)\cos(\pi n(y + \frac{1}{2}l)/l)\frac{\cosh(\pi n(z+h)/l)}{\cosh(\pi n h/l)}, \tag{4.11}$$

where $R_n(t)$ are generalized coordinates for the velocity potential.

The deformation potentials satisfy in addition to the Laplace condition and

zero Neumann conditions on $z = -h$ and $y = 0.5l$, the boundary conditions:

$$\begin{aligned} \left.\frac{\partial \Omega_{dm}}{\partial y}\right|_{y=-\frac{l}{2}} &= U_m(z), & -h < z < 0, \\ \left.\frac{\partial \Omega_{dm}}{\partial z}\right|_{z=0} &= \frac{1}{l}\int_{-h}^{0} U_m(z)dz, & -\frac{l}{2} < y < \frac{l}{2}, \end{aligned} \tag{4.12}$$

The latter condition is consistent with conservation of liquid mass and the first term of the Fourier series representation of the free surface given by (4.9).

To get an analytical solution of $\Omega_{dm}(y, z)$, we represent the wall velocity profile given by $U_m(z)$ as a Fourier series:

$$U_m(z) = \alpha_{0m} + \sum_{k=1}^{\infty} \alpha_{km} \cos(k\pi(z+h)/h), \tag{4.13}$$

where the Fourier coefficients α_{0m} and α_{km} are found by:

$$\begin{aligned} \alpha_{0m} &= \frac{1}{h}\int_{-h}^{0} U_m(z)dz = 2\frac{L}{hm\pi}\sin^2(\frac{m\pi h}{2L}), \\ \alpha_{km} &= \frac{2}{h}\int_{-h}^{0} U_m(z)\cos(k\pi(z+h)/h)dz \\ &= \frac{2L}{\pi}\frac{kL\sin(\pi k)sin(\frac{m\pi h}{L}) + hm(-1)^k cos(\frac{m\pi h}{L}) - hm}{L^2k^2 - h^2m^2}. \end{aligned}$$

Faltinsen and Timokha (2009, p. 224-225) have presented the following analytical solution

$$\begin{aligned} \Omega_{dm}(y,z) = &-\frac{\alpha_{0m}}{2l}((y-0.5l)^2 - (z+h)^2) \\ &-\sum_{k=1}^{\infty}\frac{\alpha_{km}h}{k\pi}\cos(k\pi(z+h)/h)\frac{\cosh(k\pi(y-0.5l)/h)}{\sinh(\pi kl/h)}. \end{aligned} \tag{4.14}$$

We must in the end ensure that the total velocity potential satisfies the dynamic and kinematic free surface conditions as given by (4.7)-(4.8). This set up a relation between the generalized coordinates $\beta_n(t)$ and $R_n(t)$, determines $C(t)$ and derives ordinary differential equations for the generalized coordinates β_n. To find a relation between the generalized coordinates $\beta_n(t)$ and $R_n(t)$, the kinematic boundary condition is multiplied with $\cos(\pi n(x+0.5l)/l)$ for $n \geq 1$ and integrated from $-l/2$ to $l/2$. It follows that

$$\dot{\beta}_n(t) = \kappa_n R_n(t), \tag{4.15}$$

where the wave number κ_n is

$$\kappa_n = \frac{\omega_n^2}{g} = \frac{\pi n}{l}\tanh(\frac{n\pi}{l}h), \tag{4.16}$$

with ω_n as the natural sloshing frequencies for the rigid tank.

To find $\dot{C(t)}$ we integrate the dynamic free surface condition ((4.8)) over the free surface. The result is:

$$\dot{C(t)} = -\sum_{m=1}^{\infty} \overline{\Omega_{dm}} \ddot{\nu}_m(t) - \frac{g}{l} \sum_{m=1} \nu_m(t) \int_{-h}^{0} U_m(z) dz, \tag{4.17}$$

where

$$\overline{\Omega_{dm}} = \frac{1}{l} \int_{-\frac{l}{2}}^{\frac{l}{2}} \Omega_{dm}(y,0) dy = -\frac{\alpha_{0m}}{2l}(\frac{l^2}{3} - h^2) - \sum_{k=1}^{\infty} \frac{\alpha_{km} h^2}{l k^2 \pi^2}(-1^k).$$

The ordinary differential equations for $\beta_n(t)$ follows by multiplying (4.8) with $\cos(\pi n(x + 0.5l)/l)$ for $n \geq 1$ and integrating from $-l/2$ to $l/2$. The result is

$$\ddot{\beta}_n + \omega_n^2 \beta = -\frac{\gamma_{2n}}{\overline{m}_n} \ddot{\eta}_2 - \sum_m \frac{\gamma_{dnm}}{\overline{m}_n} \ddot{\nu}_m(t) \text{ for } n = 1, 2.., \tag{4.18}$$

where

$$\overline{m}_n = \frac{\rho l}{2\kappa_n}, \quad \frac{\gamma_{2n}}{\rho_w} = \left(\frac{l}{n\pi}\right)^2 [(-1)^n - 1], \tag{4.19}$$

$$\frac{\gamma_{dnm}}{\rho_w} = -\alpha_{0m} \frac{l^2}{\pi^2 n^2} - \frac{1}{\pi^2} \sum_{k=1}^{\infty} \frac{\alpha_{km}(-1)^k l^2 h^2}{l^2 k^2 + h^2 n^2}. \tag{4.20}$$

Here $\overline{m}_n$, γ_{dnm} and γ_{2n} are the hydrodynamic coefficients associated with the water mass, wall deformations and sway motion, respectively.

Based on the found Φ, the linear dynamic pressure p on the 2D membrane is :

$$\begin{aligned} p =& -\rho_w \frac{\partial \Phi}{\partial t}(-\frac{l}{2}, z) \\ =& -\rho_w \Bigg(\sum_{m=1}^{\infty} (\Omega_{dm}(-\frac{l}{2}, z) - \overline{\Omega_{dm}}) \ddot{\nu}_m(t) - \frac{l}{2} \ddot{\eta}_2(t) \\ &+ \sum_{n=1}^{\infty} \frac{\ddot{\beta}_n(t)}{\kappa_n} \phi_n(-\frac{l}{2}, z) - \frac{g}{l} \sum_{m=1}^{\infty} \int_{-h}^{0} U_m(z) dz \nu_m(t) \Bigg) \end{aligned} \tag{4.21}$$

where ρ_w is the liquid density. The last part of the pressure contribution comes from $C(t)$ and is a quasi-steady hydrostatic pressure change due to the change in mean free surface position. This pressure part is added in Malenica et al. (2015), but should not as long as one solves a boundary value problem with the same free-surface condition as stated in (4.7) and (4.8). An additional confirmation is that we show later, by a numerical solution using the same free surface conditions and the dynamic pressure given as $-\rho_w \partial \Phi / \partial t$, that we get the same results as with the analytical solution.

Ordinary differential equations for the structural mode amplitudes ν_m can now be found by multiplying (4.1) with the mode $U_j(z)$ and integrating from $z = -h$ to

$z = L - h$. This gives

$$\ddot{\nu}_j(t) + \lambda_m^2 \nu_j(t) = \frac{\rho_w}{\overline{m}_c} \int_{-h}^{0} \frac{\partial \Phi}{\partial t}(-\frac{l}{2}, z) U_j(z) dz, \tag{4.22}$$

where the generalized modal mass, is $\overline{m}_c = \rho_c dL/2$. The term on the right hand side of (4.22) can be rewritten in terms of generalized added mass and restoring coefficients by the following definitions:

$$\int_{-h}^{0} \sum_{m=1}^{\infty} (\Omega_{dm}(-\frac{l}{2}, z) - \overline{\Omega_{dm}}) U_j(z) dz \ddot{\nu}_m(t) = -\sum_{m=1}^{\infty} \frac{a_{mj}^{(\Omega)}}{\rho_w} \ddot{\nu}_m(t), \tag{4.23}$$

$$\int_{-h}^{0} \sum_{n=1}^{\infty} \ddot{\beta}_n(t) \frac{\cosh(\pi n(z+h)/l)}{\kappa_n \cosh(\pi n h/l)} U_j(z) dz = -\sum_{n=1}^{\infty} \frac{a_{nj}^{(\phi)}}{\rho_w} \ddot{\beta}_n(t), \tag{4.24}$$

$$\frac{g}{l} \sum_{m=1}^{\infty} \int_{-h}^{0} U_m(z) dz \int_{-h}^{0} U_j(z) dz \nu_m(t) = \sum_{m=1} \frac{c_{mj}}{\rho_w} \nu_m(t), \tag{4.25}$$

$$\frac{l}{2} \int_{-h}^{0} U_j(z) dz \ddot{\eta}_2(t) = \frac{\gamma_{2j}}{\rho_w} \ddot{\eta}_2(t). \tag{4.26}$$

Superscripts are used on the coupled added mass coefficients $a_{mj}^{(\Omega)}$ and $a_{nj}^{(\phi)}$ to indicate that they are associated with Ω and ϕ, respectively. The consequences are that $a_{mj}^{(\Omega)}$ is frequency independent while $a_{nj}^{(\phi)}$ is frequency dependent. $a_{mj}^{(\Omega)}$ provide coupling between the structural modes, while $a_{nj}^{(\phi)}$ provide coupling between the structural and sloshing modes. The restoring coefficients c_{mj} are associated with quasi- static hydrostatic pressure change due to mean free-surface change described by the first term in the Fourier series (4.9) for the free surface elevation. The coefficients γ_{2j} are proportional to coupled generalized added mass between sway and structural modes. The calculation of and expression for the different parts of the pressure contribution is given in the Appendix ((A.1)- (A.4)).

The total equation for the 2D membrane becomes:

$$\ddot{\nu}_j(t) + \sum_m \frac{1}{\overline{m}_c} a_{mj}^{(\Omega)} \ddot{\nu}_m(t) + \lambda_m^2 \nu_j(t) + \sum_m \frac{c_{mj}}{\overline{m}_c} \nu_m(t) = -\sum_n \frac{a_{nj}^{(\phi)}}{\overline{m}_c} \ddot{\beta}_n(t) - \ddot{\eta}_2(t) \frac{\gamma_{2j}}{\overline{m}_c}. \tag{4.27}$$

From (4.27) it can be seen that the response of a given mode j is dependent on all the other modes, both structural modes, and free surface modes.

It follows from Greens second identity, boundary conditions on mean free surface Σ_0 and mean wetted body surface S_B and n as the normal direction to

these surfaces that

$$\begin{aligned}
&\int_{\Sigma_0+S_B}\left[(\Omega_{dm}(\frac{-l}{2},z)-\overline{\Omega_{dm}})\frac{\partial\Omega_{dj}(\frac{-l}{2},z)}{\partial n}-(\Omega_{dj}(\frac{-l}{2},z)-\overline{\Omega_{dj}})\frac{\partial\Omega_{dm}(\frac{-l}{2},z)}{\partial n}\right]dS\\
=&\int_{-h}^{0}\left[(\Omega_{dm}(\frac{-l}{2},z)-\overline{\Omega_{dm}})U_j(z)-(\Omega_{dj}(\frac{-l}{2},z)-\overline{\Omega_{dj}})U_m(z)\right]dz\\
=&a_{mj}^{(\Omega)}-a_{jm}^{(\Omega)}=0.
\end{aligned}$$

That means find if $a_{mj}^{(\Omega_d)}=a_{jm}^{(\Omega_d)}$. By exchanging the mode U_j with the Fourier representation in (4.24), we find that $a_{nj}^{\phi}=\gamma_{dnj}$.

4.1.2 Analytical frequency-domain solution

We solve both the tank and the 2D membrane problem in the frequency domain, by substituting $\nu_m=\overline{\nu}_m\exp(i\omega t)$ and $\beta_n=\overline{\beta}_n\exp(i\omega t)$ with ω as the forcing frequency in (4.18) and (4.27). The result is

$$(\omega_n^2-\omega^2)\overline{\beta}_n-\omega^2\sum_m\frac{\gamma_{dnm}}{\overline{m}_n}\overline{\nu}_m=\frac{\gamma_{2n}}{\overline{m}_n}\omega^2\overline{\eta}_2, \tag{4.28}$$

$$-\omega^2\sum_n\frac{a_{nj}^{\phi}}{\overline{m}_c}\overline{\beta}_n+(\lambda_m^2-\omega^2)\overline{\nu}_j+\sum_m\frac{1}{\overline{m}_c}(c_{jm}-\omega^2a_{mj}^{(\Omega)})\overline{\nu}_m=\omega^2\frac{\gamma_{2j}}{\overline{m}_c}\overline{\eta}_2. \tag{4.29}$$

Estimating the eigenfrequencies of the system

If we combine (4.28) and (4.29), we get:

$$\begin{aligned}
-\sum_n\sum_m\frac{\omega^4a_{nj}^{\phi}\gamma_{dnm}}{\overline{m}_c\overline{m}_n(\omega_n^2-\omega^2)}\overline{\nu}_m+(\lambda_m^2-\omega^2)\overline{\nu}_j+\sum_m\frac{c_{jm}-\omega^2a_{mj}^{(\Omega)}}{\overline{m}_c}\overline{\nu}_m=\\
\frac{\omega^2}{\overline{m}_c}(\gamma_{2j}-\sum_n\frac{\omega^2a_{nj}^{\phi}\gamma_{2n}}{\overline{m}_n(\omega_n^2-\omega^2)})\overline{\eta}_2
\end{aligned}. \tag{4.30}$$

The natural frequencies of the system is found by looking at the nontrivial solution of (4.30) for zero excitation ($\eta_2=0$). For a given mode j we can see that there are coupling to other modes both in the structural modes (m) and for the sloshing (modes n). The coupling causes the natural frequencies ω_n^* to differ from the natural frequencies ω_n of the rigid tank. Equation (4.30) will have two limits when it comes to tension T. When tension $T\to\infty$, the dry structural natural frequencies $\lambda_m\to\infty$, and (4.30) reduces to $\omega_n^*=\omega_n$. Meaning that the eigenfrequencies of the system become the eigenfrequencies of the sloshing problem. On the other hand when $T=0$, the system still have stiffness from the free surface stiffness term c_{mm}, meaning that $\omega_n^*>0$ also for the case of zero tension. However, this is a case where the linear 2D membrane theory as described here is not valid, as bending is neglected and will have an influence in reality.

A first estimate of the coupled eigenfrequency of the tank with the elastic wall is that we neglect the coupling effect between structural modes, and only considers one structural mode, together with one free surface mode. We introduce the following wet 2D membrane eigenfrequency as $\lambda_m^* = \sqrt{\frac{\overline{m}_c\lambda_m^2 + c_{mm}}{\overline{m}_c + a_{mm}^{(\Omega)}}}$. Here a_{mj}^{Ω} is used to estimate the added mass effect. This gives:

$$\left(-\omega^4 \frac{a_{nm}^{(\phi)}\gamma_{dnm}}{\overline{m}_n(\overline{m}_c + a_{mm}^{(\Omega)})} + (\omega_n^2 - \omega^2)(\lambda_m^{*\,2} - \omega^2) \right)\overline{\nu}_m = 0. \tag{4.31}$$

Equation (4.31) is a fourth order directly solvable equation with two possible positive solutions for every parameter combination. An estimate of the first two possible eigenfrequencies, based on the first structural mode ($j = 1$) and the first free surface mode ($n = 1$) are found by:

$$\omega_{1s}^{est}, \omega_{2s}^{est} = \sqrt{\frac{\omega_1^2 + \lambda_1^{*2} \mp \sqrt{(\omega_1^2 + \lambda_1^{*2})^2 - 4(1 - \frac{a_{11}^{(\phi)}}{\overline{m}_c + a_{11}^{(\Omega)}}\frac{\gamma_{d11}}{\overline{m}_1})\omega_1^2\lambda_1^{*2}}}{2(1 - \frac{a_{11}^{(\phi)}}{\overline{m}_c + a_{11}^{(\Omega)}}\frac{\gamma_{d11}}{\overline{m}_1})}}. \tag{4.32}$$

4.1.3 Numerical solution

A numerical solution using the Harmonic Polynomial Cell (HPC) method as described in Appendix B has been implemented. The HPC method is a field method initially described by Shao and Faltinsen (2014a,b) to solve the Laplace equation with boundary conditions for an unknown velocity potential. In the HPC method, the local expression of the velocity potential within a cell uses harmonic polynomials. Hence, the governing equation is satisfied naturally. The connectivity between different cells is built by overlapping the local expressions. A key feature of the HPC method is in using higher-order local expressions satisfying Laplace equation, which means that we can expect a better accuracy than for many other low order field and boundary integral formulations presently used. Moreover, the HPC method operates with a sparse coefficient matrix, so that many existing numerical matrix solvers can solve the associated problem efficiently.

The solution by the HPC method is based on representing the velocity potential as

$$\Phi = \sum_{m=0}^{M} \phi_m \dot{v}_m, \tag{4.33}$$

where $v_0 = \eta_2$ and $U_0 = 1$ and ϕ_m satisfy the body boundary condition

$$\left.\frac{\partial \phi_m}{\partial y}\right|_{y=-l/2} = U_m(z), \tag{4.34}$$

together with homogenous Neumann conditions at $y = l/2$ for $m \geq 1$ and $\partial\phi_0 \partial y = 1$ at $y = l/2$, homogenous Neumann conditions at $z = -h$ and the combined

free surface condition following from (4.7) and (4.8). The 2D membrane is solved numerically by a modal representation, as for the analytical solution, where the deformation is given by (4.5). Equation (4.22) is used to find ν_j by first expressing the right hand side in terms in terms of generalized added mass coefficients a_{jm} defined as follows

$$\rho_w \int_{-h}^{0} \frac{\partial \Phi}{\partial t} U_j(z) dz = -\sum_{m=0}^{M} a_{jm} \ddot{\nu}_m, j = 1..M, \tag{4.35}$$

$$a_{jm} = -\int_{-h}^{0} \phi_m U_j(z) dz. \tag{4.36}$$

Simpson's integration method is used. The expressions are controlled by using that $a_{jm} = a_{mj}$ for j between 1 and M. The latter follows by using Green's second identity

$$\int_{S_F+S_B} \left[\phi_j \frac{\partial \phi_m}{\partial n} - \phi_m \frac{\partial \phi_j}{\partial n} \right] dS = 0,$$

together with boundary conditions on the mean the free surface S_F and on the mean wetted tank surface S_B and using that $\partial/\partial n$ means derivative along surface normal.

4.2 Case simulation results

To better get an understanding of how the system behaves, two main test cases have been run. For both cases, a 2D sloshing tank is used. The water depth-to-tank length ratio h/l is 0.5. Furthermore, wall thickness-to-tank length ratio is $d/l = 2.5 \cdot 10^{-3}$ and water density to solid wall density is $\rho_w/\rho_c = 1$. The fist case is with a rigid movable left wall with a spring attached as described by Lu et al. (1997) and Chai et al. (1996). The second case is with a membrane left wall.

4.2.1 Case simulation results, movable wall

A special case of what we consider is that the wall moves as a rigid body, which corresponds to $U_0 = 1$ and $U_m = 0$ for $m > 0$. This case have earlier been studied by Lu et al. (1997) and Chai et al. (1996). The relations in the coupled system is given by (4.30) with the coefficients for this particular system given as $\overline{m}_c = \rho_c dh$, $\lambda_k^2 = k_s/\mu$, where k_s is a spring stiffness and the coefficients $c^{rw} = \frac{\rho_w g h^2}{l}$, $a^{rw,(\Omega)} = \frac{\rho_w h}{3l}(l^2+h^2)$ and $a^{rw,(\phi)}\gamma_d^{rw} = \rho_w \frac{2l^2}{(n\pi)^3} \tanh(k_n h)$, where rw stands for rigid wall.

The eigenfrequencies for the analytical solution has been estimated as a function of the spring stiffness k_s by considering when the determinant of the coupled system becomes zero. The non-dimensional eigenfrequencies $\omega_n^* \sqrt{l/g}$ of the system for different stiffness, for the case where the wall moves as a rigid body is plotted in Figure 4.2. The analytical and the numerical solution based on the HPC method give the same eigenfrequencies. These eigenfrequencies also agree with the eigenfrequencies found by the method of Lu et al. (1997).The eigenfrequencies

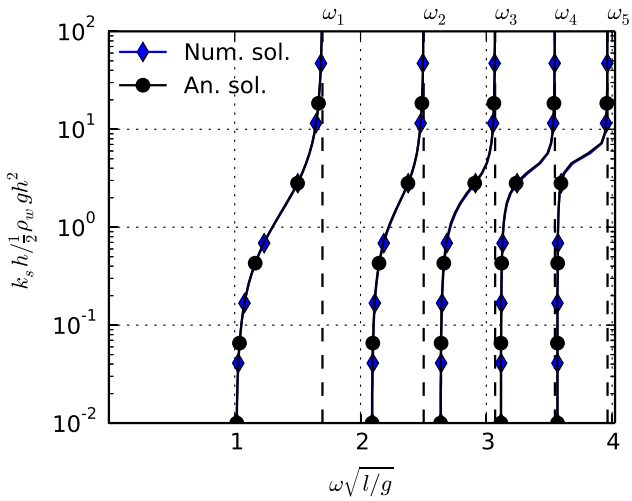

Figure 4.2: Non-dimensional eigenfrequencies of the coupled system eigenfrequencies $\omega_n^*\sqrt{l/g}$ for given stiffness $k_s h/\frac{1}{2}\rho_w g h^2$ for a rectangular tank with a rigid moving left wall. ω_n is the sloshing eigenfrequency for the rigid tank. Water depth (h)-to- l tank length ratio=0.5.

ω_n^* are dependent on the spring stiffness k_s. From Figure 4.2 we see that $\omega_n^* \leq \omega_n$ as analytically shown by Schulkes (1990). When $k_s \to 0$, the dry eigenfrequency $\lambda_k \to 0$. Since the coupled fluid structure problem still have stiffness from the free surface stiffness term c^{rw}, the first eigenfrequency ω_1^* is finite.

4.2.2 Case simulation results, flexible wall

A test case with a flexible membrane wall with two different membrane wall lengths L ($L = h$ and $L = 2h$), and different tensions were then investigated.

Eigenfrequencies of the coupled system

The eigenfrequencies for the analytical solution have been estimated as a function of the tension T by considering when the determinant of the coupled system becomes zero. Even though the hydrostatic pressure is not applied to the system, the hydrostatic pressure force equal to $\frac{1}{2}\rho_w g h^2$ is a real physical quantity to compare the amount of tension applied to the system too. We therefore define the reference tension $T_0 = \frac{1}{2}\rho_w g h^2$ and use T/T_0 which is a ratio between the tension forces and the hydrostatic pressure forces. Converged results have been obtained by increasing numbers J of structural modes and numbers N of generalized free-surface coordinates. The non-dimensional eigenfrequencies $\omega_n^*\sqrt{l/g}$ of the system for different tensions $T/T_0 \in [5 \cdot 10^{-3}, 10]$, for 2D membrane lengths $h/L = 1$ and $h/L = 2$ are plotted in Figure 4.3.

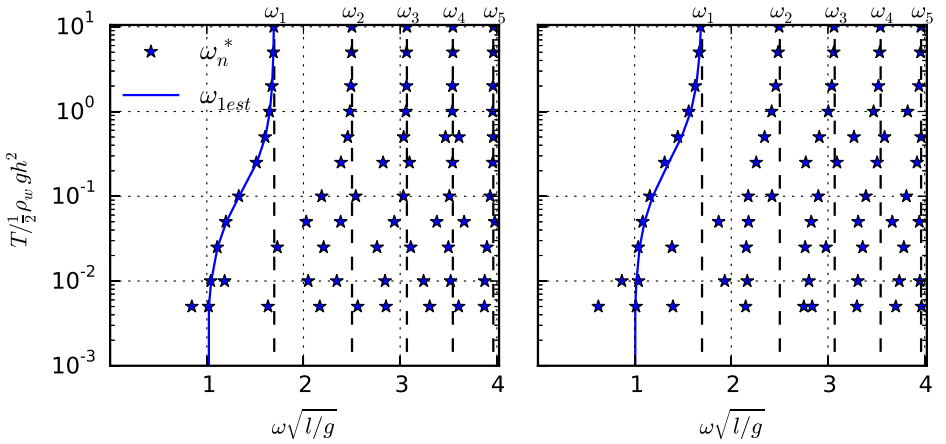

Figure 4.3: Non-dimensional eigenfrequencies of the coupled system eigenfrequencies $\omega_n^*\sqrt{l/g}$ for given tensions T/T_0 where $T_0 = \frac{1}{2}\rho_w g h^2$ for a rectangular tank with a membrane at the left wall. ω_n is the sloshing eigenfrequency for the rigid tank. Water depth (h)-to- l tank length ratio=0.5. Membrane length left: $L = h$. Right: $L = 2h$.

The eigenfrequencies of the system are highly dependent on both the tension and the 2D membrane length. If we consider a given value of T/T_0, then the eigenfrequency ω_n^* of the coupled system is smaller than the sloshing frequency ω_n of the rigid tank for any given n. When $T/T_0 \to \infty$, $\omega_n^* \to \omega_n$. If T/T_0 is small, and we consider a given ω_n, then there can be more than n eigenfrequencies of the coupled system that is lower than ω_n.

The first mode eigenfrequency of the system, from free surface mode $n = 1$, and structural mode $j = 1$ can be nicely estimated with ω_{1s}^{est}, as can be seen from Figure 4.3. The line of ω_{2s}^{est} is not plotted in the figure, and that is because it did not fit with the system frequencies. The higher ω_n^* are not direct solutions of (4.32) with other n, j combinations, which indicates that these frequencies depend on more than one set of (n, j) terms. This result was expected since the rigid tank sloshing frequencies are located so closely together that it is plausible that more than one will influence the coupled eigenfrequency ω_n^* for $\omega_n^* > \omega_1$. The Figure shows that lower eigenfrequencies ω_n^* than ω_{1s}^{est} exist for the two lowest investigated tensions T/T_0.

If the eigenfrequencies of the flexible membrane in Figure 4.3 are compared to the eigenfrequencies of the rigid moving wall case displayed in Figure 4.2, we see that one eigenfrequency ω_n^* converges to $\omega_n^*\sqrt{l/g} \approx 1$, for both the rigid movable wall and for the flexible membrane case when respectively T and $k_s h \to 0$ for the studied case. However, it is not general that this eigenfrequency of the system is close to $\sqrt{g/l}$, when $T \to 0$. The similarity of the eigenfrequencies can be explained as follows: In (4.13) we represent the deformation mode as a Fourier series. If the constant term α_{0m} gives a much larger contribution to the pressure for the first

mode than the remaining terms, the effect would be that solution of the case with the membrane wall will approach the solution of the rigid moving wall case, for frequencies lower than the first sloshing frequency. Higher eigenfrequencies ω_n^* does not show the same trend of being comparable.

For $T > 0.1T_0$ the eigenfrequencies appear to be converged within the frequency range for number of structural modes $J \geq 3$ for both the 2D membrane lengths. However, as the tension decreases more structural modes come into play. For the coupled analysis it was observed that as long as $J, N \geq 6$, the eigenfrequencies of the system did not change with increasing N, J for the given tension interval. This result would indicate that all the eigenfrequencies for the studied cases are within the first six eigenmodes.

Transfer function of free surface elevation of the coupled system

The analytical and numerical ratios ζ_a/η_{2a} (transfer function) between the wave amplitude at the right wall and the sway amplitude versus non-dimensional forcing frequency $\omega\sqrt{l/g}$ are plotted for the membrane length $L = h$ and $L = 2h$ in Figure 4.4 and 4.5, respectively. The non-dimensional tensions $T/T_0 = \frac{1}{4}, \frac{1}{2}, 1$ and 2 are examined. The analytical and numerical solutions agree very well, which support the correctness of both of them. Similar as for the eigenfrequencies plotted in Figure 4.3 we see that the transfer functions are dependent on the tension in the system. The response goes to infinity at the eigenfrequencies of the system. If a rigid tank is considered, the system will have five eigenfrequencies in the considered frequency range. However, ω_2 and ω_4 correspond to even modes, and resonance oscillations at the right wall at these frequencies cannot be excited. For the tank with a flexible wall, we note resonant response at six eigenfrequencies for $T/T_0 = \frac{1}{4}$ and $T/T_0 = \frac{1}{2}$ and $L = 2h$. There are five eigenfrequencies for the other considered cases. When $L = h$, very narrow resonant response occurs close to ω_2 with $T/T_0 = \frac{1}{2}, 1$ and 2, and close to ω_4 with $T/T_0 = 1$ and 2. When $L = 2h$, very narrow resonant response occurs close to ω_2 with $T/T_0 = 1$ and 2. A large response is seen also between ω_3 and ω_4 for $T/T_0 = \frac{1}{2}$ for $L = h$, and between ω_3 and ω_5 for $T/T_0 = \frac{1}{2}$ and 1, for $L = 2h$. The response of the free surface rises to infinity at the eigenfrequencies, in agreement with linear potential flow theory of incompressible liquid.

More modes are needed in the analytical solution for the transfer function compared to the analysis of the eigenfrequencies to find the correct amplitude. In the calculation of the transfer function, 30 generalized free-surface coordinates β_n were used.

In the numerical solution, a square grid ($dx = dz$) with $N_x = 101$ nodes in the free surface were used. A convergence study has been run, and the results are converged. It was observed that for low tensions ($T < \frac{1}{4}T_0$) peaks in the transfer function showed up in the solution at the eigenfrequencies of the tank. These peaks vanished when the grid was refined. This cancellation effect can be seen by looking at (4.30). When $\omega \to \omega_n$, the first and the last term in the (4.30) will be much larger than the rest. Also, it can be assumed that the contributions from the given mode n, will be far greater than the other modes, reducing (4.30) at the frequency limit

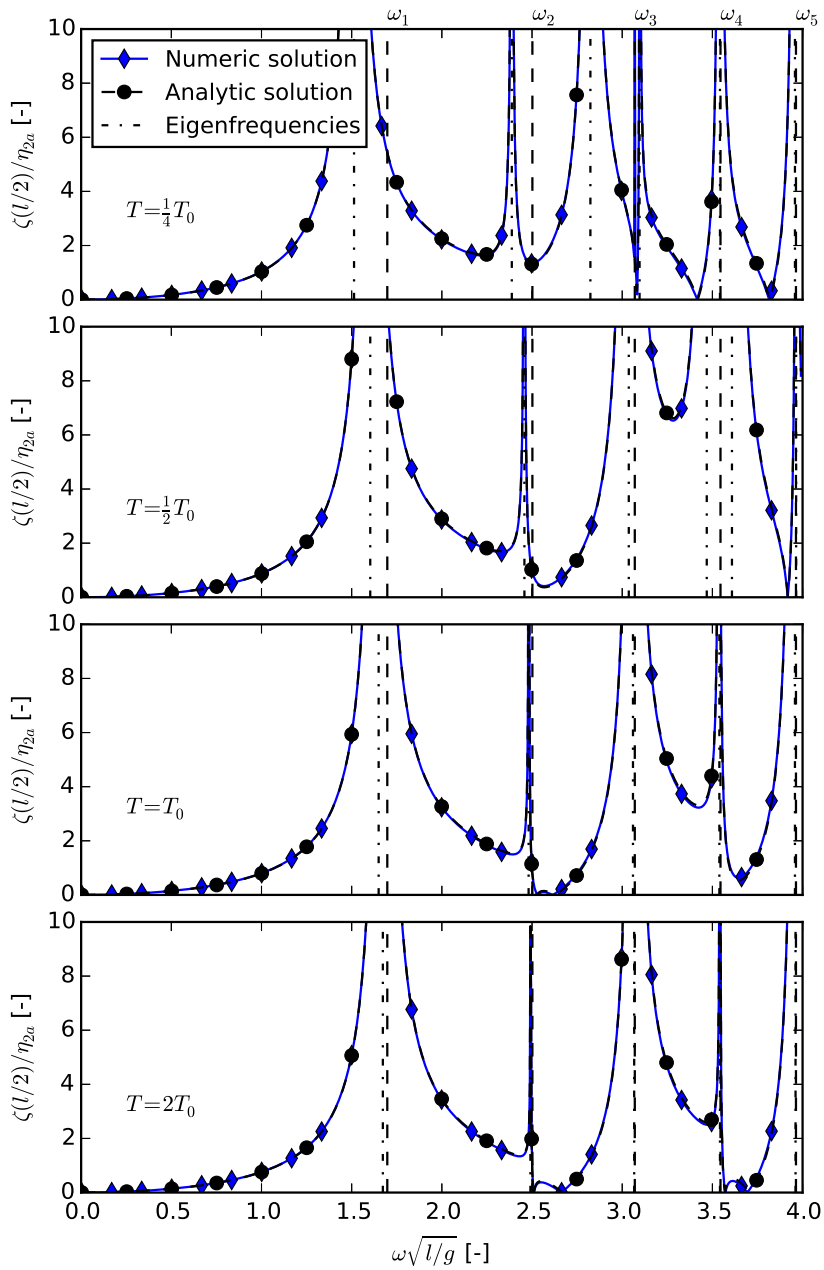

Figure 4.4: The analytical and numerical ratio $\frac{\zeta(l/2)}{\eta_{2a}}$ between the wave amplitude at the right wall ($\zeta(l/2)$) and the sway amplitude η_{2a}, versus non-dimensional forcing frequency $\omega\sqrt{l/g}$ for forced sway oscillation of a rectangular tank with a membrane as the left wall. Water depth (h)-to- l tank length ratio=0.5. Membrane length $L = h$. Influence of non-dimensional membrane tension T/T_0 where $T_0 = \frac{1}{2}\rho_w g h^2$.

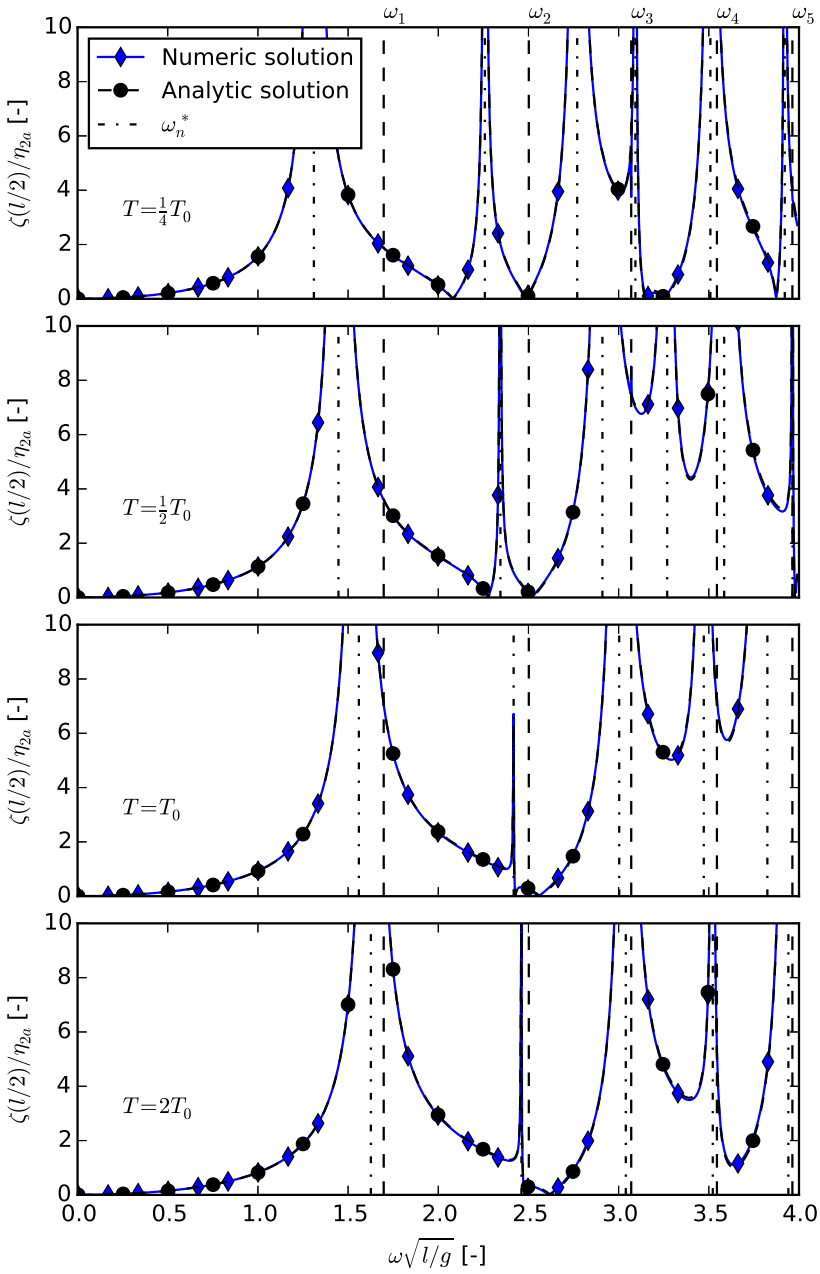

Figure 4.5: The analytical and numerical ratio $\frac{\zeta(l/2)}{\eta_{2a}}$ between the wave amplitude at the right wall ($\zeta(l/2)$) and the sway amplitude η_{2a}, versus non-dimensional forcing frequency $\omega\sqrt{l/g}$ for forced sway oscillation of a rectangular tank with a membrane as the left wall. Water depth (h)-to- l tank length ratio=0.5. Membrane length $L = 2h$. Influence of non-dimensional membrane tension T/T_0 where $T_0 = \frac{1}{2}\rho_w g h^2$.

$\omega \to \omega_n$ to:

$$\sum_m \gamma_{dnm}\overline{\nu}_m = \gamma_{2n}\overline{\eta}_2, \tag{4.37}$$

which means that at the sloshing eigenfrequency of the rigid tank, the resonance cancels and we get a frequency independent relation between the forced sway and the deformation. The practical implications of this are that for frequencies around the sloshing eigenfrequency of the rigid tank, a more refined grid is needed for this canceling effect to happen. If care is not shown in the numerical solution, numerical inaccuracies can cause unphysical resonances. It was the fact that we had the analytical solution that pointed out this numerical problem for the direct solution of the boundary value problem.

4.3 Conclusions and following work

A 2D rectangular sloshing tank with a flexible side wall has been studied analytically and numerically with a focus on the coupling effects between sloshing and the flexible wall. Analytical and numerical solutions agree well. Two cases have been analysed for a rectangular tank; one case with a rigid movable left wall with a spring attached, and one case with a flexible membrane left wall.

The eigenfrequencies of the system with a flexible membrane left wall relied heavily on both the tension and the 2D membrane length. For low tensions, more than one eigenfrequency may exist between two neighbouring sloshing frequencies for the rigid tank. For large tensions, the eigenfrequencies of the system became the sloshing frequency of a rigid tank. For a given tension, one low eigenfrequency was found to involve interaction only between the lowest structural mode and sloshing mode. The other eigenfrequencies involved combinations of several structural and sloshing modes.

The analytical solution provided important guidance for the numerical solution. If care is not shown in the numerical solution, numerical inaccuracies can cause non-physical resonances. By comparing the analytical solution with the numerical solution, it was shown that it is wrong to add a quasi-steady hydrostatic pressure change due to the time-dependent change in the mean free surface caused by the elastic wall deformations.

The response of the coupled system was infinite at the eigenfrequencies of the system. In reality, the amplitude must be finite. In order to find the actual response of the system, viscous damping and non-linear free surface effects should be included. This is left for further work. In continuation of the presented work, we wish to use the gained knowledge and the validated numerical code to analyse the response of a semi-circular closed flexible fish cage in waves. However, to do that the geometry and initial tension of the structure must first be found, this will be investigated in the following chapter.

Chapter 5

Static structural analysis of a 2D membrane tank in calm water

The initial shape and tension of the membrane must be known in order to analyse a 2D membrane in waves and/or current. For the cases examined in Strand et al. (2014), the bags were underfilled, and the shape of the bag was dependent on the load history of the bag. To be able to use linear dynamic theory in waves, the mean tension must be larger than zero. We secure a mean tension greater than zero in calm water by introducing a pressure difference over the membrane from an overfilling of the bag and a density difference between the inside volume and the outside. The shape of the membrane will then be dependent on this pressure difference.

In this Chapter a 2D static membrane under overpressure due to a hydrostatic pressure difference is analysed with the aim to find the static geometry and the tension in the membrane. Equations for the static membrane deformations are found and analysed in a case study. Under certain assumption the equations describing the geometry and the tension can be simplified, such that a direct analytical solution can be found.

5.1 Analysis of static 2D membrane tank in calm water, with overpressure

We consider a 2D membrane tank with two floaters in calm water as shown in Figure 5.1. The horizontal distance between the centerlines of the two floaters is $2R$. The floaters are free to move in the vertical direction, but are restrained from moving relative to each other in the horizontal direction, which means that we must have a rod arrangement in practice. There is a hydrostatic pressure difference at the membrane between the inside enclosed volume and the surrounding water due to different free surface levels and/or water densities.

The Cartesian coordinate system Oyz is defined in Figure 5.1 with the $y-$ axis along the free surface of the outer water domain and the $z-$ axis along the centerline of the tank. Positive $z-$ direction is upwards. The unknowns are membrane tension T per unit length in the perpendicular $x-$ direction and the geometric position

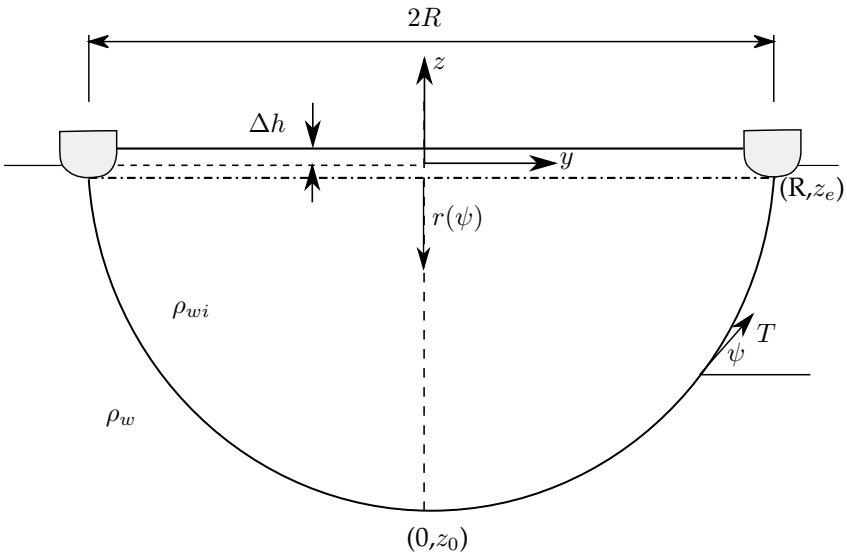

Figure 5.1: 2D membrane tank with water height difference Δh between inner and outer free-surface levels. $2R$ = horizontal distance between the centerlines of the two floaters. $(\pm R, z_e)$ are coordinates of the attachment points between the membrane and the floaters. T=membrane tension per unit length in perpendicular $x-$ direction. $(0, z_0)$ is the lowest point of the membrane where the angle ψ between the membrane tangent and the $y-$ axis is zero. ρ_{wi} and ρ_{we} are the densities of the water inside and outside the membrane, respectively.

of the wetted tank surface. We introduce a curvilinear coordinate s along the membrane starting from the lowest membrane point $(0, z_0)$ with positive direction towards the right floater. Details of the membrane and the right floater are shown in Figure 5.2 and Figure 5.3, respectively.

The analysis is inspired by the cable analysis in Chapter 8 in Faltinsen (1990). A difference is that we must account for the additional pressure difference Δp. This pressure difference is both due to a height difference Δh between the inner and outer free-surface levels, and a density difference $\Delta\rho = \rho_{wi} - \rho_w$, where ρ_{wi} is the density of the water inside the membrane, and ρ_w is the density of the water outside the membrane. The hydrostatic pressure on the inside point of the membrane is $-\rho_{wi} g(z - \Delta h)$. The hydrostatic pressure on a point outside at the membrane which is located perpendicular to the membrane from the considered inside point is $-\rho_w g(z - d\cos(\psi))$. Here, d is the membrane thickness, g is the acceleration of gravity and the angle ψ is defined in Figure 5.1. The hydrostatic pressure difference Δp for a given curvilinear coordinate s is therefore

$$\begin{aligned}\Delta p_0 =& -g((\rho_w + \Delta\rho)(z - \Delta h) + \rho_w(z - d\cos\psi)) \\ =& g(\rho_w \Delta h - \rho_w d\cos\psi - \Delta\rho z + \Delta\rho\Delta h).\end{aligned} \tag{5.1}$$

We consider an element of the membrane as illustrated in Figure 5.2. The segment length is denoted ds. Our analysis assumes an inelastic membrane in calm

water. Static force equilibrium gives that:

$$dT = m_M g \sin\psi ds, \tag{5.2}$$

$$\begin{aligned} Td\psi &= m_M g \cos\psi ds + \Delta p_0 ds \\ &= g(m_M \cos\psi + \rho_w \Delta h - \rho_w d\cos\psi - \Delta\rho z(\psi) + \Delta\rho\Delta h)ds. \end{aligned} \tag{5.3}$$

Here m_M is membrane mass per unit area in air. This equation system is for Δh and $\Delta\rho = 0$ equivalent to the cable representation as described in Faltinsen (1990).

The $z(\psi)$ term in (5.3) can be written as $z(\psi) = -r(\psi)\cos(\psi) + z_e$, where $r(\psi)$ is the radial coordinate defined in Figure 5.1, and z_e is the z-coordinate of the attachment point between floater and membrane. Neither $r(\psi)$ nor z_e in $z(\psi)$ is known a priori, and the resulting equation set is therefore implicit. To be able to solve the equation set and find a solution, a first approximation of $r(\psi) = R$ is used, and z_e is found by a vertical force equilibrium of the right floater. This force equilibrium is dependent on the tension and the end angle ψ_e at the attachment point to the floater. An iteration between the multiple equations are then necessary to find a stable equilibrium. An alternative to approximating $z(\psi)$ as $z(\psi) = -R\cos(\psi) + z_e$ is to use the actual $z(\psi)$ found in numerical calculations, and iterate the whole z-part of the pressure to find a stable equilibrium. A good start value of $z(\psi)$ is then $z(\psi) = -R\cos(\psi) + z_e$. The two approaches will be compared in the case study presented in Section 5.5. To simplify the expressions we define:

$$\tilde{w} = m_M - \rho_w d + \Delta\rho R, \tag{5.4}$$

$$\tilde{p} = \rho_w \Delta h - \Delta\rho z_e + \Delta\rho\Delta h. \tag{5.5}$$

(5.3) can then be written as:

$$Td\psi = g(\tilde{w}\cos\psi + \tilde{p})ds \tag{5.6}$$

To get an expression for the tension T we divide (5.2) and (5.3), and get

$$\frac{dT}{T} = \frac{m_M \sin\psi d\psi}{\tilde{w}\cos\psi + \tilde{p}}.$$

Since the considered problem is symmetric about the z-axis, it is sufficient to start from $\psi = 0$. Integration up to ψ gives

$$T = T_0 \left(\frac{\tilde{w} + \tilde{p}}{\tilde{w}\cos\psi + \tilde{p}} \right)^{\frac{m_M}{\tilde{w}}}, \tag{5.7}$$

where T_0 is the value of T at $(0, z_0)$. The expression shows that T is constant when $m_M = 0$, which is consistent with (5.2). We now substitute (5.7) in (5.6) and get

$$ds = \frac{T_0}{g} \frac{(\tilde{w} + \tilde{p})^{\frac{m_M}{\tilde{w}}}}{(\tilde{w}\cos\psi + \tilde{p})^{\frac{m_M}{\tilde{w}}+1}} d\psi. \tag{5.8}$$

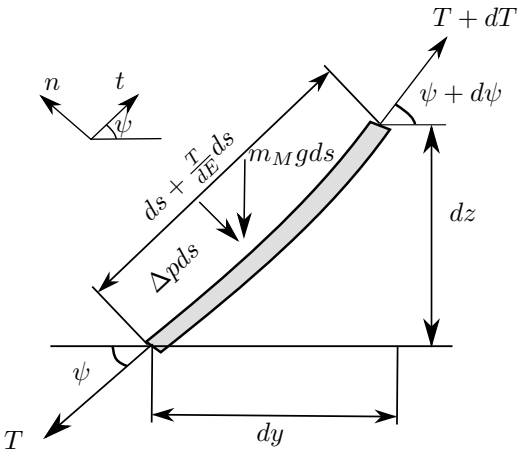

Figure 5.2: Details of the membrane shown in Figure 5.1. d = membrane thickness. E = elasticity module of membrane, our analysis assumes an inelastic membrane. s = curvilinear coordinate along the membrane. Δp is the pressure difference at a given angle ψ. m_M is membrane mass per unit area in air. n, t is the local normal tangential coordinate-system.

This means that

$$s = \frac{T_0}{g}(\tilde{w} + \tilde{p})^{\frac{m_M}{\tilde{w}}} \int_0^{\psi} \frac{d\psi}{(\tilde{w}\cos\psi + \tilde{p})^{\frac{m_M}{\tilde{w}}+1}}. \tag{5.9}$$

Since $dy = \cos\psi ds$, it follows from (5.9) and integration that

$$y = \frac{T_0}{g}(\tilde{w} + \tilde{p})^{\frac{m_M}{\tilde{w}}} \int_0^{\psi} \frac{\cos\psi d\psi}{(\tilde{w}\cos\psi + \tilde{p})^{\frac{m_M}{\tilde{w}}+1}}. \tag{5.10}$$

We now apply (5.9) and (5.10) at the right floater, i.e. for $\psi = \psi_e$ and denote half the length of the membrane as S_T. Dividing the (5.10) by (5.9) gives

$$\frac{R}{S_T} = \frac{\int_0^{\psi_e} \frac{\cos\psi d\psi}{(\tilde{w}\cos\psi+\tilde{p})^{\frac{m_M}{\tilde{w}}+1}}}{\int_0^{\psi_e} \frac{d\psi}{(\tilde{w}\cos\psi+\tilde{p})^{\frac{m_M}{\tilde{w}}+1}}}. \tag{5.11}$$

Equation (5.11) determines ψ_e, which can be done numerically. We can now use either (5.9) or (5.10) at $\psi = \psi_e$ to determine T_0.

Our next step is to determine $z_0 - z_e$ (see Figure 5.1). Since $dz = \sin\psi ds$, it follows from (5.8) and integration that

$$z - z_0 = \frac{T_0}{g}(\tilde{w} + \tilde{p})^{\frac{m_M}{\tilde{w}}} \int_0^{\psi} \frac{\sin\psi d\psi}{(\tilde{w}\cos\psi + \tilde{p})^{\frac{m_M}{\tilde{w}}+1}}. \tag{5.12}$$

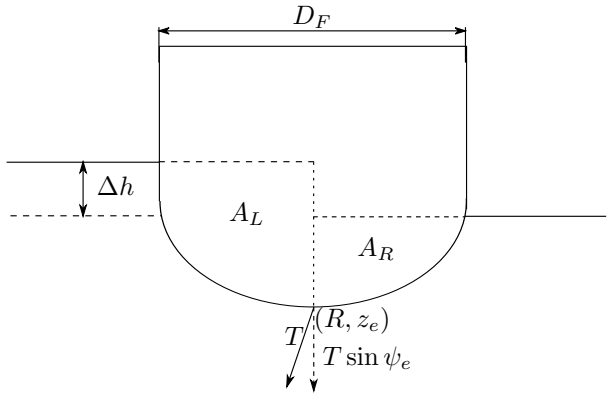

Figure 5.3: Details of force equilibrium at the right floater shown in Figure 5.1.

By applying (5.12) at $\psi = \psi_e$ we have an equation that determines $z_0 - z_e$, i.e.

$$z_0 - z_e = -\frac{T_0}{g m_M}\left(\frac{(\tilde{p} + \tilde{w})}{(\tilde{p} + \tilde{w}\cos\psi_e)}^{\frac{m_M}{\tilde{w}}} - 1\right), \tag{5.13}$$

where z_e is the coordinate of the bottom of the floater. We can now determine the coordinates (y,z) of the membrane with ψ as a parameter by using (5.10) and (5.12). The corresponding tensions are given by (5.7). The limit of all the equations when $\tilde{p} \to 0$ and $\tilde{w} \to m_M - \rho_w d$ go to the results as given in Faltinsen (1990). Since y, z and s are dependent on z_e, an iterative procedure is needed in the calculations.

Our next step is to determine the $z-$ coordinate z_e of the attachment point between the membrane and the right floater. z_e is found by setting up and solving the vertical force equilibrium for the right floater.

5.2 Global static force equilibrium

The vertical force equilibrium for the right floater is illustrated in Figure 5.3. There is a vertical force per unit length due to hydrostatic pressure that can be expressed as $\rho_{wi} g A_L + \rho_w g A_R$ where the areas A_L and A_R are defined in Figure 5.3.

We can explain the hydrostatic pressure terms as follows by first consider the hydrostatic loading inside the tank where the hydrostatic pressure is $-\rho_{wi} g(z - \Delta h)$. We then consider an artificial closed body so that we can apply Gauss theorem. The artificial closed body with area A_L has surfaces that consist of the inside wetted floater surface, the horizontal dotted line in Figure 5.3, where $-\rho_{wi} g(z - \Delta h) = 0$ and the vertical dotted line at the centerline of the floater where the $z-$ component n_3 of the outwards normal vector is zero. That means integrating $\rho_{wi} g(z - \Delta h) n_3$ along the closed surface is the same as the hydrostatic vertical force on the floater surface inside the tank. Then we apply Gauss theorem and get the result. Similar we do for the outer wetted surface of the floater. The results depend on the geometry of the floater; plausible geometries are circular and rectangular. We note that due to the density difference and overfilling we will also have a horizontal force

equilibrium here, which will if it is considered influence the distance between freely moving floaters. For a real world 3D closed flexible fish cage this distance is close to fixed, we therefore choose to keep this distance fixed, and not consider this force equilibrium. Vertical force equilibrium gives that

$$g(\rho_{wi}A_L + \rho_w A_R) - m_F g - T(\psi_e)\sin\psi_e = 0. \tag{5.14}$$

Here m_F is the mass in air of the right floater per unit length in perpendicular $x-$direction. We can express $T(\psi_e)$ by (5.7) and use either (5.9) or (5.10) at $\psi = \psi_e$ to determine T_0.

If the floater has a semi-circular shape in the lower part, we can analytically express A_L and A_R as functions of floater submergence z_e. The expressions for A_R and A_L for a floater of the type given in Figure 5.3, with a half circle at the bottom and a rectangular shape on the top is dependent on the submergence of the half circle. If the half circle part is fully submerged, i.e. $-z_e \geq R_F$:

$$\begin{aligned} A_R &= \frac{R_F^2\pi}{4} + R_F(z_e + R_F), \\ A_L &= \frac{R_F^2\pi}{4} + R_F(z_e + \Delta h + R_F). \end{aligned} \tag{5.15}$$

If the half circle part is not fully submerged, i.e $-z_e < R_F$:

$$\begin{aligned} A_R &= \frac{R_F^2}{2}\arccos\left(\frac{R_F + z_e}{R_F}\right) - \frac{(R_F + z_e)}{2}\sqrt{z_e(-2R_F - z_e)}, \\ A_L &= \frac{R_F^2}{2}\arccos\left(\frac{R_F + z_e - \Delta h}{R_F}\right) - \frac{(R_F + z_e - \Delta h)\sqrt{(\Delta h - z_e)(2R_F + z_e - \Delta h)}}{2}. \end{aligned} \tag{5.16}$$

Combining the results from present and previous section the geometry and static tension of a 2D membrane can be numerically found for a given membrane mass m_M and thickness d, overfilling Δh and density difference $\Delta\rho$. An iteration between (5.11), (5.10) or (5.9), (5.7) and (5.14) are necessary to find a stable equilibrium. Starting with finding ψ_e for $z_e = 0$ by (5.11), then finding T_0 at ψ_e by (5.10) or (5.9). The tension at ψ_e, $T(\psi_e)$ is then found by (5.7), and used in (5.14) where z_e is found. This z_e is then used in the pressure in (5.11) and the previous steps are repeated until a stable equilibrium have been reached.

For $\Delta\rho = 0$ and $\tilde{w} << \tilde{p}$, the analysis can be simplified to a large extent.

5.3 Pure overfilling, neglecting weight

We now consider a case with non-zeroΔh, and zero density difference ($\Delta\rho = 0$) between the internal and external water. We assume that the membrane is massless ($d = 0$). A massless membrane can be justified according to (5.7) if $\tilde{w} << \tilde{p}$ or $\tilde{w} >> m_M$. For $\tilde{w} << \tilde{p}$ the fraction in the expression goes to one, and for $\tilde{w} >> m_M$ the power goes to zero. For the given assumptions $dT = 0$, and the tension is constant along the cable, resulting in $T = T_0$. This assumption simplifies the equations to a large extent. We can now find the geometry and tension of the

membrane by considering the limit of (5.11) which is $\frac{2}{\pi} = \frac{\sin\psi_e}{\psi_e}$ for a circle where $S_T = R\pi/2$. The only solution to this equation is $\psi_e = \pi/2$. The resulting equations are:

$$T_0 = \frac{\rho_w g \Delta h R}{\sin\psi_e} = \rho_w g \Delta h R, \tag{5.17}$$

$$s = \psi \frac{T_0}{\rho_w g \Delta h} = R\psi, \tag{5.18}$$

$$y = \sin\psi \frac{T_0}{\rho_w g \Delta h} = R\sin\psi, \tag{5.19}$$

$$z = z_0 - (\cos\psi - 1)\frac{T_0}{\rho_w g \Delta h} = z_e - R\cos\psi. \tag{5.20}$$

These results are consistent with the limit of expression (5.6), (5.9), (5.10) and (5.12) for $\tilde{w} \to 0$. The results for $\tilde{w} = 0$ is also consistent with that we have a circular membrane shape with radius $R = \frac{T_0}{\rho_w g \Delta h}$. Combining (5.14) and (5.17) for the case where $\tilde{w} = 0$ and $\psi_e = \pi/2$ gives:

$$\rho_w g(A_L(z_e) + A_R(z_e)) - m_F g - \rho_w g \Delta h R = 0. \tag{5.21}$$

z_e can be found by solving (5.21) numerically for a given Δh.

5.4 Density differences and overfilling, neglecting weight

We now consider a case with Δh, and a density difference $\Delta\rho$ between the internal and external water. We assume that the membrane is massless ($d = 0$). As in the previous analysis we set $z(\psi) = -R\cos(\psi) + z_e$ (we will in the test case investigate the appropriateness of this assumption). As before we define $\tilde{p}$ by (5.5) and now

$$\hat{w} = \Delta\rho R. \tag{5.22}$$

The tension equation can now be written as:

$$T_0 d\psi = g(\hat{w}\cos\psi + \tilde{p})ds. \tag{5.23}$$

We use the same procedure as for the membrane with mass and overfilling. The length of the right membrane part from the bottom becomes:

$$\begin{aligned} s =& \frac{T_0}{g}\int_0^\psi \frac{d\psi}{\hat{w}\cos\psi + \tilde{p}} \\ =& -\frac{T_0}{g}\frac{2\tanh^{-1}\left(\frac{(-\hat{w}+\tilde{p})\tan(\psi/2)}{\sqrt{\hat{w}^2-\tilde{p}^2}}\right)}{\sqrt{\hat{w}^2-\tilde{p}^2}}. \end{aligned} \tag{5.24}$$

Since $dy = \cos\psi ds$, it follows from (5.24) and integration that

$$\begin{aligned} y =& \frac{T_0}{g}\int_0^\psi \frac{\cos(\psi)d\psi}{\hat{w}\cos\psi + \tilde{p}} \\ =& \frac{T_0}{g}\left(\frac{\psi}{\hat{w}} + \frac{2\tilde{p}\tanh^{-1}\left(\frac{(-\hat{w}+\tilde{p})\tan(\psi/2)}{\sqrt{\hat{w}^2-\tilde{p}^2}}\right)}{\hat{w}\sqrt{\hat{w}^2-\tilde{p}^2}}\right). \end{aligned} \tag{5.25}$$

Table 5.1: Case dimensions for bag with floater. R is the radius of the bag, d is the thickness of the fabric, E is the elasticity module of the fabric, ρ_N is the density of the fabric (nylon used), ρ_w is the density of salt water and m_F is the mass per meter of the floater. R_F is the radius of the floater.

R	d	E	ρ_N	ρ_w	m_F/R_F
1 m	$5 \cdot 10^{-5}$ m	$2 \cdot 10^9$ Pa	1150 kg/m^3	1025 kg/m^3	2.38 kg/m^2

We now apply (5.24) and (5.25) at the right floater, i.e. for $\psi = \psi_e$ and denote the length of the membrane as S_T. Dividing (5.25) by (5.24) gives

$$\begin{aligned} \frac{R}{S_T} &= \frac{\int_0^{\psi} \frac{\cos(\psi)d\psi}{\hat{w}\cos\psi+\tilde{p}}}{\int_0^{\psi} \frac{d\psi}{\hat{w}\cos\psi+\tilde{p}}} \\ &= -\frac{\psi_e}{\hat{w}} \frac{\sqrt{\hat{w}^2-\tilde{p}^2}}{2\tanh^{-1}\left(\frac{(-\hat{w}+\tilde{p})\tan(\psi_e/2)}{\sqrt{\hat{w}^2-\tilde{p}^2}}\right)} - \frac{\tilde{p}}{\hat{w}}. \end{aligned} \tag{5.26}$$

Equation (5.26) determines ψ_e, which can be done numerically. We can now use either (5.24) or (5.25) at $\psi = \psi_e$ to determine T_0.

Our next step is to determine z_0. Since $dz = \sin\psi ds$, it follows from (5.24) and integration that

$$z - z_0 = \frac{T_0}{g}\int_0^{\psi} \frac{\sin(\psi)d\psi}{\hat{w}\cos\psi+\tilde{p}} \tag{5.27}$$

$$z_0 = z_e - \frac{T_0}{g}\log\left(\frac{\tilde{p}+\hat{w}}{\tilde{p}+\hat{w}cos(\psi_e)}\right). \tag{5.28}$$

By applying this equation at $\psi = \psi_e$ we have an equation that determines z_0 as a function of z_e. We can now determine the coordinates (x,z) of the membrane with ψ as a parameter.

5.5 Case studies

We here investigate the importance of different assumptions in a model scale test study. If the weight of the cable can be neglected in the analysis of shape and tension of a 2D membrane, the expressions can be greatly simplified, as shown in Section 5.3. We, therefore, investigate the importance of the mass of the cable on the tension calculations. Also, it can be observed from (5.21) that the size of the floaters is dependent on the tension, necessary size of floaters in relation to overfilling is therefore also investigated.

We operate with nondimensional figures, but the analysis was done for a model scale of $1:12.5$ relative to the full scale case from Botngaard, presented in Appendix C. The model scale parameters are presented in Table 5.1. The values given in Table 5.1 are assembled from different sources. The mass of the floaters is from Li (2017).

The density and elasticity module of the membrane is of light weight nylon cloth, like the one used in the experiment described in Chapter 3. The thickness of the membrane is the same as for the model experiments in Chapter 3.

5.5.1 Case study of importance of weight relative to overfilling, for $\Delta\rho = 0$

The assumption of a "massless cable" holds according to (5.7) if $\tilde{p} >> \tilde{w}$, or if $\tilde{w} >> m_M$. Then the tension would be constant. The tension with and without weight for a case with pure overfilling $\Delta\rho = 0$ is displayed in Figure 5.4 top. The calculated tension follows T_0 for $\Delta h/R \geq 10^{-3}$. The bottom part of Figure 5.4 presents $(m_M - \rho_w d)/\rho_w \Delta h$, i.e $\tilde{w}/\tilde{p}$ versus $\Delta h/R$. It illustrates that $\tilde{w}/\tilde{p}$ is very small when $\Delta h/R > 10^{-3}$. The results are consistent with that a weightless membrane can be assumed in predicting the tension when $\Delta h/R \geq 10^{-3}$ and $\Delta\rho = 0$.

The calculation of necessary floater diameter is made assuming that $z_e = -R_F$. This would mean that the lower half circular part of the floater is exactly submerged. Then the floater radius R_F can be found by solving a second order equation of R_F, using m_F/R_F from Table 5.1:

$$R_F = \frac{\frac{m_F}{R_F\rho_w} - \Delta h + \sqrt{(\frac{m_F}{R_F\rho_w} - \Delta h)^2 + 2\pi\frac{T(\psi_e)}{\rho_w g}\sin(\psi_e)}}{\pi}. \tag{5.29}$$

The floater diameter R_F is highly dependent on the tension in the membrane and therefore reliant on the overfilling Δh. From the results plotted in Figure 5.5, we observe that the floater radius R_F is close to constant for $\Delta h/R < 10^{-4}$. This indicates that for this interval it is the combined mass of the floater and membrane that decides the floater size. For $\Delta h/R \geq 10^{-3}$ the nondimensional radius of the floater R_F/R increases rapidly with $\Delta h/R$. Based on the size of the floaters used today on conventional salmon aquaculture cages (Aqualine, 2017), values of $R_F/R > 0.1$ is unreasonable, giving a limit on $\Delta h/R$ of $2 \cdot 10^{-2}$.

We have operated with Δh as a known quantity. A more plausible known quantity is the inside volume of water. So, we set up the relationship between Δh and the inside volume of water. We start with an area A_0 and apply an additional amount of water $\Delta A = 2R\Delta h_0$ as illustrated in Figure 5.6 right part. Due to the overfilling the floaters will submerge and the membrane will deform, illustrated in 5.6 left part. The actual overpressure Δh will be dependent on the submergence of the floaters. Preserving volume conservation in the bag Δh accounting for reduced width of the bag related to the floater gives:

$$\frac{\pi R^2}{2} + 2R\Delta h_0 = -2\int_0^R z(y)\mathrm{d}y + 2\Delta h(R - a(z_e)) - 2A_L,$$

where $z(y)$ is the static shape of the bag when the floaters are submerged. Solving for Δh gives

$$\Delta h = \frac{R\Delta h_0 + A_L + \frac{\pi R^2}{4} + \int_0^R z(y)\mathrm{d}y}{R - a(z_e)}, \tag{5.30}$$

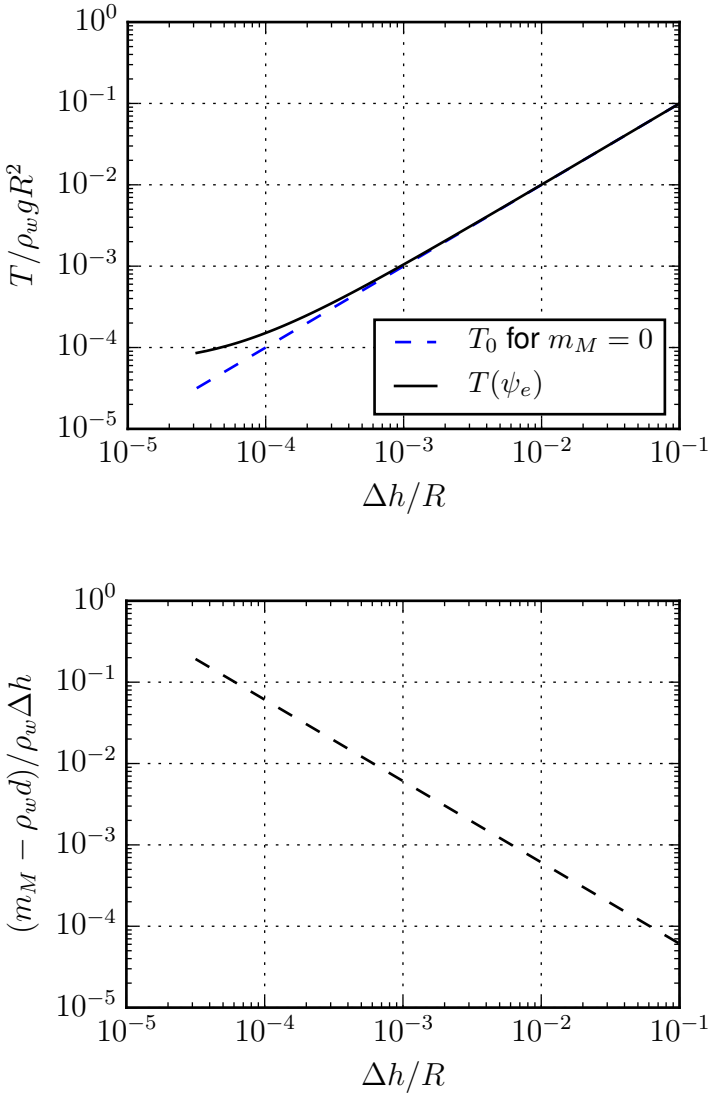

Figure 5.4: Top: Nondimensional tension $T/\rho_w g R^2$ with effect of mass $T(\psi_e)$ and without effect of mass (T_0) versus nondimensional over filling height $\Delta h/R$. Bottom: nondimensional wet weight $(m_M - \rho_w d)/\rho_w \Delta h$ versus nondimensional over filling height $\Delta h/R$.

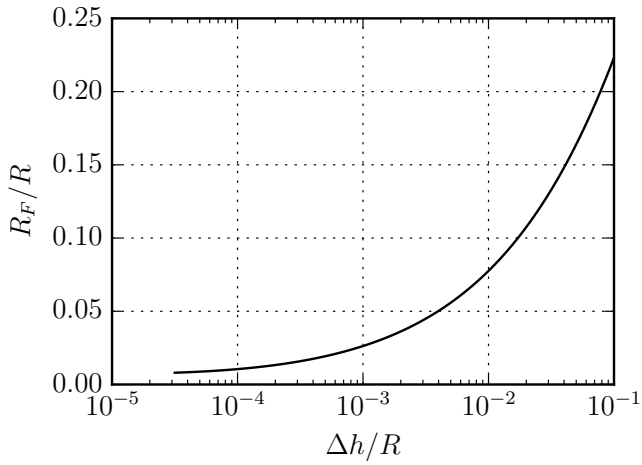

Figure 5.5: Nondimensional floater radius R_F/R vs nondimensional filling height $\Delta h/R$. Results based on (5.29) for tension included the effect of the mass of the membrane.

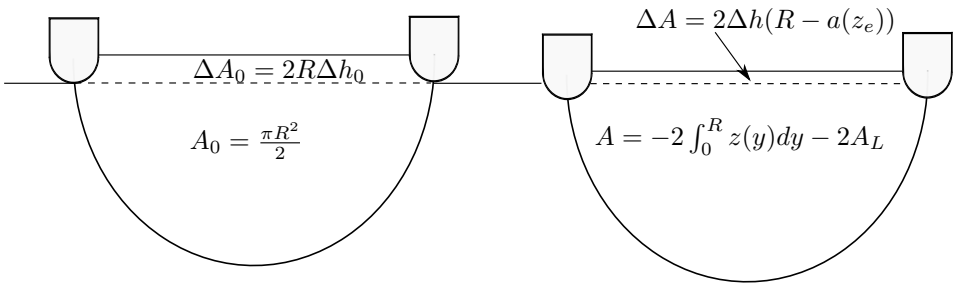

Figure 5.6: Illustration of calculation of volume conservation with overpressure, accounting for floater area.

where Δh is the overpressure corrected for the reduced free surface area due to the presence of the floaters, and $a(z_e)$ is the width of the floater at the free surface.

To find the overfilling Δh_0, an initial overfilling in the form of extra volume can be used. If an overfilling q, given relative to the theoretic volume V_0 is applied, we can find an overfilling by:

$$\Delta h_0^{q\%} = \frac{V_1 - V_0}{A_s} = \frac{Rq}{150}$$

The overfilling is applied as Δh_0 in $q\%$, V_1 is the overfilled volume and A_s is the free surface area. Two cases of pure overfilling ($\Delta\rho = 0$) have been tested, one with 10% overfilling of the bag with $R_F/R = 0.1$ and a case with 5% overfilling and $R_F/R = 0.05$. The resulting geometries with overpressure Δh and floater

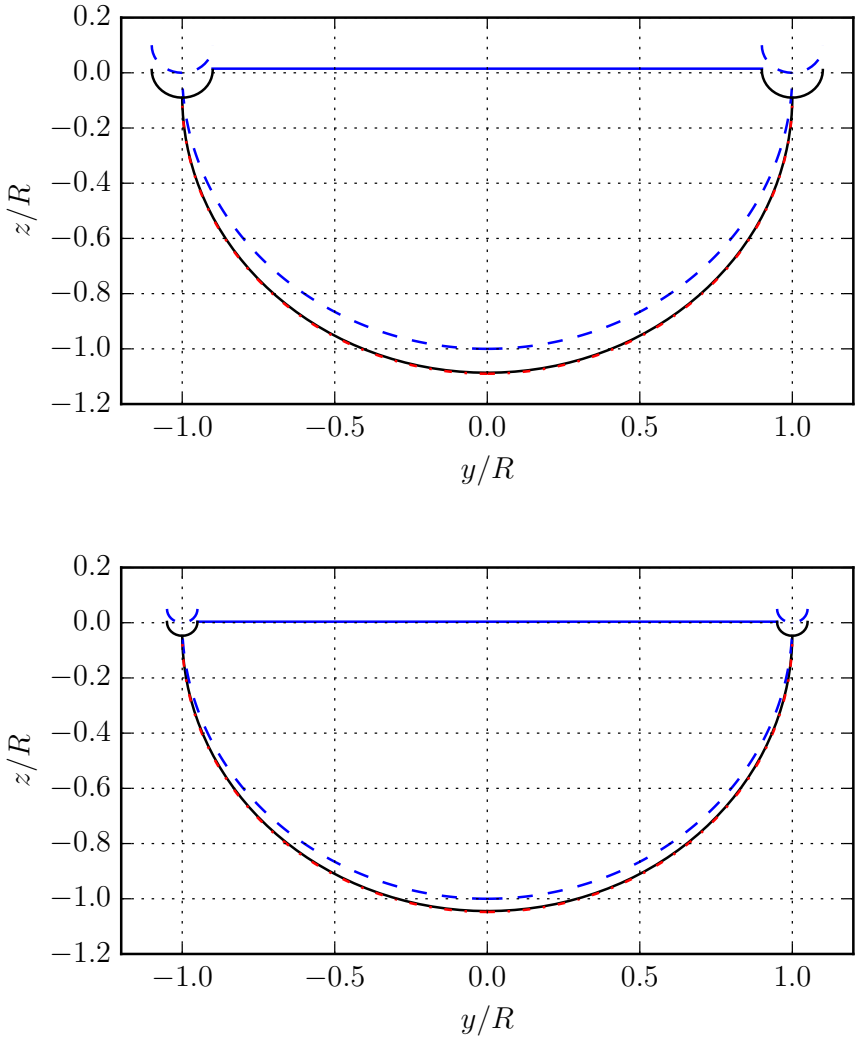

Figure 5.7: Case results of equilibrium geometry of two cases where pure overfilling is applied. Top: Equilibrium position of bag and floater for $\Delta h/R = 3.7 \cdot 10^{-3}$, $R_F/R = 0.05$. Bottom: Equilibrium position of bag and floater for$\Delta h/R = 15.0 \cdot 10^{-3}$, $R_F/R = 0.1$. The black line is the analysis by neglecting weight, while the semi-dotted red line includes weight in the analysis. The dashed blue line is the reference equilibrium position of a massless membrane with zero overpressure inside the bag.

Table 5.2: Analysis results for the three case studies. Δh is the over filling height, $\Delta\rho$ is the density difference between the water inside the membrane and the surrounding water. T_0 is the tension at the bottom of the membrane, $T(\psi_e)$ is the tension at the connection point between the right floater and the membrane. ψ_e is the top angle at the right floater, R_F is the floater radius and z_e is the floater submergence.

	$\Delta h/R$	$\Delta\rho/\rho_w$	$\frac{T_0}{\rho_w g R^2}$	$\frac{T(\psi_e)}{\rho_w g R^2}$	ψ_e	R_F/R	z_e/R
Case 1	$15.0 \cdot 10^{-3}$	$0.0 \cdot 10^{-3}$	$15.0 \cdot 10^{-3}$	$15.0 \cdot 10^{-3}$	$\pi/2$	0.10	-0.092
Case 2	$3.7 \cdot 10^{-3}$	$0.0 \cdot 10^{-3}$	$3.7 \cdot 10^{-3}$	$3.8 \cdot 10^{-3}$	$\pi/2$	0.05	-0.033
Case 3	$3.2 \cdot 10^{-4}$	$9.8 \cdot 10^{-3}$	$8.3 \cdot 10^{-3}$	$8.4 \cdot 10^{-3}$	1.34	0.10	-0.066

submergence z_e are plotted in Figure 5.7. Submergence of the floater z_e together with tension and some other parameters are given in Table 5.2.

For the first case with $\Delta h_0^{10\%}$, the results in the Table indicate that the theory for a massless membrane can be applied, since $\Delta h/R > 10^{-3}$ and $\frac{T(\psi_e)}{T_0} = 1.003$. We consider a 0.3% variation along the membrane acceptable, and will in the following dynamic analysis consider the tension constant along the membrane. Visually from Figure 5.7 lower part it can also be seen, that the red dotted line and the black line overlap, indicating that the effect of the weight of the membrane does not change the geometry significantly for this case. Also for the second case with $\Delta h_0^{5\%}$, the results in the Table indicate that the theory for a massless membrane can be applied since $\Delta h/R > 10^{-3}$ and $\frac{T(\psi_e)}{T_0} = 1.027$. We also consider a 2.7% tension variation along the membrane acceptable.

In the performed analysis it is assumed that the membrane is inelastic, for this assumption to be correct we must assume $T_0/Ed << 1$. The present analysis have been conducted for model scale, and it should be noted that this exact relation (T/Ed) will be scale dependent. The material that the membrane is made of, have an elasticity module E that will not change significantly between model and full scale. The full scale tension T_{fs} is proportional to the geometric scale defined as l_g, squared i.e $T_{fs} = l_g^2 T$. The thickness of the membrane d scale approximately linearly with l_g, For the ful scale parameters given in Appendix C with $E_{fs} = 2.25$GPa and $d_{fs} = 0.75$mm for a cage of radius $R_{fs} = 12.5$m and subscript fs stands for full scale. The nondimensional tension will then for a scale of 12.5, for $\Delta h/R < 0.02$ become $T_{fs}/E_{fs}d_{fs} < 0.02$, which can still be considered small, but the effect of elasticity may need to be considered for $\Delta h/R$ close to 0.02.

5.5.2 Case study for $\Delta\rho > 0$

The previous cases have assumed that the density difference $\Delta\rho$ have been zero. We will now turn to cases where density difference matters. We start by examining the effect on tension from $\Delta\rho$ when $\Delta h = 0$. This is plotted in Figure 5.8. For this case, the results are dependent on the floater size, and a constant floater size of $R_F/R = 0.1$ have been used. The black line in Figure 5.8 gives the tension relative to $\Delta\rho$ if the mass is included in the analysis. We observe that T appears

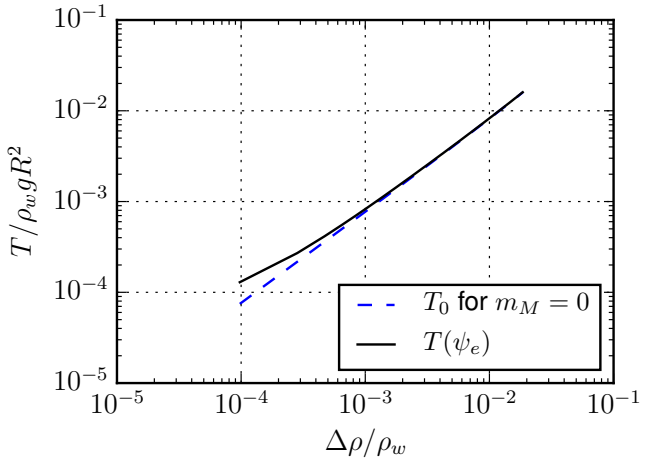

Figure 5.8: Plot of nondimensional tension $T/\rho_w g R^2$ relative to $\Delta\rho/\rho_w$, for nondimensional overfilling $\Delta h/R = 0$ and nondimensional floater radius $R_F/R = 0.1$. Density differences $\Delta\rho$ in the interval $\Delta\rho/\rho_w \in [10^{-4}, 2\cdot 10^{-2}]$ have been examined. Within the given interval, $z_e > -R_F$ meaning that the floater does not sink.

to increase linearly with $\Delta\rho$ in the given interval if the membrane is assumed massless ($T = T_0$). Based on the results in Figure 5.8, for the given analysis, we will assume the membrane massless for $\Delta\rho/\rho_w \geq 10^{-2}$.

Also here a particular test case has been examined, a given overfilling Δh and density difference $\Delta\rho$ is applied. We use $\Delta\rho = 10\text{kg/m}^3$ and $\Delta h = 3.2 \cdot 10^{-4}\text{m}$, which is a model scaled case with a scale ratio of 1:12.5 of the the Botngaard case described in Appendix C.

For the analysis given in sec 5.4 a profile on $z(\psi)$ was assumed. An alternative to approximating $z(\psi)$ as $z(\psi) = -R\cos(\psi) + z_e$ is to use the actual $z(\psi)$ found in the numerical calculations and iterate to find a stable equilibrium. A total solution using the actual $z(\psi)$ is developed on the basis of (5.2) and (5.3). The start value of $z(\psi)$ is $z(\psi) = -R\cos(\psi) + z_e$. The geometry calculated based on the "real" $z(\psi)$ and including the mass is given by the red dotted line in Figure 5.9. From this Figure, we observe that the difference between the red dotted line and the whole black line is marginal for the analysed case. It can also be observed that the geometry is no longer completely half circular (which was the case for case 1 and 2, see Figure 5.7), we have achieved a narrower geometry with a top angle ψ_e that deviates from $\pi/2$. This is to be expected since $\tilde{p}\cos(\psi)$ decreases as ψ increases from zero up to ψ_e. From a geometrical perspective, our conclusion is then that analysis with a massless membrane and an assumed profile on $z(\psi)$ is safe to use for the given case.

Since a given overfilling height Δh and a given density difference $\Delta\rho$ have been used the total volume inside the membrane was not known. The area was

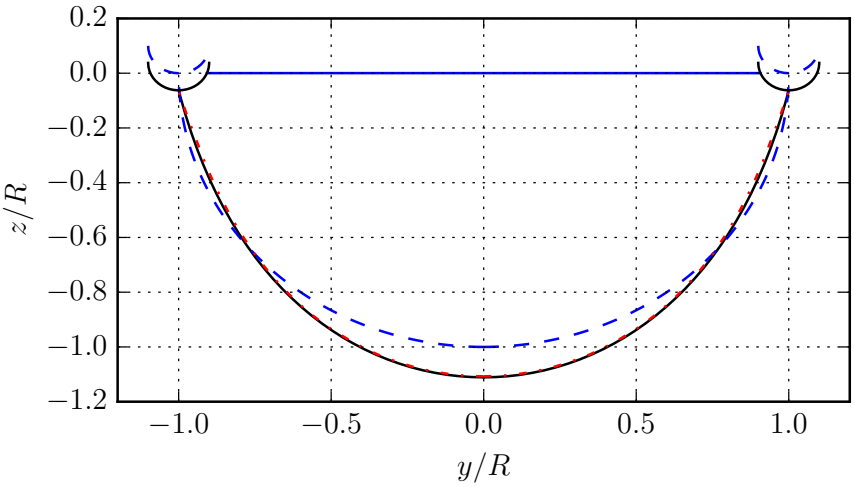

Figure 5.9: Equilibrium position of bag and floater for $\Delta\rho = 10\,\mathrm{kg/m^3}$ and $\Delta h/R = 3.2{\cdot}10^{-4}$, $R_F/R = 0.1$. Scaled case of the Botngaard case for a half circular geometry. The black line is the analysis neglecting weight, while the semi dotted red line includes weight and uses the real $z(\psi)$ in the analysis. The dashed blue line is the reference equilibrium position of a massless membrane with zero overpressure inside the bag.

calculated by integrating the profile, and an overfilling degree of $q = 7\%$ was found.

Based on the tension variations and the relative density difference the theory for a massless membrane can be applied. For this case $\Delta\rho/\rho_w = 0.98{\cdot}10^{-2}$ with a small over filling Δh in addition. For an assumed shape $z(\psi)$, we get a $T(\psi_e)/\rho_w g R^2 = 8.4 \cdot 10^{-3}$ with a $T_0/\rho_w g R^2 = 8.3 \cdot 10^{-3}$, giving $\frac{T(\psi_e)}{T_0} = 1.007$. A variation of 0.7% between $T(\psi)$ and T_0 indicates that the tension is not varying much along the membrane. We consider this difference small enough to assumed a constant tension along the membrane.

5.6 Conclusions and following work

The geometry and initial tension of the membrane must be found in order to be able to analyse the membrane in waves. Equations for the static equilibrium geometry and tension for a membrane in calm water with a hydrostatic pressure difference have been developed. The hydrostatic pressure difference at the membrane between the inside enclosed volume and the surrounding water is due to different free surface levels and/or water densities. The static geometry and tension is dependent on the load on the membrane. If the mass of the membrane can be assumed small compared to the static pressure loads, simplifications with direct

solutions to the equations can be found. When the mass can be assumed small compared to the pressure loads, the tension along the membrane became constant. The assumption of zero mass membrane was investigated, and a boundary of when this assumption can be made was found. A maximum overfilling Δh based on the largest plausible floater radius was also found.

Three special cases related to pressure forces and floater size have been investigated. For all these three cases the tension for the given non-dimensional parameters could be assumed constant. For the first two cases with no density differences $\Delta\rho = 0$, the shape of the membrane was half circular. For the third case with density differences, the shape deviated from a half circular shape, and the top angle $\psi_e < \pi/2$, giving a deeper and narrower shape.

Using the found equations for a given hydrostatic overpressure, the geometry and tension can be found. This geometry and tension will then be used in the analysis of the response of a semi-circular closed flexible fish cage in waves, presented in the following Chapter.

Chapter 6

Linear wave response of a 2D closed flexible fish cage

To predict the response of a 2D CFFC in waves three coupled sub problems must be solved: The membrane dynamics, the external problem with incident waves and the effect of the structure on the flow, and the internal problem, which is an internal sloshing problem. All these three problems are coupled. The analysis considers only a case with overfilling, i.e. no density differences will be considered, but the equations are developed to allow for more general cases. The floaters are assumed horizontally rigidly connected. Internal structures such as pumps and pipes are neglected. The initial stationary geometry and static tension for a given filling level and floater size is known from the previous chapter. When pure overfilling is considered, certain simplifications can be made in the structural equations. For large volume offshore structures second order slowly varying and mean wave forces have great importance in the design of the mooring system. These effects will not be considered in the present analysis.

In this chapter the linear theory of a 2D CFFC in waves is developed and analysed with the aim to find the response of the CFFC in waves. First a general overview of the problem and the equation of motions of the rigid body motions are presented. Then, the theory for dynamic deformation of a 2D membrane is developed and presented. It is followed by a presentation of the total equations for the coupled system. Then, theory for the pressure loads on the CFFC are presented starting with the external pressure forces, continuing with internal pressure forces and hydrostatic pressure forces. The numerical implementation is explained, and a verification case of the hydrodynamic loads on a 2D hemicircle is presented. The results from a 2D case study with relevant full scale dimensions considering a half circularly shaped CFFC with floaters is then presented. At last conclusions are given. Parts of the results in this chapter is published in Strand and Faltinsen (2018).

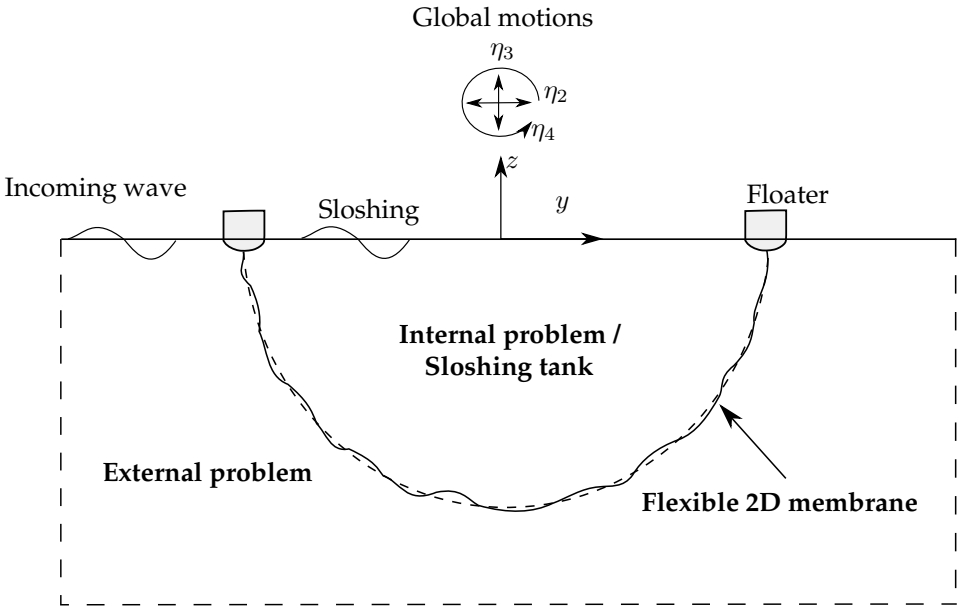

Figure 6.1: Illustration of the subproblems that needs to be solved to predict the response of a 2D CFFC in waves. The dotted line is the equilibrium position of the membrane in calm water.

6.1 System overview

The 2D CFFC consists of two floaters and a membrane, where the membrane is connected to the floaters at $(\pm R, z_e)$. The initial geometry of the membrane, the static tension T_0 and the vertical submergence of the floaters z_e are known from a static pressure analysis. We consider a 2D membrane in static equilibrium that is attached in the points $(-R, z_e)$ and (R, z_e) to two horizontally rigidly connected floaters. The static geometry and static tension T_0 was found in Chapter 5. The whole geometry including the floaters move with the rigid body motions η_2, η_3 and η_4 in sway, heave and roll, respectively. Sway and heave are for a point that coincides with the origin of the coordinate system Oyz defined in Figure 6.1 when the body is at rest. In addition, we must consider the membrane deformations which is zero at the attachment points to the floaters. We assume small rigid motions of the CFFC and small membrane deformations, then the superposition principle can be used. The water surrounding and inside the CFFC introduces pressure forces on the combined structure. The system is illustrated in Figure 6.1.

When considering the inertia, hydrodynamic and hydrostatic restoring loads associated with the rigid body motions, velocities and accelerations, we assume a rigid body. It implies that we can add the rigid body loads on the membrane to the rigid body loads on the floater. It means that the rigid-body equations of motions

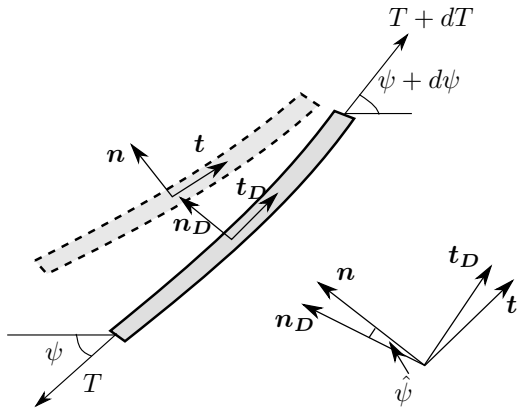

Figure 6.2: Illustration of dynamic displacement and rotation of membrane element, compared with static representation. Dynamic position of membrane element with tangential direction $\boldsymbol{t_D}$ and normal direction $\boldsymbol{n_D}$, drawn with whole line. Compared to a static membrane element with tangential direction $\boldsymbol{t}$ and normal direction $\boldsymbol{n}$, drawn in a dotted line. The two elements are rotated according to each other with a dynamic angel $\hat{\psi}$ between them.

of the CFFC becomes:

$$(m + a_{22})\ddot{\eta}_2 + b_{22}\dot{\eta}_2 + (a_{24} - z_G m)\ddot{\eta}_4 + b_{24}\dot{\eta}_4 = f_2^{exc} + f_2^{Mem}, \quad (6.1)$$

$$(m + a_{33})\ddot{\eta}_3 + b_{33}\dot{\eta}_3 + c_{33}\eta_3 = f_3^{exc} + f_3^{Mem}, \quad (6.2)$$

$$(I_{44} + a_{44})\ddot{\eta}_4 + b_{44}\dot{\eta}_4 + c_{44}\eta_4 + (a_{42} - z_G m)\ddot{\eta}_2 + b_{42}\dot{\eta}_2 = f_4^{exc} + f_4^{Mem}. \quad (6.3)$$

Here, m is the total mass of the floater and membrane, and I_{44} is the combined moment of inertia of the membrane and floaters in roll defined as $I_{44} = \int (y^2 + z^2) d(m_M + m_{Fl})$. a_{jk} is the added mass coefficient associated with the internal and external flow, b_{kj} are wave radiation coefficients, and c_{jj} are restoring coefficients associated with change in interior and exterior hydrostatic loads. c_{44} includes also roll moment change due to the body weight. z_G is the total vertical center of gravity for the floater and the membrane. Furthermore, f_j^{exc} and f_j^{Mem} are wave excitation loads and loads caused by the elastic deformations of the membrane. How to evaluate a_{jk}, b_{jk}, c_{jj} and f_j^{exc} are described in Section 6.4. We will start with analysing the elastic membrane deformations. Which will as part of the analysis give f_j^{Mem}.

6.2 Dynamic structural modelling, 2D membrane

We will solve the dynamic displacement of a 2D membrane with a free surface. Bliek (1984) has considered non-linearly a 3D cable in an accelerated coordinate system, which is partly relevant for a 2D membrane. Our formulations are based on a perturbation about the static mean position of the membrane, and allows for the general case for a static tension variation along the membrane.

The tension in the membrane works along the actual dynamic geometry, and needs to be transferred to the static representation, if linear perturbation theory is to be used to solve the deformation problem. The dynamic tangential ($\boldsymbol{t_D}$) and normal ($\boldsymbol{n_D}$) direction of the element (see Figure 6.2) can for small dynamic angles $\hat{\psi}$ be expressed as:

$$\boldsymbol{t_D} = \cos\hat{\psi}\boldsymbol{t} + \sin\hat{\psi}\boldsymbol{n} \approx \boldsymbol{t} + \hat{\psi}\boldsymbol{n}, \tag{6.4}$$

$$\boldsymbol{n_D} = -\sin\hat{\psi}\boldsymbol{t} + \cos\hat{\psi}\boldsymbol{n} \approx -\hat{\psi}\boldsymbol{t} + \boldsymbol{n}, \tag{6.5}$$

where $\boldsymbol{n}, \boldsymbol{t}$ are the normal and tangential direction respectively, at the mean static position of the membrane, with directions given according to Figure 5.2 and Figure 6.2. The tension force on a 2D membrane element of infinitesimal length ds is $\frac{\partial(T\boldsymbol{t}_D)}{\partial s}ds$. It follows that

$$\frac{\partial(T\boldsymbol{t_D})}{\partial s} = \frac{\partial T}{\partial s}\boldsymbol{t_D} + T\frac{\partial \boldsymbol{t_D}}{\partial s}. \tag{6.6}$$

The Frenet formulas (Kreyszig et al., 2006) give the relation between the normal and tangential directions:

$$\frac{\partial \boldsymbol{t}_D}{\partial s} = \boldsymbol{n}_D\frac{\partial \psi}{\partial s}, \tag{6.7}$$

$$\frac{\partial \boldsymbol{n}_D}{\partial s} = -\boldsymbol{t}_D\frac{\partial \psi}{\partial s}, \tag{6.8}$$

where ψ is the total angle as illustrated in Figure 6.2.

To find an expression for the tension in the normal tangential frame we use the given relation in (6.6):

$$\frac{\partial T}{\partial s}\boldsymbol{t_D} + T\frac{\partial \psi}{\partial s}\boldsymbol{n_D} = (\frac{\partial T}{\partial s} - T\frac{\partial \psi}{\partial s}\hat{\psi})\boldsymbol{t} + (T\frac{\partial \psi}{\partial s} + \frac{\partial T}{\partial s}\hat{\psi})\boldsymbol{n}. \tag{6.9}$$

By considering the dynamic motions of an infinitesimal element of the 2D membrane as illustrated in Figure 5.2 evaluated on the static equilibrium geometry according to (6.9), we get by disregarding structural damping the equations:

$$m_M\ddot{v} = T\frac{\partial \psi}{\partial s} + \frac{\partial T}{\partial s}\hat{\psi} - m_M g\cos\psi - \Delta p, \tag{6.10}$$

$$m_M\ddot{u} = \frac{\partial T}{\partial s} - T\frac{\partial \psi}{\partial s}\hat{\psi} - m_M g\sin\psi, \tag{6.11}$$

v is the normal deformation of the membrane along $\boldsymbol{n}$, u is the tangential deformation of the membrane along $\boldsymbol{t}$ and Δp is the total pressure difference between the internal and external pressure over the membrane. A dot above a variable represents time differentiation. It is referred to Figure 5.2 for definition of normal and tangential directions. We make a perturbation of the equations about the static solution such that

$$\begin{aligned} \psi(s,t) &= \psi_0(s) + \hat{\psi}(s,t), \\ T(s,t) &= T_0(s) + \tau(s,t) = T_0(s) + Ed\hat{e}(s,t), \\ \Delta p(s,t) &= \Delta p_0 + \Delta\hat{p}(s,t), \end{aligned} \tag{6.12}$$

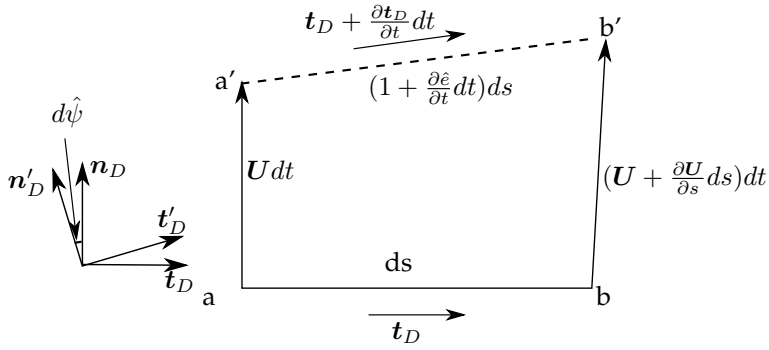

Figure 6.3: Illustration of the stretching of an element from one time instant to another, and rotation of the coordinate system from one time instant to another. $\boldsymbol{U}$ is the velocity vector and $\boldsymbol{t}$ is the tangential unit vector.

τ is the dynamic tension, and $\tau = Ed\hat{e}$, where $\hat{e}$ is the dynamic strain follows from the linear relation between strain and tension according to Hook's law. Δp_0 is the static pressure difference and $\Delta\hat{p}$ the dynamic pressure difference. To be able to apply linear theory for the structure, the total tension T of the membrane most be positive.

After subtracting the static equilibrium and keeping linear terms we get:

$$m_M \ddot{v} = T_0 \frac{\partial \hat{\psi}}{\partial s} + \tau \frac{\partial \psi_0}{\partial s} + \frac{\partial T_0}{\partial s} \hat{\psi} - m_M g \sin\psi_0 \hat{\psi} - \Delta\hat{p}, \tag{6.13}$$

$$m_M \ddot{u} = \frac{\partial \tau}{\partial s} - T_0 \frac{\partial \psi_0}{\partial s} \hat{\psi} - m_M g \cos\psi_0 \hat{\psi}. \tag{6.14}$$

Different equations were used by Ulstein (1995) who analysed the dynamic deformation of an aft flexible bag of a surface effect ship (SES) by dividing the bag into two parts, each with constant tension and radius of curvature. He has also neglected the mass forces on the bag. Therefore, $\frac{\partial T_0}{\partial s}\hat{\psi}$, $m_M g \sin\psi_0 \hat{\psi}$ and $m_M g \cos\psi_0 \hat{\psi}$ are assumed zero within his calculations. However, $T_0 \frac{\partial \psi_0}{\partial s}\hat{\psi}$ are missing in his expressions.

Compatibility relations that give the relation between the deformations (u, v), the dynamic tension τ and the dynamic angle $\hat{\psi}$ is needed to solve the equation system. Inspired by Ulstein (1995) and Bliek (1984) we study a small element ds of the 2D membrane at a given time instant t and investigate the change occurring at a small time increment dt. It is referred to Figure 6.3 for illustration and definition of the corner points $aba'b'$, where a and b are associated with a small membrane element of length ds at time t and a' and b' are associated with the membrane element at time $t + dt$. The velocity vector $\boldsymbol{U}$ of one end point at time t is

$$\boldsymbol{U} = \dot{\tilde{u}}\boldsymbol{t}_D + \dot{\tilde{v}}\boldsymbol{n}_D = (\dot{u} + \hat{\psi}\dot{v})\boldsymbol{t}_D + (\dot{v} - \hat{\psi}\dot{u})\boldsymbol{n}_D \approx \dot{u}\boldsymbol{t}_D + \dot{v}\boldsymbol{n}_D, \tag{6.15}$$

where $\tilde{u}, \tilde{v}$ is the local normal and tangential velocity in the dynamic coordinate system, which for small deformations and dynamic angles become the normal and

tangential velocities in the static coordinate system. At the other end point the velocity at time t is

$$\boldsymbol{U} + \frac{\partial \boldsymbol{U}}{\partial s} ds. \tag{6.16}$$

The element $a'b'$ has length

$$ds(1 + \frac{\partial \hat{e}}{\partial t} dt). \tag{6.17}$$

By vector addition we can write that

$$\boldsymbol{U} dt + (\boldsymbol{t}_D + \frac{\partial \boldsymbol{t}_D}{\partial t} dt) ds (1 + \frac{\partial \hat{e}}{\partial t} dt) = \boldsymbol{t}_D ds + (\boldsymbol{U} + \frac{\partial \boldsymbol{U}}{\partial s} ds) dt. \tag{6.18}$$

This can be simplified by neglecting higher order terms to:

$$\frac{\partial \boldsymbol{U}}{\partial s} = \boldsymbol{t}_D \frac{\partial \hat{e}}{\partial t} + \frac{\partial \boldsymbol{t}_D}{\partial t}. \tag{6.19}$$

By using partial differentiation on $\boldsymbol{U}$ we get:

$$\frac{\partial \boldsymbol{U}}{\partial s} = \frac{\partial \dot{u}}{\partial s} \boldsymbol{t}_D + \dot{u} \frac{\partial \boldsymbol{t}_D}{\partial s} + \frac{\partial \dot{v}}{\partial s} \boldsymbol{n}_D + \dot{v} \frac{\partial \boldsymbol{n}_D}{\partial s}. \tag{6.20}$$

From Figure 6.3 we derive:

$$\frac{\partial \boldsymbol{t}_D}{\partial t} = \boldsymbol{n}_D \frac{\partial \hat{\psi}}{\partial t} \tag{6.21}$$

By using the Frenet formulas given by (6.7) and (6.8) in (6.20) we find:

$$\frac{\partial \boldsymbol{U}}{\partial s} = (\frac{\partial \dot{u}}{\partial s} - \dot{v} \frac{\partial \psi}{\partial s}) \boldsymbol{t}_D + (\dot{u} \frac{\partial \psi}{\partial s} + \frac{\partial \dot{v}}{\partial s}) \boldsymbol{n}_D. \tag{6.22}$$

By combining (6.19), (6.21) and (6.22), and neglecting products of perturbation terms and higher order terms and assuming steady state oscillations in time with the frequency ω, the following relations are obtained:

$$\begin{bmatrix} \frac{\partial u}{\partial s} - v \frac{\partial \psi_0}{\partial s} \\ \frac{\partial v}{\partial s} + u \frac{\partial \psi_0}{\partial s} \end{bmatrix} = \begin{bmatrix} \hat{e} \\ \hat{\psi} \end{bmatrix}. \tag{6.23}$$

These relations are consistent with Ulstein (1995).

The assumption of steady state oscillations are done to be able to integrate the resulting equation in time. By assuming steady state oscillations we assume that $u(\psi, t) = u(\psi) e^{\mathrm{i}\omega t}$ and $v(\psi, t) = v(\psi) e^{\mathrm{i}\omega t}$, where i is defined according to $\mathrm{i}^2 = -1$. Equation (6.23) is used in (6.13) and (6.14), with the resulting equation system for

the normal and tangential deformations:

$$\begin{aligned}-\omega^2 m_M v =& T_0\left(\frac{\partial^2 v}{\partial s^2}+\frac{\partial u}{\partial s}\frac{\partial \psi_0}{\partial s}+u\frac{\partial^2\psi_0}{\partial s^2}\right)+Ed\left(\frac{\partial u}{\partial s}-v\frac{\partial \psi_0}{\partial s}\right)\frac{\partial \psi_0}{\partial s}\\ &+\frac{\partial T_0}{\partial s}\left(\frac{\partial v}{\partial s}+u\frac{\partial \psi_0}{\partial s}\right)-m_M g\sin\psi_0\left(\frac{\partial v}{\partial s}+u\frac{\partial \psi_0}{\partial s}\right)-\Delta\hat{p},\end{aligned} \tag{6.24}$$

$$\begin{aligned}-\omega^2 m_M u =& Ed\left(\frac{\partial^2 u}{\partial s^2}-\frac{\partial v}{\partial s}\frac{\partial \psi_0}{\partial s}-v\frac{\partial^2\psi_0}{\partial s^2}\right)-T_0\frac{\partial \psi_0}{\partial s}\left(\frac{\partial v}{\partial s}+u\frac{\partial \psi_0}{\partial s}\right)\\ &-m_M g\cos\psi_0\left(\frac{\partial v}{\partial s}+u\frac{\partial \psi_0}{\partial s}\right).\end{aligned} \tag{6.25}$$

6.2.1 Numerical modelling of the structure

The hydrodynamic load part of (6.24), is in itself dependent on the deformations i.e:

$$\Delta\hat{p}=f(v,\omega). \tag{6.26}$$

This results in that (6.24) and (6.25) can not be solved analytically for the considered membrane. A numerical model is therefore needed. However, even with a numerical model it is not trivial to solve the problem. To solve this problem, we choose to use a modal method as was done in Chapter 4. Then the deformation, velocity and acceleration dependent terms can be found directly.

A modal representation is given according to:

$$v=\Re\Big(\sum_{m=1}^{\infty}\nu_m U_m(\psi_0)e^{\mathrm{i}\omega t}\Big), \tag{6.27}$$

$$u=\Re\Big(\sum_{n=1}^{\infty}\mu_n U_n(\psi_0)e^{\mathrm{i}\omega t}\Big), \tag{6.28}$$

where $\Re$ means the real part and ν_m, μ_n are the generalized complex structural mode amplitudes in normal and tangential direction, respectively. In the following text we will omit the symbol $\Re$ and imply implicitly that we mean the real part of a complex expression involving the complex time dependence. The 2D membrane is rigidly attached to the floater in two points $(\pm R, z_e)$,then $u(-\pi), u(0), v(-\pi), v(0) = 0$. A Fourier series (modal) representation that satisfies the condition of rigid attachment at the floater implies that:

$$U_j(\psi_0)=\sin\left(\frac{\pi j(\psi_0-\psi_e)}{2\psi_e}\right). \tag{6.29}$$

Ordinary differential equations for a general geometry for the structural mode amplitudes ν_m, μ_k can now be found by multiplying (6.24) and (6.25) with the

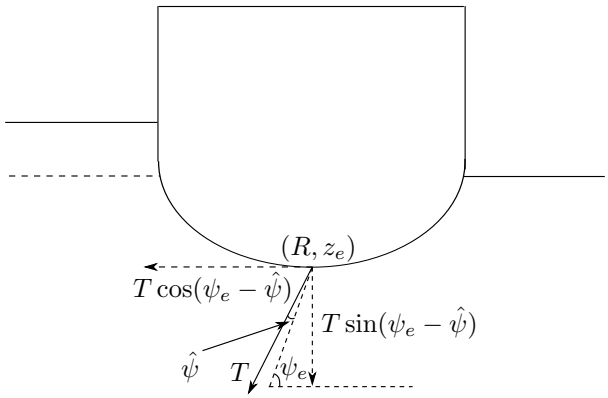

Figure 6.4: Details at the right floater shown in Figure 5.1 for the dynamic case. With dynamic angle $\hat{\psi}$ and tension $T = T_0 + \tau$.

mode $U_j(\psi_0)$, and integrating along the membrane length S_M:

$$\int_{S_M} \Big[-\omega^2 m_M v - Ed\Big(\frac{\partial u}{\partial s} - v\frac{d\psi_0}{ds}\Big)\frac{d\psi_0}{ds} - T_0\Big(\frac{\partial^2 v}{\partial s^2} + \frac{\partial u}{\partial s}\frac{d\psi_0}{ds} + u\frac{d^2\psi_0}{ds^2}\Big) - \frac{dT_0}{ds}\Big(\frac{\partial v}{\partial s} + u\frac{d\psi_0}{ds}\Big) - m_M g\sin\psi_0\Big(\frac{\partial v}{\partial s} + u\frac{d\psi_0}{ds}\Big)\Big] U_j(\psi_0)\mathrm{ds} = -\int_{S_M} \Delta\hat{p} U_j(\psi_0)\mathrm{ds}, \tag{6.30}$$

$$\int_{S_M} \Big[-\omega^2 m_M u - Ed\Big(\frac{\partial^2 u}{\partial s^2} - \frac{\partial v}{\partial s}\frac{d\psi_0}{ds} - v\frac{d^2\psi_0}{ds^2}\Big) + T_0\frac{d\psi_0}{ds}\Big(\frac{\partial v}{\partial s} + u\frac{d\psi_0}{ds}\Big) - m_M g\cos\psi_0\Big(\frac{\partial v}{\partial s} + u\frac{d\psi_0}{ds}\Big)\Big] U_j(\psi_0)\mathrm{ds} = 0. \tag{6.31}$$

The generalised pressure load in (6.30) have terms related to the external and internal generalised added mass, external generalised wave radiation damping, generalised hydrostatic restoring and generalised wave excitation loads, the evaluation of these will be described in Section 6.4.

If the geometry of the membrane is half circular, (6.30) and (6.31) can be simplified to a large extent. The equations for a half-circular membrane are given in Appendix D.

The membrane is connected to the floaters, and this connection transfers dynamic tension loads to the rigid body motions. In the next section expressions for these forces will be developed and presented.

6.2.2 Membrane-floater connection loads

When setting up the equations of motions of the CFFC we must account for the dynamic membrane forces at the connections $\pm R, z_e$ of the membrane to the floaters. There are dynamic force contributions on the floater through the dynamic angle $\hat{\psi}$ and the dynamic tension τ. The tension forces on the floaters from the membrane are illustrated in Figure 6.4. The total tension is given by (6.12), and

is $T = T_0 + \tau$. The dynamic force contribution on the floaters and thereby on the rigid body motions is the total tension force, subtracted the static tension force are

$$F_y = -T\cos(\psi_e - \hat{\psi}) + T_0\cos\psi_e, \tag{6.32}$$
$$F_z = -T\sin(\psi_e - \hat{\psi}) + T_0\sin\psi_e. \tag{6.33}$$

The first order net tension forces from the membrane on the right floater in horizontal and vertical directions are:

$$F_y = -\tau\cos\psi_e - T_0\sin\psi_e\hat{\psi}, \tag{6.34}$$
$$F_z = -T - \tau\sin\psi_e + T_0\cos\psi_e\hat{\psi}. \tag{6.35}$$

for small dynamic angles $\hat{\psi}$.

The dynamic strain $\hat{e}$ and the dynamic angle $\hat{\psi}$ are given by(6.23). Using the modal representation for the normal and tangential deformations, the dynamic tension τ and dynamic angle $\hat{\psi}$ at a given angle ψ_0 are given as

$$\tau(\psi_0) = \frac{Ed}{R}\left(\frac{\partial u}{\partial\psi} - v\right) = \frac{Ed}{R}\left(\sum_{n=1}^{\infty} nU_{cn}(\psi_0)\mu_n - \sum_{m=1}^{\infty} U_m(\psi_0)\nu_m\right), \tag{6.36}$$
$$\hat{\psi}(\psi_0) = \frac{1}{R}\left(\frac{\partial v}{\partial\psi} + u\right) = \frac{1}{R}\left(\sum_{m=1}^{\infty} mU_{cm}(\psi_0)\nu_m + \sum_{n=1}^{\infty} U_n(\psi_0)\mu_n\right). \tag{6.37}$$

Notice that it is the generalised coordinates for the normal structural motions μ_m that have been used, then the counter m is used and starts at one. If the generalised motion variable ξ_j is used the counter is j and starts at four. $nU_{cn}(\psi_0)$ is the derivative of $U_n(\psi_0)$.

The CFFC has two floaters, and the total contribution from the dynamic tension forces in horizontal and vertical direction become

$$\begin{aligned} f_1^T &= -T_0(\hat{\psi}(-\psi_e) + \hat{\psi}(\psi_e))\sin\psi_e - (\tau(\psi_e) - \tau(-\psi_e))\cos\psi_e \\ &= -\frac{T_0}{R}\sum_{m=1}^{\infty} m\nu_m(1 + (-1)^m)\sin\psi_e - \frac{Ed}{R}\sum_{n=1}^{\infty} n(1 - (-1)^n)\mu_n\cos\psi_e, \end{aligned} \tag{6.38}$$

$$\begin{aligned} f_2^T &= -(\tau(-\psi_e) + \tau(\psi_e))\sin\psi_e + T_0(\hat{\psi}(\psi_e) - \hat{\psi}(-\psi_e))\cos\psi_e \\ &= -\frac{Ed}{R}\sum_{n=1}^{\infty} n(1 + (-1)^n)\mu_n\sin\psi_e + \frac{T_0}{R}\sum_{m=1}^{\infty} m(1 - (-1)^m)\nu_m\cos\psi_e. \end{aligned} \tag{6.39}$$

The roll moment about the center of gravity of the CFFC due to the tension loads

on the floaters become

$$
\begin{aligned}
f_3^T =& \left(R^2(\tau(\psi_e) - \tau(-\psi_e)) + z_e^2 T_0(\hat{\psi}(-\psi_e) + \hat{\psi}(\psi_e)) \right) \sin\psi_e \\
&- \left(R^2 T_0(\hat{\psi}(\psi_e) + \hat{\psi}(-\psi_e)) + z_e^2(\tau(\psi_e) - \tau(-\psi_e)) \right) \cos\psi_e \\
=& \left(EdR \sum_{n=1}^{\infty} n(1-(-1)^n)\mu_n + \frac{z_e^2 T_0}{R} \sum_{m=1}^{\infty} m(1+(-1)^m)\nu_m \right) \sin\psi_e \\
&- \left(T_0 R \sum_{m=1}^{\infty} m(1-(-1)^m)\nu_m + \frac{Edz_e^2}{R} \sum_{n=1}^{\infty} n(1-(-1)^n)\mu_n \right) \cos\psi_e .
\end{aligned} \tag{6.40}
$$

The equation of motion of the rigid body motions and the equations for the structural deformations are interconnected, therefore a common framework is necessary. This framework will be presented in the following section.

6.3 Coupled system equations for the CFFC

The rigid body equation of motion given by (6.1)-(6.3) and the equations for the structural deformations of the membrane by (6.30) and (6.31) combined with (6.27) and (6.28), together give a representation of the dynamics of the CFFC. The membrane influences the rigid body motion through the hydrodynamic coupling terms between rigid body motions and the structural normal deformation modes, and through the connection forces on the floater from dynamic tension and dynamic angle. The coupled equation system can be given as:

$$
\begin{bmatrix} -\omega^2(\boldsymbol{m_S} + \boldsymbol{m_{M\xi}} + \boldsymbol{a_f}) + \mathrm{i}\omega \boldsymbol{b}_f + \boldsymbol{c_f} + \boldsymbol{c_{M\xi}} + \boldsymbol{c}_{T\xi} & \boldsymbol{c_{M\xi\mu}} + \boldsymbol{c_{T\xi\mu}} \\ \boldsymbol{c_{M\mu\xi}} & -\omega^2 \boldsymbol{m_{M\mu}} + \boldsymbol{c_{M\mu}} \end{bmatrix} \begin{bmatrix} \boldsymbol{\xi} \\ \boldsymbol{\mu} \end{bmatrix} = \begin{bmatrix} \boldsymbol{f_{exc}} \\ 0 \end{bmatrix}, \tag{6.41}
$$

where $\boldsymbol{\xi}$ is the motion variable vector defined as $\boldsymbol{\xi} = [\eta_2, \eta_3, \eta_4, \nu_1 ... \nu_M]^T$ and $\boldsymbol{\mu}$ is the tangential deformation vector defined as $\boldsymbol{\mu} = [\mu_1 ... \mu_N]^T$. $\boldsymbol{m_S}$ is the total mass matrix of the membrane and floaters in air for the rigid body motions. $\boldsymbol{m_s}$ is defined according to

$$
\boldsymbol{m_s} = \begin{bmatrix} m_M + 2m_{Fl} & & -z_G(\pi R m_M + 2m_{Fl)}) \\ & m_M + 2m_{Fl} & \\ -z_G(\pi R m_M + 2m_{Fl)} & & I_{33}^M + I_{33}^{Fl} \end{bmatrix},
$$

where $\boldsymbol{m_s} = 0$ for $j > 4$. $\boldsymbol{a_f}$ is the total generalised added mass matrix with contributions from the internal and external added mass defined as $\boldsymbol{a_f} = \boldsymbol{a^{(e)}}(\omega) + \boldsymbol{a^{(i)}}(\omega)$. Here $\boldsymbol{a^{(e)}}(\omega)$ is the generalised external added mass matrix for all motions containing the elements $a_{jk}^{(e)}$ and $\boldsymbol{a^{(i)}}(\omega)$ is the generalised internal added mass matrix for all motions containing the elements $a_{jk}^{(i)}$. $\boldsymbol{b_f}$ is the generalised wave radiation damping matrix from the external problem, containing the elements $b_{jk}^{(e)}$. $\boldsymbol{c_f}$ is the generalised hydrostatic restoring matrix. $\boldsymbol{m_{M\xi}}, \boldsymbol{m_{M\mu}}$ are the membrane

mass matrices of $\boldsymbol{\xi}$ and $\boldsymbol{\mu}$, respectively. They are defined according to

$$\boldsymbol{m_{M\xi\xi}} = m_M \int_{S_M} \sum_{j=4}^{\infty} \sum_{m=1}^{\infty} \xi_j U_m(\psi_0) U_j(\psi_0) \mathrm{ds},$$

$$\boldsymbol{m_{M\mu\mu}} = m_M \int_{S_M} \sum_{n=1}^{\infty} \sum_{k=1}^{\infty} \mu_n U_k(\psi_0) U_n(\psi_0) \mathrm{ds}.$$

The structural stiffness matrices of $\boldsymbol{\xi}$; $\boldsymbol{c_{M\xi\xi}}$ and the structural stiffness matrix of $\boldsymbol{\mu}$; $\boldsymbol{c_{M\mu\mu}}$ are defined according to:

$$\begin{aligned}
\boldsymbol{c_{M\xi\xi}} = \int_{S_M} \sum_{j=4}^{\infty} \sum_{m=1}^{\infty} \xi_j \Bigg(& EdU_m(\psi_0) \frac{d\psi_0}{ds} - T_0 \frac{d^2 U_m(\psi_0)}{ds^2} - \frac{dT_0}{ds} \frac{dU_m(\psi_0)}{ds} \\
& - m_M g \sin\psi_0 \left(\frac{dU_m(\psi_0)}{ds} \right) U_{(j-3)}(\psi_0) \mathrm{ds}, \\
\boldsymbol{c_{M\mu\mu}} = \int_{S_M} \sum_{n=1}^{\infty} \sum_{k=1}^{\infty} \mu_n \Bigg(& - Ed \frac{d^2 U_k(\psi_0)}{ds^2} + T_0 \frac{d\psi_0}{ds} \frac{d\psi_0}{ds} U_k(\psi_0) \\
& - m_M g \cos\psi_0 U_k(\psi_0) \frac{d\psi_0}{ds} \Bigg) U_n(\psi_0) \mathrm{ds}.
\end{aligned}$$

The coupling stiffness matrix between $\boldsymbol{\xi}$ and $\boldsymbol{\mu}$; $\boldsymbol{c_{M\xi\mu}}$, and the coupling stiffness matrix between $\boldsymbol{\mu}$ and $\boldsymbol{\xi}$; $\boldsymbol{c_{M\mu\xi}}$, are defined according to:

$$\begin{aligned}
\boldsymbol{c_{M\xi\mu}} = \int_{S_M} \sum_{j=4}^{\infty} \sum_{n=1}^{\infty} \mu_n \Bigg(& - Ed \frac{dU_n(\psi_0)}{ds} - T_0 \left(\frac{dU_n(\psi_0)}{ds} \frac{d\psi_0}{ds} + U_n(\psi_0) \frac{d^2\psi_0}{ds^2} \right) \\
& - \frac{dT_0}{ds} U_n(\psi_0) \frac{d\psi_0}{ds} - m_M g \sin\psi_0 U_n(\psi_0) \frac{d\psi_0}{ds} \Bigg) U_{(j-3)}(\psi_0) \mathrm{ds}, \\
\boldsymbol{c_{M\mu\xi}} = \int_{S_M} \sum_{n=1}^{\infty} \sum_{j=4}^{\infty} \xi_j \Bigg(& Ed \left(\frac{dU_{(j-3)}(\psi_0)}{ds} \frac{d\psi_0}{ds} + U_{(j-3)}(\psi_0) \frac{d^2\psi_0}{ds^2} \right) \\
& + T_0 \frac{d\psi_0}{ds} \frac{dU_{(j-3)}}{ds} - m_M g \cos\psi_0 \frac{dU_{(j-3)}}{ds} \Bigg) U_n(\psi_0) \mathrm{ds}.
\end{aligned}$$

$\boldsymbol{c_{T\xi}}$ and $\boldsymbol{c_{T\xi\mu}}$ represent the membrane floater connection loads on the rigid body motions, and are defined according to:

$$\boldsymbol{f}^T = -\boldsymbol{c_{T\xi}} \boldsymbol{\xi} - \boldsymbol{c_{T\xi\mu}} \boldsymbol{\mu}, \tag{6.42}$$

where f_1^T is given by (6.38), f_2^T is given by (6.39), f_3^T is given by (6.40) and $f_j^T = 0$ for $j > 3$.

To solve (6.41) the generalized water pressure loads must be found.

6.4 Pressure loads

The pressure loads are divided in external and internal pressure loads. We will start by looking at the external pressure loads.

6.4.1 Generalised external pressure loads

To find the total dynamic pressure difference on the membrane we start by finding the external flow and resulting generalised pressure loads. We consider a 2D initially half circularly shaped CFFC with floaters in equilibrium in incident regular waves of amplitude ζ_a, with wave number k and frequency ω at constant depth h. The wave steepness is small, and linear theory is assumed. We assume a steady state condition. No transient effects are present due to initial conditions. This makes it possible to do the analysis in the frequency domain. For linear waves propagating in the y- direction, Faltinsen (1990) gives the velocity potential for incident waves at finite constant depth h as:

$$\phi_0 = \frac{g\zeta_a}{\omega}\frac{\cosh k(z+h)}{\cosh kh}e^{(\mathrm{i}\omega t - \mathrm{i}ky)}, \tag{6.43}$$

with the dispersion relation

$$\frac{\omega^2}{g} = k\tanh kh. \tag{6.44}$$

The presence of the body modifies the flow field in terms of a diffraction velocity potential ϕ_d and radiation velocity potentials $\phi_j^{(e)}$ associated with the body motions. The total external velocity potential Φ_e is given as:

$$\Phi_e = \phi_0 + \phi_d + \sum_{j=1}^{\infty}\phi_j^{(e)}\xi_j. \tag{6.45}$$

The general boundary value problem satisfies:

$$\frac{\partial^2\Phi_e}{\partial y^2} + \frac{\partial^2\Phi_e}{\partial z^2} = 0 \text{ in } Q_0^{(e)}, \tag{6.46}$$

$$\frac{\partial\Phi_e}{\partial z} = 0 \text{ at } z = -h, \tag{6.47}$$

$$-\omega^2\Phi_e + g\frac{\partial\Phi_e}{\partial z} = 0 \text{ on } \Sigma_{0e}, \tag{6.48}$$

in addition to body boundary conditions and a radiation condition ensuring outgoing far-field waves caused by the body. Here $Q_0^{(e)}$ is the mean external liquid domain and $\Sigma_0^{(e)}$ is the external mean free surface. The body boundary condition on the total exterior mean wetted structural surface including membrane and floaters for the diffraction potential is:

$$\frac{\partial\phi_d}{\partial n} = -\frac{\partial\phi_0}{\partial n} \text{ on } S_M^{(e)} + S_{Fl}^{(e)}, \tag{6.49}$$

where $S_M^{(e)}$ and $S_{Fl}^{(e)}$ denote mean wetted external membrane surface and floater surface, respectively. $\frac{\partial}{\partial n}$ denotes the normal derivative to the mean wetted external body surface. The corresponding normal vector $\vec{n}$ has positive direction into the

external water. Its components along the $y-$ and $z-$ axes are denoted n_y and n_z, respectively. The body boundary conditions for the radiation problems are:

$$\frac{\partial \phi_j^{(e)}}{\partial n} = \mathrm{i}\omega n_j \text{ on } S_M^{(e)} + S_{Fl}^{(e)}. \tag{6.50}$$

Here $j = 1..3$ represent the rigid body motions; $\xi_1 = \eta_2$ (sway),$\xi_2 = \eta_3$ (heave) and $\xi_3 = \eta_4$ (roll). It follows that

$$n_j = \begin{cases} n_y & \text{for } j = 1 \\ n_z & \text{for } j = 2 \\ yn_z - zn_y & \text{for } j = 3. \end{cases} \tag{6.51}$$

$j = 4..\infty$ are the prescribed normal deformation motions; $\xi_4 = \nu_1, \xi_5 = \nu_2 ....\xi_\infty = \nu_\infty$. It implies for $j \geq 4$ that

$$n_j = \begin{cases} U_{j-3}(\psi_0) & \text{on } S_M^{(e)} \\ 0 & \text{on } S_{Fl}^{(e)}. \end{cases} \tag{6.52}$$

The tangential membrane motions do not cause any potential flow.

To ensure that the waves caused by the body are outgoing two far-field velocity potentials are included, given as:

$$\phi_R^+ = \frac{g}{\omega} A^{(+)} \frac{\cosh k(z+h)}{\cosh kh} e^{(\mathrm{i}\omega t - \mathrm{i}ky)} \text{ for } y \to \infty, \tag{6.53}$$

$$\phi_R^- = \frac{g}{\omega} A^{(-)} \frac{\cosh k(z+h)}{\cosh kh} e^{(\mathrm{i}\omega t + \mathrm{i}ky)} \text{ for } y \to -\infty. \tag{6.54}$$

Here $A^{(+)}$ and $A^{(-)}$ represent far-field complex wave amplitudes and are unknowns in solving the problem.

Generalised added mass and damping terms for the external flow problem follows from properly integrating the time derivative of $\phi_j^{(e)}$, originating from the dynamic pressure part in Bernoulli's equation. The expressions are given by

$$\begin{aligned} \mathrm{i}\omega\rho_w \int_{S_{Fl}^{(e)}+S_M^{(e)}} \phi_j^{(e)} n_k \xi_j \mathrm{d}s &= \left(\omega^2 a_{jk}^{(e)}(\omega) - \mathrm{i}\omega b_{jk}^{(e)}(\omega)\right)\xi_j \text{ for } k = 1..3, j, \\ \mathrm{i}\omega\rho_w \int_{S_M^{(e)}} \phi_j^{(e)} n_k \xi_j \mathrm{d}s &= \left(\omega^2 a_{jk}^{(e)}(\omega) - \mathrm{i}\omega b_{jk}^{(e)}(\omega)\right)\xi_j \text{ for } k \geq 4, j, \end{aligned} \tag{6.55}$$

where $a_{kj}^{(e)}$ and $b_{kj}^{(e)}$ are the external 2D added mass and damping contribution in k direction, due to a motion in j direction. Small letters are used as notation for added mass and damping for the two-dimensional condition.

The generalised excitation load $f_{exc,j}$ as a combination of Froude Kriloff and diffraction forces, can be found according to

$$\begin{aligned} \mathrm{i}\omega\rho_w \int_{S_{Fl}^{(e)}+S_M^{(e)}} (\phi_0 + \phi_d) n_k \mathrm{d}s &= f_{exc,k}(\omega) \text{ for } k = 1..3, \\ \mathrm{i}\omega\rho_w \int_{S_M^{(e)}} (\phi_0 + \phi_d) n_k \mathrm{d}s &= f_{exc,k}(\omega) \text{ for } k \geq 4. \end{aligned} \tag{6.56}$$

Analytical relations

Two known relations between the damping and the far-field wave amplitude, and between excitation force and damping, together with a symmetry relation based on Green's second identity were used to verify the correctness of the numerical code. It is stated in Faltinsen (1990) that (6.57) and (6.59) holds for $j = 1 - 3$ (sway, heave and roll). However, in the development of these relation, the normal velocity $i\omega n_j$ is used, and therefore the relations will hold for all j, including the normal deformation modes.

The estimated diagonal damping coefficient b_{jj}^{est} has the following relation to the far-field wave amplitude $|A^+|$ for constant finite water depth (Faltinsen and Timokha, 2009):

$$b_{jj}^{est} = \frac{\rho_w g^2}{\omega^3} \left(\frac{|A^+|}{|\xi_j|} \right)^2 2kI_1. \tag{6.57}$$

where

$$I_1 = \int_{-h}^{0} \frac{\cosh^2 k(z+h)}{\cosh^2 kh} \mathrm{dz} = \frac{\sinh(kh)\cosh(kh) + kh}{2k\cosh^2 kh}. \tag{6.58}$$

For an infinitely long cylinder in beam sea, at infinite depth the estimated excitation force amplitude $|f_j|^{est}$ has a known relation to the two-dimensional diagonal damping coefficient b_{jj} (Newman, 1962). For finite water depth this relation were found to be:

$$|f_j|^{est} = \zeta_a \sqrt{\frac{\rho_w g^2}{\omega} b_{jj} 2kI_1}. \tag{6.59}$$

The derivation of (6.59) is given in Appendix E.

Green's second identity tells that

$$\int_{\Sigma_{0e}+S_{Fl}^{(e)}+S_M^{(e)}+S_\infty} \left[\phi_j^{(e)} \frac{\partial \phi_k^{(e)}}{\partial n} - \phi_k^{(e)} \frac{\partial \phi_j^{(e)}}{\partial n} \right] ds = 0. \tag{6.60}$$

Here S_∞ are vertical control surfaces between $z = 0$ and $z = -h$ at $y = \pm\infty$. If we use (6.60) together with boundary conditions on the mean the free surface Σ_{0e}, S_∞ and on the mean wetted tank surface $S_{Fl}^{(e)} + S_M^{(e)}$ we can derive symmetry properties of the added mass and damping coefficients. For $S_{Fl}^{(e)} = 0$, $a_{jk}^{(e)} = a_{kj}^{(e)}$ and $b_{jk}^{(e)} = b_{kj}^{(e)}$ for all j, k. However, when $S_{Fl}^{(e)}$ is non-zero the relations will only hold for $j, k < 4$ and $j, k \geq 4$.

6.4.2 Internal water pressure loads

Linear potential flow theory of an incompressible liquid is assumed for the internal domain. For the internal flow it is most convenient to operate in a tank fixed coordinate system. At rest, the origin of the tank fixed coordinate system is placed at the origin of the global inertial coordinate system. Since we assume small

motions and deformations, the collocation of the origins of the inertial and tank-fixed coordinate system at rest, implies that the representation of the rigid body motions and membrane deformations are the same when considering the inertial and external problems. In the tank fixed coordinate system, Bernoulli's equation in its original form must be modified to an accelerated coordinate system (Faltinsen and Timokha, 2009, page 48). The linearised version of the pressure, or more precisely excess pressure to atmospheric pressure is

$$p = -\rho_{wi}\frac{\partial \Phi_i}{\partial t} - \rho_{wi} g \eta_4 y - \rho_{wi} g (z - \Delta h), \tag{6.61}$$

with Φ_i as the internal velocity potential. The equation is consistent with that the excess pressure to atmospheric pressure is zero at $z = \Delta h$ when the tank is at rest.

The internal velocity potential Φ_i can be expressed as

$$\Phi_i = \sum_{j=1}^{\infty} \phi_j^{(i)} \xi_j. \tag{6.62}$$

The velocity potential $\phi_j^{(i)}$ satisfies

$$\frac{\partial^2 \phi_j^{(i)}}{\partial y^2} + \frac{\partial^2 \phi_j^{(i)}}{\partial z^2} = 0 \text{ in } Q_0^{(i)}, \tag{6.63}$$

$$\frac{\partial \phi_j^{(i)}}{\partial n} = \mathrm{i}\omega n_j^{(i)} \text{ on } S_M^{(i)} + S_{Fl}^{(i)}. \tag{6.64}$$

Here $Q_0^{(i)}$ is the mean internal liquid domain, $S_{Fl}^{(i)}$ is the mean internal wetted floater surface and $S_M^{(i)}$ is the internal wetted surface of the membrane.

The internal normal vector $\vec{n}^{(i)}$ has positive direction into the internal water. As for the external problem is

$$n_j^{(i)} = \begin{cases} n_y & \text{for } j = 1 \\ n_z & \text{for } j = 2 \\ y n_z - z n_y & \text{for } j = 3. \end{cases} \tag{6.65}$$

For the prescribed normal deformation modes for $j = 4..$ are

$$n_j^{(i)} = \begin{cases} -U_{j-3}(\psi_0) & \text{on } S_M^{(i)} \\ 0 & \text{on } S_{Fl}^{(i)}. \end{cases} \tag{6.66}$$

At the free surface, we linearise (6.61) at the internal free surface $z - \Delta h - \zeta_i = 0$, where ζ^i describes the internal wave elevation relative to the movable, tank fixed coordinate system. We then arrive at the linearised dynamic free surface conditions in the body fixed coordinate system:

$$\frac{\partial \Phi_i}{\partial t}|_{\Sigma_0^{(i)}} + y g \eta_4 + g \zeta^i = 0. \tag{6.67}$$

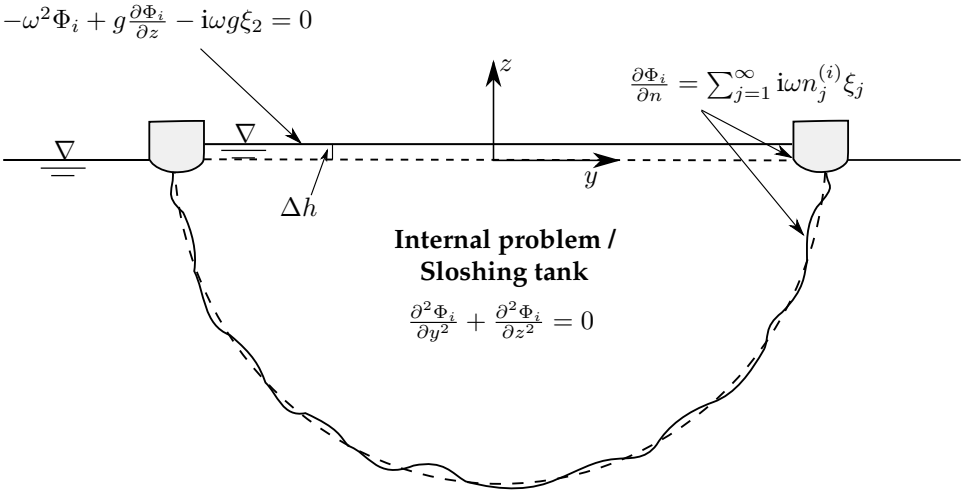

Figure 6.5: Boundary conditions for a two-dimensional half circular closed flexible fish cage with floaters in the frequency domain.

Where $\Sigma_0^{(i)}$ is the mean free surface inside the tank. The kinematic linearised free surface conditions is (Faltinsen and Timokha, 2009, page 198):

$$\frac{\partial\Phi_i}{\partial z} - \dot{\xi}_2 - y\dot{\xi}_3 - \frac{\partial\zeta^i}{\partial t} = 0 \tag{6.68}$$

In addition, conservation of liquid mass

$$\int_{\Sigma_0^{(i)}} \zeta^i dy = \int_{S_M^{(i)}} \sum_{j\geq 4} n_j\xi_j \mathrm{ds}, \tag{6.69}$$

must be satisfied. Equation (6.68) is not the same as in an Earth fixed coordinate system. Changes had to be made to include the rigid body motions and due to the effect of the gravitational acceleration in the body fixed coordinate system, since the body rotates relative to the Earth. Equation (6.69) expresses that the free surface elevation must be consistent with conservation of liquid volume. If $\int_{S_M^{(i)}} n_j\xi_j \mathrm{ds} \neq 0$ for $j \geq 4$ for a given non-zero ξ_j, a time dependent constant change in the free surface exist. By combining (6.68) with the time derivative of (6.67) in the frequency domain, we get the linearised free surface condition

$$-\omega^2\Phi_i + g\frac{\partial\Phi_i}{\partial z} - \mathrm{i}\omega g\xi_2 = 0. \tag{6.70}$$

The boundary value problem for the liquid flow in the internal domain is illustrated in Figure 6.5.

The free surface condition of $\phi_j^{(i)}$ will be dependent on j:

$$\begin{aligned} -\omega^2\phi_j^{(i)} + g\frac{\partial\phi_j^{(i)}}{\partial z} &= \mathrm{i}\omega g \text{ on } \Sigma_0^{(i)} \text{ for } j = 2, \\ -\omega^2\phi_j^{(i)} + g\frac{\partial\phi_j^{(i)}}{\partial z} &= 0 \text{ on } \Sigma_0^{(i)} \text{ for } j \neq 2. \end{aligned} \tag{6.71}$$

As a consequence of properly integrating the time derivative part of the pressure as given by Bernoulli's equation related to the tank fixed coordinate system, we obtain the following added mass coefficients $a_{jk}^{(i)}$

$$\begin{aligned} \mathrm{i}\rho_{wi}\omega \int_{S_{Fl}^{(i)}+S_M^{(i)}} \phi_j^{(i)} n_k \xi_j \mathrm{ds} &= \omega^2 a_{jk}^{(i)}(\omega)\xi_j \text{ for } k = 1..3, j, \\ \mathrm{i}\rho_{wi}\omega \int_{S_M^{(i)}} \phi_j^{(i)} n_k \xi_j \mathrm{ds} &= \omega^2 a_{jk}^{(i)}(\omega)\xi_j \text{ for } k \geq 4, j, \end{aligned} \tag{6.72}$$

where ρ_{wi} is the density of the water inside the CFFC and $a_{jk}^{(i)}$ is the internal 2D added mass contribution in j direction, due to a motion in k direction. There are no damping coefficients according to potential flow theory for the interior problem. The hydrodynamic damping coefficients associated with viscous boundary layer at the wetted body surface will be neglected. However, this damping is in reality small (Faltinsen and Timokha, 2009, page 377).

Symmetry of coefficients can also be used to verify the internal added mass coefficients. Again we use Green's second identity:

$$\int_{\Sigma_0^{(i)}+S_{Fl}^{(i)}+S_M^{(i)}} \left[\phi_j^{(i)}\frac{\partial\phi_k^{(i)}}{\partial n} - \phi_k^{(i)}\frac{\partial\phi_j^{(i)}}{\partial n}\right] ds = 0, \tag{6.73}$$

together with boundary conditions on the mean the free surface $\Sigma_0^{(i)}$ and on the mean wetted tank surface $S_{Fl}^{(i)} + S_M^{(i)}$. For $S_{Fl}^{(i)} = 0$, $a_{jk}^{(i)} = a_{kj}^{(i)}$ for all $j \neq 2$. Due to the free surface condition for heave, we will not have this property for coupling terms between heave and the normal deformation modes. When $S_{Fl}^{(i)} > 0$, the relation will only hold for $j, k < 4$ and $j, k > 3$.

The internal relative wave elevation ζ^i follows from the dynamic free-surface condition (6.67):

$$\zeta^i = -\frac{i\omega}{g}\sum_{j=1}^{\infty}\phi_j^{(i)}\xi_j|_{\Sigma_0^{(i)}} - y\eta_4. \tag{6.74}$$

6.4.3 Restoring coefficients

The considered restoring coefficients in the equation of motions of the floater and the membrane are due to quasi-steady change in the hydrostatic pressure and weight considerations. The effect of a mooring system is not considered. If the hydrostatic pressure i.e $-\rho_w g z$, is integrated over the instantaneous position of

the structure, it will contribute to restoring forces and moments. The change of hydrostatic pressure do not contribute to any restoring in sway ($\eta_2 = \xi_1$). The only potential restoring in sway must come from a mooring system. We have not considered the effect a mooring system, so there will be no restoring in sway. Since the whole internal water moves when considering heave ($\eta_3 = \xi_2$), there is no relative change in hydrostatic pressure internally. When we consider roll, there are contributions as described in Faltinsen and Timokha (2009, page 79). The restoring coefficients in heave (c_{22}) and roll (c_{33}) by considering both internal and external contributions are given according to:

$$c_{22} = \rho_w g A_w(z_e), \tag{6.75}$$

$$c_{33} = -mgz_G + \rho_w g\left(\nabla z_B + \int_{A_w} y^2 dy - \overbrace{\frac{\rho_{wi}}{\rho_w}\left(\frac{1}{12}b_t^3 + \int_{Q_0^{(i)}} (\Delta h + z) dQ\right)}^{\text{Tank correction terms}}\right). \tag{6.76}$$

When defining variables in (6.75) and (6.76), we refer to a fictitious body including the floaters, the membrane and the water inside. Then, $A_w(z_e)$ is the waterplane area of the fictitious body, defined in 2D as $A_w(z_e) = 2(R+a(z_e))$. ∇ is the displaced volume of water of the fictitious body per unit length; m is the combined mass of the floater and membrane and z_G is the combined center of gravity of the floaters and membrane of the CFFC. z_B is the $z-$ coordinate of the center of buoyancy of the fictitious body and $b_t = 2(R - a(z_e))$ is the internal distance between the floaters at the free surface. For the center of buoyancy the equation for c_{33} must be corrected for the internal hydrostatic pressure, or the "frozen" liquid effect as it is called in Faltinsen and Timokha (2009, page 79-82).

The generalised pressure loads due to the change in hydrostatic pressure integrated over the instantaneous body surface will give a hydrostatic restoring force also for the normal structural deformation modes. When considering change in the hydrostatic pressure due to the elastic deformation, we introduce first the change $U_{j-3}(\psi_0)\xi_j n_2$ that the normal deformation $U_{j-3}(\psi_0)\xi_j$ causes in vertical motion. Here n_2 is the external normal vector in heave. Then we must account for a possible density difference $\Delta\rho = \rho_{wi} - \rho_w$ between the internal and external water. It means that the change in hydrostatic pressure loading on the membrane is

$$-\Delta\rho_w g U_{j-3}(\psi_0)\xi_j n_2. \tag{6.77}$$

The unit normal vector of the internal and external domain points in the opposite direction. We assume that $S_M^{(i)} \approx S_M^{(e)}$, this is plausible as long as the thickness of the membrane d is small. The restoring coefficients for a given mode k, can be calculated as:

$$\sum_{j=4}^{\infty} c_{jk}\xi_j = -\Delta\rho_w g \int_{S_M^{(e)}} \sum_{j=4}^{\infty} U_{(j-3)}(\psi_0) n_2 U_{(k-3)}(\psi_0)\xi_j \text{ds for } j,k > 4. \tag{6.78}$$

This means that we will only have an additional restoring due to the normal structural deformation modes if the density of the internal and external liquid

differ ($\Delta\rho \neq 0$). For limited density differences, the restoring coefficients of the structural deformation modes are small compared to the restoring coefficients of heave and roll.

Several papers have studied the effect of hydrostatic restoring for elastic bodies; Malenica et al. (2015, 2009); Senjanovic et al. (2008); Newman (1994). The given calculations deviate from these studies. Common for all of the cited papers are that they define the structural modes in a Cartesian xyz coordinate system. This complicates the calculations and leads to other terms. Senjanovic et al. (2008) and Newman (1994) only considered the restoring from the hydrostatic pressure on the external body, and did not account for hydrostatic pressure from any internal liquid. Malenica et al. (2015, 2009) considers hydrostatic pressure on both an internal and an external domain, but have a different free surface condition for the internal domain, leading to a restoring term from the rise of the free surface which is included in my internal added mass.

6.5 Numerical implementation and verification

To find the pressure loads on the CFFC, the potential theory formulations have to be solved in a numerical framework. The HPC method presented in Appendix B was used. For the rectangular tank with a flexible wall analysed in Chapter 4 the computational domain was rectangular, and easily discretized with quadratic cells. Since the geometry of the CFFC is not quadratic, a method to account for the non-rectangular boundary must be used. The main alternatives are either to use a boundary fitted grid, or to use an immersed boundary method. Ma et al. (2017) have found that the HPC method have best accuracy for quadratic grid cells, and that severe stretching or distortion of the cells should be avoided. Inspired by Hanssen et al. (2015), who successfully implemented an immersed boundary method (IBM) for a moving body we use a fixed Cartesian quadratic grid, with an immersed boundary method to capture the boundary. Then, the cells remain quadratic.

Ghost nodes inside (for the external problem) and outside (for the internal problem) the body are applied to reconstruct the velocity at the immersed boundary (Hanssen et al., 2015). The body- boundary condition on immersed boundaries are projected onto the surrounding ghost nodes. The applied code uses one layer of ghost nodes and uses the harmonic polynomials of the HPC method to interpolate the coordinate of the boundary to the ghost cell. The ghost nodes are connected to cells inside the liquid domain.

The numerical HPC framework was implemented in Python. To find the immersed boundary, the Python package "shapely" was used. Based on predefined structure input points defining the geometry, the function approximated a point on the boundary inside the cell based on linear approximation between the predefined structural input points.

6.5.1 Numerical theory for the external domain

The boundary value problem for the external sea keeping problem of the CFFC is illustrated in Figure 6.6. The far-field velocity potential assumes that the domain is

"infinite". However, according to Billingham and King (2009), the far-field velocity potential is sufficient as long as $l \geq 4h$, where l is the total length of the domain.

The velocity potentials caused by the body have symmetric and antisymmetric properties with respect to a symmetry line containing the z-axis. The later fact follows from symmetry and antisymmetry properties of n_j. n_1 and n_3 are antisymmetric while n_2 is symmetric. When $j > 3$, the odd sine modes ($(j-3) = 1, 3, 5...$) are symmetric while the even ($(j-3) = 2, 4, 6...$) sine-modes are antisymmetric. Furthermore, the body boundary condition for the diffraction potential can be divided into symmetric and antisymmetric parts. The symmetric and antisymmetric properties allow us to only consider half the water domain. When the body boundary condition is antisymmetric, the far-field complex wave amplitude $A^{(+)} = -A^{(-)}$ and $\phi = 0$ at the symmetry line. While for symmetric potentials $A^{(+)} = A^{(-)}$, and $\partial\phi/\partial y = 0$ at the symmetry line. These conditions are used as a boundary conditions at the symmetry line.

Due to the symmetry and antisymmetry properties of the system it is sufficient to only consider the right part of the tank. The boundary condition on the right wall of the tank then become:

$$\frac{\partial \Phi_e}{\partial y} = -\mathrm{i}\omega A^{(+)} \frac{\cosh k(z+h)}{\sinh kh} e^{(\mathrm{i}\omega t - \mathrm{i}k\frac{l}{2})} \text{ on } y = \frac{l}{2}. \tag{6.79}$$

6.5.2 Verification case with a water-filled hemicircle in waves

The non-dimensional squared frequency range $0.2 \leq \omega^2 R/g \leq 5.6$ is considered, this is compareable to wave peak periods in the weather range from moderate to extreme in Table 2.1 for a CFFC with full scale radius $R = 12.5$m.

For a hemicircle (CFFC withouth floaters) reference values for the pressure loads can be found both related to the external added mass and damping for sway and heave, and for the sloshing eigenfrequencies for the given frequency range.

External added mass and damping coefficients

An external domain with $h/R = 4$ and $l/h = 4$, where only the right half of the tank (on the right side of the symmetry line) as illustrated in Figure 6.6 were used. The claim by Billingham and King (2009) that $l/h = 4$ was sufficient, was confirmed by a convergence study of domain size.

Calculated two-dimensional added mass and damping coefficient in sway and heave for a hemicircle in infinite water depth and infinite horizontal extent for a given range of non-dimensional frequencies are given in Faltinsen and Timokha (2009). Finite depths results can be found in Bai and Yeung (1974). The frequency dependent added mass and damping in sway, heave and roll for a hemicircle are plotted in Figure 6.7 with superscript (e) to indicate that they are relevant for our exteriour fluid problem. These results compare well to the results for infinite water given in Faltinsen and Timokha (2009) for non-dimensional squared frequencies $\omega^2 R/g > 1$. For lower frequencies the simulated results deviate. However, this is expected and are due to the influence of finite depth. In Bai and Yeung (1974) results for water depth-to-cylinder radius $h/R = 2$ are given, while $h/R = 4$ have

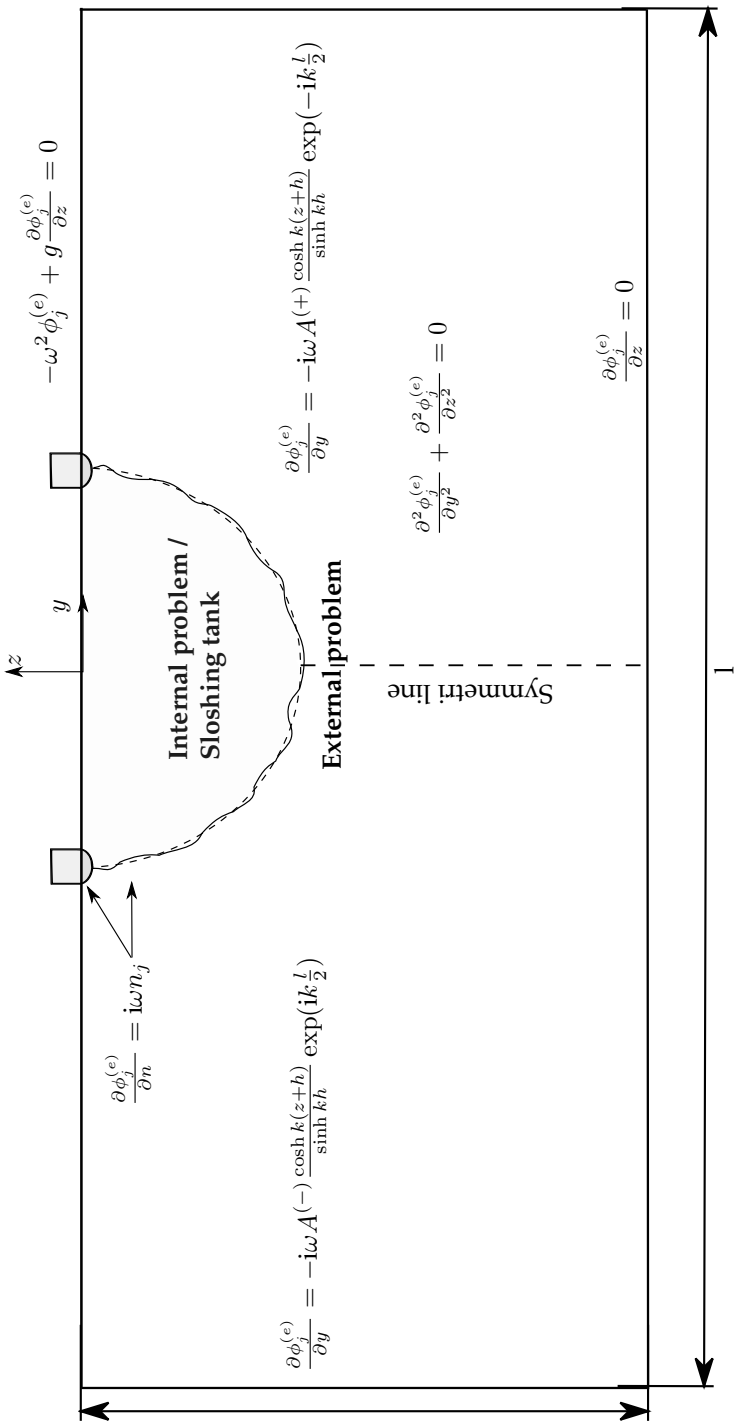

Figure 6.6: Boundary conditions for the external radiation problem, $\phi_j^{(e)}$ is the external potential due to forced motion ξ_j in the frequency domain. In a Cartesian $y-z$ coordinate system. h is the depth and l is the total length of the domain.

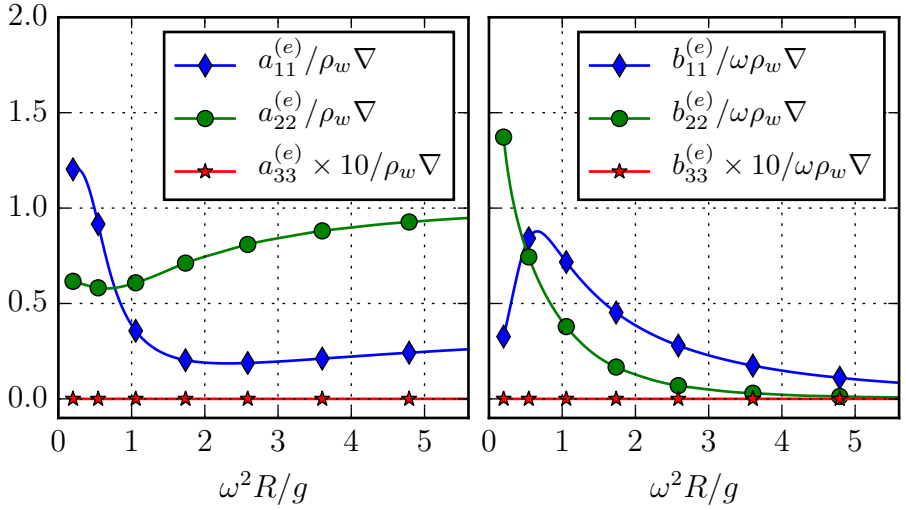

Figure 6.7: Non-dimensional added mass coefficients (left) and damping coefficients (right) for sway, heave and roll for a hemicircle versus non-dimensional squared frequency $\omega^2 R/g$. $\nabla = \frac{\pi R^2}{2}$ is the displaced volume per meter. The water depth- to- radius ratio $h/R = 4.0$.

been used in our case. However, $h/R = 2$ has also been tested with good results. The results are not given here. For a hemicircle the normal vector component $n_3 = yn_z - zn_y = 0$, resulting in that the pressure loads cannot cause any roll moment. The result is that the added mass, damping and excitation in roll is zero.

The non-dimensional generalised added mass and damping for the hemicircle for the normal structural modes from one to ten is plotted in Figure 6.8. Plot of the shape of the first ten structural normal modes are given in Figure F.1 in Appendix F. The non-dimensional added mass and damping coefficients of the first two structural modes are comparable in magnitude to the non-dimensional coefficients in sway and heave, and the added mass and damping coefficients of the first mode is actually equal to the added mass and damping coefficients in heave. The latter fact follows from the body boundary condition and the definition of the generalised added mass and damping. However, this will not be the case for our considered membrane with floaters. We can observe from the Figure that the magnitude of the added mass and damping coefficients decreases with increasing mode number. This can also be seen analytically by considering the high frequency asymptotic behaviour of symmetric modes and is related to both the oscillatory behaviour of the pressure and the multiplying mode. For the four highest modes plotted, it appears that the added mass becomes frequency independent.

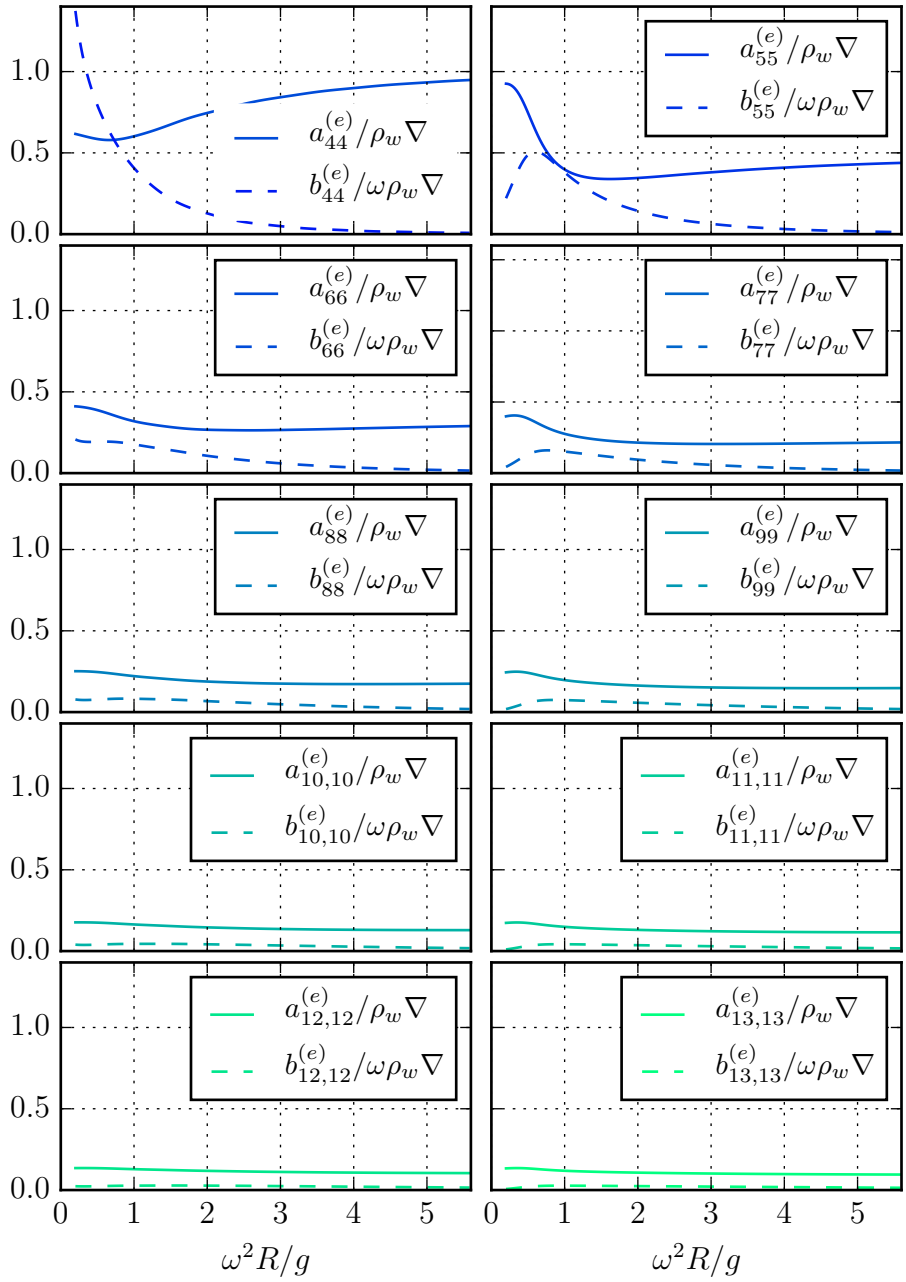

Figure 6.8: Non-dimensional added mass and damping coefficients for normal deformation modes from 1-10 for a hemicircle versus non-dimensional squared frequency $\omega^2 R/g$. $\nabla = \frac{\pi R^2}{2}$ is the displaced volume per meter. The water depth-to- radius ratio $h/R = 4.0$.

Internal added mass coefficients

The internal added mass coefficients in sway, heave and roll can be found in Figure 6.9. Theoretical values for the internal sloshing eigenfrequencies of a hemicircle can be found in (Faltinsen and Timokha, 2009, page 173). The theoretical values of the sloshing eigenfrequencies (k_1^*R, k_2^*R and k_3^*R) within the considered non-dimensional squared frequency range are illustrated with vertical dotted lines. We can see that there is good agreement between the theoretically and numerically found sloshing eigenfrequencies, by the fact that the absolute value of the sway added mass becomes infinite at the sloshing frequencies k_1^*R and k_3^*R. We note both negative and positive sway added mass with a large frequency dependence at k_1^*R and k_3^*R. The added mass in heave is constant and equal to the mass of the enclosed water. For a hemicircle the added mass in roll is zero.

Non-dimensional generalised internal added mass for the structural normal modes of the hemicircle are plotted in Figure 6.10. We can observe due to the infinite absolute values of added mass that the even modes (except the first one) will have a sloshing resonance at the second sloshing eigefrequency, while the odd modes have sloshing resonances at the first and third sloshing frequency. The reason why the first mode does not, is that it is the same as considering forced heave. However, the difference in free surface condition for the first mode and heave make them unequal. For the hemicircle the velocity potential of the first mode can be written as $\phi_4^{(i)}\xi_4 = \mathrm{i}\omega\xi_4(z + \frac{g}{\omega^2})$. This gives an internal generalised added mass of $a_{44}^i = \frac{\pi R^2}{2} - \frac{2g}{\omega^2}$. This added mass is consistent with the added mass of the first mode as plotted in Figure 6.10. When ω goes to zero, the internal generalised added mass goes to minus infinity, while when ω goes to infinity the generalised added mass for this mode approaches the fluid mass of the hemicircle. The generalised internal added mass of the first mode have no resonances. The internal added mass coefficients of the even modes does not approach a constant value when ω goes to zero, this is because the internal added mass coefficient for these modes include as described in Chapter 4, a restoring coefficient associated with the quasi- static hydrostatic pressure change due to the change in mean free surface. The internal added mass coefficient can then be described according to $a_{jk}^{(i)}(\omega) = \frac{c_{jk}^{(i)}}{\omega^2} + a_{jk}^{(i*)}(\omega)$. From this equation we see that when $c_{jk}^{(i)}$ is negative the response of $a_{jk}^{(i)}(\omega)$ is that it goes to minus infinite when ω goes to zero.

Validation and convergence

For validation of the code several given relations have been used. The relation between the far-field wave amplitude $|A^+|$ and the estimated external diagonal damping coefficient given by (6.57), together with the relation between the calculated two-dimensional diagonal damping coefficient b_{jj} and the excitation force for finite depth given by (6.59) have been used for verification of the code. In addition, the error between the calculated and estimated damping, and between the calculated and estimated excitation force have been used as a measure of convergence. For increased grid refinement it has been found that this error decreases. Error plots related to the difference between the estimated and calculated damping

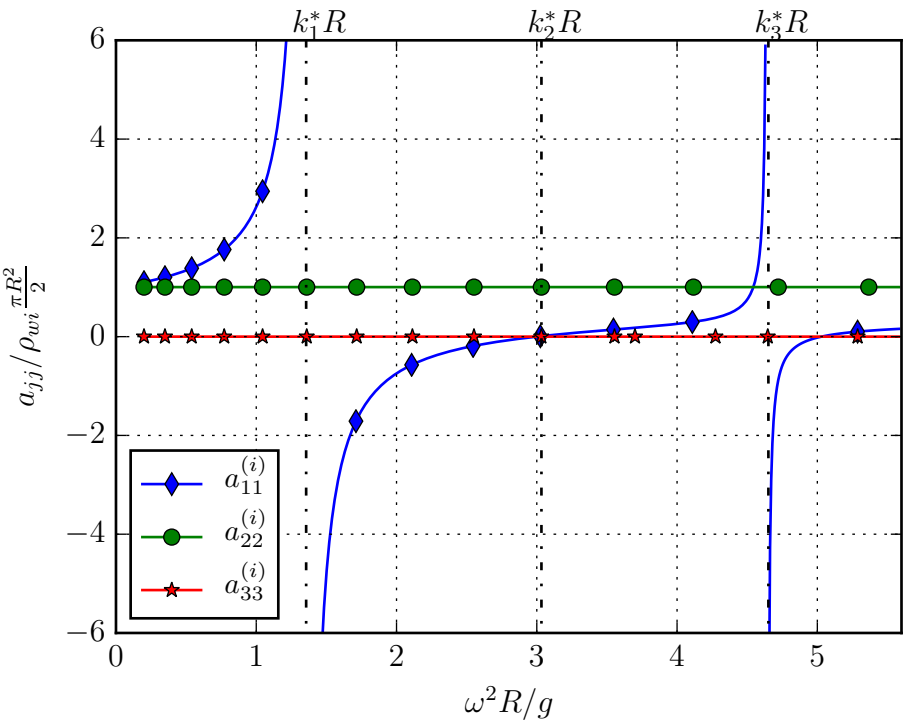

Figure 6.9: Nondimentional internal added mass coefficients for a hemicircle, for sway, heave and roll versus non-dimensional squared frequency $\omega^2 R/g$. k_1^*R, k_2^*R and k_3^*R are the theoretical values of the sloshing eigenfrequencies.

and excitation force can be found in Appendix G, for a quadratic grid with node resolution $N_y/R = 100$, where N_y is the total number of nodes in the y direction in the domain.

Green's second identity for the external problem (6.60) has been used to derive symmetry properties of the added mass and damping coefficients, requiring that $a_{jk}^{(e)} = a_{kj}^{(e)}$ and $b_{jk}^{(e)} = b_{kj}^{(e)}$. Since the external wet surface of the floater $S_{Fl}^{(e)} = 0$, this will hold for all j, k, including the coupling coefficients between the structural deformation modes and the rigid body motions. Numerically a difference will exist between $a_{jk}^{(e)}$ and $a_{kj}^{(e)}$ which can be expressed as an error: $a_{jk}^{(e)} - a_{kj}^{(e)} = e_{a,kj} \neq 0$ and $b_{jk}^{(e)} - b_{kj}^{(e)} = e_{b,kj} \neq 0$. For increased grid refinement it has been found that this error decreases. The coefficients of the highest used structural deformation mode have the slowest convergence. This is to be expected since the spatial variation of the velocity along the boundary are largest for the structural modes with the highest mode number, requiring a finer grid to resolve the deformations. In simulations a resolution of 20 nodes per modal wave length along the boundary have been found sufficient to reach an acceptable convergence.

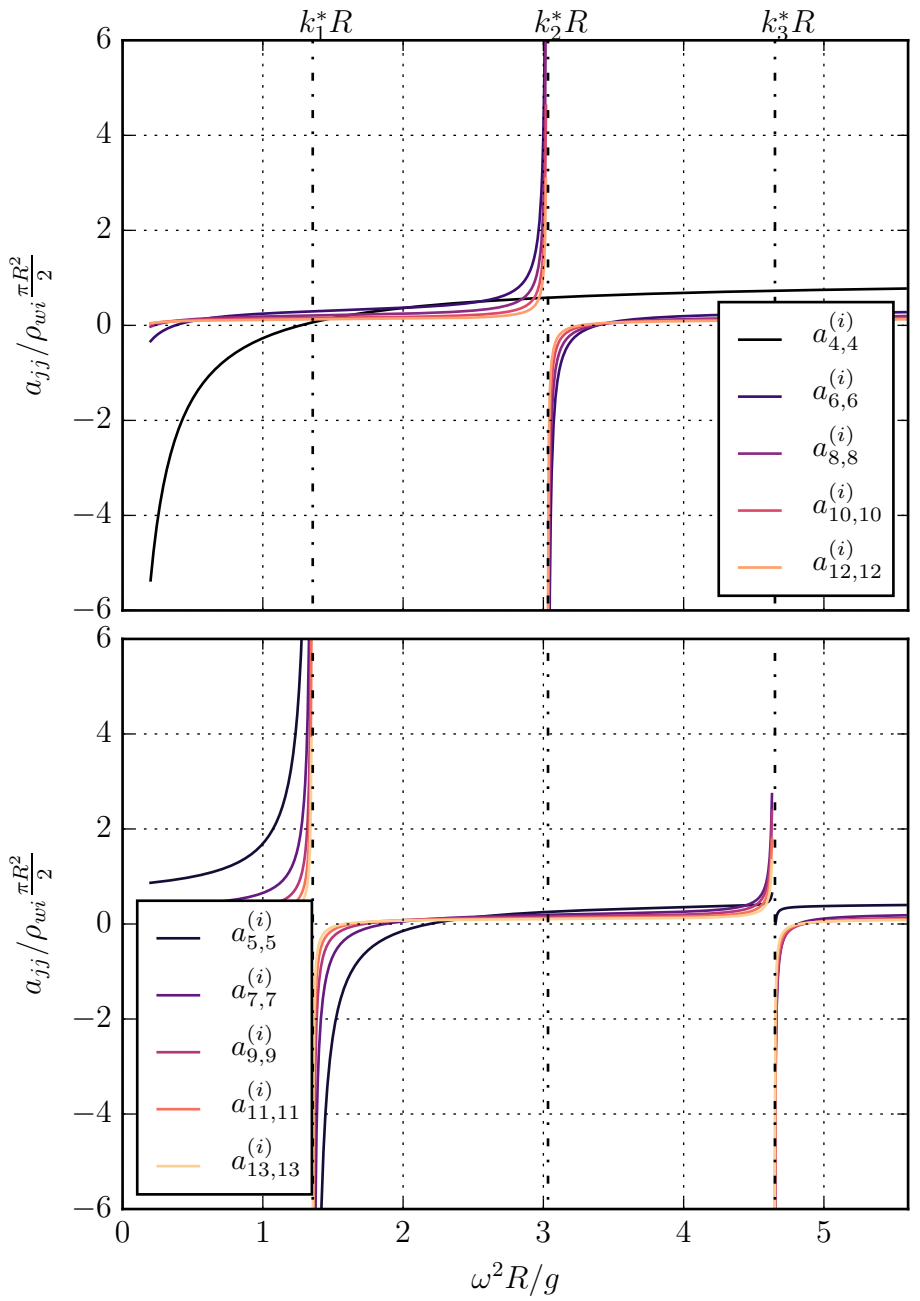

Figure 6.10: Non-dimensional internal added mass coefficients for a hemicircle, for symmetric(top) and asymmetric (bottom) modes versus non-dimensional squared frequency $\omega^2 R/g$. k_1^*R, k_2^*R and k_3^*R are the theoretical values of the sloshing eigenfrequencies.

Table 6.1: Case dimensions for CFFC with floaters. R is the radius of the bag, d is the thickness of the fabric, E is the elasticity module of the fabric, ρ_N is the density of the fabric, ρ_w is the density of salt water and R_F is the radius of the floater.

R	d	E	ρ_N	ρ_w	R_F/R
12.5 m	$7.5 \cdot 10^{-4}$ m	$2.25 \cdot 10^9$ Pa	1150 kg/m^3	1025 kg/m^3	0.1

Also for the internal problem Green's second identity given by (6.73) is used to derive symmetry properties for the added mass coefficients, requiring that $a_{jk}^{(i)} = a_{kj}^{(i)}$. Since the internal wet surface of the floater $S_{Fl}^{(i)} = 0$, this relation holds for all j, k not equal to 2. Due to the free-surface condition the relation will not hold for any coefficients involving heave. As for the external problem the error difference between $a_{jk}^{(i)}$ and $a_{kj}^{(i)}$ decreases for increasing grid refinement.

6.6 Case study of a CFFC in waves

The wave-induced response of a CFFC with a static equilibrium geometry based on case one from Chapter 5, with overfilling and no density differences has been analysed in the frequency domain, at finite water depth for depth-to-radius ratio $h/R = 4.0$. For this case the geometry of the 2D membrane can be assumed half circular, and the top angle $\psi_e = \pi/2$, which simplifies the expressions for the structural deformations found in Section 6.2 to a large extent. The expression for a half circular membrane are given in Appendix D. Relevant used full scale values are given in Table 6.1. Compared to the floaters used today, the floaters used here are large floaters.

6.6.1 External added mass and damping

An external computational domain with water depth to bag radius ratio $h/R = 4$ and horisontal extent-to-water depth ratio $l/h = 4$, where only the right half of the tank (on the right side of the symmetry line) as illustrated in Figure 6.6 were used. The non-dimensional external added mass and damping coefficients in sway, heave and roll for a CFFC in waves are plotted in Figure 6.11. The coefficients in sway and heave are comparable in size and behaviour to the coefficient for the hemicircle. However, opposite to the hemicircle, the structure now have a small non-zero added mass, damping and excitation in roll due to the presence of the floaters.

The external non-dimensional added mass and damping coefficients for the CFFC for the normal structural modes from one to ten are plotted in Figure 6.12. The behaviour of the non-dimensional added mass and damping coefficients are in general comparable to the hemicircle. The magnitude of the added mass and damping decreases with increasing mode number. For the plotted four highest modes it appears that the added mass becomes frequency independent.

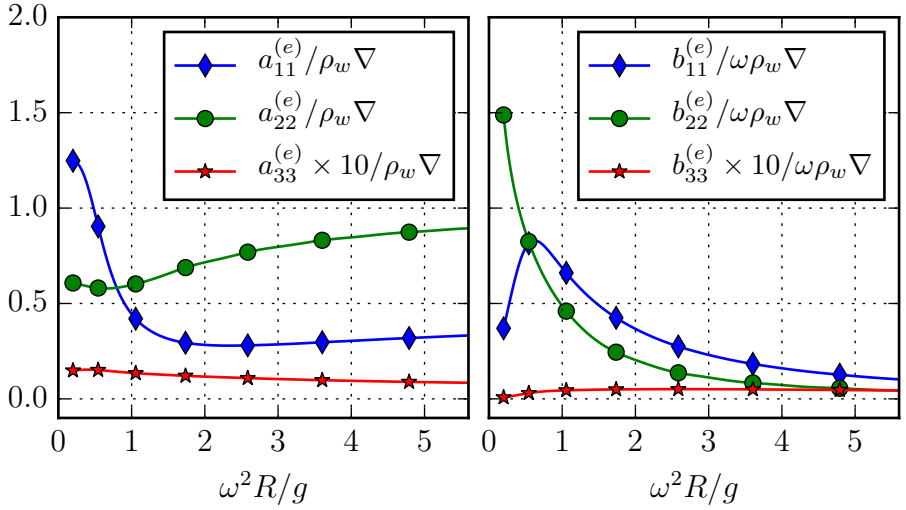

Figure 6.11: Non-dimensional added mass (left) and damping coefficients (right) for sway, heave and roll for a CFFC with large floaters versus non-dimensional squared frequency $\omega^2 R/g$. ∇ is the displaced volume per meter of a fictitious body containing the submerged floaters, the membrane and the internal water.

6.6.2 Internal added mass

The internal added mass coefficients in sway, heave and roll can be found in Figure 6.13. When floaters are added to the geometry and the equilibrium geometry is used for the analysis the results will deviate from the reference values for the sloshing frequencies for the hemicircle given by Faltinsen and Timokha (2009). All the new non-dimensional eigenfrequencies $k_1 R, k_2 R$ and $k_3 R$, are larger than the reference values $k_1^* R, k_2^* R$ and $k_3^* R$.

To find a bound on the non-dimensional eigenfrequencies $k_1 R, k_2 R$ and $k_3 R$ for the CFFC we can use the comparison theorem given in (Faltinsen and Timokha, 2009, page 150). If the liquid domain of tank can be completely contained within the domain of a bigger tank, given that the two tanks have equal mean free surface, then the smallest tank have smaller natural frequency. We construct two domains to obtain a bound on the natural frequency of the CFFC, one circular domain Q_c that contain the fluid domain of the CFFC, and one rectangular domain Q_R that is contained within the domain of the CFFC. The two constructed domains are illustrated in Figure 6.14. The constructed circular tank intersects the boundary of the CFFC at the intersection between the free surface and the floaters $(\pm\frac{b_t}{2}, 0)$ and at the connection points between the floaters and the membrane of the CFFC (R, z_e). The radius of the calculated constructed circle R_c is $R_c = \sqrt{\frac{b_t^2}{2} + b_t R_F + R_F^2}$ and the filling level is $h_f = R_c + \frac{b_t}{2} + R_F$. Values for the non-dimensional eigenfrequencies

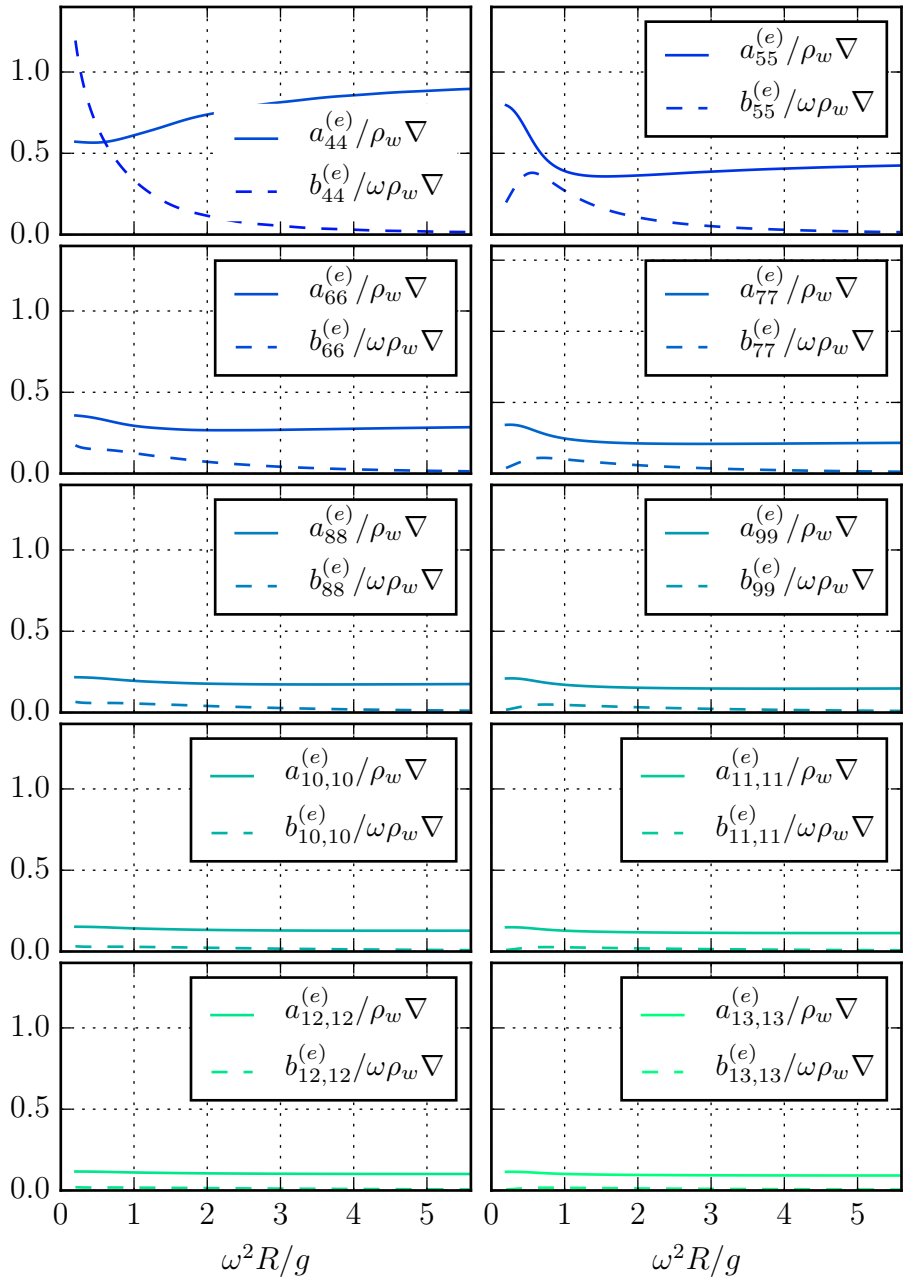

Figure 6.12: External non-dimensional added mass and damping coefficients for normal deformation modes from 1-10 for a CFFC versus non-dimensional squared frequency $\omega^2 R/g$. ∇ is the displaced volume per meter.

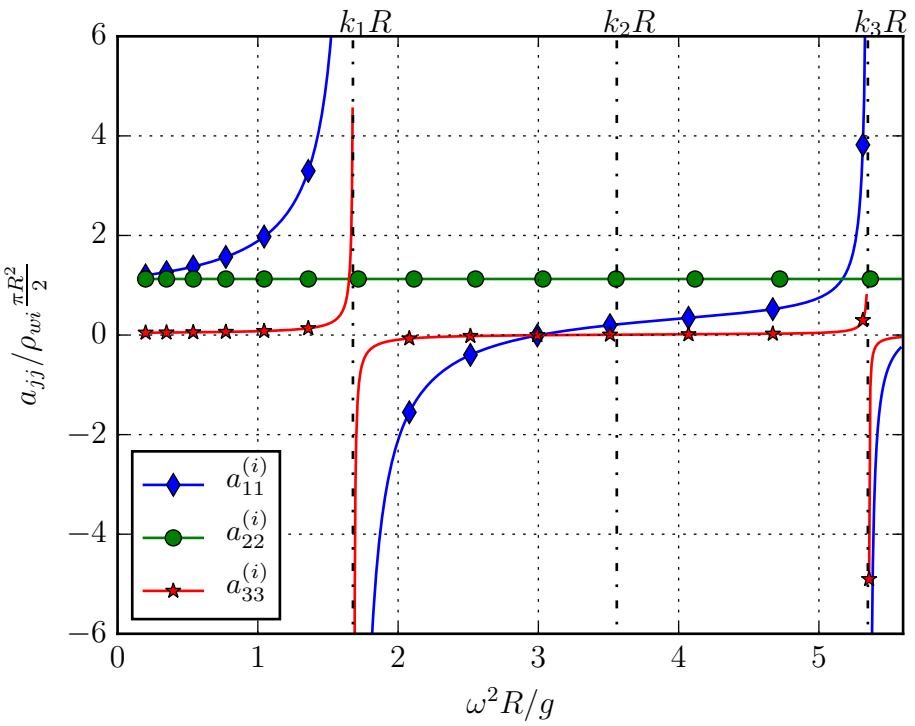

Figure 6.13: Non-dimensional internal added mass for a CFFC for sway, heave and roll versus non-dimensional squared frequency $\omega^2 R/g$. k_1R, k_2R and k_3R are non-dimensional sloshing frequencies for the CFFC.

for a circular tank for given filling ratios are given in (Faltinsen and Timokha, 2009, page 172-173). The calculated filling depth to radius of the constructed circle is $h_f/R_c = 1.74$. For this filling depth to radius the non-dimensional eigenfrequencies of the constructed circular domain is $k_1^c R = 2.7, k_2^c R = 4.9$ and $k_3^c R = 7.3$. The smaller domain is constructed as a rectangle where the whole rectangle is within the domain of the CFFC. The rectangle has width b_t and calculated draft $h_R = 0.64R$. The non-dimensional eigenfrequencies of the constructed rectangular domain Q_R is calculated as

$$k_n^R R = \frac{\pi n R}{b_t} \tanh(\frac{\pi n h_R}{b_t}).$$

The calculation gives $k_1^R R = 1.36, k_2^R R = 3.38$ and $k_3^R R = 5.22$. The non-dimensional eigenfrequencies of the CFFC have been found to be $k_1 R = 1.68, k_2 R = 3.56$ and $k_3 R = 5.35$, these eigenfrequencies are within the calculated bounds. The upper bounds of the on the non-dimensional eigenfrequencies are large, this is because the domain of the constructed circle Q_c is much larger than the domain of the

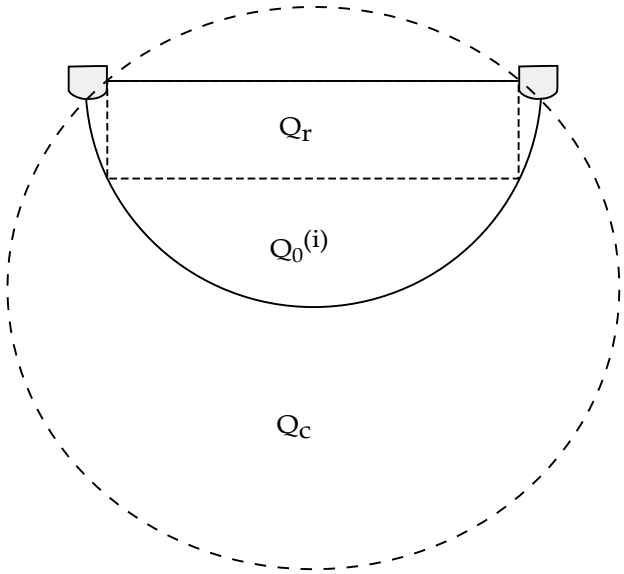

Figure 6.14: Geometrical domains used in the comparison theorem for estimating bounds on the nondimensional eigenfrequency of the CFFC. Q_c is the circular domain, $Q_0^{(i)}$ is the domain of the CFFC and Q_R is the domain of the rectangle.

CFFC $Q_0^{(i)}$. An alternative to using a circle as a domain for the upper bound is to use an ellipse, this have not been further pursued.

Non-dimensional internal added mass for the structural normal modes of the CFFC are plotted in Figure 6.15. We can observe that the even modes will have a sloshing resonance at the second sloshing eigenfrequency, while the odd modes have sloshing resonances at the first and third sloshing frequency. For the CFFC we also observe a resonance at the second sloshing frequency for the first structural mode, which was not present for the hemicircle. For the hemicircle it was possible to derive a simplified expression for the added mass of this mode, showing that it did not have any resonances. However, for the CFFC with floaters the solution is more complex and the vertical velocity can vary along the free surface allowing for resonances.

6.6.3 Rigid body motion response of the CFFC

The linear steady-state motion can be expressed as

$$\xi_j = \xi_{ja} e^{\mathrm{i}\epsilon_j} e^{\mathrm{i}\omega t}, \tag{6.80}$$

where ξ_{ja} is the amplitude of the motion and ϵ_j is the phase of the motion relative to the incoming wave, defined as $\epsilon_j = \arctan 2(\Im(\xi_{ja}e^{\mathrm{i}\epsilon_j}), \Re(\xi_{ja}e^{\mathrm{i}\epsilon_j}))$. Here, $\Re$ is the real part of ξ_j and $\Im$ signifies the imaginary part of $\xi_{ja}e^{\mathrm{i}\epsilon_j}$. Positive ϵ_j means a phase lead relative to the wave elevation at $y = 0$. The ratio ξ_{ja}/ζ_a is here called a transfer function for motion j as in Faltinsen (2005), it is also known as a response

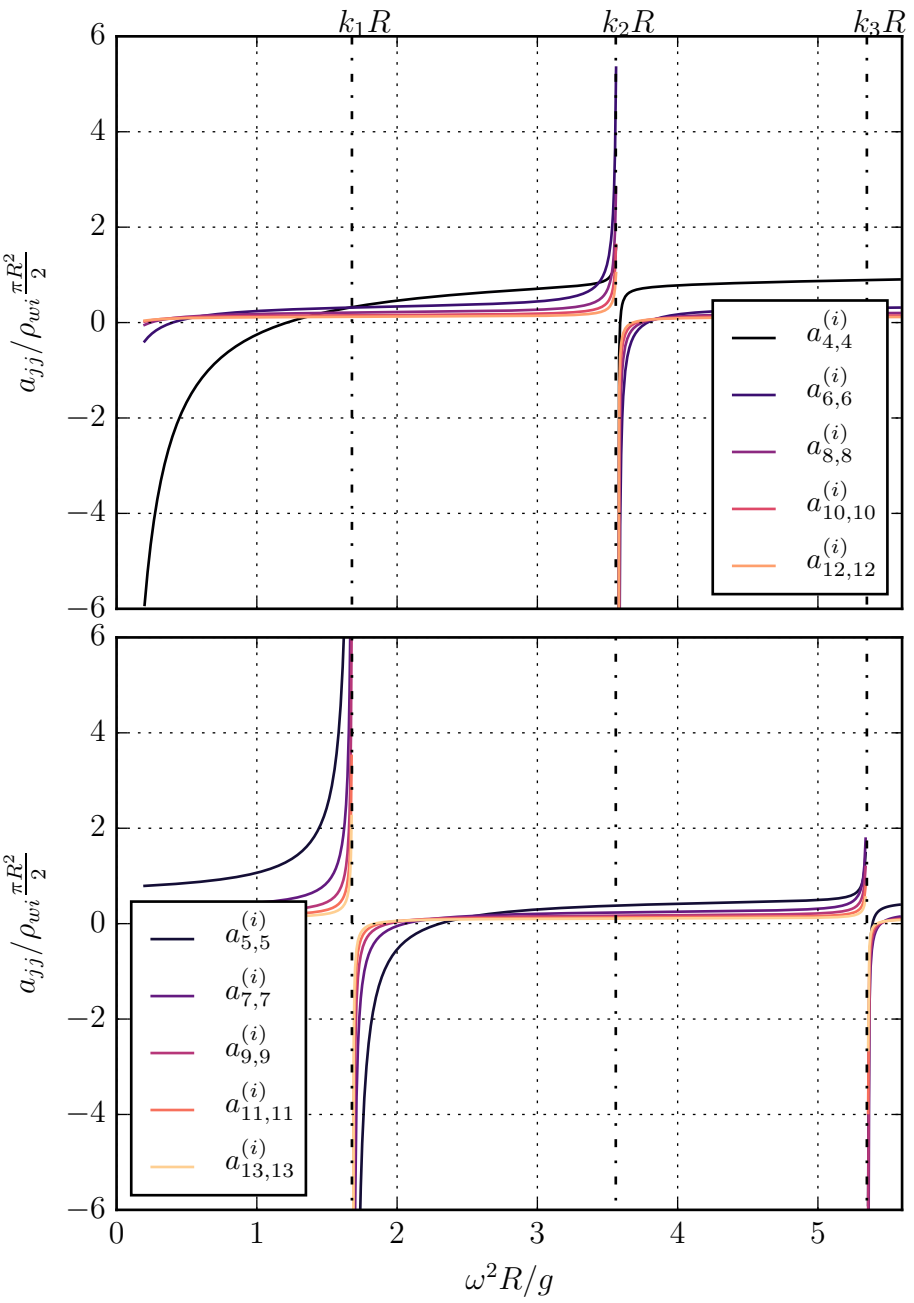

Figure 6.15: Non-dimensional internal added mass for a CFFC, for even(top) and odd (bottom) modes versus non-dimensional squared frequency $\omega^2 R/g$. k_1R, k_2R and k_3R are non-dimensional sloshing frequencies for the CFFC.

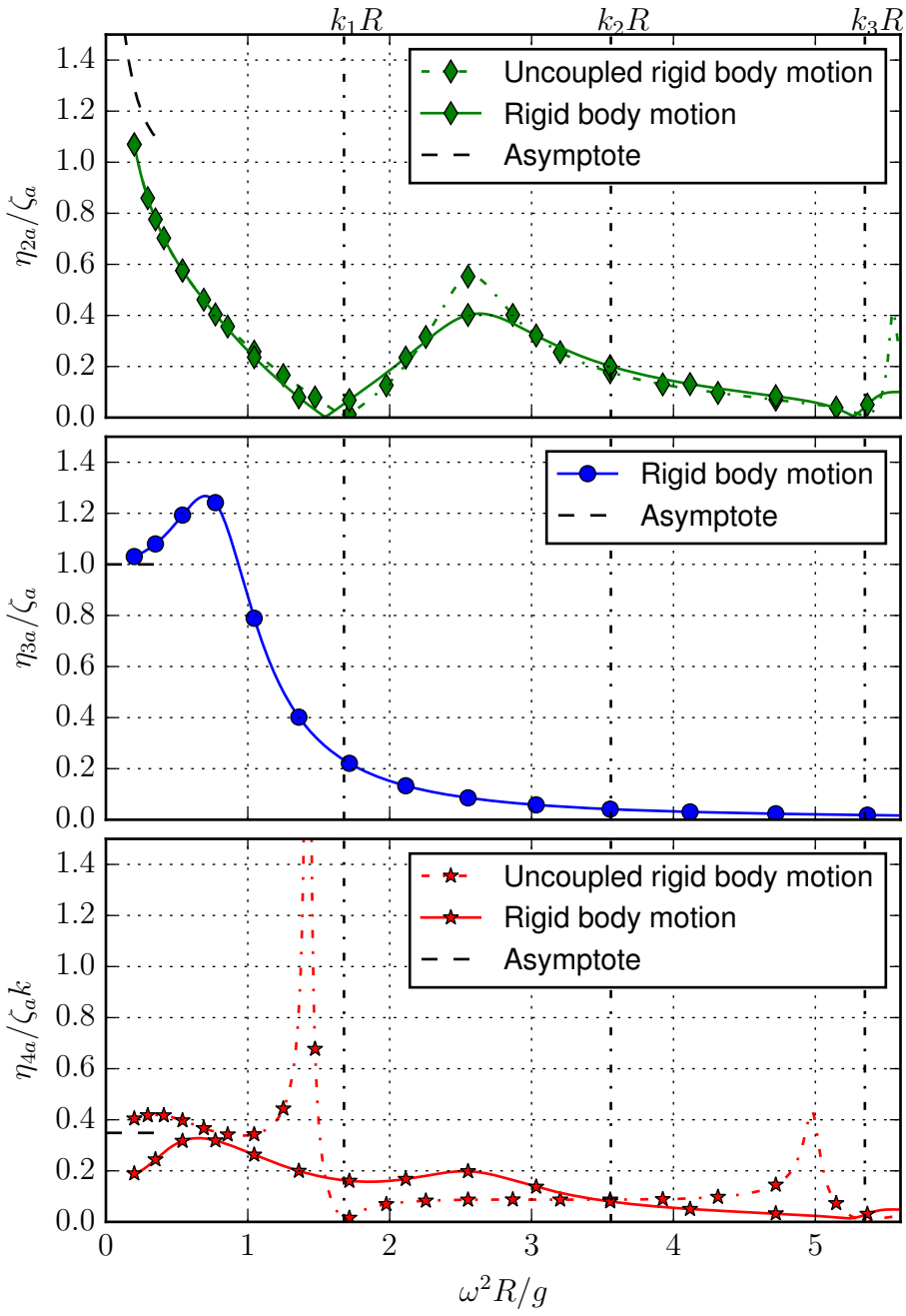

Figure 6.16: Transfer functions of motion of CFFC for sway (top), heave(middle) and roll (bottom), uncoupled and coupled response between the rigid body motions with asymptotes versus non-dimensional squared frequency $\omega^2 R/g$. k_1R, k_2R and k_3R are non-dimensional sloshing frequencies for the CFFC.

amplitude operator, RAO. The transfer function for the coupled and uncoupled rigid body motions in sway, heave and roll of a rigid CFFC are plotted in Figure 6.16. The phases in sway, heave and roll of the coupled rigid body motions of a rigid CFFC are plotted in Figure 6.18.

The asymptote of the uncoupled sway motion when ω goes to zero can be found from

$$-\omega^2 a_{11}\xi_1 = a_{11}a_y = -\omega^2 a_{11}\zeta_a \frac{1}{\tanh kh},$$

where a_y is the wave particle acceleration in y- direction at the free surface at the center of the CFFC, $a_{11} = a_{11}^{(i)} + a_{11}^{(e)}$ at $\omega = 0$ and the mass of the membrane and floaters are neglected compared to the added mass in sway. Then the asymptote of the transfer function should approach $\frac{\xi_{1a}}{\zeta_a} \to \frac{1}{\tanh kh}$. Physically this means that the horizontal CFFC motion approaches the horizontal wave particle motion. The rigid body motion of sway is coupled to the rigid body motion of roll. When ω goes to zero the equation of motion for coupled sway and roll can be given as $-\omega^2 a_{11}\xi_1 - \omega^2 a_{13}\xi_3 = a_{11}a_y$. However, the roll response is so small that $a_{13}(\omega = 0)\xi_3$ can be neglected compared to $a_{11}(\omega = 0)\xi_1$, and the response at the asymptote approaches the response of uncoupled sway. From Figure 6.16 we see that the asymptote of the sway motion appear to approach $\frac{1}{\tanh kh}$ for both the coupled and uncoupled sway motion.

The asymptote of the heave motion when ω goes to zero, can be found by considering the equation of motion of heave when ω goes to zero, which is $c_{22}\xi_2 = f_2$. The excitation force in heave f_2 can be approximated as $f_2 = \rho_w g A_w \zeta_a$. Resulting in that the asymptote of the transfer function for heave $\frac{\xi_{2a}}{\zeta_a} = \frac{f_2}{c_{22}} \to 1$ when ω goes to zero. Physically this means that the vertical motion of the CFFC follows the vertical particle motion in heave. This can be compared to that the structure behaves like a cork floating in water.

The asymptote of the uncoupled roll motion when ω goes to zero can be found from $c_{33}\xi_3 = f_3$. The pressure for long wave length at one time instance can for asymmetric boundary conditions be approximated as $p = \rho_w g k y$, by integrating this pressure the Froude Kriloff force for roll f_3^{FK} at $\omega = 0$ becomes

$$f_3^{FK} = \rho_w g k \zeta_a \int_{S_M^{(e)} + S_{fl}^{(e)}} y(z n_y - y n_z) ds.$$

The asymptote of the wave slope is then for the given geometry and restoring $\frac{\xi_{3a}}{\zeta_a k} = \frac{f_3^{FK}}{c_{33}k} = 0.35$. For roll we could expect that $\frac{\xi_{3a}}{\zeta_a k} = \frac{\eta_{4a}}{\zeta_a k} \to 1$, meaning that the body follows the wave slope. However, for the hemicircle the excitation force and restoring coefficient are zero. For the given case it can therefore not automatically be expected that the structure should follow the wave slope. From Figure 6.16 we see that the uncoupled roll response appear to approach $\frac{\xi_{3a}}{\zeta_a k} = 0.35$ when ω goes to zero. The coupled rigid body response for roll and sway have a significantly different response than uncoupled roll, this is because even for small frequencies sway will have an effect since $\frac{\xi_{1a}}{\zeta_a} \to \frac{1}{\tanh kh}$, and roll is coupled to sway trough added mass terms.

Uncoupled sway and roll have cancellations at the first and third sloshing frequency. This is consistent with previous results as published by Newman (2005) and discussed in Faltinsen and Timokha (2009). Newman (2005) analysed coupled vessel motion and sloshing of a hemispheriod vessel with three internal rectangular tanks containing liquid at zero forward speed. Beam sea, regular waves at deep water were considered. Due to the geometry of this vessel, it did not have any external added mass, damping and excitation moment in roll. For the CFFC in coupled sway and roll, no cancellation of the response appear at the first and third sloshing frequency, instead a cancellation appear at a frequency significantly lower than the sloshing frequencies. Compared to the hemispheriod vessel analysed by Newman (2005), the CFFC have both excitation, added mass and damping in roll. An explanation for this phenomenon can be found by examining the coupled equation of motion for sway and roll (Faltinsen and Timokha, 2009, page 102). The coupled equations of sway and roll can be expressed as:

$$(-\omega^2 a_{11} + \mathrm{i}\omega b_{11})\xi_1 + (-\omega^2 a_{13} + \mathrm{i}\omega b_{13})\xi_3 = f_1, \tag{6.81}$$

$$(-\omega^2 a_{31} + \mathrm{i}\omega b_{31})\xi_1 + (-\omega^2 a_{33} + \mathrm{i}\omega b_{33} + c_{33})\xi_3 = f_3, \tag{6.82}$$

where $a_{jk} = a_{jk}^{(e)}(\omega) + a_{jk}^{(i)}(\omega)$ and the mass of the membrane and the floaters have been neglected compared to the added mass. The solution of ξ_1 and ξ_3 can be found by solving (6.81) combined with (6.82). The solution is:

$$\xi_1 = \frac{f_1(-\omega^2 a_{33} + \mathrm{i}\omega b_{33} + c_{33}) - f_3(-\omega^2 a_{13} + \mathrm{i}\omega b_{13})}{(-\omega^2 a_{11} + \mathrm{i}\omega b_{11})(-\omega^2 a_{33} + \mathrm{i}\omega b_{33} + c_{33}) - (-\omega^2 a_{13} + \mathrm{i}\omega b_{13})^2}, \tag{6.83}$$

$$\xi_3 = \frac{f_3(-\omega^2 a_{11} + \mathrm{i}\omega b_{11}) - f_1(-\omega^2 a_{13} + \mathrm{i}\omega b_{13})}{(-\omega^2 a_{11} + \mathrm{i}\omega b_{11})(-\omega^2 a_{33} + \mathrm{i}\omega b_{33} + c_{33}) - (-\omega^2 a_{13} + \mathrm{i}\omega b_{13})^2}. \tag{6.84}$$

(Faltinsen and Timokha, 2009, page 211) have shown that when the frequency is equal to the eigenfrequency i.e at $\omega = \omega_n$, $a_{33}a_{11} - a_{13}^2 = 0$, meaning that these terms will cancel out. If (6.83) and (6.84) is divided by $\omega^2 a_{11}$ we can find the response at $\omega = \omega_n$. In addition, we use that $\frac{c_{33}}{a_{11}} << 1$, and $\frac{b_{kj}}{a_{11}} << 1$ at $\omega = \omega_n$. Equation (6.83) and (6.84) can then be approximated as:

$$\xi_1 = \frac{f_1 \frac{a_{33}}{a_{11}} - f_3 \frac{a_{13}}{a_{11}}}{i\omega(b_{33} + b_{11}\frac{a_{33}}{a_{11}} - 2b_{13}\frac{a_{13}}{a_{11}}) + c_{33}}, \tag{6.85}$$

$$\xi_3 = \frac{f_3 - f_1 \frac{a_{13}}{a_{11}}}{i\omega(b_{33} + b_{11}\frac{a_{33}}{a_{11}} - 2b_{13}\frac{a_{13}}{a_{11}}) + c_{33}}, \tag{6.86}$$

which gives a non-zero real value at the sloshing frequency for sway (ξ_1) as long as c_{33} is not equal to zero. If on the other hand c_{33} is equal to zero, only a small, marginally larger than zero real response at the sloshing frequency will occur, which was the case for Newman (2005). Related to the cancellations observed for coupled sway and roll at frequencies lower than the sloshing frequency, a cancellation in the response will appear if the numerator is zero, or the denumerator is infinite. For frequencies significantly different from ω_n, the denumerator is finite. The numerator of (6.83) was plotted related to non-dimensional squared frequency

we observed that it was zero at $\frac{\omega^2 R}{g} = 1.53$ and $\frac{\omega^2 R}{g} = 5.26$. Which is consistent with the coupled sway-roll response for sway as plotted in Figure 6.16.

Since the internal heave added mass is constant, the rigid body motion in heave is unaffected by sloshing. Heave has a damped eigenfrequency at the non-dimensional eigenfrequency $\frac{\omega^2 R}{g} = 0.73$. The undamped eigenfrequency can be estimated as:

$$\frac{\omega_{n2}^2 R}{g} = \frac{c_{22} R}{g a_{22}} = 0.79. \tag{6.87}$$

Since both sides of (6.87) are dependent on the frequency, the eigenfrequency have been found by finding the minimum of $|\frac{\omega_{n2}^2 R}{g} - \frac{c_{22} R}{g a_{22}}|$ for the applied frequency resolution, and then visually verifying that this is a resonance frequency. The damped non-dimensional eigenfrequency is lower than the undamped non-dimensional eigenfrequency. This is to be expected since damping is known to reduce the eigenfrequency.

From Figure 6.16, we see that roll have an uncoupled eigenfrequency at the non-dimensional squared frequency $\frac{\omega^2 R}{g} = 1.42$. The uncoupled and undamped non-dimensional eigenfrequency can be estimated as:

$$\frac{\omega_{n3}^2 R}{g} = \frac{c_{33} R}{g a_{33}} = 1.42. \tag{6.88}$$

Since both sides of (6.88) are dependent on the frequency, the eigenfrequency have been found by finding the first minimum of $|\frac{\omega_{n3}^2 R}{g} - \frac{c_{33} R}{g a_{33}}|$ for the applied frequency resolution, and then visually verifying that this is a resonance frequency. The estimated uncoupled frequency with and without damping is approximately equal. This signifies that the damping level is low, which is the reason that the response appear to approach infinity at this frequency. The coupled rigid body roll-sway response do not have any resonance. The undamped eigenfrequency can be found by considering the denominator of (6.84) for zero damping, which is

$$\frac{\omega_{n3*}^2 R}{g} = \frac{c_{33} a_{11} R}{g(a_{33} a_{11} - a_{13} a_{31})}.$$

No eigenfrequencies can be found within the considered non-dimensional frequency squared range. Therefore, no resonances will be observed.

6.6.4 Wave induced response of the CFFC including the effect of membrane deformations

The transfer functions for the rigid body motions in sway, heave and roll of the CFFC with the flexible membrane are plotted in Figure 6.17 and the phase of the motion relative to the incoming wave in Figure 6.18. From these figures we observe a large change in both transfer functions of the rigid body motions in sway, heave and roll and in the phase of the coupled response of the CFFC compared to the response of the rigid CFFC.

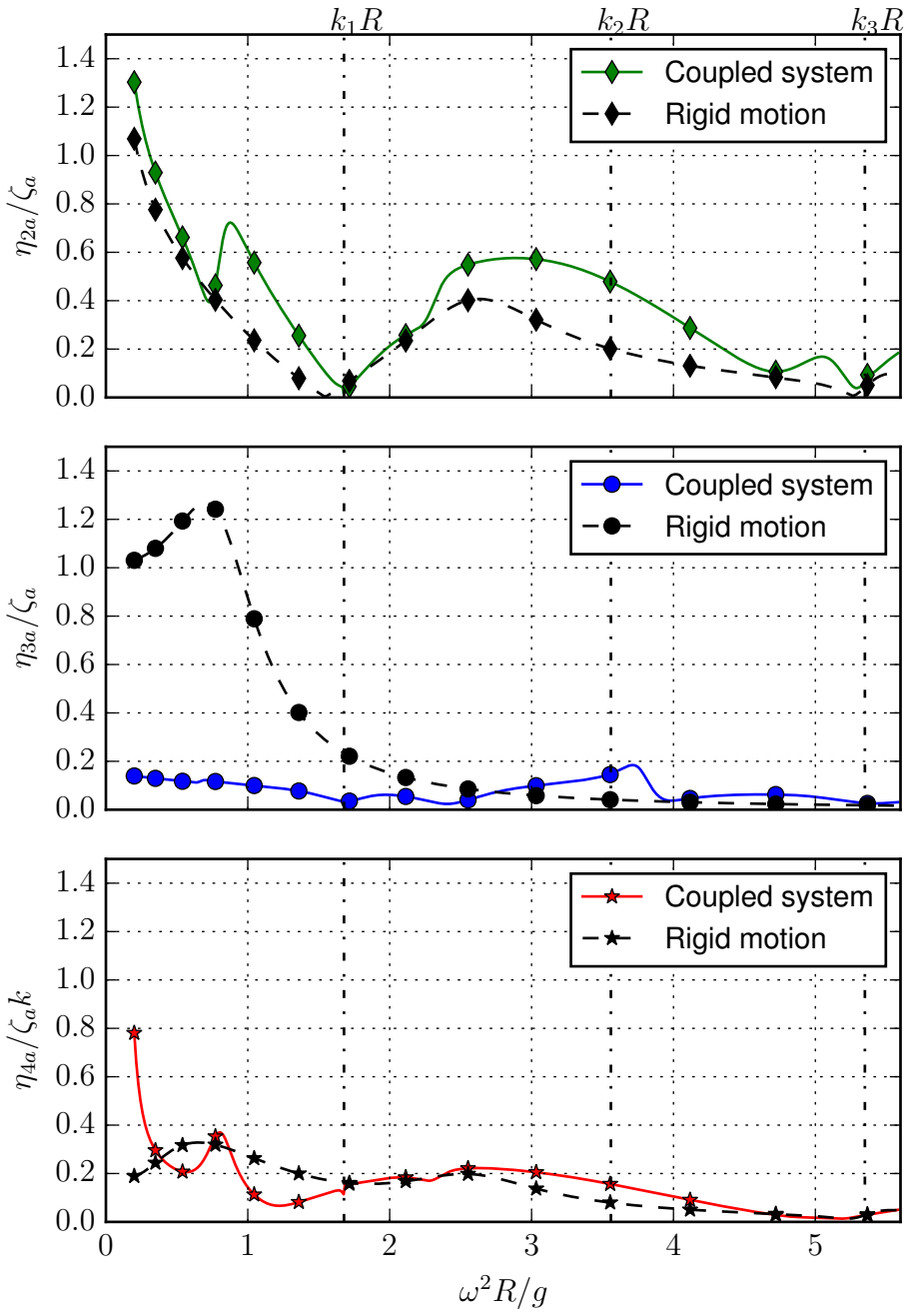

Figure 6.17: Transfer functions of motion of CFFC for sway (top), heave(middle) and roll (bottom), with and without the effect of the membrane versus non-dimensional squared frequency $\omega^2 R/g$. k_1R, k_2R and k_3R are non-dimensional sloshing frequencies for the CFFC.

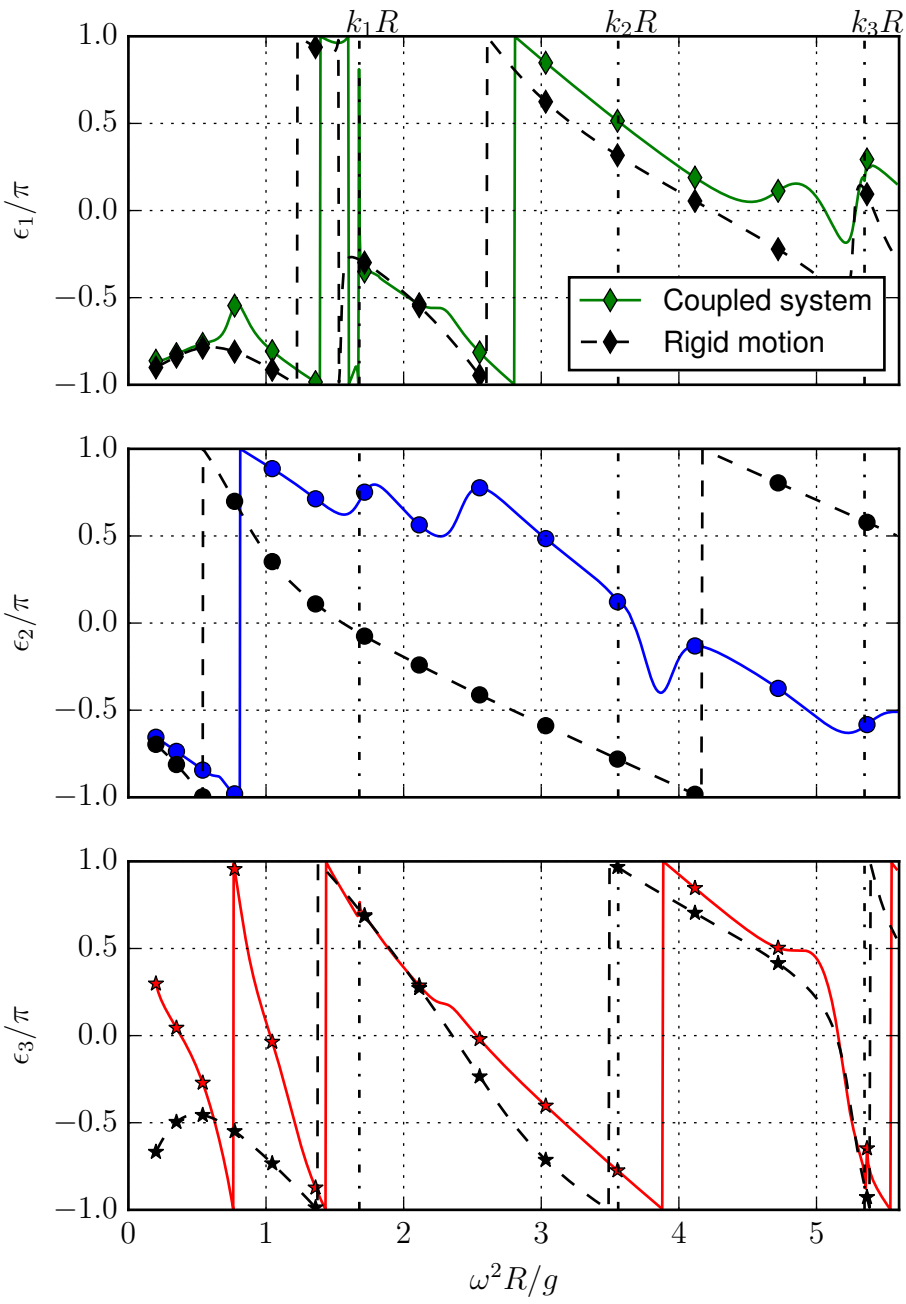

Figure 6.18: Phase of motion of CFFC for sway (top), heave(middle) and roll (bottom), with and without the effect of the membrane versus non-dimensional squared frequency $\omega^2 R/g$. k_1R, k_2R and k_3R are non-dimensional sloshing frequencies for the CFFC.

The transfer functions for the first ten normal and tangential structural modes are plotted in Figure 6.19 together with the phase of the motion relative to the incoming wave in Figure 6.20. From (D.3) and (D.4) we observe that there is a coupling between symmetrical normal structural modes and antisymmetrical tangential structural modes, and between antisymmetrical normal structural modes and symmetrical tangential structural modes. This can also be seen in Figure 6.19. From (6.38), (6.39) and (6.40) we see that the symmetrical normal structural modes are coupled with heave and the antisymmetrical normal structural modes are coupled with sway and roll.

A structural damping on both the normal and tangential structural modes have been added to the structural model of the membrane. The material that most resembles the membrane used in CFFCs, that have available figures on the structural damping is nylon. The damping level of nylon is known to be both humidity, frequency and temperature dependent (Quistwater and Dunell, 1958). Based on the frequency range and the humidity (wet) a structural damping of 2% of the critical damping was chosen for each mode. Coupling effects were neglected. Instead of using a damping related to the critical damping, a Reighley damping model with mass and structural stiffness terms is possible. Both these damping models were tried and the critical damping model appeared to have the best convergence related to the number of tangential structural modes. The critical damping of motion j for $j > 3$ for the normal structural modes have been calculated as $b_j^{str,\xi} = (m_M + a_{f,jj})d_c\sqrt{\frac{c_{M\xi,jj}+c_{T\xi,jj}}{m_M+a_{f,jj}}}$ where d_c is the damping ratio. For the tangential structural modes the critical damping of motion n have been calculated as $b_j^{str,\mu} = m_M d_c\sqrt{\frac{c_{M\mu,jj}+c_{T\mu,jj}}{m_M}}$. For the future the structural damping of the actual used fabric, for a wet condition for the relevant temperatures and frequency range should be found.

From Figure 6.17 we see that for a coupled system the resonance in heave has disappeared and that the asymptote when ω goes to zero of the heave response have significantly decreased. The change in asymptote can be explained if we consider (6.41) when ω goes to zero. Recall that for symmetric structural normal modes additional stiffness exist from the internal added mass, since $\omega^2 a_{kj}^{(i)} = c_{kj}^{(i)}$ is constant. To find the asymptote we must find the generalised excitation force when ω goes to zero. For the symmetric structural modes the wave excitation pressure amplitude can be approximated as constant $\rho_w g\zeta_a$ and the generalized wave excitation force as

$$f_j = \rho_w g\zeta_a \int_{S_M} U_{j-3}(\psi_0)\mathrm{ds} = -2\rho_w g\zeta_a R\frac{\sin^2(\pi(j-3)/2)}{j-3} \text{ for } j > 3. \quad (6.89)$$

If we look at the heave part of (6.41) for $\omega = 0$

$$c_{22}\xi_2 + \frac{Ed}{R}\sum_k k(1+(-1)^k)\mu_k = f_2, \quad (6.90)$$

the decrease in response at $\omega = 0$ can be connected to a reduction in the applied force, for positive μ_k. From Figure 6.19 it appears that μ_j converge to a constant

value for the antisymmetrical tangential structural modes when ω goes to zero. If (6.89) is applied to (6.41) at $\omega = 0$, the asymptote of heave for the coupled case is found to be $\xi_2/\zeta_a = 0.21$. From Figure 6.17 we see that the asymptote of heave appear to converge to this value. An small amplification of the response of heave can be seen around $\omega^2 R/g = 3.71$, close to the second sloshing eigenfrequency, this coincides with the top in the internal sloshing plot at this frequency visible in Figure 6.21. An increase can also be seen at this frequency for the symmetrical normal structural modes in Figure 6.19.

From Figure 6.17 we see that the asymptote of roll deviates from the rigid body case. Again, this can be explained if we consider (6.41) when ω goes to zero. For the antisymmetric structural modes the largest wave excitation amplitude for a given time instance when ω goes to zero can be approximated as constant $\rho_w g \zeta_a k y$. For a half circular geometry, $y = R \sin \psi_0$. The generalized wave excitation force amplitude at $\omega = 0$ can then be approximated as

$$f_j = \rho_w g \zeta_a k \int_{S_M} R \sin \psi_0 U_{j-3}(\psi_0) \mathrm{ds} = -\rho_w g \zeta_a k R^2 \frac{1 + (-1)^{j-3}}{(j-3)^2 - 1} \text{ for } j > 3. \quad (6.91)$$

If we consider the roll part of (6.41) for $\omega = 0$

$$c_{33}\xi_3 - EdR \sum_k k(1 - (-1)^k)\mu_k - \frac{z_e^2 T_0}{R} \sum_{j>3} (j-3)(1 + (-1)^{(j-3)})\xi_j = f_3. \quad (6.92)$$

The increase in roll asymptote can be explained by an increase in the applied force, for positive μ_k and ξ_j for $j > 3$. From Figure 6.19 it appears that both μ_k for symmetric tangential modes and ξ_j for $j > 3$ for asymmetric normal modes converge to a constant value for $\omega = 0$. If (6.91) is applied to (6.41) at $\omega = 0$, the asymptote of roll for the coupled case is found to be $\xi_{3a}/\zeta_a = 6.33$. This is significantly larger than the rigid response.

A narrow cancellation of the motion for the coupled motion at the first and third sloshing frequency can be seen from Figure 6.17 for both the sway and roll response. This is different from the coupled response of the rigid CFFC where it was found that this cancellation did not happen. It appears that when the structure deforms the effect of infinite added mass at the sloshing eigenfrequency becomes too large, and a cancellation appears. A clear shift in phase at the first and third sloshing eigenfrequency response for sway and roll can also be observed from Figure 6.18.

All the phases of the normal structural modes have a response at the sloshing frequencies. The phases of the symmetric modes at the second sloshing eigenfrequency and the phases of the antisymmetric modes at the first and third sloshing eigenfrequency. From Figure 6.19 we see that the asymmetric normal structural modes have a smaller response at the first and third sloshing eigenfrequency, while the symmetric normal structural modes have a smaller response at the second sloshing eigenfrequency. At the sloshing frequencies the generalised internal added mass approaches infinity, and a small response is therefore plausible.

Considering (D.1) and (D.2) it should be expected that the deformation of the membrane goes to zero when T_0 goes to infinity, and thereby that the response

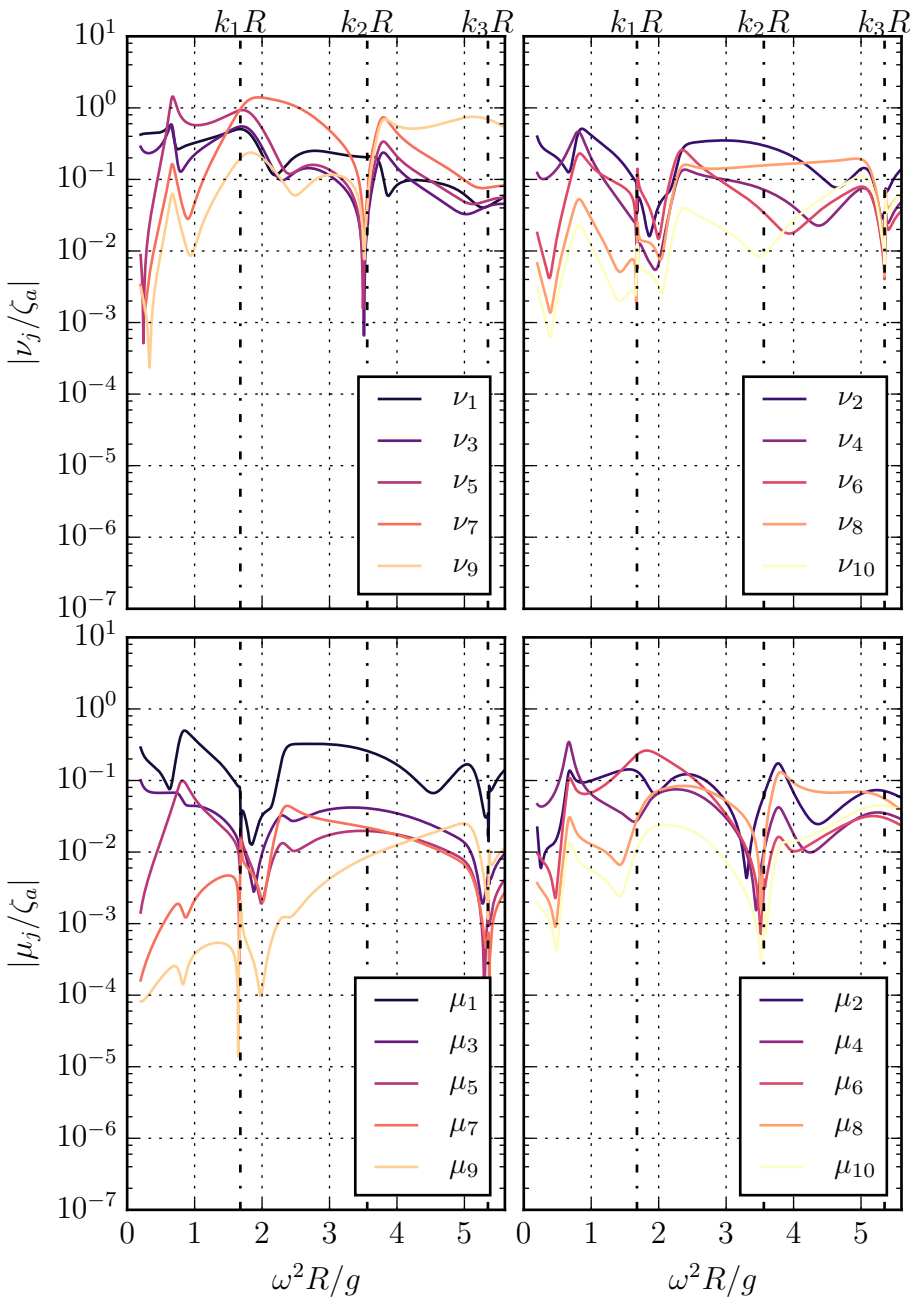

Figure 6.19: Transfer functions of normal (top) and tangential (bottom) structural modes for a CFFC versus non-dimensional squared frequency $\omega^2 R/g$, for the first 10 normal and tangential structural modes. Structural damping 2% of critical damping. k_1R, k_2R and k_3R are non-dimensional sloshing frequencies for the CFFC.

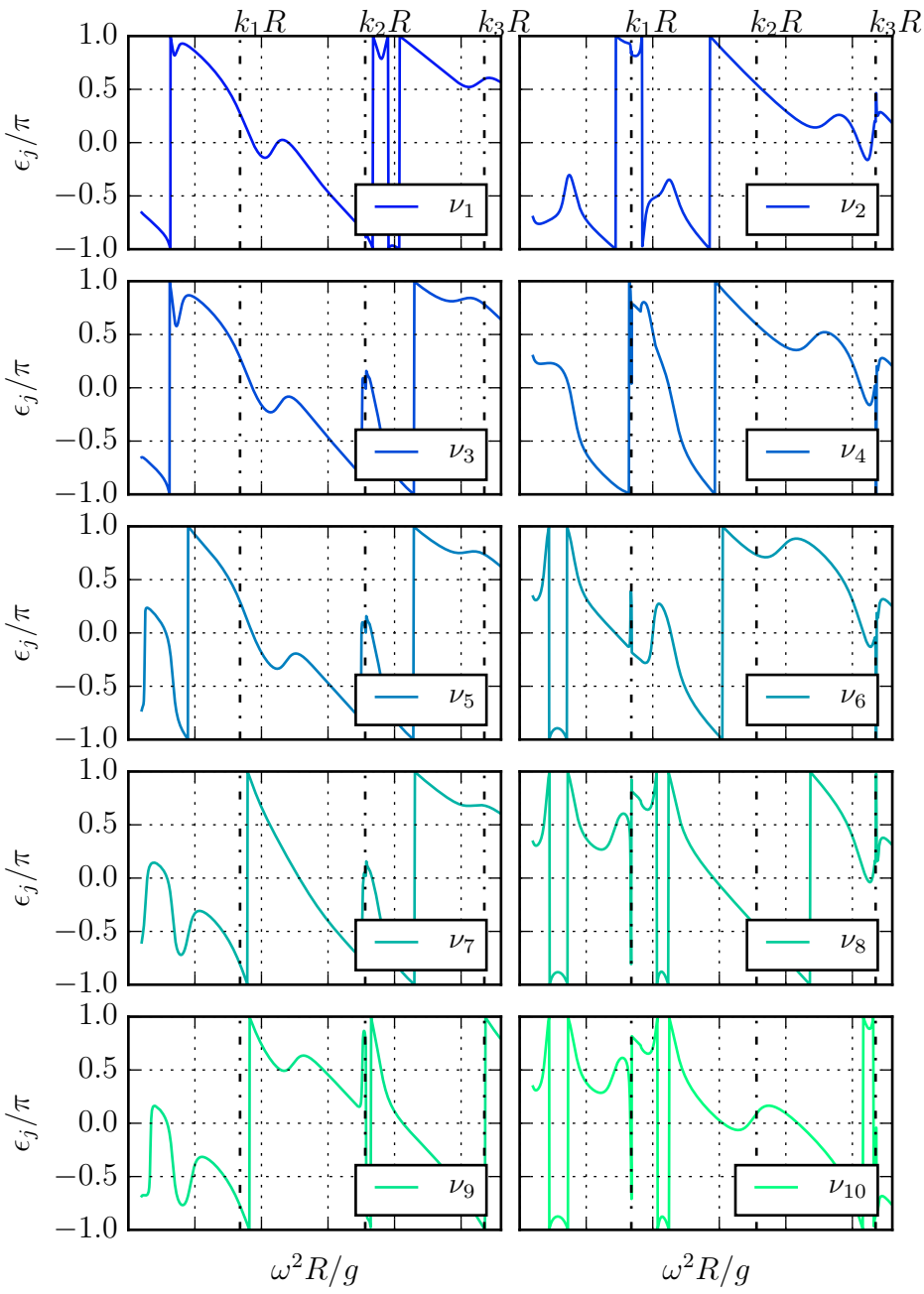

Figure 6.20: Phase of normal structural modes for a CFFC versus non-dimensional squared frequency ω^2R/g. For the first 10 normal modes. Structural damping 2% of critical damping.k_1R, k_2R and k_3R are non-dimensional sloshing frequencies for the CFFC.

of the coupled system goes to the response of the rigid body system. For heave the system will approach the rigid body solution when the tension approaches infinity. For roll and sway, this is not the case. The reason why the response for roll and sway does not approach the rigid response is that the response is dependent on the static tension multiplied with the dynamic angle. When the static tension approaches infinity, bending will not be negligible at the attachment point between the membrane and the floater. This have not been accounted for in the structural response described by (6.41). If bending is accounted for, the dynamic angle will go to zero and the response of the coupled system will also for roll and sway be the response of rigid body. That T_0 goes to infinity is not a physical case since the tension is dependent on the overfilling Δh, and Δh cannot physically go to infinity. However, it is a good check on the asymptotic behaviour of the structural equations.

The structural convergence related to the number of structural modes in normal and tangential direction have been investigated, by looking at the convergence of the tranferfunction of the coupled rigid body motions. It have been found that 30 normal and 250 tangential modes are sufficient. The results are given in Figure H.1 in Appendix G. The number of tangential modes converges slowly, this can mainly be explained by the low level of structural damping. Compared to the normal structural modes that have both wave radiation damping and higher structural damping due to the influence of the added mass on the structure, the damping level of the tangential modes are small. The wave radiation damping decreases for increasing frequency and both the wave radiation damping and added mass decreases with increasing mode number, but even for the highest modes the normal modes have a higher damping. The number of normal structural modes converges faster, this is probably due to the higher level of damping. The maximum number of normal modes that have been run is 30. The normal structural modes give a hydrodynamic pressure load contribution which must be found from the HPC potential flow solver. It is computationally expensive to add a large number of normal structural modes, because the highest structural mode must be sufficiently resolved in the grid, and that requires a finer grid.

6.6.5 Internal wave amplitude

The internal wave amplitude at the right floater and at the center of the CFFC are plotted in Figure 6.21. The internal wave amplitude of the coupled system response at the right floater is comparable to the internal wave amplitude of the rigid CFFC response. For the internal wave amplitude at the right floater the response goes to infinity at the first and third sloshing frequency for the rigid structure. A hypothesis during the work was that the membrane causing wave radiation damping would have less sloshing than a rigid tank, because the membrane deformations would work as a damper on the sloshing. That did not appear to happen. Instead an additional resonance/ amplification by the second sloshing frequency were observed, where there were no pronounced response for the rigid case. The shape of the internal wave at $\omega^2 R/g = 3.71$ is plotted in Figure 6.22. Here it can be seen that the shape of the free surface have a top both by the right floater and at the center of the CFFC.

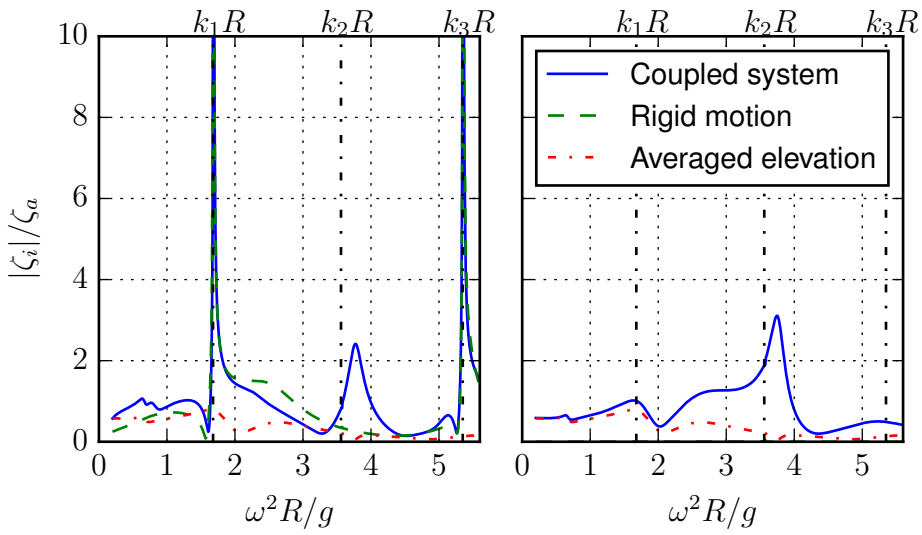

Figure 6.21: Total non-dimensional internal wave amplitude at the right floater (left figure) and at the center (right figure) of the CFFC versus non-dimensional squared frequency $\omega^2 R/g$. k_1R, k_2R and k_3R are non-dimensional sloshing frequencies for the CFFC.

Since no damping is included for the internal potential flow theory analysis, the response will in theory be infinite at the sloshing frequencies. External wave radiation damping does not appear to affect the results at the first and third sloshing eigenfrequency. However, the exact sloshing eigenfrequency to the finest precision have not been found, so it is not possible to determine if the response is infinite or just very large. To predict the correct internal wave amplitude close to the first and third sloshing eigenfrequencies a non-linear analysis for a realistic wave environment for the internal flow will be needed.

The spatially averaged internal wave amplitude is also plotted in Figure 6.21, this is consistent with volume conservation by (6.69), and is the accumulated effect of the structural deformation on the internal free surface. We observe that the spatially averaged internal wave amplitude is significant at several frequencies compared to the incident wave amplitude ζ_a.

6.6.6 Dynamic tension

Within linear structural theory we require that the dynamic tension τ is smaller than the static tension T_0, because we must require that the total tension in the membrane at all times is larger than zero. The dynamic tension is dependent on both the wave height and the wave frequency. To find out if the requirement is fulfilled the static tension must be compared to the stochastic amplitude found from a relevant wave spectrum.

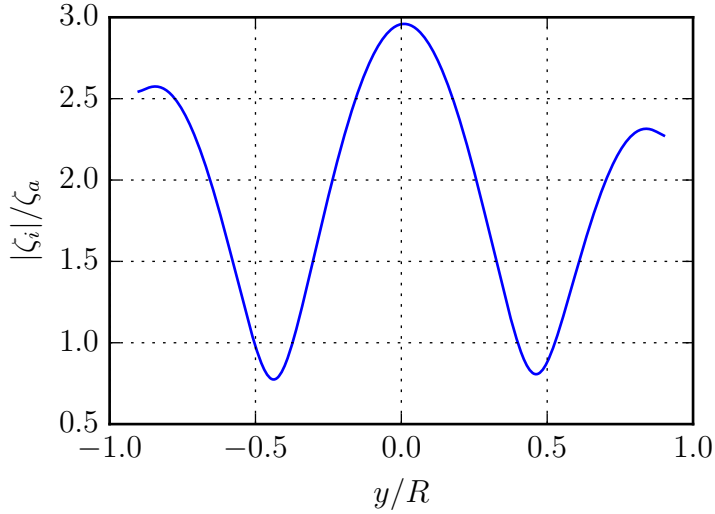

Figure 6.22: Non-dimensional internal wave amplitude along the free surface of the CFFC at non-dimensional squared frequency $\omega^2 R/g = 3.71$.

The results here are based on the full scale values given in Table 6.1 and for a given overfilling and thereby given static tension T_0. For the calculations of the transfer functions of the dynamic tension τ_a/ζ_a, the tension at the connection point between the membrane and the right floater have been used. The dynamic tension varies along the membrane and the tension at the right floater is not the highest tension for all non-dimensional frequencies. However, for a large part of the frequency range it is the largest dynamic tension or close to largest dynamic tension. It was decided to use the tension at a fixed position on the membrane and the tension at the connection point between the membrane and the right floater was then considered the best choice.

The standard deviation of the dynamic tension σ_τ for a given sea state spectrum $S(\omega)$ can be calculated as:

$$\sigma_\tau^2 = \int_0^\infty S(\omega) \left(\frac{\tau_a}{\zeta_a} \right)^2 \mathrm{d}\omega. \tag{6.93}$$

The Norwegian standard for design of aquaculture fish farm in the sea NS9415 requires for calculation of response from irregular sea that the JONSWAP spectrum shall be used with $\gamma = 2.5$ for wind-generated seas, where γ is the spectral peakedness parameter. The JONSWAP spectrum is for limited fetch, and in the standard it is required that a fully developed sea state is assumed. A γ value of 2.5 is lower than for ships and offshore structures where $\gamma = 3.3$.

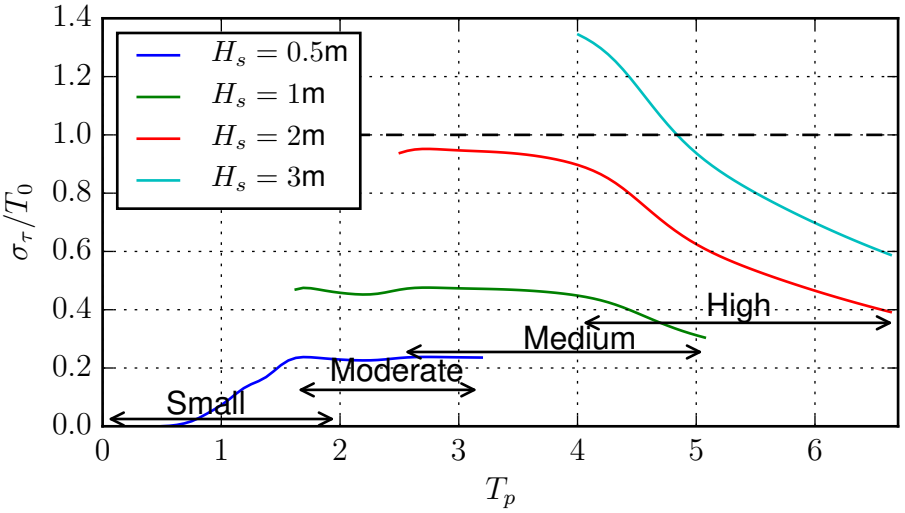

Figure 6.23: Non-dimensional dynamic tension variance σ_τ/T_0 for given exposure versus wave peak period T_p. The small, moderate, medium and high refers the classification related to exposure as given in Table 2.1. The dotted black line is the limit of linear structural theory, related to dynamic tension.

The JONSWAP spectrum can be given as:

$$S(\omega) = \frac{\alpha_p g^2}{\omega^5} \exp\left(\frac{-20\pi^4}{T_p^4 \omega^4}\right) \gamma^{Y_p}, \tag{6.94}$$

where α_p is the Philips constant given as:

$$\alpha_p = \frac{5.061 H_s^2}{T_p^4}(1 - 0.287 \ln \gamma),$$

and Y_p is given as:

$$Y_p = \exp\left(-\frac{1}{2}\left(\frac{\frac{\omega T_p}{2\pi} - 1}{\sigma_p}\right)^2\right),$$

where σ_p is the spectral width parameter given as

$$\sigma_p = \begin{cases} 0.07 \text{ for } \omega \leq \frac{2\pi}{T_p} \\ 0.09 \text{ for } \omega > \frac{2\pi}{T_p}. \end{cases}$$

The non-dimensional dynamic tension variance σ_τ/T_0 versus wave peak period T_p for given significant wave heights are plotted in Figure 6.23. The peak periods

T_p and significant wave heights are related to the classification of exposure as given in Table 2.1. From Figure 6.23 we see that σ_τ exceeds T_0 for $H_s = 3$m for high exposure. If we assume a Rayleigh distribution, the most probable largest value for τ is approximately $4\sigma_\tau$ in a sea state of limited duration. $4\sigma_\tau$ exceeds T_0 for all H_s except $H_s = 0.5$m. That the most probable largest value of τ is exceeded for H_s larger than 0.5 m at small exposure is critical, and indicates that other structural models should be used. For floating liquid filled storage bags, the linear theory is only valid for small incident wave amplitudes (Zhao and Aarsnes, 1998), due to the requirement of positive total tension. The analysed CFFC is a small cage if the radius R of the cage is compared to industry sizes of aquaculture net cages used by the industry today. If the dynamic tension is within the limit of linear structural theory should be investigated for other relevant dimensions and static tension levels, for relevant exposures and sea state conditions. For dynamic tension in the same order as the static tension, zero tension could be expected. This would introduce snap loads in the material and would contribute to fatigue loads. Fatigue loads are repeated loads that limits the life expectancy of a material. Fatigue loads will however not be covered within this thesis.

6.6.7 Model scale challenges

Model scale experiments are often used to validate numerical models and to gain knowledge of the physics of a new system. For the model to represent the full scale structure in waves we require that the frequency dependent Froude number $F_n = \omega\sqrt{\frac{R}{g}}$ is equal in model and full scale. From (D.1) and (D.2) we find the non-dimensional structural equation for the membrane as:

$$\frac{-\omega^2 m_M}{\rho_w g R} v - \frac{T_0}{\rho_w g R^3}\left(\frac{\partial^2 v}{\partial \psi^2} + \frac{\partial u}{\partial \psi}\right) - \frac{Ed}{\rho_w g R^3}\left(\frac{\partial u}{\partial \psi} - v\right) = -\frac{\Delta \hat{p}}{\rho_w g R}, \tag{6.95}$$

$$\frac{-\omega^2 m_M}{\rho_w g R} u - \frac{Ed}{\rho_w g R^3}\left(\frac{\partial^2 u}{\partial \psi^2} - \frac{\partial v}{\partial \psi}\right) + \frac{T_0}{\rho_w g R^3}\left(\frac{\partial v}{\partial \psi} + u\right) = 0. \tag{6.96}$$

From the given equations we observe that for the elasticity, the Froude scale leads to a pure geometric scale. This means that the elasticity modulus E should scale as $\frac{E}{\rho_w g R}$ and the thickness of the membrane as $\frac{d}{R}$, combined this becomes $\frac{Ed}{\rho_w g R^2}$. Since the gravity g is constant and the water density ρ_w is close to constant, the scaling ratio puts combined requirements on the elasticity modulus and the thickness of the material used in model scale. In the real world this material does not exist for normal model scales. If we use a model scale of $1:12.5$ and use the model scale values as given in Table 5.1 we end up using a material that is approximately ten times too stiff for the scale. And, if a larger scale is used the deviation between the sought material stiffness and the used material stiffness becomes even larger.

The coupled rigid body response of the CFFC both for a stiffness used in full scale and the stiffness used in model scale are plotted in Figure 6.24. The response of the rigid CFFC in model and full scale is equal, but the coupled system response included the flexible modes deviate to a great extent. This raises severe questions of the use of the results from model experiments. The model scale results should

not be scaled and used directly as the "truth" for full scale cases. However, this does not mean that model scale experiments are useless for validation. The results should be used to validate a numerical model using the model scale stiffness and then the numerical model with the full scale stiffness can be used to predict the full scale values.

6.7 Conclusions

In this chapter the linear theory of a 2D closed flexible fish cage in waves was developed and analysed with the aim to find the response of the CFFC in waves. The numerical code related to the pressure loads have been validated with results for a hemicircle for both the external and internal pressure loads. The results from a 2D case study with relevant full scale dimensions, considering a half circularly shaped CFFC with floaters were presented. Investigations only consider the 2D case. However, the findings can be considered a starting point for analysing 3D structures.

We observe a large change in response of the rigid body motions in sway, heave and roll of the coupled response of the CFFC compared to the response of the rigid CFFC. The resonance in heave for the rigid CFFC has disappeared and the asymptote when the forcing frequency ω goes to zero of the heave response have significantly decreased. For the sway and roll response a narrow cancellation of the motion for the coupled motion at the first and third sloshing frequency can be observed. This is different from the coupled response of the rigid CFFC where it was found that this cancellation did not happen. For a rigid CFFC, uncoupled sway and roll have cancellation at the first and third sloshing frequency. For the CFFC in coupled sway and roll, no cancellation of the response appears at the first and third sloshing frequency.

A structural damping of both the normal and tangential structural modes have been added to the structural model of the membrane. The damping for nylon have been used, but this is uncertain. For the future the structural damping of the actual used fabric, for a wet condition for the relevant temperatures and frequency range should be found.

The sloshing wave amplitudes of the coupled system are comparable to the sloshing wave amplitudes of the rigid system, for most non-dimensional frequencies and the maximum values occurs typically by the floater. However, a non-negligible sloshing wave amplitude response can also be seen at the center of the CFFC for the coupled analysis at frequencies slightly higher than the second sloshing frequency, which is not present for the rigid body motion. To predict the correct sloshing wave amplitude close to the first and third sloshing eigenfrequencies a non-linear analysis for the internal flow is needed.

Within linear structural theory we require that the dynamic tension τ is smaller that the static tension T_0. To find out if the requirement was fulfilled the static tension was compared to the stochastic amplitude found from a JONSWAP spectrum for relevant exposure levels. The non-dimensional dynamic tension variance σ_τ/T_0 were calculated. The most probable largest value of τ is exceeded for H_s larger than 0.5 m at small exposure. This is critical and indicates trouble and that other

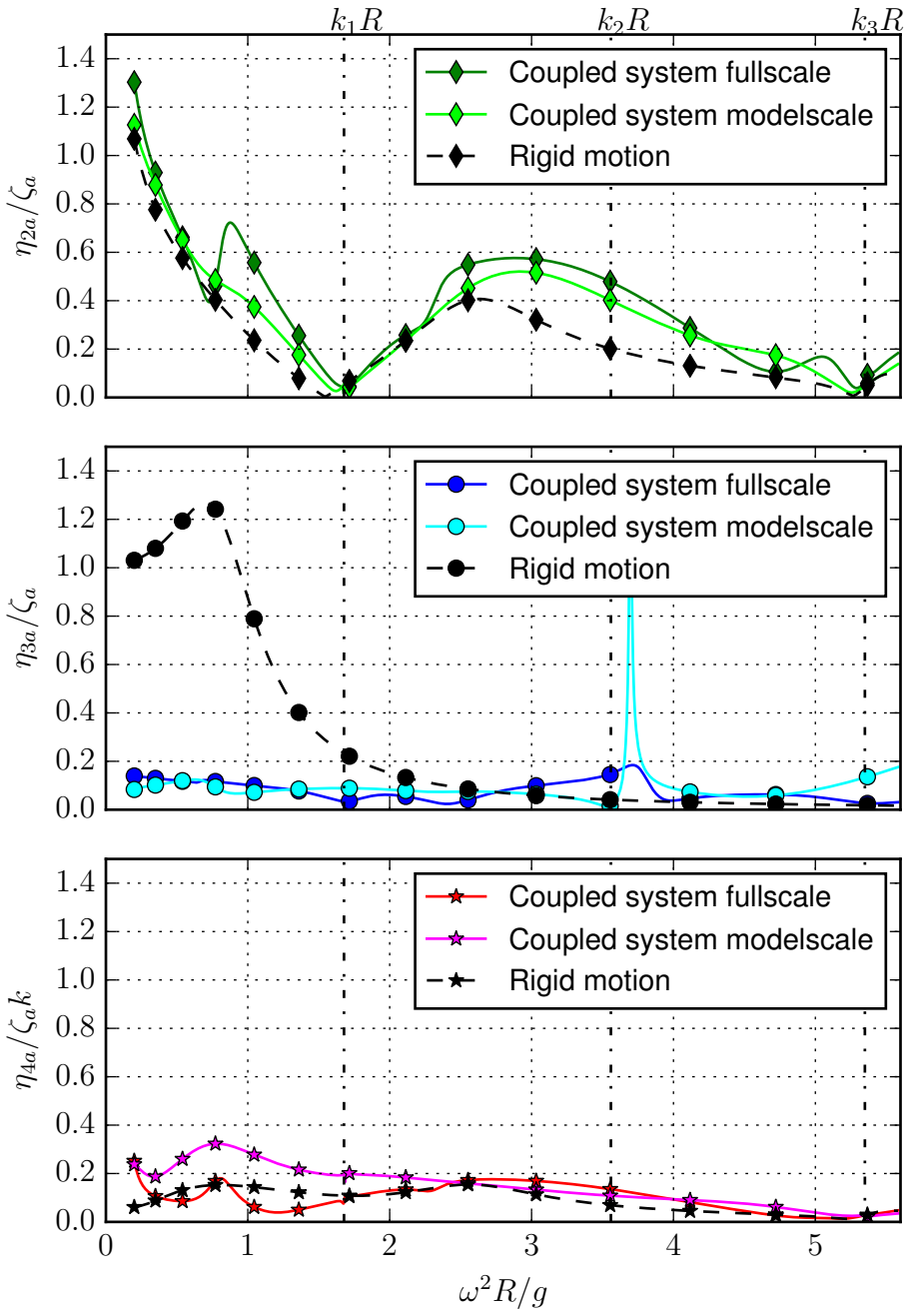

Figure 6.24: Transfer functions of motion of CFFC for sway (top), heave(middle) and roll (bottom), with and without the effect of the membrane versus nondimensional frequency $\omega^2 R/g$. For an elasticity modulus used in model experiments and for an elasticity modulus used in full scale. k_1R, k_2R and k_3R are non-dimensional sloshing frequencies for the CFFC.

structural models should be used. The presented results are for a given structural dimension and a given static tension. Other relevant dimensions and static tension levels, for relevant exposures and sea state conditions should also be investigated. For dynamic tension in the same order as the static tension zero tension could be expected, this would introduce snap loads in the material and would contribute to fatigue loads.

The coupled rigid body response of the CFFC both for a stiffness used in full scale and the stiffness used in model scale were compared. The response of the rigid CFFC in model and full scale is equal, but the coupled system response including the flexible modes deviate to a great extent. This raises severe questions of the use of the results from model experiments.

Chapter 7

Conclusions and further work

In this thesis, detailed conclusions are given after the chapters where the research results are presented. Here, broader conclusions and suggestions for further work are presented.

7.1 Conclusions

The research methodology in this work combined experimental, theoretical and numerical studies. As an answer to the research challenges we have acquired basic understanding of the physics of the closed flexible fish cages (CFFCs), also denoted as bags, through observations and response measurements in model experiments and by studying the effect of varying filling level on the drag forces acting on the CFFC in ambient current. We have develop mathematical models in order to describe the physics of a closed membrane structure with a free surface and internal water motions under hydrostatic pressure and in waves.

Model experiments of scaled models of the closed flexible fish cage (CFFC) in current for different filling levels have been conducted in multiple rounds to build knowledge of the system. Model experiments are often used in model validation, where a mathematical model of the physics of the system already exists, and it needs to be asserted that this model represents the "real world." We have used model experiments to develop a qualitative and quantitative understanding of the physics of the system through observations and response measurements.

In current, the response of the CFFC was found to be highly filling-level dependent. The initial hypothesis in the project was that by reducing the filling level in the bag, the response of the CFFC would be similar to a conventional net based fish cage. We initially assumed that the bag would in a favourable manner adjust its shape to the current, and thereby reducing the total drag forces on the bag. We therefore aimed at controlling the response of the cage by regulating the filling level. However, early experiments made it clear that this hypothesis was partly wrong. Contrary to our hypothesis we found the drag forces on the bag increased when the filling level was reduced (Strand et al., 2013; Lader et al., 2014). This result lead to a shift in focus to an increased need for the development of fundamental knowledge and understandings of the physics in terms of mathematical models. To

better predict the forces and deformations on the bag, mathematical models taking into account the dependency between force and deformation should be developed.

From the experiments it was observed that the problem of a CFFC in current can be characterised by a complex interaction between the membrane, the water masses within the CFFC and the outside water flow. To reduce the complexity of the problem, it was decided to continue the work by modelling the system in 2D and to capture some of the main deformation patterns and loads by the reduced 2D model. Due to considerations related to linearity of models, it was decided to focus on conditions where the bag was full, or overfilled. In addition, it was chosen to shift the focus in modelling to waves, allowing for the use of potential flow theory.

To develop theory and understanding of the membrane structure, and the coupling between structural response and internal water motions, a 2D rectangular sloshing tank with a fabric membrane side wall subject to forced sway motion was studied. Both an analytical and a numerical solution, to the problem were developed. The eigenfrequencies of the system with a flexible membrane left wall relied heavily on both the tension and the 2D membrane length. For low tensions, more than one eigenfrequency may exist between two neighbouring sloshing frequencies for the rigid tank. The gained knowledge of the studied problem and a validated numerical code were then further developed in order to analyse the response of a semi-circular CFFC in waves.

A linear mathematical model of a 2D CFFC in waves was developed. A mathematical model for the static equilibrium geometry and tension for a membrane in calm water, with a hydrostatic pressure difference, was developed, and then used in the analysis of the response of a semi-circular CFFC in waves. The wave response of the rigid body motions in sway, heave and roll of a CFFC were found to be significantly different from the response of a rigid CFFC. Very large ratios between free-surface elevation amplitudes and incident wave amplitude are predicted inside the tank at the first and third natural sloshing frequencies. It implies that nonlinear free surface effects must be accounted for inside the tank in realistic sea conditions, as well known from other marine sloshing applications (Faltinsen and Timokha, 2009). Within linear structural theory we required that the dynamic tension was smaller than the static tension. For the analysed geometry, for significant wave heights larger than 0.5 meter, the most probable largest dynamic tension was larger than the static tension. For negative total tensions the structural model is not valid. Therefore, a higher order structural model should be used. The effect of scaling of elasticity on the rigid body motion was also investigated. To scale the results correctly it requires that the modulus of elasticity of the membrane material should scale as the diameter, this is unfortunately not straight forward. The response of the CFFC using an elasticity available in model scale have been compared to the response of the CFFC using the elasticity for full scale. These responses where found to deviate to a large extent. This raises severe questions of the direct use of results from model scale experiments for the CFFC.

7.2 Further work

The presented work can be considered as a starting point in the modelling of sea loads on CFFCs. However, significant work in several scientific areas are left for further work.

- 2D structures do not exist in the real world. To develop knowledge that can be directly used on the existing full scale systems, the 2D models must be expanded to 3D. The 3D model should be verified against full scale tests, or model experiments considering the results related to scaling of elasticity.
- A requirement to use linear structural theory is that the dynamic tension is smaller than the static tension. From Section 6.6.6 we observed that this was not the case for significant wave heights larger than 0.5 m for the analysed case. Here, a non-linear dynamic structural analysis should be conducted to find the response in design sea states. To conduct a non-linear analysis is not trivial. Then, the structural deformations and the internal and external pressure must be solved simultaneously in the time domain. Furthermore, it must be stressed that non-linear sloshing must be considered to find the correct sloshing amplitude close to the sloshing eigenfrequencies.
- "Large volume structures" cause far field waves, which again result in second order mean and slowly varying lateral forces and yaw moments, that matters in the design of mooring systems for floating offshore structures. Since a CFFC also causes non-negligible far-field waves, mean and slowly varying wave loads should also be investigated in the design of their mooring system. Furthermore, current-wave interaction matters in this context. The mean drift forces with current effects must therefore be considered and is very different from a net cage. A second order external fluid pressure analysis should therefore be conducted to investigate if the mooring systems used for conventional aquaculture net cages are sufficient.
- Negative total tension are connected to snap loads in the fabric and to fatigue damage. The fatigue damage limits the life time of a material and should be investigated to assert that the life time of the membrane is not exceeded.
- The CFFC have an internal circulation and flow to assert adequate water quality for the fish with internal circulation velocities in the range 0.07-0.28 m/s (Klebert et al., 2018). This water circulation will also introduce pressure loads on the fabric structure and will most probably alter the internal pressure forces found from the potential flow theory. However, the circulation pressure cannot be found within potential flow theory. Therefore, the full Navier Stokes equations must be solved. This is not trivial when the cage boundary in the simulations is a deformable membrane.
- We still believe that with sufficient system understanding, control strategies should be applied to optimise the behaviour of the CFFC in the sea, as illustrated in Figure 7.1. Then, it will be vital to formulate control objectives, and propose control strategies to meet the objectives.

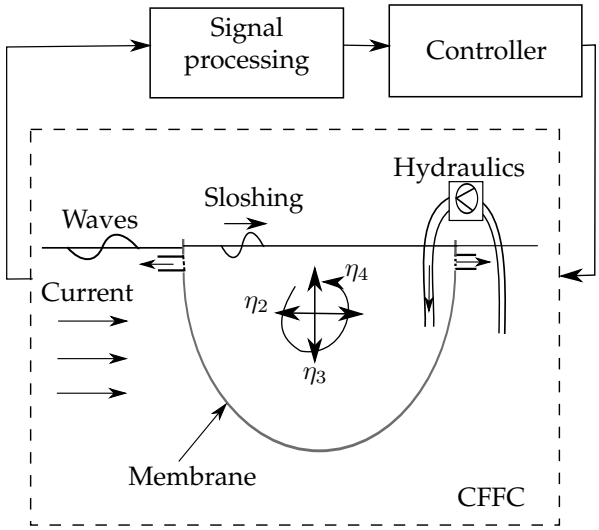

Figure 7.1: Future work including control of the system.

References

C. Aadland. Se alt de gjør for å få lukket fisken i sjøen inne. [look at all they do to close the fish cage.], 2015. URL https://sysla.no/fisk/se-alt-de-gjor-for-a-fa-lukket-fisken-i-sjoen-inne. [Online; accessed 22-August-2017].

Akvafuture. Akva future: Om akvadesign systems. [about akvadesign systems], 2017. URL http://www.akvafuture.com. [Online; accessed 23-August-2017].

Aqualine. Aqualine:cages, 2017. URL http://aqualine.no/en/products/cages. [Online; accessed 15-August-2017].

K. J. Bai and R.W. Yeung. Numerical solutions to free-surface flow problems. In *10th Symposium on Naval Hydrodynamics: Hydrodynamics for Safety, Fundamental Hydrodynamics. Cambridge, Mass., June 24-28, 1974*. U.S. Government Printing Office, 1974.

H. F. Bauer. Hydroelastic vibrations in a rectangular container. *International Journal of Solids and Structures*, 17(7):639 – 52, 1981.

H. F. Bauer and W. Eidel. Hydroelastic vibrations in a two-dimensional rectangular container filled with frictionless liquid and a partly elastically covered free surface. *Journal of Fluids and Structures*, 19(2):209 – 220, 2004.

J. Billingham and A. King. *Wave Motion (Cambridge texts in applied mathematics)*. Cambridge: Cambridge Unviersity Press., 2009.

R. D. Blevins. *Applied Fluid Dynamics Handbook*. Van Nostrand, New York, 1984.

A. Bliek. *Dynamic Analysis of Single Span Cables*. Massachusetts Institute of Technology, Trondheim, 1984.

Botngaard Systems. Botngaard systems: Lukket ventemerd og lukket postsmolt/matfisk. [closed waiting cage and cage for postsmolt production], 2017. URL http://botngaardsystem.no/lukket-ventemerd/. [Online; accessed 23-August-2017].

X. J. Chai, J. M. Genevaux, and J. P. Brancher. Fluid-solid interaction in a rectangular container. *European journal of mechanics. B, Fluids*, 15(6):865–883, 1996.

C. Crawford and C. MacLeod. Predicting and assessing the environmental impact of aquaculture. In *New Technologies in Aquaculture*, pages 679–706. CRC, 2009.

O. M. Faltinsen. *Sea Loads on Ships and Offshore Structures*. Cambridge University Press, 1990.

O. M. Faltinsen. *Hydrodynamics of High-speed Marine Vehicles*. Cambridge University Press, Cambridge, 2005.

O. M. Faltinsen and A. N. Timokha. *Sloshing*. Cambridge, 2009.

P. Gullestad, S. Bjørgo, I. Eithun, A. Ervik, R. Gudding, H. Hansen, R. Johansenand A. B. Osland, M. Rødseth, I. O. Røsvik, H. T. Sandersen, and H. Skarra. Effektiv og bærekraftig arealbruk i havbruksnæringen - areal til begjær. [Efficient and sustainable area use in the aquaculture industry-area for desire.]. Technical report, Rapport fra et ekspertutvalg oppnevnt av fiskeri- og kystdepartementet, 2011.

F. W. Hanssen, M. Greco, and Y. Shao. The harmonic polynomial cell method for moving bodies immersed in a Cartesian background grid. In *ASME. International Conference on Offshore Mechanics and Arctic Engineering, Volume 11: Prof. Robert F. Beck Honoring Symposium on Marine Hydrodynamics*, 2015.

W.R. Hawthorne. The early development of the Dracone flexible barge. *Proceedings of the Institution of Mechanical Engineers 1847-1982*, 1961.

W. A. Hægermark. Mer kontroll i lukkede oppdrettsanlegg. [more control in closed aquaculture systems .], 2013. URL `http://forskning.no/fiskehelse-oppdrett/2013/08/mer-kontroll-i-lukkede-oppdrettsanlegg`. [Online; accessed 22-August-2017].

S. Hoerner. *Fluid-Dynamic Drag*. Midland Park, NJ, 1958.

R. A. Ibrahim. *Liquid Sloshing Dynamics: Theory and Applications*. Cambridge: Cambridge UP, 2005.

M. H. Irvine. *Cable Structures*. Cambridge, Mass. : The MIT Press, 1st edition, 1981.

T. W. Johannessen. Final reportsummary - closedfishcage (Development of an innovative, cost-effective environmetally friendly closed cage for sea-based fish farming), 2013. URL `http://cordis.europa.eu/result/rcn/58197_en.html`. [Online; accessed 23-August-2017].

H. Johari and K. J. Desabrais. Vortex shedding in the near wake of a parachute canopy. *Journal of Fluid Mechanics*, 536:185 – 207, 2005.

P. Klebert, Z. Volent, and T Rosten. Measurement and simulation of the three-dimensional flow pattern and particle removal efficiencies in a large floating closed sea cage with multiple inlets and drains. *Aquacultural Engineering*, 80 (Supplement C):11 – 21, 2018.

E. Kreyszig, H. Kreyszig, and E.J. Norminton. *Advanced Engineering Mathematics*. Hoboken, N.J. : Wiley, 2006.

D. Kristiansen, P. Lader, Ø. Jensen, and D. Fredriksson. Experimental study of an aquaculture net cage in waves and current. *China Ocean Engineering*, 29(3): 325–340, Jun 2015.

T. Kristiansen and O. M. Faltinsen. Modelling of current loads on aquaculture net cages. *Journal of Fluids and Structures*, 34(0):218 – 235, 2012.

T. Kristiansen and O. M. Faltinsen. Experimental and numerical study of an aquaculture net cage with floater in waves and current. *Journal of Fluids and Structures*, 54:1–26, 2015.

P. Lader, D. W. Fredriksson, Z. Volent, J. DeCew, T. Rosten, and I. M. Strand. Drag forces on, and deformation of, closed flexible bags. In *Proceedings of 33rd International Conference on Ocean, Offshore and Arctic Engineering. June 8-13, 2014, San Francisco, USA*, 2014.

P. Lader, D. W. Fredriksson, Z. Volent, J. DeCew, T. Rosten, and I. M. Strand. Drag forces on, and deformation of, closed flexible bags. *Journal of Offshore Mechanics and Arctic Engineering*, 137(August):041202, 2015.

P. Lader, D. W. Fredriksson, Z. Volent, J. DeCew, T. Rosten, and I. M. Strand. Wave Response of Closed Flexible Bags. In *ASME 2016 35th International Conference on Ocean, Offshore and Arctic Engineering*, volume 6: Ocean Space Utilization; Ocean Renewable Energy, 2016.

P. Lader, D. W. Fredriksson, Z. Volent, J. DeCew, T. Rosten, and I. M. Strand. Wave response of closed flexible bags. *Journal of Offshore Mechanics and Arctic Engineering*, 139(5), 2017.

P. F. Lader and B. Enerhaug. Experimental investigation of forces and geometry of a net cage in uniform flow. *Oceanic Engineering, IEEE Journal of*, 30(1), jan 2005.

P. F. Lader and A. Fredheim. Dynamic properties of a flexible net sheet in waves and current—a numerical approach. *Aquacultural Engineering*, 35(3):228 – 238, 2006.

P. Li. *A Theoretical and Experimental Study of Wave-induced Hydroelastic Response of a Circular Floating Collar*, volume 2017:75 of *Doktoravhandlinger ved NTNU (trykt utg.)*. Norwegian University of Science and Technology, Faculty of Engineering Science and Technology, Department of Marine Technology, Trondheim, 2017.

G. Løland and J.V. Aarsnes. Fabric as construction material for marine applications. In *Hydroelasticity in Marine Technology*, pages 275–286, 1994.

D. Lu, A. Takizawa, and S. Kondo. Overflow-induced vibration of a weir coupled with sloshing in a downstream tank. *Journal of Fluids and Structures*, 11(4):367 – 393, 1997.

S. Ma, F.-C. W. Hanssen, M. A. Siddiqui, M. Greco, and O. M. Faltinsen. Local and global properties of the harmonic polynomial cell method: In-depth analysis in two dimensions. *International Journal for Numerical Methods in Engineering*, September 2017.

S. Malenica, B. Molin, J.T. Tuitman, F. Bigot, and I. Senjanovic. Some aspects of hydrostatic restoring for elastic bodies. In *Abstract for 24th IWWWFB, Saint Petersbourg, Russia, 2009*, 2009.

S. Malenica, N. Vladimir, Y.M. Choi, I. Senjanovic, and S.H. Kwon. Global hydroelastic model for liquid cargo ships. In *Seventh International Conference on Hydroelasticity in Marine Technology, Split, Croatia*, pages 493–505, 2015.

E. C. Maskell. A theory of the blockage effects on bluff bodies and stalled wings in a closed wind tunnel. Technical report, AERONAUTICAL RESEARCH COUNCIL LONDON (UNITED KINGDOM), 1965.

E. P. Michael, G. Chadwick, J. Parsons, and Boumy Sayavong. Evaluation of closed - containment aquaculture. In *Evaluation of Closed - Containment Technologies for Saltwater Salmon Aquaculture*. Ottawa : NRC Research Press, 2010.

H. Moe, A. Fredheim, and O.S. Hopperstad. Structural analysis of aquaculture net cages in current. *Journal of Fluids and Structures*, 26(3):503 – 516, 2010.

J. N. Newman. The exciting forces on fixed bodies in waves. *Journal of Ship Research*, 6(4):10–17, 1962.

J. N. Newman. Wave effects on deformable bodies. *Applied Ocean Research*, 16(1): 47–59, 1994.

J. N. Newman. Wave effects on vessels with internal tanks. In *20th Workshop on Water Waves and Floating Bodies - Spitsbergen - 29 May - 1 June 2005*. 2005.

Norwegian Directorate of Fisheries. Fiskeridirektoratet:utviklingstillatelser. [norwegian directorate of fisheries: Development licences], 2017. URL `https://www.fiskeridir.no/Akvakultur/Tildeling-og-tillatelser/Saertillatelser/Utviklingstillatelser`. [Online; accessed 22-August-2017].

NS9415. Marine fish farms - Requirements for site survey, risk analyses, design, dimensioning, production, installation and operation. Norwegian standard, SN / K 509, 2009.

M. P. Paidoussis and B.-K. Yu. Elastohydrodynamics of towed slender bodies: The effect of nose and tail shapes on stability. *Journal of Hydronautics*, 10(4):127 – 134, 1976.

A.C. Phadke and K. F. Cheung. Resonance and response of fluid-filled membrane in gravity waves. *Applied Ocean Research*, 23(1):15 – 28, 2001.

J. M. R. Quistwater and B. A. Dunell. Dynamic mechanical properties of nylon 66 and the plasticizing effect of water vapor on nylon. *Journal of Polymer Science*, 28 (117):309–318, 1958.

O. F. Rognebakke and O. M. Faltinsen. Coupling of sloshing and ship motions. *Journal of Ship Research*, 47(3):208 – 221, 2003.

F. W. Roos and W. W. Willmarth. Some experimental results on sphere and disk drag. *AIAA Journal*, Vol.9(2):285–291, 1971.

T. Rosten, Y. Ulgenes, K. Henriksen, and U Winther. Oppdrett av laks i lukkede anlegg:forprosjekt. [Salmon farming in closed plants: Preproject]. Technical report, SINTEF Fiskeri og havbruk, Trondheim, 2011.

T Rosten, B. F. Terjesen, Y. Ulgenes, K. Henriksen, E. Biering, and U. Winther. Lukkede oppdrettsanlegg i sjø - økt kunnskap er nødvendig. [more knowledge is needed about aquaculture in closed fish farms at sea]. *Vann*, 1:5–13, 2013.

T. Sarpkaya. *Wave Forces on Offshore Structures.* Cambridge University Press, 2010.

R. M. S. M. Schulkes. Fluid oscillations in an open, flexible container. *Journal of Engineering Mathematics*, 24(3):237–259, 1990.

I. Senjanovic, M. Tomic, and S. Tomasevic. An explicit formulation for restoring stiffness and its performance in ship hydroelasticity. *Ocean Engineering*, 35(13): 1322–1338, 2008.

Y. Shao and O. M. Faltinsen. Fully-nonlinear wave-current- body interaction analysis by a Harmonic Polynomial Cell Method. *Journal of Offshore Mechanics and Arctic Engineering*, 136(August):8–13, 2014a.

Y. Shao and O. M. Faltinsen. A harmonic polynomial cell (HPC) method for 3D Laplace equation with application in marine hydrodynamics. *Journal of Computational Physics*, 274:312–332, 2014b.

A. Shaw and D. Roy. Improved procedures for static and dynamic analyses of wrinkled membranes. *Journal of Applied Mechanics*, 74(3):590 –594, 2007.

A. Skaar and T Bodvin. Fullscale production of salmon in floating enclosed systems. In *International Conference on Fish Farming Technology*, pages 325–328, 1993.

F. Solaas, H. Rudi, A. Berg, and K. Tvinnereim. Floating fish farms with bag pens. In *International Conference on Fish Farming Technology*, pages 317–323, 1993.

I. M. Strand and O. M. Faltinsen. Linear sloshing in a 2d rectangular tank with a flexible sidewall. *Journal of Fluids and Structures*, 73:70 – 81, 2017.

I. M. Strand and O. M. Faltinsen. Linear wave response of a 2d closed flexible fish cage. *Submitted to: Journal of Fluids and Structures*, 2018.

I. M. Strand, A. J. Sørensen, P. Lader, and Z. Volent. Modelling of drag forces on a closed flexible fish cage. In *9th IFAC Conference on Control Applications in Marine Systems. Osaka, Japan*, 2013.

I. M. Strand, A. J. Sørensen, and Z. Volent. Closed flexible fish cages: Modelling and control of deformations. In *Proceedings of 33rd International Conference on Ocean, Offshore and Arctic Engineering. June 8-13, 2014, San Francisco, USA*, 2014.

I. M. Strand, A. J. Sørensen, Z. Volent, and P. Lader. Experimental study of current forces and deformations on a half ellipsoidal closed flexible fish cage. *Journal of Fluids and Structures*, vol. 65, 2016.

J. H. Tidwell and G. Allan. The role of aquaqulture. In *Aquaculture Production Systems*, pages 3–13. Wiley-Blackwell, 2012.

T. Ulstein. *Nonlinear Effects of a Flexible Stern Seal Bag on Cobblestone Oscillations of an SES*, volume 1995:60 of *Doktor ingeniøravhandling (Trondheim : trykt utg.)*. Universitetet i Trondheim, Norges tekniske høgskole, Institutt for marin hydrodynamikk, Trondheim, 1995. ISBN 8271198076.

G. S. West and C. J. Apelt. Effects of tunnel blockage and aspect ratio on the mean flow past a circular cylinder with reynolds numbers between 10^4 and 10^5. *Journal of Fluid Mechanics*, 114:361 – 377, 1982.

R. Zhao. A complete linear theory for a two-dimensional floating and liquid-filled membrane structure in waves. *Journal of Fluids and Structures*, 9(8):937–956, 1995.

R. Zhao and J. V. Aarsnes. Numerical and experimental studies of a floating and liquid-filled membrane structure in waves. *Ocean Engineering*, 25(9):753 – 765, 1998.

R. Zhao and M. Triantafyllou. Hydroelastic analyses of a long flexible tube in waves. In *Hydroelasticity in Marine Technology*, pages 287 – 287, Trondheim, Norway, 1994.

Y.-P. Zhao, Y-C. Li, G.-H. Dong, F.-K. Gui, and B. Teng. A numerical study on dynamic properties of the gravity cage in combined wave-current flow. *Ocean Engineering*, 34(17):2350 – 2363, 2007.

Appendix A

Coefficient calculation of linear sloshing in a 2D rectangular tank with a flexible side wall

The different parts of the pressure contribution on the membrane with modes are calculated as:

$$\int_{-h}^{0}(\Omega_{dm}(-\frac{l}{2},z)-\overline{\Omega_{dm}})U_j(z)dz = \frac{a_{mj}^{(\Omega)}}{\rho_w} \tag{A.1}$$

$$\begin{aligned}=&\alpha_{0m}\frac{L}{\pi jl}\Bigg((\frac{2l^2}{3}+2\frac{L^2}{\pi^2j^2})\sin^2(\frac{\pi hj}{2L})\\&-\frac{L}{\pi j}h\sin(\frac{\pi hj}{L})+\frac{h^2}{2}\Bigg)\\&+\sum_{k=1}^{\infty}\alpha_{km}L\left(\frac{h}{k\pi}\right)^2\Bigg(\frac{kjh((-1)^k\cos(\frac{j\pi h}{L})-1)}{\tanh(\pi kl/h)(L^2k^2-h^2j^2)}\\&-\frac{2(-1)^k\sin^2(\frac{j\pi h}{2L})}{lj\pi}\Bigg)\end{aligned}$$

$$\frac{l}{2}\int_{-h}^{0}U_j(z)dz = \frac{\gamma_{2j}}{\rho_w} = \frac{lL}{j\pi}\sin^2(\frac{j\pi h}{2L}) \tag{A.2}$$

$$\int_{-h}^{0}\frac{\cosh(\pi n(z+h)/l)}{\kappa_n\cosh(\pi nh/l)}U_j(z)dz = \frac{a_{nj}^{(\phi)}}{\rho_w} \tag{A.3}$$

$$= \frac{l^2L(jl\cosh(\frac{\pi nh}{l})\cos(\frac{j\pi h}{L})-Ln\sinh(\frac{\pi nh}{l})\sin(\frac{j\pi h}{L})-jl)}{\pi^2n\sinh(\frac{\pi nh}{l})(L^2n^2+j^2l^2)}$$

$$\frac{g}{l}\int_{-h}^{0}U_m(z)dz\int_{-h}^{0}U_j(z)dz = \frac{c_{mj}}{\rho_w} = \frac{g}{l}\frac{4L^2}{mj\pi^2}\sin^2(\frac{j\pi h}{2L})\sin^2(\frac{m\pi h}{2L}) \tag{A.4}$$

Appendix B

Formulations of the numerical potential theory harmonic polynomial cell (HPC) method

The internal sloshing problem and the external wave induced motion problem can be solved within potential flow theory. To solve these problems a numerical method is needed. We have chosen to apply the harmonic polynomial cell method (HPC method).

The basic formulation of the HPC method is based on Shao and Faltinsen (2014a). A local Cartesian x, y coordinates system is used and the domain is divided into cells with nine nodes, as illustrated in Figure B.1. The velocity potential in each cell is described by an interpolation function

$$\phi(x,y) = \sum_{j=1}^{8} b_j f_j(x,y) \tag{B.1}$$

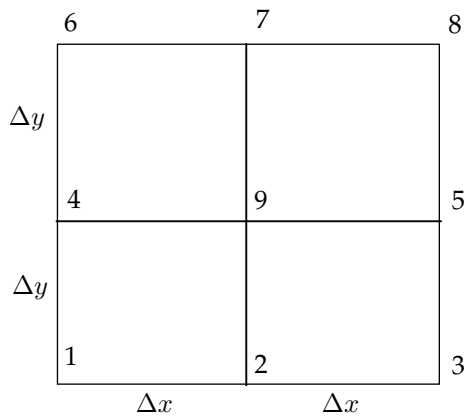

Figure B.1: Dimension and node numbering of a regular cell

where b_j and $f_j(x,y)$ are coefficients and harmonic polynomials respectively. The harmonic polynomial automatically satisfies the Laplace equation ($\nabla^2\phi = 0$) everywhere in space.

The Harmonic Polynomials are chosen as follows:

$$\begin{aligned} F(x,y) &= [f_1(x,y), f_2(x,y), f_3(x,y), f_4(x,y), f_5(x,y), f_6(x,y), f_7(x,y), f_8(x,y)] \\ &= [1,\ x,\ y,\ x^2-y^2,\ 2xy,\ x^3-3xy^2,\ 3x^2y-y^3,\ x^4-6x^2y^2+y^4\ ] \end{aligned} \tag{B.2}$$

By calculating the velocity potential for nodes 1-8 we get an equation system on the form of

$$\begin{bmatrix} \phi_1 \\ \vdots \\ \phi_8 \end{bmatrix} = \begin{bmatrix} f_1(x_1,y_1)\dots f_8(x_1,y_1) \\ \vdots \ddots \vdots \\ f_1(x_8,y_8)\dots f_8(x_8,y_8) \end{bmatrix} \begin{bmatrix} b_1 \\ \vdots \\ b_8 \end{bmatrix} \tag{B.3}$$

Where x, and y is given in local coordinates calculated with center in node 9.

If (B.3) is solved for b_j we get an expression for the unknown coefficients, given according to

$$\begin{bmatrix} b_1 \\ \vdots \\ b_8 \end{bmatrix} = \underbrace{\begin{bmatrix} f_1(x_1,y_1)\dots f_8(x_1,y_1) \\ \vdots \ddots \vdots \\ f_1(x_8,y_8)\dots f_8(x_8,y_8) \end{bmatrix}^{-1}}_{C} \begin{bmatrix} \phi_1 \\ \vdots \\ \phi_8 \end{bmatrix} = \begin{bmatrix} c_{1,1}\dots c_{1,8} \\ \vdots \ddots \vdots \\ c_{8,1}\dots c_{8,8} \end{bmatrix} \begin{bmatrix} \phi_1 \\ \vdots \\ \phi_8 \end{bmatrix} \tag{B.4}$$

The resulting velocity potential in the cell can be found from the previous equations according to:

$$\phi(x,y) = \sum_{j=1}^{8} b_j f_j(x,y) = \sum_{i=1}^{8} \left[\sum_{j=1}^{8} c_{j,i} f_j(x,y) \right] \phi_i \tag{B.5}$$

Equations (B.2)-(B.5) are given for the local coordinate system (x,y). We choose this coordinate system such that node 9 is located at the origin. This gives a governing relation for the internal nodes in the internal domain, according to

$$\phi(x_9,y_9) = \phi_9 = \sum_{i=1}^{8} c_{1,i}\phi_i \tag{B.6}$$

For nodes at the boundary of the domain the Neumann and Dirichlet boundary conditions are given according to:

$$\frac{\partial\phi}{\partial n} = \sum_{i=1}^{8} \left[\sum_{j=1}^{8} c_{j,i} \nabla f_j(x,y) \cdot \vec{n}(x,y) \right] \phi_i \tag{B.7}$$

$$\phi^* = \phi(x,y) \tag{B.8}$$

where ϕ^* is a known solution and $\vec{n}(x,y)$ is the normal vector at x,y.

A global matrix system is established by inserting the local matrix equations and boundary conditions into the global coefficient matrix, given as:

$$\mathbf{A}_G \phi_G = \mathbf{B}_G \tag{B.9}$$

where $\mathbf{A}_G$ is the global coefficient matrix, ϕ_G is the global velocity potential vector and $\mathbf{B}_G$ is the boundary condition vector.

Appendix C

Full scale parameters of a CFFC by Botngaard

Botngaard systems have designed and made full scale systems deployed in the sea. One of these systems is designed as a rectangular bag in a steel cage. From personal conversation with them, the following parameters were obtained: The bag is made of cloth (produced by Dyneema) of thickness $d_F = 0.75$mm, with an elasticity module of $E = 2.25 \cdot 10^9$Pa. The bag is $h = 12$ m depth, $L = B = 25$m wide and have a total volume of $\nabla = 4000\text{m}^3$, the geometry is illustrated in figure C.1. The bag is overfilled, the overfilling $\Delta h = 4$mm (can reach $\Delta h = 6$mm), and the density difference $\Delta\rho = 10\text{kg/m}^3$, for a given site. The cage uses cylindrical tube floaters, with diameter $D_F = 0.836$m.

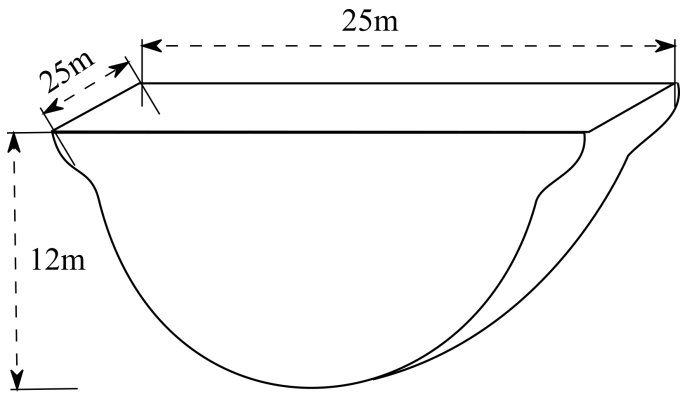

Figure C.1: Sketch of full scale dimensions of a Botngaard closed flexible fish cage in a square steel frame.

Appendix D

Membrane equation system for the membrane deformations for a semi-circular membrane

For a case with static tension T_0 from pure overfilling as described in Section 5.3, the membrane will have an half circular shape. For the shape to be fully half circular the static tension must be much larger than the mass forces on the 2D membrane, i.e $T_0 >> m_M g$, then the static tension variations along the membrane $\partial T_0/\partial s = 0$, and the mass terms can be neglected. For a half circular membrane, the static curvature is constant, then $\frac{\partial \psi_0}{\partial s} = \frac{1}{R}$.

For the given problem the equations simplifies to:

$$-\omega^2 m_M v = \frac{T_0}{R^2}\left(\frac{\partial^2 v}{\partial \psi^2} + \frac{\partial u}{\partial \psi}\right) + \frac{Ed}{R^2}\left(\frac{\partial u}{\partial \psi} - v\right) - \Delta\hat{p} \tag{D.1}$$

$$-\omega^2 m_M u = \frac{Ed}{R^2}\left(\frac{\partial^2 u}{\partial \psi^2} - \frac{\partial v}{\partial \psi}\right) - \frac{T_0}{R^2}\left(\frac{\partial v}{\partial \psi} + u\right) \tag{D.2}$$

Numerical expression for a half circular membrane

If the membrane has a half circular shape, the ordinary differential equations for the structural mode amplitudes ν_m, μ_k can be found by multiplying (D.1) and (D.2) with the mode $U_j(\psi_0)$ and integrating along the membrane length. For a half circular shape $\psi_e = \pi/2$. $U_j(\psi_0) = \sin(j(\psi_0 - \frac{\pi}{2}))$. By using orthogonal properties, the resulting membrane equation system become:

$$-\omega^2 m_M R\frac{\pi}{2}\nu_j + \frac{\pi(Ed + j^2 T_0)}{2R}\nu_j - \frac{(Ed + T_0)}{R}\sum_{n=1}^{\infty} n\alpha_{jn}\mu_n = f_j(\omega) \tag{D.3}$$

$$-\omega^2 m_M R\frac{\pi}{2}\mu_j + \frac{\pi(Edj^2 + T_0)}{2R}\mu_j + \frac{Ed + T_0}{R}\sum_{m=1}^{\infty} m\alpha_{jm}\nu_m = 0 \tag{D.4}$$

where α_{jm} is defined according to:

$$\int_{-\pi}^{0} U_{cm}(\psi_0)U_j(\psi_0)d\psi = \alpha_{jm} = \begin{cases} 0 \text{ for } m = j \\ \frac{j((-1)^j(-1)^m-1)}{j^2-m^2} \text{ for } m \neq j \end{cases} \tag{D.5}$$

where $U_{cj}(\psi_0)$ comes from the first derivative of $U_j(\psi_0)$ and is defined as $U_{cj}(\psi_0) = \cos(j(\psi_0 - \frac{\pi}{2}))$. Symmetry properties can be oberved from the α_{jm} value defined in (D.5), symmetric normal modes are structurally coupled to asymmetric tangential modes and asymmetric normal modes are coupled to symmetric tangential modes.

The membrane is connected to the floaters, and this connection transfers dynamic tension loads to the rigid body motions. The total contribution from the dynamic tension forces in horizontal and vertical direction for the half circular membrane become

$$f_1^T = -\frac{T_0}{R}\sum_{m=1}^{\infty} m\nu_m(1+(-1)^m) \tag{D.6}$$

$$f_2^T = -\frac{Ed}{R}\sum_{n=1}^{\infty} n(1+(-1)^n)\mu_n \tag{D.7}$$

Th roll moment about the center of gravity of the CFFC due to the tension loads on the floaters for the half circular membrane become

$$f_3^T = EdR\sum_{n=1}^{\infty} n(1-(-1)^n)\mu_n + \frac{z_e^2 T_0}{R}\sum_{m=1}^{\infty} m(1+(-1)^m)\nu_m \tag{D.8}$$

For the halfcircular membrane described by (D.3) and (D.4) the expressions for the mass and stiffness matrices in (6.41) can be simplified to a great extent. $\boldsymbol{m_{M\xi}}, \boldsymbol{m_{M\mu}}$ is now defined according to $\boldsymbol{m_{M\xi}} = \boldsymbol{m_{M\mu}} = \boldsymbol{I} m_M \frac{\pi R}{2}$, where $\boldsymbol{I}$ is the identity matrix. For $j < 4$, $\boldsymbol{m_{M\xi}}, \boldsymbol{m_{M\mu}} = 0$. The structural stiffness matrices of $\boldsymbol{\xi}$ is defined according to $\boldsymbol{c_{M\xi}\xi} = \sum_{j=4}^{\infty} \frac{\pi}{2R}(Ed + (j-3)^2 T_0)\xi_j$ where $\boldsymbol{c_{M\xi}} = 0$ for $j < 4$. The structural stiffness matrix of $\boldsymbol{\mu}$ is defined according to $\boldsymbol{c_{M\mu}\mu} = \sum_{n=1}^{\infty} \frac{\pi}{2R}(n^2 Ed + T_0)\mu_n$ where $\boldsymbol{c_{M\mu}} = 0$ for $j < 4$. The coupling stiffness matrix between $\boldsymbol{\xi}$ and $\boldsymbol{\mu}$ is defined according to $\boldsymbol{c_{M\xi\mu}\mu} = \sum_{j=4}^{\infty}\sum_{n=1}^{\infty} n\alpha_{(j-3)n}\mu_n$, while the coupling stiffness matrix between $\boldsymbol{\mu}$ and $\boldsymbol{\xi}$ is defined according to $\boldsymbol{c_{M\mu\xi}\xi} = \sum_{j=4}^{\infty}\sum_{n=1}^{\infty}(j-3)\alpha_{n(j-3)}\xi_j$. The membrane floater connection loads $\boldsymbol{c_{T\xi}}$ and $\boldsymbol{c_{T\xi\mu}}$ are given by (6.42) where f_j^T for $j > 4$ are given by (D.6)- (D.8).

Appendix E

Damping and excitation, radiated waves at finite water depth

Newman (1962) first gave the relation between the damping coefficient and the excitation force for infinite water depth based on the Haskind-relation. In the present analysis this is extended to finite water depths.

The two dimensional incident wave potential ϕ_0 for a wave propagating in the $y-$ direction is given by (6.43). While the asymptotic incident-wave system propagating in the positive y-direction are given according to:

$$\phi_j(y,z,t) = \frac{A^+ g}{\omega^2}\frac{\cosh k(z+h)}{\cosh kh} e^{(\mathrm{i}\omega t - \mathrm{i}ky)} \tag{E.1}$$

The far-field wave amplitude $|A^+|$ and far-field wave amplitude $|A^-|$ are related for bodies symmetric about the $y - axis$, the magnitude are the same and for symmetric and antisymmetric motions they are related as described in Chapter 6.5.1.

The exciting forces on a body in waves can be found from (Newman, 1962):

$$f_j = \mathrm{i}\omega\rho_w e^{\mathrm{i}\omega t}\int_{-h}^{0} \phi_0 \frac{\partial \phi_j}{\partial y} - \phi_j \frac{\partial \phi_0}{\partial y}\Big]_{y=-\infty}^{y=\infty} \mathrm{d}z \tag{E.2}$$

where the partial partial derivative of ϕ_0 and ϕ_j in $y-$ direction are

$$\frac{\partial \phi_0}{\partial y} = -\frac{\mathrm{i}k\zeta_a g}{\omega}\frac{\cosh k(z+h)}{\cosh kh} e^{(\mathrm{i}\omega t - \mathrm{i}ky)} \tag{E.3}$$

$$\frac{\partial \phi_j}{\partial y} = -\frac{\mathrm{i}kA^+ g}{\omega^2}\frac{\cosh k(z+h)}{\cosh kh} e^{(\mathrm{i}\omega t - \mathrm{i}ky)} \tag{E.4}$$

The estimated excitation force can then be calculates as:

$$\begin{aligned} f_j^{est} &= \rho_w g^2 \zeta_a 2A^+ k e^{\mathrm{i}\omega t}\frac{1}{\omega^2}\int_{-h}^{0}\frac{\cosh^2 k(z+h)}{\cosh^2 kh}\mathrm{d}z \\ &= 2\rho_w g^2 \zeta_a A^+ k e^{\mathrm{i}\omega t}\frac{I_1}{\omega^2} \end{aligned} \tag{E.5}$$

where I_1 is given by (6.58) as $I_1 = \int_{-h}^{0} \frac{\cosh^2 k(z+h)}{\cosh^2 kh} \mathrm{dz} = \frac{\sinh(kh)\cosh(kh)+kh}{2k\cosh^2 kh}$.

From (Faltinsen and Timokha, 2009, page 118) we know that the relation between the far-field wave amplitude $|A^+|$ and the damping is given by (6.57) as $b_{jj} = \frac{2\rho g^2 k}{\omega^3} I_1 A^{+2}$. We can now find the relation between the amplitude of the excitation force $|f_j|$ and the damping coeffcient for a given motion j by combining eq. 6.57 and eq. E.5

$$|f_j|^{est} = \zeta_a \sqrt{\frac{\rho_w g^2}{\omega} b_{jj} 2k I_1}. \tag{E.6}$$

Appendix F

Mode shape plots

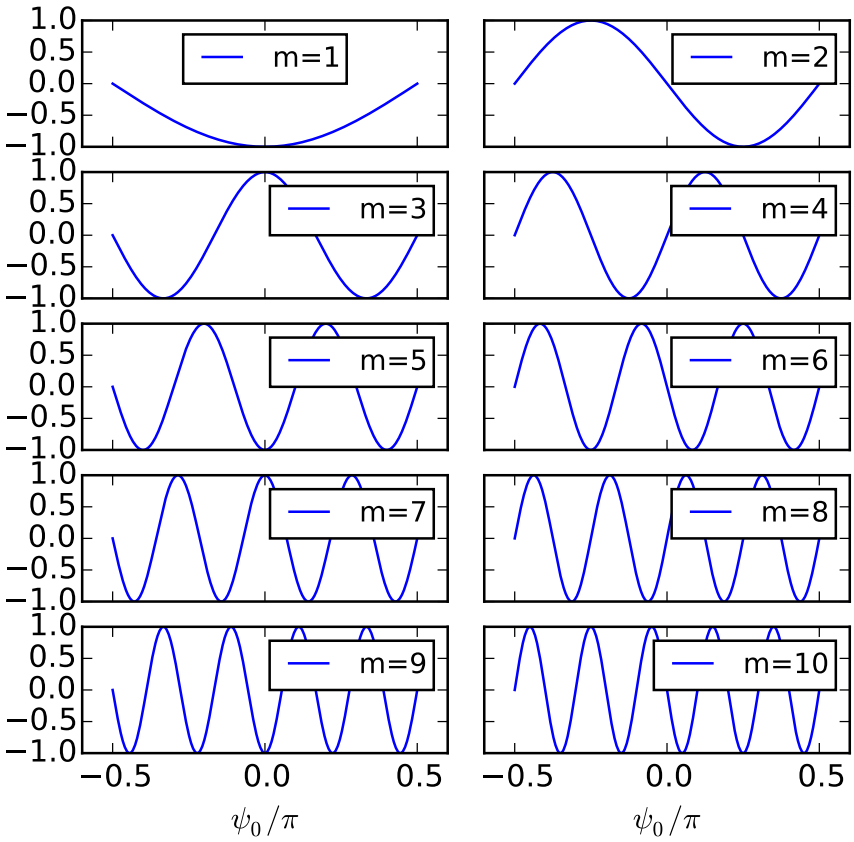

Figure F.1: Normal deformation modes $U_m(\psi_0)$ from 1-10.

Appendix G

Error estimation of hydrodynamic coefficients

The accumulated L_2 error over all frequencies for the damping based on the damping part of (6.55) related to the estimated damping calculated by (6.57) is calculated according to:

$$e_{b_{jj}} = \frac{\sum (b_{jj}^{est}(\omega) - b_{jj})^2(\omega)}{\sum b_{jj}^2(\omega)} \tag{G.1}$$

The accumulated L_2 error over all frequencies for the excitation force based on (6.56) related to the estimated excitation force based on the damping by (6.59) is calculated according to:

$$e_{f_j} = \frac{\sum (f_{exc,j}^{est} - f_{exc,j})^2}{\sum f_{exc,j}^2} \tag{G.2}$$

The damping error for a given motion j; $e_{b_{jj}}$ and the wave excitation error for a given motion j; e_{f_j} for j from 1 to 13 for the hemicircle are plotted in Figure G.1. $j = 1$ is sway, $j = 2$ is heave, $j = 3$ is roll and $j = 4..13$ are the first ten normal structural modes. The results are for $N_y = N_z$=100 nodes/m.

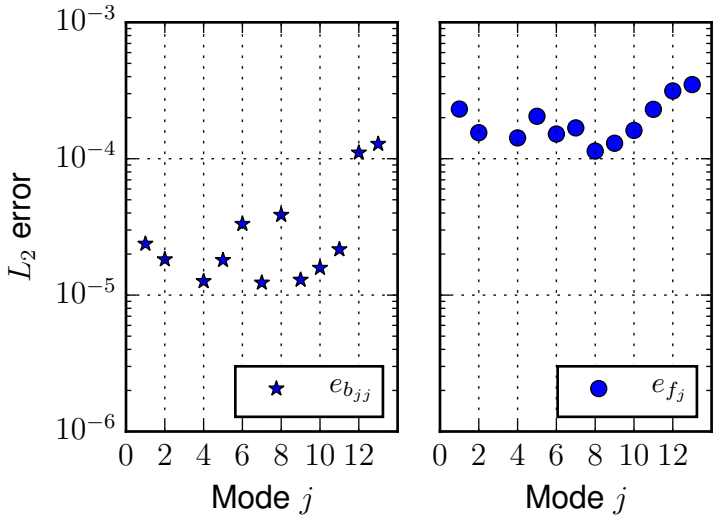

Figure G.1: L_2 error of damping ($e_{b_{jj}}$) and L_2 error of excitation force e_{f_j} for a given motion j.

Appendix H

Convergence study of number of structural modes

The accumulated L_2 error over all frequencies for the sway, heave and roll response have been been calculated for different numbers of normal and tangential structural modes. Structural normal modes from $j = 1$ to $j = 30$ have been run, and tangential modes up to 350 have been run. The error is calculated according to:

$$e_j^{J,N} = \frac{\sum(\xi_j(\omega) - \xi_j^{ref}(\omega))^2}{\sum \xi_j^{ref}(\omega)^2} \tag{H.1}$$

The reference motion $\xi_j^{ref}(\omega)$ have been calculated with $J = 30$ normal modes and $N = 350$ tangential modes. The convergence is shown in Figure H.1. Large difference in the convergence rate for sway, heave and roll can be observed from Figure H.1, where sway converges first. N=250 modes in the tangential direction and J=30 modes in the normal direction were used in the results.

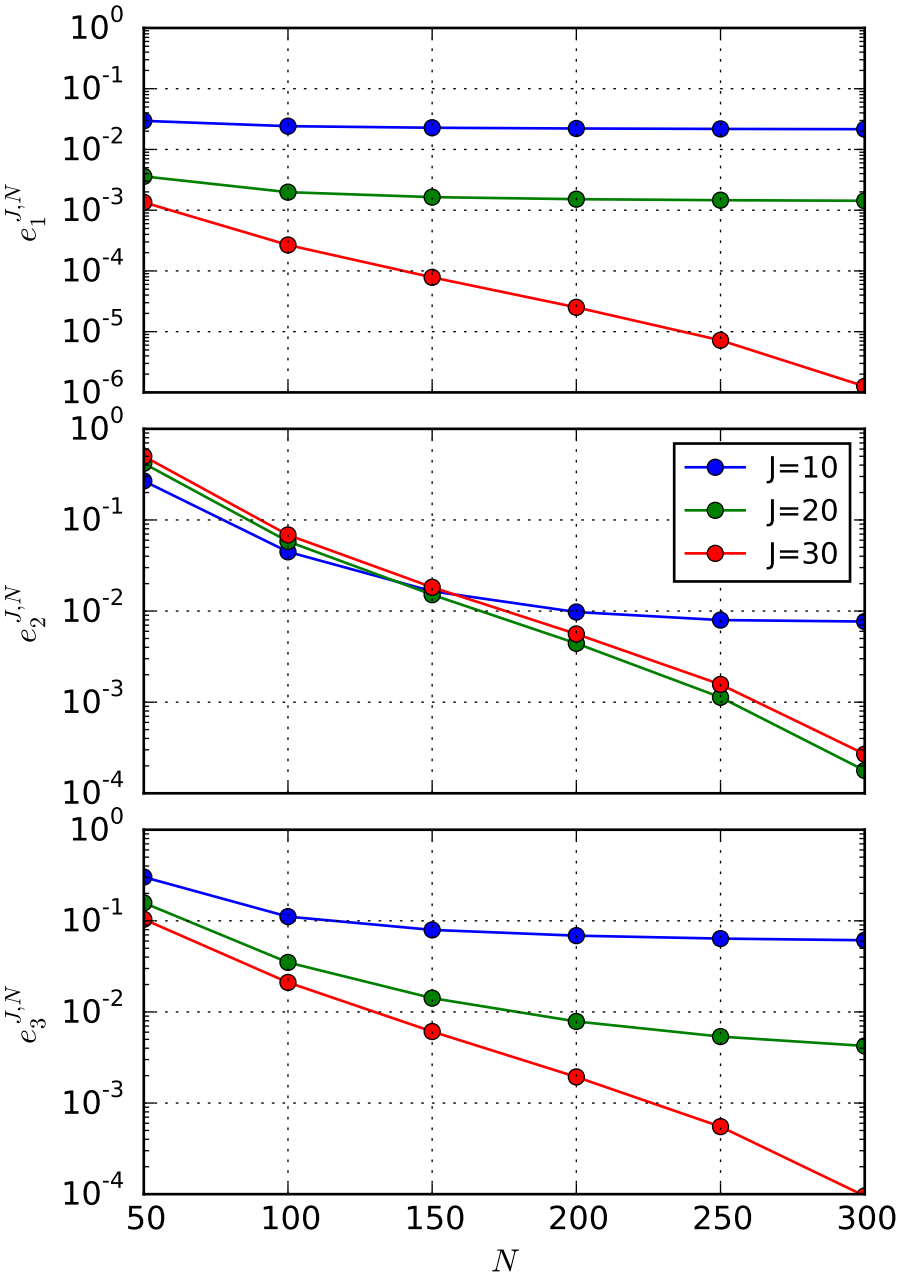

Figure H.1: Convergence plot of numbers of necessary modes in normal and tangential direction, in sway, heave and roll.

Previous PhD theses published at the Departement of Marine Technology
(earlier: Faculty of Marine Technology)
NORWEGIAN UNIVERSITY OF SCIENCE AND TECHNOLOGY

Report No.	Author	Title
	Kavlie, Dag	Optimization of Plane Elastic Grillages, 1967
	Hansen, Hans R.	Man-Machine Communication and Data-Storage Methods in Ship Structural Design, 1971
	Gisvold, Kaare M.	A Method for non-linear mixed -integer programming and its Application to Design Problems, 1971
	Lund, Sverre	Tanker Frame Optimalization by means of SUMT-Transformation and Behaviour Models, 1971
	Vinje, Tor	On Vibration of Spherical Shells Interacting with Fluid, 1972
	Lorentz, Jan D.	Tank Arrangement for Crude Oil Carriers in Accordance with the new Anti-Pollution Regulations, 1975
	Carlsen, Carl A.	Computer-Aided Design of Tanker Structures, 1975
	Larsen, Carl M.	Static and Dynamic Analysis of Offshore Pipelines during Installation, 1976
UR-79-01	Brigt Hatlestad, MK	The finite element method used in a fatigue evaluation of fixed offshore platforms. (Dr.Ing. Thesis)
UR-79-02	Erik Pettersen, MK	Analysis and design of cellular structures. (Dr.Ing. Thesis)
UR-79-03	Sverre Valsgård, MK	Finite difference and finite element methods applied to nonlinear analysis of plated structures. (Dr.Ing. Thesis)
UR-79-04	Nils T. Nordsve, MK	Finite element collapse analysis of structural members considering imperfections and stresses due to fabrication. (Dr.Ing. Thesis)
UR-79-05	Ivar J. Fylling, MK	Analysis of towline forces in ocean towing systems. (Dr.Ing. Thesis)
UR-80-06	Nils Sandsmark, MM	Analysis of Stationary and Transient Heat Conduction by the Use of the Finite Element Method. (Dr.Ing. Thesis)
UR-80-09	Sverre Haver, MK	Analysis of uncertainties related to the stochastic modeling of ocean waves. (Dr.Ing. Thesis)
UR-81-15	Odland, Jonas	On the Strength of welded Ring stiffened cylindrical Shells primarily subjected to axial Compression
UR-82-17	Engesvik, Knut	Analysis of Uncertainties in the fatigue Capacity of Welded Joints
UR-82-18	Rye, Henrik	Ocean wave groups
UR-83-30	Eide, Oddvar Inge	On Cumulative Fatigue Damage in Steel Welded Joints

UR-83-33	Mo, Olav	Stochastic Time Domain Analysis of Slender Offshore Structures
UR-83-34	Amdahl, Jørgen	Energy absorption in Ship-platform impacts
UR-84-37	Mørch, Morten	Motions and mooring forces of semi submersibles as determined by full-scale measurements and theoretical analysis
UR-84-38	Soares, C. Guedes	Probabilistic models for load effects in ship structures
UR-84-39	Aarsnes, Jan V.	Current forces on ships
UR-84-40	Czujko, Jerzy	Collapse Analysis of Plates subjected to Biaxial Compression and Lateral Load
UR-85-46	Alf G. Engseth, MK	Finite element collapse analysis of tubular steel offshore structures. (Dr.Ing. Thesis)
UR-86-47	Dengody Sheshappa, MP	A Computer Design Model for Optimizing Fishing Vessel Designs Based on Techno-Economic Analysis. (Dr.Ing. Thesis)
UR-86-48	Vidar Aanesland, MH	A Theoretical and Numerical Study of Ship Wave Resistance. (Dr.Ing. Thesis)
UR-86-49	Heinz-Joachim Wessel, MK	Fracture Mechanics Analysis of Crack Growth in Plate Girders. (Dr.Ing. Thesis)
UR-86-50	Jon Taby, MK	Ultimate and Post-ultimate Strength of Dented Tubular Members. (Dr.Ing. Thesis)
UR-86-51	Walter Lian, MH	A Numerical Study of Two-Dimensional Separated Flow Past Bluff Bodies at Moderate KC-Numbers. (Dr.Ing. Thesis)
UR-86-52	Bjørn Sortland, MH	Force Measurements in Oscillating Flow on Ship Sections and Circular Cylinders in a U-Tube Water Tank. (Dr.Ing. Thesis)
UR-86-53	Kurt Strand, MM	A System Dynamic Approach to One-dimensional Fluid Flow. (Dr.Ing. Thesis)
UR-86-54	Arne Edvin Løken, MH	Three Dimensional Second Order Hydrodynamic Effects on Ocean Structures in Waves. (Dr.Ing. Thesis)
UR-86-55	Sigurd Falch, MH	A Numerical Study of Slamming of Two-Dimensional Bodies. (Dr.Ing. Thesis)
UR-87-56	Arne Braathen, MH	Application of a Vortex Tracking Method to the Prediction of Roll Damping of a Two-Dimension Floating Body. (Dr.Ing. Thesis)
UR-87-57	Bernt Leira, MK	Gaussian Vector Processes for Reliability Analysis involving Wave-Induced Load Effects. (Dr.Ing. Thesis)
UR-87-58	Magnus Småvik, MM	Thermal Load and Process Characteristics in a Two-Stroke Diesel Engine with Thermal Barriers (in Norwegian). (Dr.Ing. Thesis)
MTA-88-59	Bernt Arild Bremdal, MP	An Investigation of Marine Installation Processes – A Knowledge - Based Planning Approach. (Dr.Ing. Thesis)
MTA-88-60	Xu Jun, MK	Non-linear Dynamic Analysis of Space-framed

		Offshore Structures. (Dr.Ing. Thesis)
MTA-89-61	Gang Miao, MH	Hydrodynamic Forces and Dynamic Responses of Circular Cylinders in Wave Zones. (Dr.Ing. Thesis)
MTA-89-62	Martin Greenhow, MH	Linear and Non-Linear Studies of Waves and Floating Bodies. Part I and Part II. (Dr.Techn. Thesis)
MTA-89-63	Chang Li, MH	Force Coefficients of Spheres and Cubes in Oscillatory Flow with and without Current. (Dr.Ing. Thesis
MTA-89-64	Hu Ying, MP	A Study of Marketing and Design in Development of Marine Transport Systems. (Dr.Ing. Thesis)
MTA-89-65	Arild Jæger, MH	Seakeeping, Dynamic Stability and Performance of a Wedge Shaped Planing Hull. (Dr.Ing. Thesis)
MTA-89-66	Chan Siu Hung, MM	The dynamic characteristics of tilting-pad bearings
MTA-89-67	Kim Wikstrøm, MP	Analysis av projekteringen for ett offshore projekt. (Licenciat-avhandling)
MTA-89-68	Jiao Guoyang, MK	Reliability Analysis of Crack Growth under Random Loading, considering Model Updating. (Dr.Ing. Thesis)
MTA-89-69	Arnt Olufsen, MK	Uncertainty and Reliability Analysis of Fixed Offshore Structures. (Dr.Ing. Thesis)
MTA-89-70	Wu Yu-Lin, MR	System Reliability Analyses of Offshore Structures using improved Truss and Beam Models. (Dr.Ing. Thesis)
MTA-90-71	Jan Roger Hoff, MH	Three-dimensional Green function of a vessel with forward speed in waves. (Dr.Ing. Thesis)
MTA-90-72	Rong Zhao, MH	Slow-Drift Motions of a Moored Two-Dimensional Body in Irregular Waves. (Dr.Ing. Thesis)
MTA-90-73	Atle Minsaas, MP	Economical Risk Analysis. (Dr.Ing. Thesis)
MTA-90-74	Knut-Aril Farnes, MK	Long-term Statistics of Response in Non-linear Marine Structures. (Dr.Ing. Thesis)
MTA-90-75	Torbjørn Sotberg, MK	Application of Reliability Methods for Safety Assessment of Submarine Pipelines. (Dr.Ing. Thesis)
MTA-90-76	Zeuthen, Steffen, MP	SEAMAID. A computational model of the design process in a constraint-based logic programming environment. An example from the offshore domain. (Dr.Ing. Thesis)
MTA-91-77	Haagensen, Sven, MM	Fuel Dependant Cyclic Variability in a Spark Ignition Engine - An Optical Approach. (Dr.Ing. Thesis)
MTA-91-78	Løland, Geir, MH	Current forces on and flow through fish farms. (Dr.Ing. Thesis)
MTA-91-79	Hoen, Christopher, MK	System Identification of Structures Excited by Stochastic Load Processes. (Dr.Ing. Thesis)
MTA-91-80	Haugen, Stein, MK	Probabilistic Evaluation of Frequency of Collision between Ships and Offshore Platforms. (Dr.Ing. Thesis)

MTA-91-81	Sødahl, Nils, MK	Methods for Design and Analysis of Flexible Risers. (Dr.Ing. Thesis)
MTA-91-82	Ormberg, Harald, MK	Non-linear Response Analysis of Floating Fish Farm Systems. (Dr.Ing. Thesis)
MTA-91-83	Marley, Mark J., MK	Time Variant Reliability under Fatigue Degradation. (Dr.Ing. Thesis)
MTA-91-84	Krokstad, Jørgen R., MH	Second-order Loads in Multidirectional Seas. (Dr.Ing. Thesis)
MTA-91-85	Molteberg, Gunnar A., MM	The Application of System Identification Techniques to Performance Monitoring of Four Stroke Turbocharged Diesel Engines. (Dr.Ing. Thesis)
MTA-92-86	Mørch, Hans Jørgen Bjelke, MH	Aspects of Hydrofoil Design: with Emphasis on Hydrofoil Interaction in Calm Water. (Dr.Ing. Thesis)
MTA-92-87	Chan Siu Hung, MM	Nonlinear Analysis of Rotordynamic Instabilities in Highspeed Turbomachinery. (Dr.Ing. Thesis)
MTA-92-88	Bessason, Bjarni, MK	Assessment of Earthquake Loading and Response of Seismically Isolated Bridges. (Dr.Ing. Thesis)
MTA-92-89	Langli, Geir, MP	Improving Operational Safety through exploitation of Design Knowledge - an investigation of offshore platform safety. (Dr.Ing. Thesis)
MTA-92-90	Sævik, Svein, MK	On Stresses and Fatigue in Flexible Pipes. (Dr.Ing. Thesis)
MTA-92-91	Ask, Tor Ø., MM	Ignition and Flame Growth in Lean Gas-Air Mixtures. An Experimental Study with a Schlieren System. (Dr.Ing. Thesis)
MTA-86-92	Hessen, Gunnar, MK	Fracture Mechanics Analysis of Stiffened Tubular Members. (Dr.Ing. Thesis)
MTA-93-93	Steinebach, Christian, MM	Knowledge Based Systems for Diagnosis of Rotating Machinery. (Dr.Ing. Thesis)
MTA-93-94	Dalane, Jan Inge, MK	System Reliability in Design and Maintenance of Fixed Offshore Structures. (Dr.Ing. Thesis)
MTA-93-95	Steen, Sverre, MH	Cobblestone Effect on SES. (Dr.Ing. Thesis)
MTA-93-96	Karunakaran, Daniel, MK	Nonlinear Dynamic Response and Reliability Analysis of Drag-dominated Offshore Platforms. (Dr.Ing. Thesis)
MTA-93-97	Hagen, Arnulf, MP	The Framework of a Design Process Language. (Dr.Ing. Thesis)
MTA-93-98	Nordrik, Rune, MM	Investigation of Spark Ignition and Autoignition in Methane and Air Using Computational Fluid Dynamics and Chemical Reaction Kinetics. A Numerical Study of Ignition Processes in Internal Combustion Engines. (Dr.Ing. Thesis)
MTA-94-99	Passano, Elizabeth, MK	Efficient Analysis of Nonlinear Slender Marine Structures. (Dr.Ing. Thesis)
MTA-94-100	Kvålsvold, Jan, MH	Hydroelastic Modelling of Wetdeck Slamming on Multihull Vessels. (Dr.Ing. Thesis)
MTA-94-102	Bech, Sidsel M., MK	Experimental and Numerical Determination of Stiffness and Strength of GRP/PVC Sandwich

		Structures. (Dr.Ing. Thesis)
MTA-95-103	Paulsen, Hallvard, MM	A Study of Transient Jet and Spray using a Schlieren Method and Digital Image Processing. (Dr.Ing. Thesis)
MTA-95-104	Hovde, Geir Olav, MK	Fatigue and Overload Reliability of Offshore Structural Systems, Considering the Effect of Inspection and Repair. (Dr.Ing. Thesis)
MTA-95-105	Wang, Xiaozhi, MK	Reliability Analysis of Production Ships with Emphasis on Load Combination and Ultimate Strength. (Dr.Ing. Thesis)
MTA-95-106	Ulstein, Tore, MH	Nonlinear Effects of a Flexible Stern Seal Bag on Cobblestone Oscillations of an SES. (Dr.Ing. Thesis)
MTA-95-107	Solaas, Frøydis, MH	Analytical and Numerical Studies of Sloshing in Tanks. (Dr.Ing. Thesis)
MTA-95-108	Hellan, Øyvind, MK	Nonlinear Pushover and Cyclic Analyses in Ultimate Limit State Design and Reassessment of Tubular Steel Offshore Structures. (Dr.Ing. Thesis)
MTA-95-109	Hermundstad, Ole A., MK	Theoretical and Experimental Hydroelastic Analysis of High Speed Vessels. (Dr.Ing. Thesis)
MTA-96-110	Bratland, Anne K., MH	Wave-Current Interaction Effects on Large-Volume Bodies in Water of Finite Depth. (Dr.Ing. Thesis)
MTA-96-111	Herfjord, Kjell, MH	A Study of Two-dimensional Separated Flow by a Combination of the Finite Element Method and Navier-Stokes Equations. (Dr.Ing. Thesis)
MTA-96-112	Æsøy, Vilmar, MM	Hot Surface Assisted Compression Ignition in a Direct Injection Natural Gas Engine. (Dr.Ing. Thesis)
MTA-96-113	Eknes, Monika L., MK	Escalation Scenarios Initiated by Gas Explosions on Offshore Installations. (Dr.Ing. Thesis)
MTA-96-114	Erikstad, Stein O., MP	A Decision Support Model for Preliminary Ship Design. (Dr.Ing. Thesis)
MTA-96-115	Pedersen, Egil, MH	A Nautical Study of Towed Marine Seismic Streamer Cable Configurations. (Dr.Ing. Thesis)
MTA-97-116	Moksnes, Paul O., MM	Modelling Two-Phase Thermo-Fluid Systems Using Bond Graphs. (Dr.Ing. Thesis)
MTA-97-117	Halse, Karl H., MK	On Vortex Shedding and Prediction of Vortex-Induced Vibrations of Circular Cylinders. (Dr.Ing. Thesis)
MTA-97-118	Igland, Ragnar T., MK	Reliability Analysis of Pipelines during Laying, considering Ultimate Strength under Combined Loads. (Dr.Ing. Thesis)
MTA-97-119	Pedersen, Hans-P., MP	Levendefiskteknologi for fiskefartøy. (Dr.Ing. Thesis)
MTA-98-120	Vikestad, Kyrre, MK	Multi-Frequency Response of a Cylinder Subjected to Vortex Shedding and Support Motions. (Dr.Ing. Thesis)
MTA-98-121	Azadi, Mohammad R. E., MK	Analysis of Static and Dynamic Pile-Soil-Jacket Behaviour. (Dr.Ing. Thesis)
MTA-98-	Ulltang, Terje, MP	A Communication Model for Product Information.

122		(Dr.Ing. Thesis)
MTA-98-123	Torbergsen, Erik, MM	Impeller/Diffuser Interaction Forces in Centrifugal Pumps. (Dr.Ing. Thesis)
MTA-98-124	Hansen, Edmond, MH	A Discrete Element Model to Study Marginal Ice Zone Dynamics and the Behaviour of Vessels Moored in Broken Ice. (Dr.Ing. Thesis)
MTA-98-125	Videiro, Paulo M., MK	Reliability Based Design of Marine Structures. (Dr.Ing. Thesis)
MTA-99-126	Mainçon, Philippe, MK	Fatigue Reliability of Long Welds Application to Titanium Risers. (Dr.Ing. Thesis)
MTA-99-127	Haugen, Elin M., MH	Hydroelastic Analysis of Slamming on Stiffened Plates with Application to Catamaran Wetdecks. (Dr.Ing. Thesis)
MTA-99-128	Langhelle, Nina K., MK	Experimental Validation and Calibration of Nonlinear Finite Element Models for Use in Design of Aluminium Structures Exposed to Fire. (Dr.Ing. Thesis)
MTA-99-129	Berstad, Are J., MK	Calculation of Fatigue Damage in Ship Structures. (Dr.Ing. Thesis)
MTA-99-130	Andersen, Trond M., MM	Short Term Maintenance Planning. (Dr.Ing. Thesis)
MTA-99-131	Tveiten, Bård Wathne, MK	Fatigue Assessment of Welded Aluminium Ship Details. (Dr.Ing. Thesis)
MTA-99-132	Søreide, Fredrik, MP	Applications of underwater technology in deep water archaeology. Principles and practice. (Dr.Ing. Thesis)
MTA-99-133	Tønnessen, Rune, MH	A Finite Element Method Applied to Unsteady Viscous Flow Around 2D Blunt Bodies With Sharp Corners. (Dr.Ing. Thesis)
MTA-99-134	Elvekrok, Dag R., MP	Engineering Integration in Field Development Projects in the Norwegian Oil and Gas Industry. The Supplier Management of Norne. (Dr.Ing. Thesis)
MTA-99-135	Fagerholt, Kjetil, MP	Optimeringsbaserte Metoder for Ruteplanlegging innen skipsfart. (Dr.Ing. Thesis)
MTA-99-136	Bysveen, Marie, MM	Visualization in Two Directions on a Dynamic Combustion Rig for Studies of Fuel Quality. (Dr.Ing. Thesis)
MTA-2000-137	Storteig, Eskild, MM	Dynamic characteristics and leakage performance of liquid annular seals in centrifugal pumps. (Dr.Ing. Thesis)
MTA-2000-138	Sagli, Gro, MK	Model uncertainty and simplified estimates of long term extremes of hull girder loads in ships. (Dr.Ing. Thesis)
MTA-2000-139	Tronstad, Harald, MK	Nonlinear analysis and design of cable net structures like fishing gear based on the finite element method. (Dr.Ing. Thesis)
MTA-2000-140	Kroneberg, André, MP	Innovation in shipping by using scenarios. (Dr.Ing. Thesis)
MTA-2000-141	Haslum, Herbjørn Alf, MH	Simplified methods applied to nonlinear motion of spar platforms. (Dr.Ing. Thesis)

MTA-2001-142	Samdal, Ole Johan, MM	Modelling of Degradation Mechanisms and Stressor Interaction on Static Mechanical Equipment Residual Lifetime. (Dr.Ing. Thesis)
MTA-2001-143	Baarholm, Rolf Jarle, MH	Theoretical and experimental studies of wave impact underneath decks of offshore platforms. (Dr.Ing. Thesis)
MTA-2001-144	Wang, Lihua, MK	Probabilistic Analysis of Nonlinear Wave-induced Loads on Ships. (Dr.Ing. Thesis)
MTA-2001-145	Kristensen, Odd H. Holt, MK	Ultimate Capacity of Aluminium Plates under Multiple Loads, Considering HAZ Properties. (Dr.Ing. Thesis)
MTA-2001-146	Greco, Marilena, MH	A Two-Dimensional Study of Green-Water Loading. (Dr.Ing. Thesis)
MTA-2001-147	Heggelund, Svein E., MK	Calculation of Global Design Loads and Load Effects in Large High Speed Catamarans. (Dr.Ing. Thesis)
MTA-2001-148	Babalola, Olusegun T., MK	Fatigue Strength of Titanium Risers – Defect Sensitivity. (Dr.Ing. Thesis)
MTA-2001-149	Mohammed, Abuu K., MK	Nonlinear Shell Finite Elements for Ultimate Strength and Collapse Analysis of Ship Structures. (Dr.Ing. Thesis)
MTA-2002-150	Holmedal, Lars E., MH	Wave-current interactions in the vicinity of the sea bed. (Dr.Ing. Thesis)
MTA-2002-151	Rognebakke, Olav F., MH	Sloshing in rectangular tanks and interaction with ship motions. (Dr.Ing. Thesis)
MTA-2002-152	Lader, Pål Furset, MH	Geometry and Kinematics of Breaking Waves. (Dr.Ing. Thesis)
MTA-2002-153	Yang, Qinzheng, MH	Wash and wave resistance of ships in finite water depth. (Dr.Ing. Thesis)
MTA-2002-154	Melhus, Øyvin, MM	Utilization of VOC in Diesel Engines. Ignition and combustion of VOC released by crude oil tankers. (Dr.Ing. Thesis)
MTA-2002-155	Ronæss, Marit, MH	Wave Induced Motions of Two Ships Advancing on Parallel Course. (Dr.Ing. Thesis)
MTA-2002-156	Økland, Ole D., MK	Numerical and experimental investigation of whipping in twin hull vessels exposed to severe wet deck slamming. (Dr.Ing. Thesis)
MTA-2002-157	Ge, Chunhua, MK	Global Hydroelastic Response of Catamarans due to Wet Deck Slamming. (Dr.Ing. Thesis)
MTA-2002-158	Byklum, Eirik, MK	Nonlinear Shell Finite Elements for Ultimate Strength and Collapse Analysis of Ship Structures. (Dr.Ing. Thesis)
IMT-2003-1	Chen, Haibo, MK	Probabilistic Evaluation of FPSO-Tanker Collision in Tandem Offloading Operation. (Dr.Ing. Thesis)
IMT-2003-2	Skaugset, Kjetil Bjørn, MK	On the Suppression of Vortex Induced Vibrations of Circular Cylinders by Radial Water Jets. (Dr.Ing. Thesis)
IMT-2003-3	Chezhian, Muthu	Three-Dimensional Analysis of Slamming. (Dr.Ing. Thesis)
IMT-	Buhaug, Øyvind	Deposit Formation on Cylinder Liner Surfaces in

2003-4		Medium Speed Engines. (Dr.Ing. Thesis)
IMT-2003-5	Tregde, Vidar	Aspects of Ship Design: Optimization of Aft Hull with Inverse Geometry Design. (Dr.Ing. Thesis)
IMT-2003-6	Wist, Hanne Therese	Statistical Properties of Successive Ocean Wave Parameters. (Dr.Ing. Thesis)
IMT-2004-7	Ransau, Samuel	Numerical Methods for Flows with Evolving Interfaces. (Dr.Ing. Thesis)
IMT-2004-8	Soma, Torkel	Blue-Chip or Sub-Standard. A data interrogation approach of identity safety characteristics of shipping organization. (Dr.Ing. Thesis)
IMT-2004-9	Ersdal, Svein	An experimental study of hydrodynamic forces on cylinders and cables in near axial flow. (Dr.Ing. Thesis)
IMT-2005-10	Brodtkorb, Per Andreas	The Probability of Occurrence of Dangerous Wave Situations at Sea. (Dr.Ing. Thesis)
IMT-2005-11	Yttervik, Rune	Ocean current variability in relation to offshore engineering. (Dr.Ing. Thesis)
IMT-2005-12	Fredheim, Arne	Current Forces on Net-Structures. (Dr.Ing. Thesis)
IMT-2005-13	Heggernes, Kjetil	Flow around marine structures. (Dr.Ing. Thesis
IMT-2005-14	Fouques, Sebastien	Lagrangian Modelling of Ocean Surface Waves and Synthetic Aperture Radar Wave Measurements. (Dr.Ing. Thesis)
IMT-2006-15	Holm, Håvard	Numerical calculation of viscous free surface flow around marine structures. (Dr.Ing. Thesis)
IMT-2006-16	Bjørheim, Lars G.	Failure Assessment of Long Through Thickness Fatigue Cracks in Ship Hulls. (Dr.Ing. Thesis)
IMT-2006-17	Hansson, Lisbeth	Safety Management for Prevention of Occupational Accidents. (Dr.Ing. Thesis)
IMT-2006-18	Zhu, Xinying	Application of the CIP Method to Strongly Nonlinear Wave-Body Interaction Problems. (Dr.Ing. Thesis)
IMT-2006-19	Reite, Karl Johan	Modelling and Control of Trawl Systems. (Dr.Ing. Thesis)
IMT-2006-20	Smogeli, Øyvind Notland	Control of Marine Propellers. From Normal to Extreme Conditions. (Dr.Ing. Thesis)
IMT-2007-21	Storhaug, Gaute	Experimental Investigation of Wave Induced Vibrations and Their Effect on the Fatigue Loading of Ships. (Dr.Ing. Thesis)
IMT-2007-22	Sun, Hui	A Boundary Element Method Applied to Strongly Nonlinear Wave-Body Interaction Problems. (PhD Thesis, CeSOS)
IMT-2007-23	Rustad, Anne Marthine	Modelling and Control of Top Tensioned Risers. (PhD Thesis, CeSOS)
IMT-2007-24	Johansen, Vegar	Modelling flexible slender system for real-time simulations and control applications
IMT-	Wroldsen, Anders Sunde	Modelling and control of tensegrity structures.

2007-25		(PhD Thesis, CeSOS)
IMT-2007-26	Aronsen, Kristoffer Høye	An experimental investigation of in-line and combined inline and cross flow vortex induced vibrations. (Dr. avhandling, IMT)
IMT-2007-27	Gao, Zhen	Stochastic Response Analysis of Mooring Systems with Emphasis on Frequency-domain Analysis of Fatigue due to Wide-band Response Processes (PhD Thesis, CeSOS)
IMT-2007-28	Thorstensen, Tom Anders	Lifetime Profit Modelling of Ageing Systems Utilizing Information about Technical Condition. (Dr.ing. thesis, IMT)
IMT-2008-29	Refsnes, Jon Erling Gorset	Nonlinear Model-Based Control of Slender Body AUVs (PhD Thesis, IMT)
IMT-2008-30	Berntsen, Per Ivar B.	Structural Reliability Based Position Mooring. (PhD-Thesis, IMT)
IMT-2008-31	Ye, Naiquan	Fatigue Assessment of Aluminium Welded Box-stiffener Joints in Ships (Dr.ing. thesis, IMT)
IMT-2008-32	Radan, Damir	Integrated Control of Marine Electrical Power Systems. (PhD-Thesis, IMT)
IMT-2008-33	Thomassen, Paul	Methods for Dynamic Response Analysis and Fatigue Life Estimation of Floating Fish Cages. (Dr.ing. thesis, IMT)
IMT-2008-34	Pákozdi, Csaba	A Smoothed Particle Hydrodynamics Study of Two-dimensional Nonlinear Sloshing in Rectangular Tanks. (Dr.ing.thesis, IMT/ CeSOS)
IMT-2007-35	Grytøyr, Guttorm	A Higher-Order Boundary Element Method and Applications to Marine Hydrodynamics. (Dr.ing.thesis, IMT)
IMT-2008-36	Drummen, Ingo	Experimental and Numerical Investigation of Nonlinear Wave-Induced Load Effects in Containerships considering Hydroelasticity. (PhD thesis, CeSOS)
IMT-2008-37	Skejic, Renato	Maneuvering and Seakeeping of a Singel Ship and of Two Ships in Interaction. (PhD-Thesis, CeSOS)
IMT-2008-38	Harlem, Alf	An Age-Based Replacement Model for Repairable Systems with Attention to High-Speed Marine Diesel Engines. (PhD-Thesis, IMT)
IMT-2008-39	Alsos, Hagbart S.	Ship Grounding. Analysis of Ductile Fracture, Bottom Damage and Hull Girder Response. (PhD-thesis, IMT)
IMT-2008-40	Graczyk, Mateusz	Experimental Investigation of Sloshing Loading and Load Effects in Membrane LNG Tanks Subjected to Random Excitation. (PhD-thesis, CeSOS)
IMT-2008-41	Taghipour, Reza	Efficient Prediction of Dynamic Response for Flexible amd Multi-body Marine Structures. (PhD-thesis, CeSOS)
IMT-2008-42	Ruth, Eivind	Propulsion control and thrust allocation on marine vessels. (PhD thesis, CeSOS)
IMT-2008-43	Nystad, Bent Helge	Technical Condition Indexes and Remaining Useful Life of Aggregated Systems. PhD thesis, IMT

IMT-2008-44	Soni, Prashant Kumar	Hydrodynamic Coefficients for Vortex Induced Vibrations of Flexible Beams, PhD thesis, CeSOS
IMT-2009-45	Amlashi, Hadi K.K.	Ultimate Strength and Reliability-based Design of Ship Hulls with Emphasis on Combined Global and Local Loads. PhD Thesis, IMT
IMT-2009-46	Pedersen, Tom Arne	Bond Graph Modelling of Marine Power Systems. PhD Thesis, IMT
IMT-2009-47	Kristiansen, Trygve	Two-Dimensional Numerical and Experimental Studies of Piston-Mode Resonance. PhD-Thesis, CeSOS
IMT-2009-48	Ong, Muk Chen	Applications of a Standard High Reynolds Number Model and a Stochastic Scour Prediction Model for Marine Structures. PhD-thesis, IMT
IMT-2009-49	Hong, Lin	Simplified Analysis and Design of Ships subjected to Collision and Grounding. PhD-thesis, IMT
IMT-2009-50	Koushan, Kamran	Vortex Induced Vibrations of Free Span Pipelines, PhD thesis, IMT
IMT-2009-51	Korsvik, Jarl Eirik	Heuristic Methods for Ship Routing and Scheduling. PhD-thesis, IMT
IMT-2009-52	Lee, Jihoon	Experimental Investigation and Numerical in Analyzing the Ocean Current Displacement of Longlines. Ph.d.-Thesis, IMT.
IMT-2009-53	Vestbøstad, Tone Gran	A Numerical Study of Wave-in-Deck Impact usin a Two-Dimensional Constrained Interpolation Profile Method, Ph.d.thesis, CeSOS.
IMT-2009-54	Bruun, Kristine	Bond Graph Modelling of Fuel Cells for Marine Power Plants. Ph.d.-thesis, IMT
IMT 2009-55	Holstad, Anders	Numerical Investigation of Turbulence in a Sekwed Three-Dimensional Channel Flow, Ph.d.-thesis, IMT.
IMT 2009-56	Ayala-Uraga, Efren	Reliability-Based Assessment of Deteriorating Ship-shaped Offshore Structures, Ph.d.-thesis, IMT
IMT 2009-57	Kong, Xiangjun	A Numerical Study of a Damaged Ship in Beam Sea Waves. Ph.d.-thesis, IMT/CeSOS.
IMT 2010-58	Kristiansen, David	Wave Induced Effects on Floaters of Aquaculture Plants, Ph.d.-thesis, CeSOS.
IMT 2010-59	Ludvigsen, Martin	An ROV-Toolbox for Optical and Acoustic Scientific Seabed Investigation. Ph.d.-thesis IMT.
IMT 2010-60	Hals, Jørgen	Modelling and Phase Control of Wave-Energy Converters. Ph.d.thesis, CeSOS.
IMT 2010- 61	Shu, Zhi	Uncertainty Assessment of Wave Loads and Ultimate Strength of Tankers and Bulk Carriers in a Reliability Framework. Ph.d. Thesis, IMT/ CeSOS
IMT 2010-62	Shao, Yanlin	Numerical Potential-Flow Studies on Weakly-Nonlinear Wave-Body Interactions with/without Small Forward Speed, Ph.d.thesis,CeSOS.
IMT 2010-63	Califano, Andrea	Dynamic Loads on Marine Propellers due to Intermittent Ventilation. Ph.d.thesis, IMT.

IMT 2010-64	El Khoury, George	Numerical Simulations of Massively Separated Turbulent Flows, Ph.d.-thesis, IMT
IMT 2010-65	Seim, Knut Sponheim	Mixing Process in Dense Overflows with Emphasis on the Faroe Bank Channel Overflow. Ph.d.thesis, IMT
IMT 2010-66	Jia, Huirong	Structural Analysis of Intect and Damaged Ships in a Collission Risk Analysis Perspective. Ph.d.thesis CeSoS.
IMT 2010-67	Jiao, Linlin	Wave-Induced Effects on a Pontoon-type Very Large Floating Structures (VLFS). Ph.D.-thesis, CeSOS.
IMT 2010-68	Abrahamsen, Bjørn Christian	Sloshing Induced Tank Roof with Entrapped Air Pocket. Ph.d.thesis, CeSOS.
IMT 2011-69	Karimirad, Madjid	Stochastic Dynamic Response Analysis of Spar-Type Wind Turbines with Catenary or Taut Mooring Systems. Ph.d.-thesis, CeSOS.
IMT - 2011-70	Erlend Meland	Condition Monitoring of Safety Critical Valves. Ph.d.-thesis, IMT.
IMT – 2011-71	Yang, Limin	Stochastic Dynamic System Analysis of Wave Energy Converter with Hydraulic Power Take-Off, with Particular Reference to Wear Damage Analysis, Ph.d. Thesis, CeSOS.
IMT – 2011-72	Visscher, Jan	Application of Particla Image Velocimetry on Turbulent Marine Flows, Ph.d.Thesis, IMT.
IMT – 2011-73	Su, Biao	Numerical Predictions of Global and Local Ice Loads on Ships. Ph.d.Thesis, CeSOS.
IMT – 2011-74	Liu, Zhenhui	Analytical and Numerical Analysis of Iceberg Collision with Ship Structures. Ph.d.Thesis, IMT.
IMT – 2011-75	Aarsæther, Karl Gunnar	Modeling and Analysis of Ship Traffic by Observation and Numerical Simulation. Ph.d.Thesis, IMT.
Imt – 2011-76	Wu, Jie	Hydrodynamic Force Identification from Stochastic Vortex Induced Vibration Experiments with Slender Beams. Ph.d.Thesis, IMT.
Imt – 2011-77	Amini, Hamid	Azimuth Propulsors in Off-design Conditions. Ph.d.Thesis, IMT.
IMT – 2011-78	Nguyen, Tan-Hoi	Toward a System of Real-Time Prediction and Monitoring of Bottom Damage Conditions During Ship Grounding. Ph.d.thesis, IMT.
IMT- 2011-79	Tavakoli, Mohammad T.	Assessment of Oil Spill in Ship Collision and Grounding, Ph.d.thesis, IMT.
IMT- 2011-80	Guo, Bingjie	Numerical and Experimental Investigation of Added Resistance in Waves. Ph.d.Thesis, IMT.
IMT- 2011-81	Chen, Qiaofeng	Ultimate Strength of Aluminium Panels, considering HAZ Effects, IMT

IMT-2012-82	Kota, Ravikiran S.	Wave Loads on Decks of Offshore Structures in Random Seas, CeSOS.
IMT-2012-83	Sten, Ronny	Dynamic Simulation of Deep Water Drilling Risers with Heave Compensating System, IMT.
IMT-2012-84	Berle, Øyvind	Risk and resilience in global maritime supply chains, IMT.
IMT-2012-85	Fang, Shaoji	Fault Tolerant Position Mooring Control Based on Structural Reliability, CeSOS.
IMT-2012-86	You, Jikun	Numerical studies on wave forces and moored ship motions in intermediate and shallow water, CeSOS.
IMT-2012-87	Xiang ,Xu	Maneuvering of two interacting ships in waves, CeSOS
IMT-2012-88	Dong, Wenbin	Time-domain fatigue response and reliability analysis of offshore wind turbines with emphasis on welded tubular joints and gear components, CeSOS
IMT-2012-89	Zhu, Suji	Investigation of Wave-Induced Nonlinear Load Effects in Open Ships considering Hull Girder Vibrations in Bending and Torsion, CeSOS
IMT-2012-90	Zhou, Li	Numerical and Experimental Investigation of Station-keeping in Level Ice, CeSOS
IMT-2012-91	Ushakov, Sergey	Particulate matter emission characteristics from diesel enignes operating on conventional and alternative marine fuels, IMT
IMT-2013-1	Yin, Decao	Experimental and Numerical Analysis of Combined In-line and Cross-flow Vortex Induced Vibrations, CeSOS
IMT-2013-2	Kurniawan, Adi	Modelling and geometry optimisation of wave energy converters, CeSOS
IMT-2013-3	Al Ryati, Nabil	Technical condition indexes doe auxiliary marine diesel engines, IMT
IMT-2013-4	Firoozkoohi, Reza	Experimental, numerical and analytical investigation of the effect of screens on sloshing, CeSOS
IMT-2013-5	Ommani, Babak	Potential-Flow Predictions of a Semi-Displacement Vessel Including Applications to Calm Water Broaching, CeSOS
IMT-2013-6	Xing, Yihan	Modelling and analysis of the gearbox in a floating spar-type wind turbine, CeSOS
IMT-7-2013	Balland, Océane	Optimization models for reducing air emissions from ships, IMT
IMT-8-2013	Yang, Dan	Transitional wake flow behind an inclined flat plate-----Computation and analysis, IMT
IMT-9-2013	Abdillah, Suyuthi	Prediction of Extreme Loads and Fatigue Damage for a Ship Hull due to Ice Action, IMT
IMT-10-2013	Ramìrez, Pedro Agustìn Pèrez	Ageing management and life extension of technical systems- Concepts and methods applied to oil and gas facilities, IMT

IMT-11-2013	Chuang, Zhenju	Experimental and Numerical Investigation of Speed Loss due to Seakeeping and Maneuvering. IMT
IMT-12-2013	Etemaddar, Mahmoud	Load and Response Analysis of Wind Turbines under Atmospheric Icing and Controller System Faults with Emphasis on Spar Type Floating Wind Turbines, IMT
IMT-13-2013	Lindstad, Haakon	Strategies and measures for reducing maritime CO2 emissons, IMT
IMT-14-2013	Haris, Sabril	Damage interaction analysis of ship collisions, IMT
IMT-15-2013	Shainee, Mohamed	Conceptual Design, Numerical and Experimental Investigation of a SPM Cage Concept for Offshore Mariculture, IMT
IMT-16-2013	Gansel, Lars	Flow past porous cylinders and effects of biofouling and fish behavior on the flow in and around Atlantic salmon net cages, IMT
IMT-17-2013	Gaspar, Henrique	Handling Aspects of Complexity in Conceptual Ship Design, IMT
IMT-18-2013	Thys, Maxime	Theoretical and Experimental Investigation of a Free Running Fishing Vessel at Small Frequency of Encounter, CeSOS
IMT-19-2013	Aglen, Ida	VIV in Free Spanning Pipelines, CeSOS
IMT-1-2014	Song, An	Theoretical and experimental studies of wave diffraction and radiation loads on a horizontally submerged perforated plate, CeSOS
IMT-2-2014	Rogne, Øyvind Ygre	Numerical and Experimental Investigation of a Hinged 5-body Wave Energy Converter, CeSOS
IMT-3-2014	Dai, Lijuan	Safe and efficient operation and maintenance of offshore wind farms ,IMT
IMT-4-2014	Bachynski, Erin Elizabeth	Design and Dynamic Analysis of Tension Leg Platform Wind Turbines, CeSOS
IMT-5-2014	Wang, Jingbo	Water Entry of Freefall Wedged – Wedge motions and Cavity Dynamics, CeSOS
IMT-6-2014	Kim, Ekaterina	Experimental and numerical studies related to the coupled behavior of ice mass and steel structures during accidental collisions, IMT
IMT-7-2014	Tan, Xiang	Numerical investigation of ship's continuous- mode icebreaking in leverl ice, CeSOS
IMT-8-2014	Muliawan, Made Jaya	Design and Analysis of Combined Floating Wave and Wind Power Facilities, with Emphasis on Extreme Load Effects of the Mooring System, CeSOS
IMT-9-2014	Jiang, Zhiyu	Long-term response analysis of wind turbines with an emphasis on fault and shutdown conditions, IMT
IMT-10-2014	Dukan, Fredrik	ROV Motion Control Systems, IMT
IMT-11-2014	Grimsmo, Nils I.	Dynamic simulations of hydraulic cylinder for heave compensation of deep water drilling risers, IMT

IMT-12-2014	Kvittem, Marit I.	Modelling and response analysis for fatigue design of a semisubmersible wind turbine, CeSOS
IMT-13-2014	Akhtar, Juned	The Effects of Human Fatigue on Risk at Sea, IMT
IMT-14-2014	Syahroni, Nur	Fatigue Assessment of Welded Joints Taking into Account Effects of Residual Stress, IMT
IMT-1-2015	Bøckmann, Eirik	Wave Propulsion of ships, IMT
IMT-2-2015	Wang, Kai	Modelling and dynamic analysis of a semi-submersible floating vertical axis wind turbine, CeSOS
IMT-3-2015	Fredriksen, Arnt Gunvald	A numerical and experimental study of a two-dimensional body with moonpool in waves and current, CeSOS
IMT-4-2015	Jose Patricio Gallardo Canabes	Numerical studies of viscous flow around bluff bodies, IMT
IMT-5-2015	Vegard Longva	Formulation and application of finite element techniques for slender marine structures subjected to contact interactions, IMT
IMT-6-2015	Jacobus De Vaal	Aerodynamic modelling of floating wind turbines, CeSOS
IMT-7-2015	Fachri Nasution	Fatigue Performance of Copper Power Conductors, IMT
IMT-8-2015	Oleh I Karpa	Development of bivariate extreme value distributions for applications in marine technology,CeSOS
IMT-9-2015	Daniel de Almeida Fernandes	An output feedback motion control system for ROVs, AMOS
IMT-10-2015	Bo Zhao	Particle Filter for Fault Diagnosis: Application to Dynamic Positioning Vessel and Underwater Robotics, CeSOS
IMT-11-2015	Wenting Zhu	Impact of emission allocation in maritime transportation, IMT
IMT-12-2015	Amir Rasekhi Nejad	Dynamic Analysis and Design of Gearboxes in Offshore Wind Turbines in a Structural Reliability Perspective, CeSOS
IMT-13-2015	Arturo Jesùs Ortega Malca	Dynamic Response of Flexibles Risers due to Unsteady Slug Flow, CeSOS
IMT-14-2015	Dagfinn Husjord	Guidance and decision-support system for safe navigation of ships operating in close proximity, IMT
IMT-15-2015	Anirban Bhattacharyya	Ducted Propellers: Behaviour in Waves and Scale Effects, IMT
IMT-16-2015	Qin Zhang	Image Processing for Ice Parameter Identification in Ice Management, IMT

IMT-1-2016	Vincentius Rumawas	Human Factors in Ship Design and Operation: An Experiential Learning, IMT
IMT-2-2016	Martin Storheim	Structural response in ship-platform and ship-ice collisions, IMT
IMT-3-2016	Mia Abrahamsen Prsic	Numerical Simulations of the Flow around single and Tandem Circular Cylinders Close to a Plane Wall, IMT
IMT-4-2016	Tufan Arslan	Large-eddy simulations of cross-flow around ship sections, IMT
IMT-5-2016	Pierre Yves-Henry	Parametrisation of aquatic vegetation in hydraulic and coastal research,IMT
IMT-6-2016	Lin Li	Dynamic Analysis of the Instalation of Monopiles for Offshore Wind Turbines, CeSOS
IMT-7-2016	Øivind Kåre Kjerstad	Dynamic Positioning of Marine Vessels in Ice, IMT
IMT-8-2016	Xiaopeng Wu	Numerical Analysis of Anchor Handling and Fish Trawling Operations in a Safety Perspective, CeSOS
IMT-9-2016	Zhengshun Cheng	Integrated Dynamic Analysis of Floating Vertical Axis Wind Turbines, CeSOS
IMT-10-2016	Ling Wan	Experimental and Numerical Study of a Combined Offshore Wind and Wave Energy Converter Concept
IMT-11-2016	Wei Chai	Stochastic dynamic analysis and reliability evaluation of the roll motion for ships in random seas, CeSOS
IMT-12-2016	Øyvind Selnes Patricksson	Decision support for conceptual ship design with focus on a changing life cycle and future uncertainty, IMT
IMT-13-2016	Mats Jørgen Thorsen	Time domain analysis of vortex-induced vibrations, IMT
IMT-14-2016	Edgar McGuinness	Safety in the Norwegian Fishing Fleet – Analysis and measures for improvement, IMT
IMT-15-2016	Sepideh Jafarzadeh	Energy effiency and emission abatement in the fishing fleet, IMT
IMT-16-2016	Wilson Ivan Guachamin Acero	Assessment of marine operations for offshore wind turbine installation with emphasis on response-based operational limits, IMT
IMT-17-2016	Mauro Candeloro	Tools and Methods for Autonomous Operations on Seabed and Water Coumn using Underwater Vehicles, IMT
IMT-18-2016	Valentin Chabaud	Real-Time Hybrid Model Testing of Floating Wind Tubines, IMT
IMT-1-2017	Mohammad Saud Afzal	Three-dimensional streaming in a sea bed boundary layer

IMT-2-2017	Peng Li	A Theoretical and Experimental Study of Wave-induced Hydroelastic Response of a Circular Floating Collar
IMT-3-2017	Martin Bergström	A simulation-based design method for arctic maritime transport systems
IMT-4-2017	Bhushan Taskar	The effect of waves on marine propellers and propulsion
IMT-5-2017	Mohsen Bardestani	A two-dimensional numerical and experimental study of a floater with net and sinker tube in waves and current
IMT-6-2017	Fatemeh Hoseini Dadmarzi	Direct Numerical Simualtion of turbulent wakes behind different plate configurations
IMT-7-2017	Michel R. Miyazaki	Modeling and control of hybrid marine power plants
IMT-8-2017	Giri Rajasekhar Gunnu	Safety and effiency enhancement of anchor handling operations with particular emphasis on the stability of anchor handling vessels
IMT-9-2017	Kevin Koosup Yum	Transient Performance and Emissions of a Turbocharged Diesel Engine for Marine Power Plants
IMT-10-2017	Zhaolong Yu	Hydrodynamic and structural aspects of ship collisions
IMT-11-2017	Martin Hassel	Risk Analysis and Modelling of Allisions between Passing Vessels and Offshore Installations
IMT-12-2017	Astrid H. Brodtkorb	Hybrid Control of Marine Vessels – Dynamic Positioning in Varying Conditions
IMT-13-2017	Kjersti Bruserud	Simultaneous stochastic model of waves and current for prediction of structural design loads
IMT-14-2017	Finn-Idar Grøtta Giske	Long-Term Extreme Response Analysis of Marine Structures Using Inverse Reliability Methods
IMT-15-2017	Stian Skjong	Modeling and Simulation of Maritime Systems and Operations for Virtual Prototyping using co-Simulations
IMT-1-2018	Yingguang Chu	Virtual Prototyping for Marine Crane Design and Operations
IMT-2-2018	Sergey Gavrilin	Validation of ship manoeuvring simulation models
IMT-3-2018	Jeevith Hegde	Tools and methods to manage risk in autonomous subsea inspection
IMT-4-2018	Ida M. Strand	Sea Loads on Closed Flexible Fish Cages